

Forschungszentrum Karlsruhe
Technik und Umwelt

Wissenschaftliche Berichte
FZKA 5858
EUR 17512 EN

Nuclear Fusion Project
Annual Report of the
Association Forschungszentrum
Karlsruhe/EURATOM
October 1995 – September 1996

Projekt Kernfusion

Januar 1997

Forschungszentrum Karlsruhe
Technik und Umwelt

Wissenschaftliche Berichte

FZKA 5858

EUR 17512 EN

Nuclear Fusion Project
Annual Report of the
Association Forschungszentrum
Karlsruhe/EURATOM
October 1995 - September 1996

compiled by G. Kast
Projekt Kernfusion

Januar 1997

Als Manuskript vervielfältigt
Für diesen Bericht behalten wir uns alle Rechte vor

Forschungszentrum Karlsruhe GmbH
Postfach 3640, 76021 Karlsruhe

ISSN 0947-8620

Preface

The Fusion Project of the Karlsruhe Research Center (FZK) was founded in 1982 under an association agreement with the Commission of the European Communities to support the European Fusion Technology Programme.

Various nuclear fission programmes and earlier component development for particle accelerators were the basis for a broad input of FZK in almost all areas of the newly founded Next Step and Long Term Fusion Technology Programmes.

Major test facilities were built or upgraded during the past decade. To name only the most important ones: TOSKA, a test facility for large (up to 5 m size) superconducting magnets, the tritium laboratory TLK with more than 1000 m² of experimental area and 20 g of tritium inventory, and the dual beam facility to simulate irradiation effects under fusion conditions.

Having been developed for the requirements of the Next European Torus Programme initially, most of the installations are equally well suited for the International Tokamak Experimental Reactor ITER (TOSKA, TLK and smaller facilities for the test of vacuum pumping systems, plasma facing materials and microwave components). Today about fifty percent of FZK's fusion programme is contracted to ITER via the contribution of the European home team.

Medium term, cooperation on the recently approved Wendelstein 7X Stellarator will form an increasing constituent of our programme concentrating on the areas of gyrotron development and qualification of superconducting coils.

The FZK fusion project has permanently put emphasis on supporting the development of breeding blankets and related materials research. After selection of blanket concepts in the European frame, a concentration process resulted in restructuring the blanket programme. FZK activities now concentrate on the helium cooled ceramic pebble bed blanket. A module of this blanket shall be tested in ITER.

Closely related to blanket development is the long term materials programme. FZK work is focused on reduced activation ferritic-martensitic steels. Important project resources for irradiations and hot cell work are devoted over long periods of time to characterize and improve the performance of suitable structural materials. A major fraction of underlying technology support (support for not strongly task oriented effort) is applied to this work area.

The yearly report of the FZK-EURATOM association is structured according to the organizational scheme of the European Technology Programme. ITER references are given in the nomenclature valid during the reporting period.

The annexes provide the reader with some information on participating departments and on the project management structure.

The achievements documented in this report were made possible due to the support of the partners of FZK, the Federal Republic of Germany, the State of Baden-Württemberg and by additional funds of the Commission of the European Community. The involvement of industry and the cooperation with many research institutes sharing with us the interest in the development of nuclear fusion is particularly acknowledged.

J.E. Vetter

Report on the Next Step Technology Programme

Plasma Facing Components and Plasma Engineering			1
G 17 TT 25	(T 227)	Tritium Permeation and Inventory	2
CTA-EU-T 9		Fabrication and Test of Water-Cooled, Small Size FW Mockups	3
G 17 TT 25	(T 226 b)	Plasma Disruption Simulation	7
G 55 TT 01	(T 26/T 246)	Ceramics for Heating and Current Drive and Diagnostic Systems	9
Superconducting Magnets			11
MCOI		ITER TF-Model Coil Development	12
N 11 TT 19 94-02-15 FE 02	(MTOS 1)	Preparation of ITER TF-Model Coil Test Facility	13
MBAC		High Field Operation of NbTi at 1.8 K	16
M 27		Critical Current vs. Strain Tests on EU Strands and Subsize CICC's with Stainless Steel and Incoloy Jackets	18
M 31		Development of 60 kA Current Leads Using High Temperature Superconductors	19
N 11 TD 58	(SEA 3)	Reference Accident Sequences - Magnet Systems	23
CTA-EU-D 36	(SEP 2)	Environment Impact	25
Vacuum and Fuel Cycle			27
G 18 TT 22	(T 228)	Cryopump Development	28
T 234 A		Oil-Free Mechanical Pump Development	36
N 32 TT 06	(T 299/T 332 b)	Plasma Exhaust Processing Technology	38
TEP 3		Tritium Storage	42
Vessel in-Vessel			44
G 16 TT 82	(T 218)	Shielding Neutronics Experiments	44
G 16 TD 21	(D 203)	ITER Breeding Blanket Development and Design	48
Studies for ITER / NET			50
ERB 5000 CT 95 0064 NET	(NET/95-384)	ITER Magnets and TFMC Stress Analysis	51
ERB 5004 CT 960050	(NET/96-405)	(Subtask of ITER Task MD9 for 1996) Transient Voltage Behaviour for the ITER TF Coil	53
ERB 5004 CT 960053	(NET/96-408)	Characterization of Jacket Material	56

Gyrotron and Window Development	59
Gyrotron Development (includes ITER Tasks T 24 and T 245/6)	60
High Power ECW Windows (includes ITER Tasks T 25, T 245/6 and D 321)	65
<u>Long-Term Technology Programme</u>	67
Blanket Development Programme	68
WP A 1 Design and Analysis	
A 1.1.1 Design and Fabrication Alternatives for the Blanket Box	70
A 1.4.1 Availability Analysis and Data Base	71
WP A 3 Pb-17Li Physico-Chemistry Experiments	
A 3.1.1 Radiological Important Impurities and Nuclides	72
A 3.1.2 Behavior and Removal of Corrosion Products	73
A 3.3.1 Li Behavior and Adjustment	74
WP A 4 MHD	
A 4.1.1 / 4.2.1 Theoretical and Experimental Investigations on Natural Convection in WCLL under MHD Conditions	75
WP A 5 Tritium Control including Permeation Barriers	
A 5.1.1 Coating and Tritium Barrier Development	79
A 5.3.2 Influence of the Magnetic Field on the Self-healing of Tritium Permeation Barriers in Flowing Pb-17Li	81
WP A 7 Safety related Activities for DEMO and ITER Test Module	
A 7.1.1 Safety Studies for DEMO Blanket and ITER Test Module	82
WP B 1 Design and Analysis	
B 1.1.1 Design Optimization/Adaptation to Updated DEMO Conditions	83
B 1.2.1 Design, Layout and Integration of ITER Test Module and Internal Circuits	85
B 1.3.1 Electromagnetic Effects with a Ferromagnetic Structural Material	92
B 1.3.2 Calculation of the Combined Stresses in the Blanket and Test Module	100
B 1.4.1 Reliability Assessment including Ancillary Systems	102
WP B 2 Fabrication, Assembly and Development Studies of Blanket Segments	
B 2.1.1 Fabrication, Assembly and Development Studies of Segment Box and Cooling Plates	104
WP B 3 Ceramic Breeder Pebbles	
B 3.1.1 Li ₄ SiO ₄ Pebbles Characterization and Optimization of Large Scale Production	107
B 3.2.1 Irradiation of Li ₄ SiO ₄ + TeO ₂ pebbles	109

WP B 4 Beryllium Pebble Development		
B 4.1.1	Characterization and Optimization of 2 mm and 0.1-0.2 mm Beryllium Pebbles	110
B 4.2.1	Evaluation of Beryllium Irradiation Experiments and Improvements of ANFIBE	113
WP B 5 Tritium Control including Permeation Barriers		
B 5.1.1	Calculation of Tritium Permeation Losses from Purge Gas System and First Wall	119
B 5.2.1	Permeation Tests in Martensitic Structural Material and INCOLOY 800	122
WP B 6 Tritium Extraction		
B 6.1.1	Design of Helium Purification and Tritium Purge Flow Systems including Tritium Extraction	123
WP B 7 Safety related Activities for DEMO and ITER Test Module		
B 7.1.1	Safety Studies for DEMO and ITER Test Module	126
WP B 8 ITER Test Module System and Testing		
B 8.1.1	Tests in HEBLO and Preparation of a Submodule for HEFUS-3 ...	128
Long Term Materials Programme		
WP 1 Martensitic Steels		
1.1	Metallurgical and Mechanical Characterization MANET	131
1.2.1	Metallurgical and Mechanical Characterization F82H mod.	132
1.2.2	Fatigue and Creep Properties of Base Material on LA Martensitic Steels F82H Mod	136
1.4.1	Metallurgical and Mechanical Characterization of OPTIFER Alloys	138
1.4.2	Fatigue and Creep Properties of Base Material on LA Martensitic Steels OPTIFER	141
1.5.0 / 1.5.1	MANITU Irradiation Program	142
1.6.1 / 1.6.2	Effects of Radiation Hardening and He in LAM / In-Beam Fatigue	145
WP 4 Materials Application and Technology		
4.1.2	Fracture Mechanics Studies	149
4.3.1	Weldability Tests (Diffusion Welding)	150
Neutron Source		
ERB 5000 CT 950013 NET (NET/94-366)	Conceptual Design of the International Fusion Materials Irradiation Facility IFMIF (Phase 2)	151
Nuclear Data Base		
Safety and Environmental Assessment - Long Term Programme		
		164

Appendix I: Allocation of Tasks	167
Appendix II: Table of ITER / NET Contracts	170
Appendix III: FZK Departments Contributing to the Fusion Project	171
Appendix IV: Fusion Project Management Staff	172

Plasma Facing Components and Plasma Engineering

window materials and their performance under x-rays has been demonstrated.

Introduction:

Tasks in this area which are all linked to ITER issues have been pursued at FZK with an essentially constant effort but an increasing number of highly interesting results.

H.D. Röhrig

Within T 227 (connected with T 221) where the experiments have been concentrated on tritium retention in irradiated beryllium, it was possible to distinguish the effects of tritium accumulation by nuclear reactions from those of plasma exposure (simulated by gas loading), and it was found that the number of tritium traps in Be is increased by neutron irradiation but drastically reduced at temperatures above ca. 900°C.

Within T 9 (now T 216) small scale First Wall mockups with artificial defects were thermocycled in FIWATKA, and intermediate non-destructive inspections were carried out on the propagation of cracks as a function of the number of cycles. After about 60 000 cycles a gradual arrest of the cracks at the different types of artificial defects was detected so that the test was stopped after 75 000 cycles. A destructive inspection revealed that competing longitudinal cracks had developed at locations which could be identified later on by transient plastic finite element analysis as being the most critical ones.

As a first step for validation of the current FW design further transient calculations have been made to define the goal and parameters of a testing program in FIWATKA, and mockups have been designed accordingly. Experimental work will start as soon as the test pieces have been provided.

Within T 226 b the modelling of disruption erosion has been continued and the codes have been verified by simulation experiments performed in the RF. The agreement concerning the directed total radiation flux was satisfactory, for the soft x-ray component the agreement was good. First 2D analyses of the impact of hot plasma on inclined divertor surfaces showed that instabilities are developing which will drastically decrease the plasma shield efficiency.

What concerns the plasma interaction with the entrance window for ECRH heating, direct particle impact can be avoided by proper design, however it is hardly possible to fully suppress a certain radiation level. Therefore, within T 26/T 246 the effects of radiation on the dielectric properties of window materials are further investigated. Dielectric losses for neutron irradiation at cryogenic temperatures were measured in comparison to ambient temperature irradiation. The expected difference has luckily not been found for sapphire with a certain caveat that the target fluence value, which is presently identified as "tolerable" for ECRH windows, has not fully been attained in the cryogenic irradiation. Advanced grades of silicon and diamond have been characterized and identified as forthcoming candidate

G 17 TT 25 (T 227) Tritium Permeation and Inventory

Subtask 2: H/T Retention Studies in Neutron Irradiated Graphites, CFCs and Doped C Composites

Carbon-based materials and beryllium are candidates for protective layers on plasma-facing components of fusion reactors. In contact with the D-T-plasma these materials absorb tritium and it is anticipated that tritium retention increases with neutron damage due to neutron-induced traps, leading eventually to tritium inventories which represent a safety problem. Previous investigations indeed show that for carbon-based materials tritium retention increases with neutron damage in the range ≤ 0.1 dpa by two to three orders of magnitude [1,2]. For beryllium only one data set exists, indicating a gradual increase of tritium retention with neutron damage in the range < 40 dpa by about a factor ten, which is assumed to be due to irreversible changes of the microstructure of the samples [2].

Because of the poor data base for beryllium, the work concentrated on this material. Tritium retention and its dependence on neutron damage is studied by loading unirradiated and irradiated samples at elevated temperatures in a H_2/T_2 atmosphere ($H_2 + 5$ ppm T_2 , 2 bar, 850 °C, 7 h) and determining the tritium uptake by annealing (850 °C, ~ 1 h, purging with He + 0.1 % H_2). For irradiated beryllium this is difficult because of the huge amount of neutron-produced tritium. To determine the amount of loaded tritium, the two types of tritium must be separated, which is possible due to the different release kinetics. The separation is accomplished by subtracting the normalized release curve of an unloaded irradiated sample from that of the loaded irradiated sample. Normalizing is done at the end of the annealing run, where the loaded tritium is essentially released (Fig. 1).

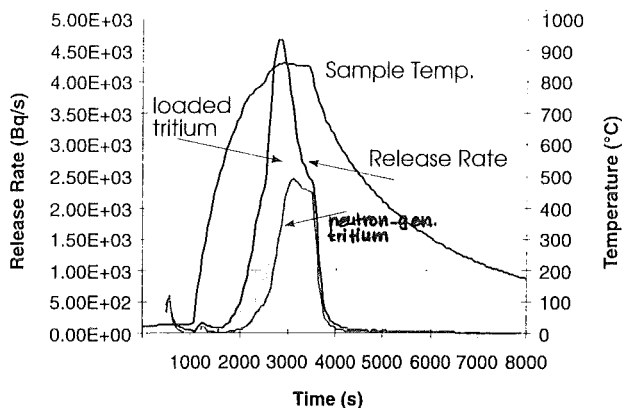


Fig. 1: Release of loaded and neutron-generated tritium from irradiated beryllium.

The samples studied were manufactured by Brush-Wellman (type S200 HIP) and irradiated in the BR2 reactor in Mol (irradiation MOL F-BSBE1) at temperatures between 235 and 600 °C to a neutron fluence of $\sim 1.6 \times 10^{21}$ (~ 1.6 dpa).

To check the reproducibility of the results and the thermal stability of tritium traps, a series of loading/annealing cycles were performed with the same samples. After the first two loadings the tritium uptake of the irradiated sample was found to be 10 to 20 times larger than that of the unirradiated sample. The tritium uptake of both the irradiated and the unirradiated sample and also the uptake ratio (irradiated/unirradiated) decreased steadily from cycle to cycle (after several ten hours at 850 °C and 6 h at 950 °C the uptake of the irradiated sample decreased by more than a factor ten). The following conclusions can be drawn from these results:

- tritium traps exist already in unirradiated beryllium
- further traps are produced by neutrons
- at 850 °C the traps are slowly and at 950 °C they are rapidly destroyed.

In addition, first tests with advanced silicon doped carbon fibre composites (CFC) of type SEP-N31C and SEP-N31C showed that the tritium retention of both types is similar and pretty low, compared to other carbon-based materials [3].

Literature:

- [1] H. Kwast et al., J. Nucl. Mater. 212 - 215 (1994) 1472.
- [2] H. Kwast, H. Werle, C.H. Wu, Physica Scripta T 64 (1996) 41.
- [3] C.H. Wu et al., "Evaluation of an Advanced Silicon Doped CFC for Plasma Facing Materials", SOFT-19, Lisbon, Sept. 6 - 20, 1996.

Staff:

E. Damm
S. Rübél
H. Werle
H. Ziegler

CTA-EU-T 9 Fabrication and Test of Water-Cooled, Small Size FW Mockups

1. Thermal Fatigue Testing of Small Mockups with and without Artificial Defects

First wall mockups with artificial defects were tested in the thermal-fatigue facility FIWATKA. The observed failure is reported and is compared to a prediction of crack growth. Additional cracks that started from intact surfaces and are predictable by standard codes have limited the crack growth at some of the defects.

1.1 Introduction

The First Wall (FW) may contain defects in the form of cracks originating from manufacture, overloads (disruptions), or earlier fatigue. Due to the pulsed nature of the present day Tokamak operation the FW area is subjected to cyclic thermal loads and corresponding stresses and strains. In addition stress concentrations caused by defects could shorten the fatigue life time of the component. In this context thermal fatigue experiments under purely thermal load were performed in order to contribute to answers to three questions:

(a) where and how would defective specimens fail, (b) are there indications of crack arrest, and (c) how well predictable by analysis is crack growth under these conditions?

1.2 Specimens

The specimens were rectangular bars made from stainless steel AISI 316L with a cross section shown in Fig. 1 and 260 mm long. They were designed by the NET-Team and manufactured by Sulzer Innotech in 1993.

Each one contained two cooling channels drilled into the bars at dimensions typical for a FW structure; the water supply lines to each channel were connected through the back wall close to both the top and bottom ends. Most of the specimens carried artificial defects in the form of electro-eroded notches in positions at that time expected to be weak points.

There were three specimens selected to be tested simultaneously in the present program: Specimen No. 3, as a

reference, did not have artificial defects. Specimen No. 13 carried three notches eroded into the wall of one of its cooling channels at position A of Fig. 1 and oriented normal to the channel axis. Specimen No. 11 carried three notches eroded into the heated surface at position B of Fig. 1. The 0.1 mm wide notches were distributed over the length of the specimens, their shapes were nearly semi-elliptical, and their initial dimensions may be read from Fig. 1. To increase its emissivity the heated surface of the specimens was coated with a 20 μm thick layer of plasma-sprayed $\text{Al}_2\text{O}_3 + 13\% \text{TiO}_2$.

1.3 Experiment

The three specimens were tested in the thermal-fatigue facility FIWATKA [1] at FZK. They were positioned side by side in a window of the water-cooled heater housing (Fig. 2) and

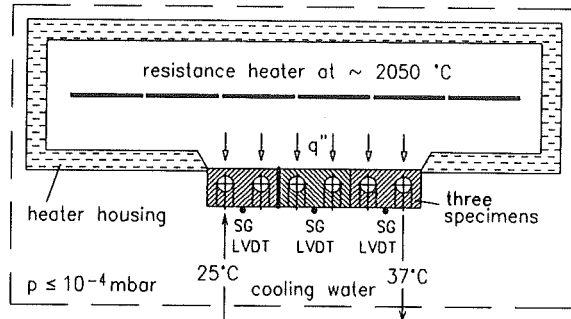


Fig. 2: Experimental setup

surface-heated cyclically by thermal radiation from a graphite resistance heater in vacuum. For each 180-s-cycle the quick (low-mass) heater was energized for the first 80 seconds and transferred a heat flux of 75 W/cm^2 to the surface of the specimens. The specimens were cooled continuously with water (8 bar and 30 °C, demineralised and low oxygen); the heat transfer in the cooling channel was 2.2 $\text{W}/(\text{cm}^2\cdot\text{K})$ and the water heated up about 4 K when it passed through two cooling channels of a specimen in series. The heat flux received by the surface of the specimen was determined calorimetrically from flow rate and heat-up of the cooling water at the end of a heating phase. The hottest point at the surface of the specimens reached about 450 °C and cooled down during the 100 seconds of the dwell phase to almost

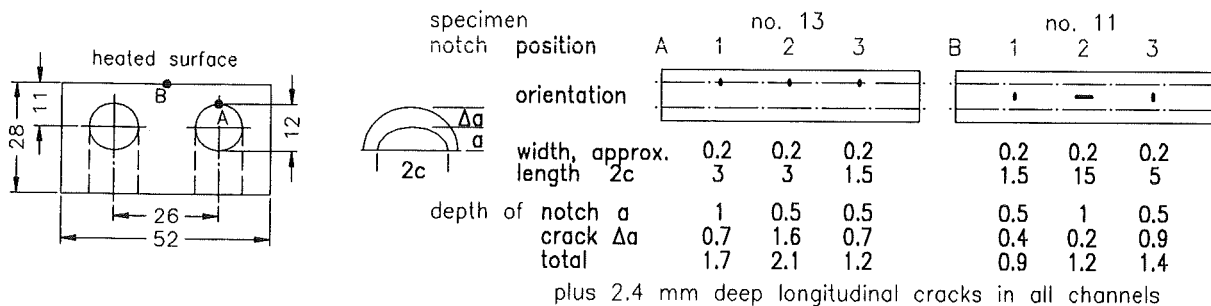


Fig. 1: Shapes and sizes of specimens, notches and cracks

room temperature. The specimens were unconstrained since they were fixed in only one point and since the water supply lines were flexible hoses.

As a reference for uniform cycle operation each specimen was equipped at its rear surface with a thermocouple and two strain gauges (longitudinal and transverse) in its center and with three displacement sensors (LVDT) along a 200 mm line to monitor the bending. In Fig. 3 the measured quantities are

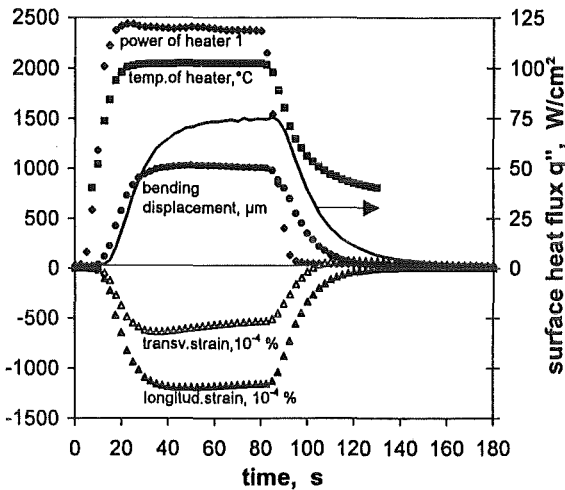


Fig. 3: Experimental behaviour during a cycle

plotted for one cycle indicating that the specimens reached equilibrium at the ends of the heating and cooling phases. The experiment was interrupted every about 10000 cycles when the specimens were taken out for an examination of the crack depth.

1.4 Observed Failure

1.4.1 Examination techniques

Failure was expected to be initiated at the artificial notches and to propagate into the specimens. The eddy current technique was utilized for the non-destructive examination (NDE) of the crack growth since the expected crack propagation is normal to the respective surface, an orientation for which this technique promises to result in high resolution.

A differential sensor (two coils) with 1 mm effective width was operated typically at a frequency of 2 MHz. The sensor was positioned over the center of a notch and moved in steps along its length by rotating it along the inner notch (type A) or by traversing it over the outer ones (type B). All notch areas were destructively examined after the test by breaking them open (mechanical fatigue) which showed the final depths, shapes, and surfaces of the cracks. The sensor signal was interpreted as crack depth by calibrating it with both the signals for the initial notch and the final crack depths.

NDE was applied to the notch areas only; longitudinal cracks away from the notches, which were not expected and were discovered only after the test, were located with the naked

eye and with the dye penetrant method (PT); they also were examined optically after a section was broken open. The crack surface revealed beach-marks that could be correlated with the fatigue test interruptions and hence with the number of cycles.

1.4.2 Measured crack growth

For each of the failures the application of the above techniques yielded the crack growth as a function of the number of cycles:

Crack growth at the inner notches (type A) is plotted in Fig. 4 and the final crack depths at the summits are listed in Fig. 1.

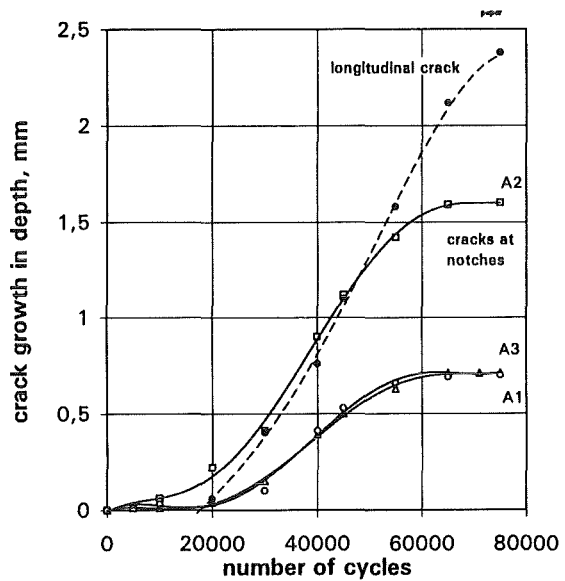


Fig. 4: Growth of cracks at channel inside

Cracks were detectable after 10⁴ cycles. They grew at a maximum rate of around 4·10⁴ cycles and stopped growing at about 6.5·10⁴ cycles, a reason why the test was terminated; after the longitudinal cracks had been discovered this crack arrest could be explained primarily as a result of a local stress relief by competition of the faster growing longitudinal cracks initiated during the test. The maximum growth of a crack was 1.6 mm, i.e. it stopped after it had penetrated 42% of the channel wall. Fig. 5 illustrates the elliptical shape of the final crack at A1 and the position of the competing longitudinal cracks.

For cracks at the outer notches (type B) the measurement was disturbed by the blackening coating applied after 10⁴ cycles and by some carbon deposition in the notches originating from the heater. Therefore only B3 could be measured and because of data scattering it is not clear whether a crack arrest was reached. Data are not displayed here. The cracks grew up to 0.6 mm from the bottom of the notch.

Growth of the longitudinal cracks is plotted also in Fig. 4. These cracks started from the intact surfaces of the cooling channel walls; they appeared uniformly in each of the six cooling channels in positions about 10° left of A in Fig. 1

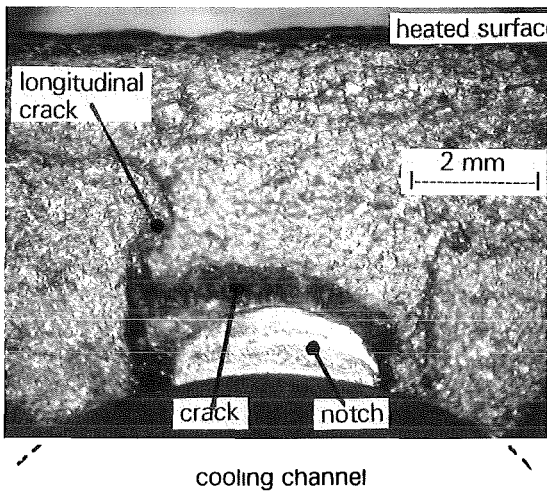


Fig. 5: Crack at notch A1 after 75000 cycles

(compare section 5 for the maximum of the strain range in this position). The cracks extend over the whole length of the channels. They obviously were initiated during the first $2 \cdot 10^4$ cycles and grew in depth almost linearly until the end of the test when they had penetrated 2.4 mm or almost half the channel wall. From the data in Fig. 4 there is no strong indication of a crack arrest if the test would have been continued. Fig. 6 shows the flank of a crack after it was

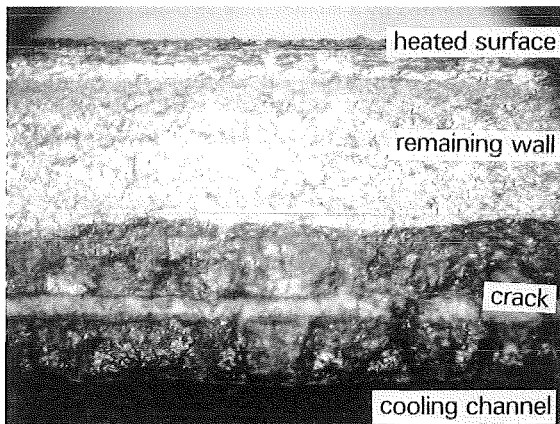


Fig. 6: Flank of a longitudinal crack

broken open and it indicates the almost straight crack front. Micrographs reveal that the cracks are transgranular.

1.5 Failure Prediction

Prediction may be focused on two different aspects of failure:

1.5.1 Crack initiation from an intact surface

As a result of a transient, 2-D, plastic FEM analysis (Fig. 7) the maximum mechanical strain range $\Delta\varepsilon$ of 0.52 % is located 10° left of A in Fig. 1 where the longitudinal cracks actually appeared. Crack initiation in this study compares reasonably well with other thermal fatigue failure results in Fig. 8 and

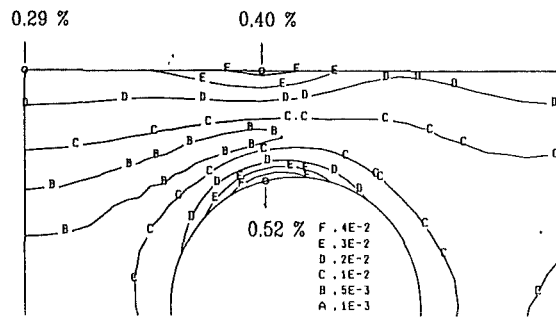


Fig. 7: Mech. strain range $\Delta\varepsilon$ from plast. analysis

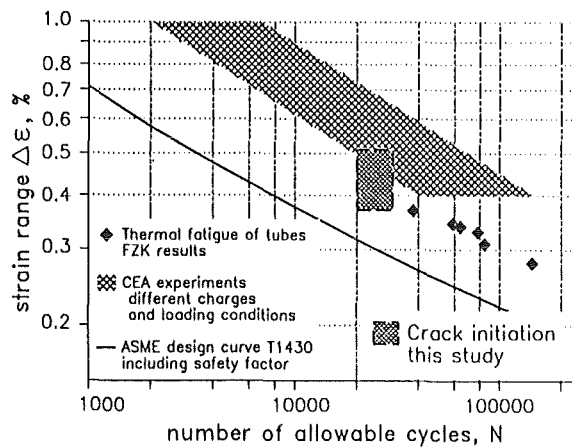


Fig. 8: Standard lifetime assessment

confirms the safety margin of the ASME design curve.

1.5.2 Crack growth from a notched surface

The stress concentration at the bottom of an artificial notch is assumed to initiate a sharp-edged crack during several thousands of cycles. Growth of such cracks may be predicted on the basis of 'simplified elastic-plastic' fracture mechanics:

The loading parameter controlling fatigue crack growth is the range of the stress intensity factor ΔK which is given as $\Delta K = \Delta\sigma \cdot \sqrt{a} \cdot Y$

A fracture mechanical analysis was carried out

- using the elastically calculated cyclic stress field and assuming elast.-plast. shake-down conditions, i.e. $\Delta\sigma = \Delta\sigma_{\text{elastic}}$ and $\sigma_{\text{min}}/\sigma_{\text{max}} = -1$.
- considering the notch an initially sharp semi-elliptical surface crack with the two axes a (depth) and c .
- applying a geometry function $Y = f(a/c, \text{mock-up geometry, crack shape, and loading conditions})$ which has been developed for the geometry of the benchmark specimen [2].

The relation for incremental crack growth $da/dN = f(\Delta K)$ was taken from [3].

Crack growth was calculated for the conditions of the artificial notches in the test. As an example calculated and measured crack growths are plotted for notch A1 in Fig. 9. It

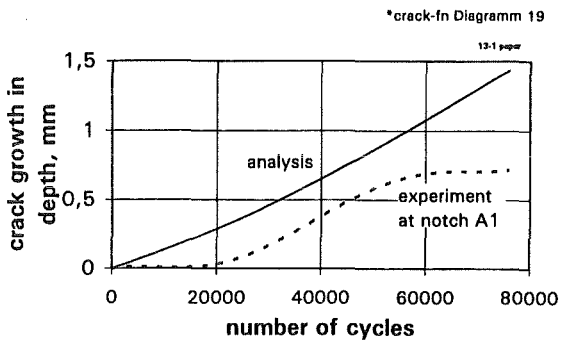


Fig. 9: Crack growth at notch A 1

seems that the model over-predicts the crack growth but a closer look reveals that in the experiment the crack starts rather slowly (sharp crack forms), reaches the predicted growth rate and comes to an arrest possibly due to the presence and depth of a competing longitudinal crack (not modeled). Yet at other notches in the channel the actual maximum growth rate was under-predicted.

1.6 Conclusions

All notches inside the channel developed cracks that were arrested, possibly by competing longitudinal cracks that grew faster and continued to grow at the end of the test. Also all notches in the heated surface developed cracks, for which the measured data would not allow a statement on crack arrest.

Initiation of the longitudinal cracks seems predictable from the calculated strain range.

Literature:

- [1] G. Hofmann et al., KfK 5381 (1994)
- [2] E. Diegele et al., submitted to Int.J.Fract.(1994)
- [3] R.W.Watson et al., J. Press.Vess.Techn., Vol.105(1983), pp.144-152.

Staff:

- E. Diegele
- E. Eggert
- G. Hofmann
- M. Kamlah
- S. Müller
- G. Thun

2. Thermo-mechanical Tests of Small Scale Primary Wall Mockups

In preparation of the forthcoming task T 216 work has been done for the testing of critical issues in the new design of the integrated First Wall and Shield Blanket as an ITER Test Module. As part of the European program four small scale first wall mockups will be thermal-fatigue-tested with 13 000 cycles in the FIWATKA facility. The mockups will be of the present ITER FW design with stainless steel (SS) tubes embedded in 20 mm of copper and the copper plate joined to the SS shield blanket area. The mockups will include those made of DS-copper as well as those made of CuCrZr and different joining techniques like diffusion welding (solid HIP), powder HIP, and explosion welding will be employed. The heated surface of the mockups will be 250 by 110 mm.

It is considered the main goal of the program to find out whether the copper to SS joints survive thermal cycling; the stress range at the joints (during a cycle) is considered the main local load parameter responsible for possible fatigue failure. In order to subject the mockups to reasonable loads the stress ranges calculated (by Siemens/KWU) for the real ITER module were used as a guide line and the small scale mockups were designed such that according to FEM calculations they will, under test conditions, experience similar stress ranges at the joints.

This resulted in a mockup design in which the shield blanket area is represented by a 60 mm thick SS plate containing two rows of channels, a central one to receive radiative heaters and a rear one to be used for water cooling in series with the FW channels. Testing is expected to start as soon as the mockups are provided by the NET Team by the end of 1996.

A NET Study Contract for the definition of a test program on a medium scale mock-up at FIWATKA is imminent.

Staff:

- E. Eggert
- G. Hofmann
- M. Kamlah

G 17 TT 25 (T 226 b)
Plasma Disruption Simulation

Three main activities were performed during the period to be reported. These are: 1) development and application of the 2D radiation-magnetohydrodynamics (R-MHD) code FOREV-2 for analysis of disruption erosion under realistic ITER conditions [1, 2]; 2) verification of modelling codes against results from simulation experiments performed at TRINITI Troitsk, at Efremov St. Petersburg and IPP Charkov [3-6]; 3) detailed scenario calculations of ITER disruption erosion using the 1D R-MHD code FOREV-1 [7]. Additionally activities on benchmarking of 2D radiation transport were performed as a joint exercise together with Livermore [8].

The experimental results on physical properties of carbon plasma shields as obtained at TRINITI Troitsk were used for validation of the models used for description of disruptive plasma wall interaction. Distribution and time evolution of plasma temperature and electron density was reproduced quite well. The calculated directed total radiation fluxes as obtained from 2D radiation transport calculations were a factor of 4 less than the measured ones, calculated directed soft x-ray line radiation fluxes were in agreement with measured values [3].

Detailed scenario calculations for power densities of the incoming hot plasma in the range 1 - 10 MW/cm² were performed to determine erosion, melt layer thickness and properties of low Z plasma shields. It was found that the plasma shield is a two temperature non-LTE plasma with a high temperature ($T_e \leq 300$ eV) plasma corona of atomic density of $10^{15} - 10^{16}$ cm⁻³ and a low temperature ($T_e \leq 2$ eV) plasma of density $10^{17} - 10^{19}$ cm⁻³ close to the target. The plasma shield efficiently converts the incoming energy into radiation and thus damage of side walls due to intense lateral radiation may occur [7, 8].

Rather interesting results were obtained from a first 2D analysis [1, 2]. Inclined impact of hot plasma produces instabilities in the density distribution of the plasma shield which result in a periodic modulation of erosion as is seen from Figs. 1a and b showing the time evolution of plasma density and velocity in a carbon plasma shield for an inclined graphite target (Fig. 1a) and the time evolution of the erosion pattern (Fig. 1b). Tilting of divertor plates (ITER vertical targets) results in a drastic decrease of the shielding efficiency because of movement of the plasma shield along the inclined surface. The guiding magnetic field (toroidal component $B_z \geq 5$ T) guarantees that a part of the plasma shield produced during one single ELM of energy density of 1 MJ/cm² arrives at the SOL despite its distance of at least 2 m from the divertor target. The question of impurity penetration across the SOL into the main plasma still needs to be addressed. First boundary conditions at the SOL (density and temperature of the impurity plasma) have been defined by detailed FOREV-2 calculations.

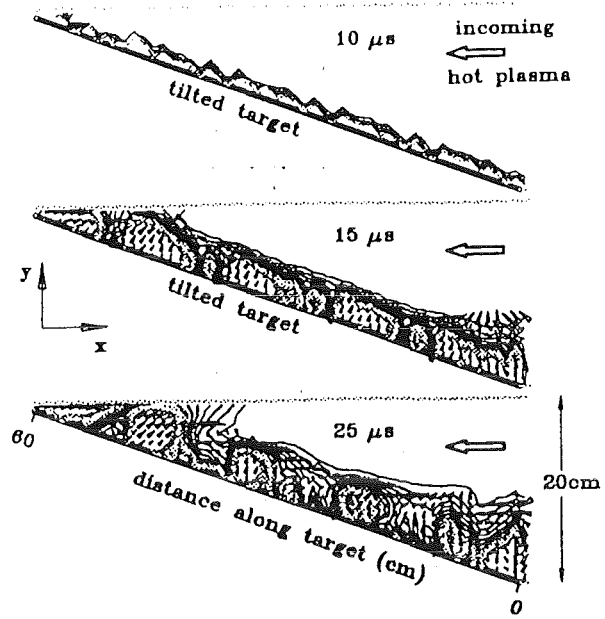


Fig. 1a: Time evolution of plasma density and velocity in the plasma shield for inclined target.

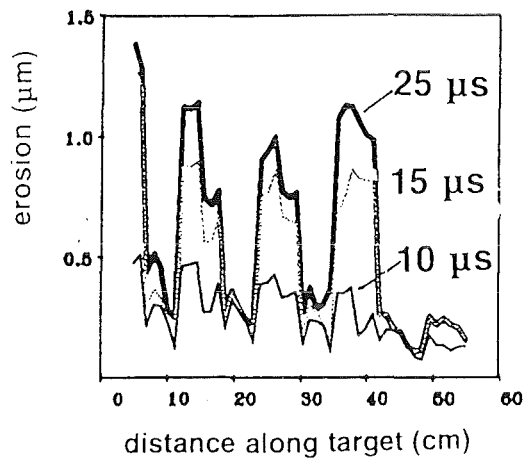


Fig. 1b: Time evolution of erosion pattern due to plasma shield instability.

Literature:

- [1] H. Würz et al., The plasma shield in ITER plasma wall interactions, SOFT 19th, Sept. 16 - 20, 1996, Lisboa.
- [2] H. Würz et al., Plasma shield formation and divertor plate erosion for ITER tokamak plasma disruptions, ICFRM-7, Obninsk, Sept. 25 - 29, 1995.
- [3] H. Würz et al., Plasma surface interaction in ITER tokamak disruption simulation experiments. Paper submitted and accepted for publication in Fusion Technology.

- [4] H. Würz et al., Radiation in plasma target interaction events typical for ITER tokamak disruptions, ANS annual meeting 1996 and 12th Topical Meeting on Technology of Fusion, June 16 - 20, 1996 Reno.
- [5] A. Burdakov et al., Explosive like erosion of solids under ITER disruption conditions, PSI-12, May 20 - 24, 1996. St. Raphael.
- [6] N. Arkhipov et al., Study of plasma target interactions with plasma streams of power density of 40 MW/cm², SOFT 19th, Sept. 16 - 20, 1996, Lisboa.
- [7] B. Bazylev et al., 22nd EPS Conf. on Controlled Fusion and Plasma Physics, Bournemouth July 3 - 7, 1995, Vol. 19C, part II, p. 277.
- [8] A. Koniges et al., Side radiation damage from ablated vapor following on ITER scale disruption, PSI-12, May 20 - 24, 1996. St. Raphael.

Staff:

B. Bazylev¹⁾
F. Kappler
I. Landman²⁾
S. Pestchanyi²⁾
G. Piazza
M. Würz

1) Lykov Institute of Heat and Mass Transfer, Minsk, Belarus

2) Troitsk Institute for Innovation and Fusion Research, Troitsk, Russia

G 55 TT 01 (T 26/T 246)
Ceramics for Heating and Current Drive and Diagnostic Systems

Following the given frame of the ITER tasks, the effects of radiation on candidate insulator materials, especially on window materials for electron cyclotron (EC) systems, are studied under application relevant conditions. The targets are to fill the remaining gaps in the database for the "cryo-window" concept based on sapphire and to establish the forthcoming alternative concepts based on special silicon grades and on CVD diamond.

The dielectric parameters were determined at 145 GHz i.e. close to the ECRH frequencies. The thorough level of development of the "cryo-window" is documented by a well established understanding for the intrinsic losses [1]. Ongoing research on Sapphire serves as product qualification of the windows selected for European gyrotron development for Cadarache [2]. The open question of Sapphire windows at the torus was concerned with a potential reduction of the presently identified tolerable neutron fluence limit of 10^{21} n/m² ($E > 0.1$ MeV). This limit might still be lower because of defect stability enhancement which may be expected when the window is irradiated at cryogenic temperatures. For that purpose, dielectric measurements were continued with the specimen set from the cryogenic irradiation (HFR) which was obtained just before the reporting period. The data were compared to those of the previous specimens from the ambient irradiation (GKSS). No significant difference in the temperature function of the losses could be seen (Fig. 1).

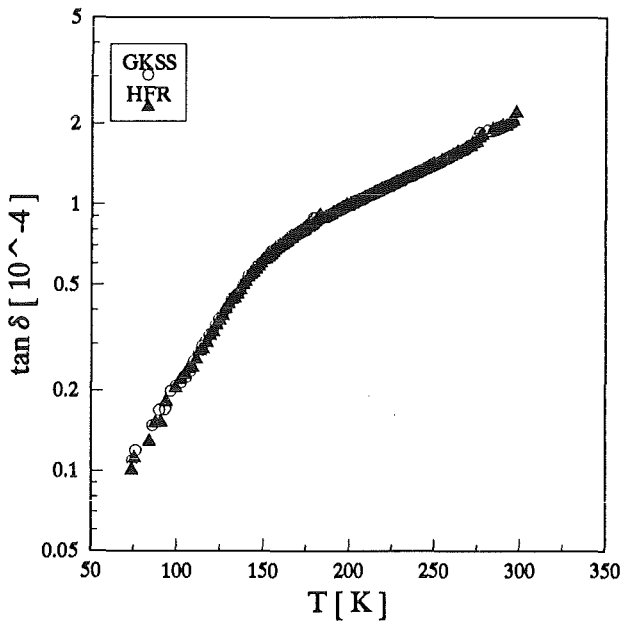


Fig. 1: The dielectric loss at 145 GHz in HEMEX Sapphire (o.r.) observed after a neutron irradiation at ambient (GKSS) and cryogenic (HFR) temperature.

In contrast to HEMEX Sapphire, monocrystalline quartz showed a clear increase of the dielectric loss relative to the unirradiated material (Fig. 2).

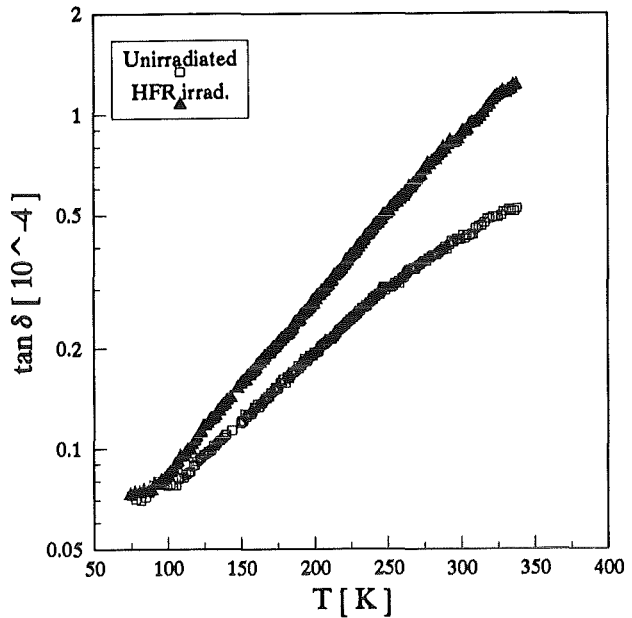


Fig. 2: The dielectric loss of 145 GHz in monocrystalline quartz (o.r.) observed after the cryogenic irradiation (HFR) in comparison to the unirradiated material.

The final evaluation of the fluence monitors at Petten showed that instead of the target value of $1.0 \cdot 10^{21}$ n/m² only a fluence of $0.3 - 0.4 \cdot 10^{21}$ n/m² had been reached. Thermal cycling occurring between the scheduled irradiation periods, and during transport and specimen handling is considered to be equivalent to the case of an actual torus window.

The materials development of the forthcoming candidate materials was guided with dielectric property measurements. As could be shown, the doping process of Silicon had reached a degree of perfection that the losses at room temperature were close to the intrinsic levels [3]. A new extended size CVD diamond disc (40 mm dia x 1 mm) could be procured which shows virtually constant permittivity and loss values in a wide temperature range around the ambient. After their characterization, these advanced grades of Silicon and Diamond were included in the specimen set for the neutron irradiation at GKSS. The set was sent to the reactor in September, and the irradiation is now pending.

The in-beam demonstration of the materials performance under X-rays was performed and concluded for the advanced grades of the alternative window materials [4]. The previous inspection limit of the X-ray dose rate in neutron-irradiated HEMEX Sapphire (10^{23} n/m²) could be extended for the alternative grades from 0.5 to 0.8 Gy/s. But still, as for Sapphire, no additional in-beam loss term was observed in these experiments at 35 - 45 GHz.

Literature:

- [1] R. Heidinger, G. Link; The MM-Wave Absorption in Sapphire and its Description by the 2-Phonon Model; Digest of the 20th Int. Conf. on Infrared and MM Waves, Orlando (USA), 11.-15.12.1995, pp 16 - 17

- [2] G. Garin, G. Bon-Mardion, M. Pain, R. Heidinger, M. Thumm, A. Dubrovin, E. Giguet, C. Tran; Cryogenically Cooled Window: a New Step toward Gyrotron CW Operation; Digest of the 20th Int. Conf. on Infrared and MM Waves, Orlando (USA), 11.-15.12.1995, pp 271 - 272

- [3] R. Heidinger, J. Molla, V. V. Parshin; Step to intrinsic absorption in doped Silicon; Digest of the 21 st Int. Conf. on Infrared and MM-Waves, Berlin (D), 14. - 19.7.96, ISBN 3-00-000800-4, p. AW 8

- [4] R. Heidinger, L. Steinbock; The effect of X-ray irradiation gyrotron window materials; Digest of the 21 st Int. Conf. on Infrared and MM-Waves, Berlin (D), 14. - 19.7.96, ISBN 3-00-000800-4, p. AT 8

Staff:

M. Blumhofer
R. Heidinger
P. Severloh
L. Steinbock
H. Zimmermann

Superconducting Magnets

Introduction:

Next step fusion experiments plan for plasma pulses of extended duration (ITER) or even quasicontinuous operation (Stellarator W7X). Superconducting magnets are mandatory under these conditions.

The confinement of ITER relies on a superconducting magnet system consisting of 20 D-shaped toroidal field (TF) coils, a central solenoid (CS) to drive the plasma current, and a set of poloidal field coils to stabilize the plasma position. Tests of industrially fabricated model coils for TF and CS are part of the seven large experimental programmes within the ITER Engineering Design Activity. The FZK-EURATOM Association was entrusted by the European ITER Home Team to upgrade the TOSKA Magnet Test Facility and to perform the tests for the ITER TF model coil.

An important step in the facility preparation activity was reached in 1996. The former LCT coil was reinforced to withstand higher stresses and was tested in TOSKA to the limits of current capability of the NbTi conductor at superfluid helium temperatures. This LCT coil will serve as background coil in future experiments with W7X and ITER model coils, respectively.

Further work for ITER consists of component development (high temperature superconductor feedthrough), characterization of low temperature structural materials and of studies related to magnet safety and overall system behaviour.

After inauguration of the Wendelstein W7X project in 1996, an extended cooperation is being implemented of FZK and IPP with the aim of qualifying the complete set of superconducting W7X coils before assembly at the Greifswald site.

The current FZK programme for W7X concentrates on flat coil tests in the STAR test facility to examine the superconducting quality of the newly designed W7X conductor in longer production lengths.

A fully prototypic W7X coil is expected to be tested in 1997/8 in TOSKA, preceding the ITER model coil test, which is scheduled for 1998/9. A more detailed programme to test the 70 W7X line item coils is under preparation, making optimum use of the capacities of the TOSKA installation and the connected refrigerators.

MCOI ITER TF-Model Coil Development

Staff:

Subtask 1: Monitoring Manufacture of the Toroidal Field Model Coil (TFMC)

S. Fink (Subtask 3)
M. Irmisch (till 31.12.95)
V. Zwecker
A. Ulbricht (Subtask 1)
I. Meyer (since 15.6.96)
G. Wiczorek (till 31.5.96)
G. Zahn

The aim of the subtask is the support of the NET Team in design and the fabrication of the ITER TF model coil.

A specification for the fabrication was sent out to European industry July 1995. FZK participated in the evaluation group to elaborate the technical assessment for the received offers. The contract for the selected consortium was sent in December 1995 for signature of the EU to Brussels. FZK participated with its experts in a series of technical and progress meetings (about 14) to start up and monitor the TF model coil fabrication by the European industry consortium AGAN. FZK contributed to the following items:

- a.) Analyses and optimization of the mechanical support structure (see also ERB 5000 CT 950064 NET (NET 95-384)) for the TFMC test configuration.
- b.) Contributions to the design work and test facility related items (instrumentation, superconducting busbars, gravitational support structure) were elaborated and presented at the meetings.

Subtask 3: Basic Development of High Voltage Technique for Components used in Model Coil and Test Facility (Feedthroughs, Insulation, Breaks, Current Leads etc.)

The aim of the subtask is the transfer of the know-how in the development of high voltage components gained in the POLO project to the ITER model coils. A partial discharge free high voltage supply system was ordered and taken in operation for performing partial discharge measurements with the TF model coil. The system consists of a control and measuring unit, a control transformer, and a high voltage transformer. The system is designed for a maximum voltage of 10 kV and an output of 10 kVA. The unit was taken in operation and fulfilled the specifications.

An experimental study was performed by investigating the effort of partial discharge (PD) measurements for unipolar voltages to find a relation between periodic and single shot operation. It was found that the apparent charge depends predominantly on the peak-peak voltage. The PD pattern for curves with the same peak-peak voltage and the same steepness are identical. This work was performed in collaboration with the Institut für Energie und High Voltage Technique (IEH) at the Karlsruhe University [1].

Literature:

- [1] M.C. Thoma, Teilentladungsmessung bei unipolarer Spannung an Gießharzkörpern, Diplomarbeit, IEH, Universität Karlsruhe, 1995.

**N 11 TT 19 94-02-15 FE 02 (MTOS 1)
Preparation of ITER TF-Model Coil Test Facility**

Subtask 1: Preparation of TOSKA Facility for the Test of the ITER TF Model-Coil

The order for fabrication of the ITER toroidal field model coil (TFMC) was placed in the European industry, a consortium called AGAN (Ansaldo, GEC-Alsthom, ACCEL, Noell). The work performed for the model coil is described in subtask MCOI-1.

In the frame of upgrading the TOSKA facility to test the ITER-TFMC, the 1.8 K operation of the LCT coil was successfully performed in July. After the termination of the POLO experiment, it was the first test operation of the TOSKA facility with the extended cryogenic and electrical supply system as well as a new configuration of the measuring and control system, including data acquisition. Therefore an import milestone was passed by this test in the programme of preparing TOSKA for the TFMC test.

1. Upgrading of the TOSKA Facility

The main activity was the installation of the LCT coil after about 9 years idle time (Fig. 1). The coil will be used in the ITER TF model coil test as background coil. All work performed for the facility will be reported in this section while the specific test results of the LCT coil at 1.8 K are reported under subtask MBAC.

1.1 Cryogenic Supply System

To respond to the future requirements a new flow scheme had to be realized in the TOSKA facility (Fig. 2). The 2 kW refrigerator was connected to the control cryostat B 250. The 400 W refrigerator was connected to the control cryostat B 1000 for the subatmospheric operation at 1.8 K. During the LCT coil test at 1.8 K it must be possible to supply the winding with supercritical superfluid helium. It was therefore foreseen to valve on and off the winding to the forced flow superfluid supercritical circuit of the control cryostat B 1000 or alternatively to the forced flow supercritical circuit of the of the control cryostat B 250. For the superfluid supercritical operation the venting lines had to be separated by a thermal barrier. A cold storage medium pressure vessel (20 bar) was installed for collection of the expelled helium gas to avoid response of the safety valves. Three different pump types (3 cylinder piston, centrifugal and thermomechanical) were installed in the superfluid control cryostat. The whole system was controlled by programmable logic controllers (PLC). The circuits were operated by a control and visualisation system (VXL) on a VAX station [1]. Both forced flow circuits were tested separately. It was demonstrated in the test of the LCT coil at 1.8 K (MBAC) that the cryogenic supply system is now fully available for testing the ITER TF model coil.

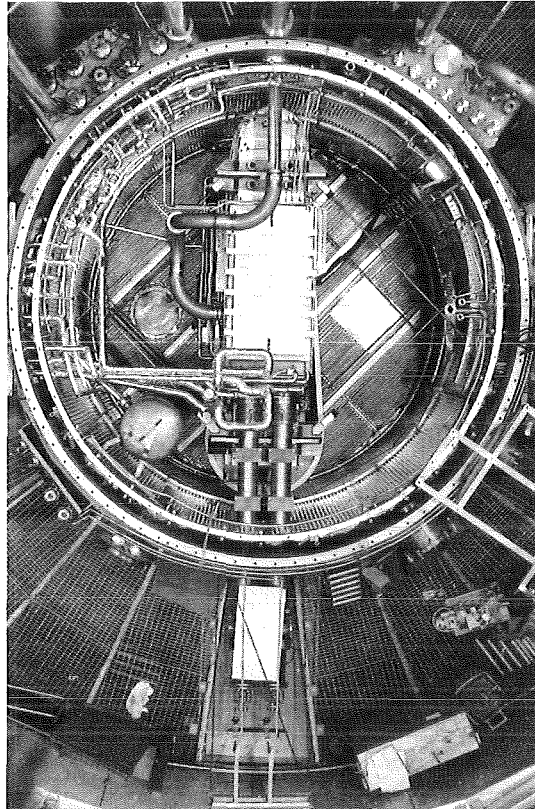


Fig. 1: A view into the TOSKA vacuum vessel with the installed LCT coil. On the right side of the LCT coil is the space for the ITER TFMC and W7X-demonstration coil

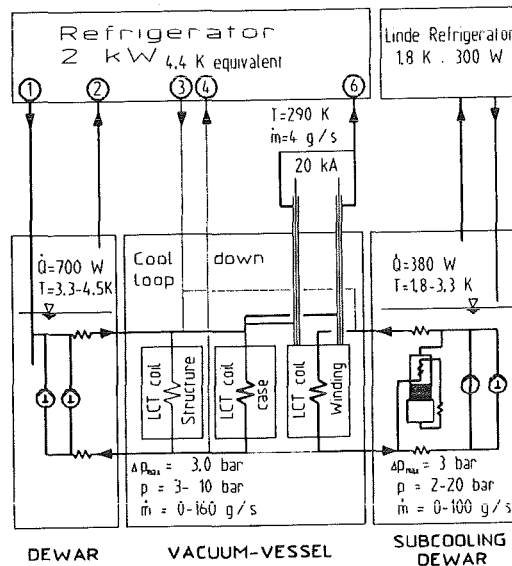


Fig. 2: Flow diagram of the cooling system

1.2 Electric Supply System

The 50 kA, 30 V DC power supply was used as current source for the LCT coil which was connected across a separation switch (ST) in the positive and negative busbars (Fig. 3).

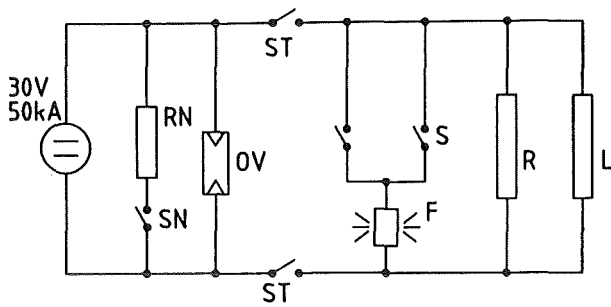


Fig. 3: Electrical power supply with dump circuit

The dump resistor (R) was switched parallel to the coil (L). The short circuit path of the coil consists of two arc chute breakers (S) in parallel with a pyro breaker (F) in series for having simple redundancy if one of the arc chute breakers does not close or open. The switching sequence is controlled by a PLC with a backup relays circuit for the safety discharge. In case of a dump trigger the arc chute switches are closed and the power supply is switched in the inverter mode. The coil is now short circuited by the branch (S,F). Then the separation switches ST open and isolate the power supply from the dump circuit. After that the arc chute breakers open and commutate the current in the dump resistor. The time constant was 12.5 s and the dump voltage 2.5 kV at 20 kA. In case of a power supply fault the power supply is protected by an overvoltage protection device (OV) and a short circuit branch in parallel to the main short circuit with a current limiting resistor (RN) for arc free opening of the separation switches.

The delay time between trigger and breaker opening was about 675 ms with a jitter of 20 ms, mainly determined by the opening time of the separation switches. The maximum switching power handled for extracting 300 MJ was 48 MW.

The 20 kA power supply, which will be the current source for the LCT coil in the TFMC test, will be ordered in the 4. quarter 96. Technical clarifications and negotiations about the received offers are running. The conceptual design of the 80 kA TFMC dump circuit was concluded. The detailed technical specification is now elaborated by a company. It is planned to use the POLO switching circuit for testing the transient behaviour of the TFMC. On the basis of the results gained with POLO counteracting current, a fast discharge was calculated for the TFMC (Fig. 4) [2]. Using that method at higher current levels requires larger capacitor banks, capacitor banks that are charged to higher voltage values than the nominal voltage U_N , or a faster discharge of the capacitor bank. In the latter two cases switching surges must be expected which can cause oscillating overvoltages inside of the superconducting winding. A solution has to be found to make suitable changes in the POLO switching circuit.

1.3 Instrumentation and Data Acquisition

The cryogenic supply system was equipped by sensors necessary for control and protection. All sensors were

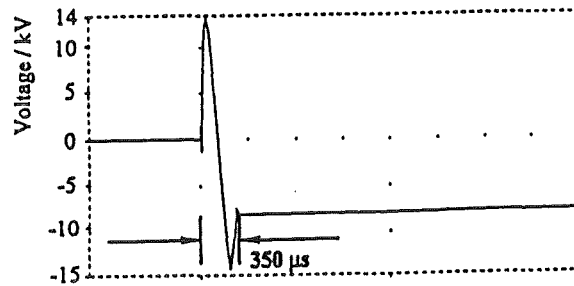


Fig. 4: Calculated coil voltage at HV discharge of the ITER TFMC ($I_0 = 25$ kA, $U_N = 10$ kV) using the Polo circuit described in the previous annual report

connected to the new data acquisition system (Fig. 5). The necessary data for controlling the facility were adapted in their engineering units. All measured data were finally stored in engineering units in the data base ORACLE where they were available for later analysis procedures. For the usual operation the data were collected by a scanner with < 5 s repetition rate. Fast changes during experiments were acquired by transient recorders with 1 MHz sampling rate. In the present state the scanner has 500 channels and the transient recorders about 32. The channel number can be adapted to the requirements of the experiment. The LCT coil instrumentation was used as existing. The additional instrumentation will be described under task MBAC.

1.4 The 80 kA Current Lead

Based on the principle of the POLO current lead a 80 kA current lead was designed (Fig. 6). The most critical parts are the warm end and the cold end of the current lead. For the warm end a special flexible water cooled busbar has to be developed for a definite feed in of the current in the current lead heat exchanger. Heat loss reduction at the cold end required the use of copper with a high residual resistance ratio (RRR) of about 6 as compared to the copper rod of the heat exchanger. The originally planned friction welding technique had to be rejected because of a lack of a suitable friction welding machine for 90 mm (diameter) copper rods. Now, a brazing technique is planned to be used. The preparations for construction of the heat exchangers are running in the workshops.

Literature:

- [1] A. Augenstein, H. Barthel, P. Gruber, R. Kaufmann, P. Klingenstein, U. Padligur, K. Rietzschel, G. Wuerz, H.P. Zinnecker, Data Acquisition, Control and Visualisation System for the Upgraded TOSKA Facility at FZK, Proc. 19th SOFT, Lisbon, Portugal, Sept. 16 - 20, 1996
- [2] M. Darweschad, P. Komarek, G. Noether, C. Sihler, A. Ulbricht, W. Weigand, F. Wüchner, Switching Circuit for generating Fast Field Transients in Superconducting Coils, Proc. 19th SOFT, Lisbon, Portugal, Sept. 16 - 20, 1996

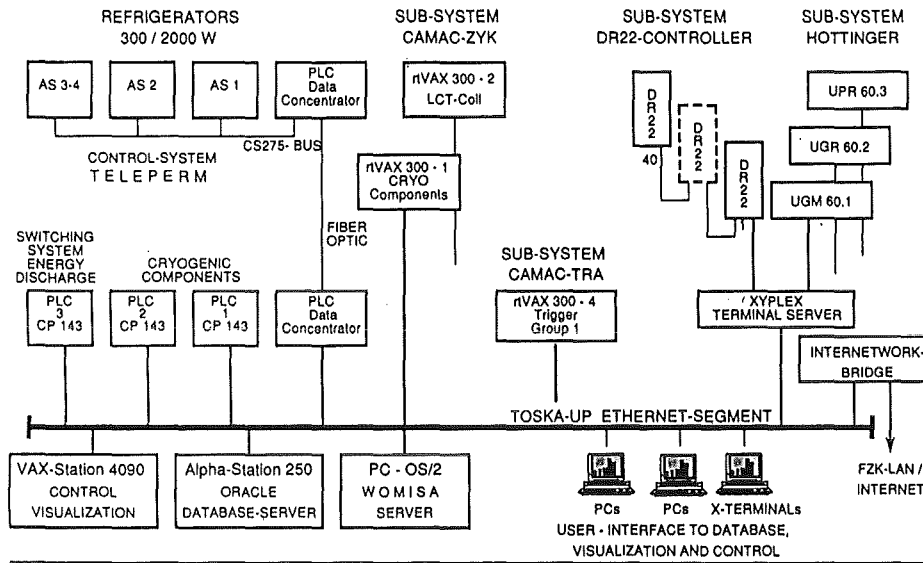


Fig. 5: Data acquisition system

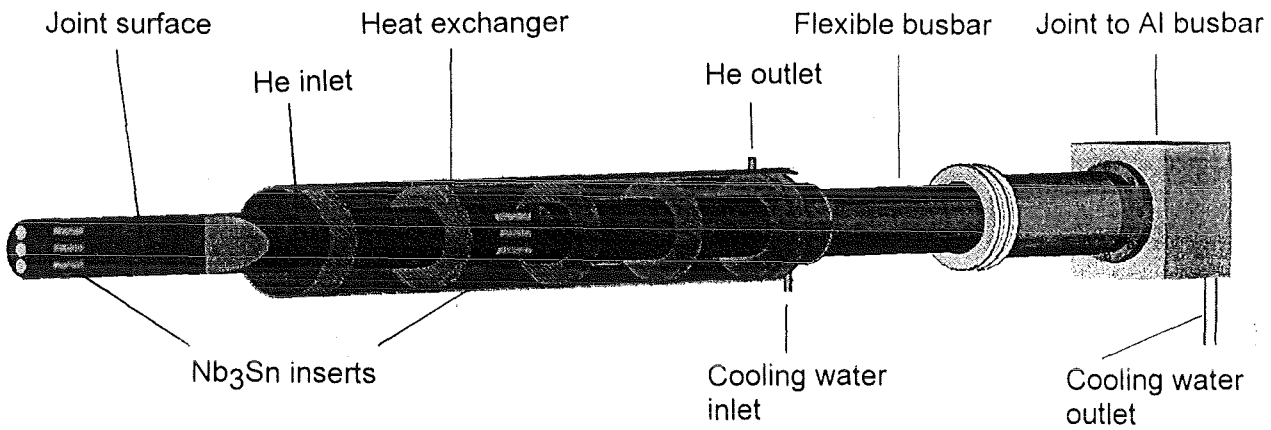


Fig. 6: Artist's view of the 80 kA current lead

Staff:

A. Augenstein
 H. Barthel
 F. Becker (till 30.6.96)
 S. Darweschad
 G. Dittrich
 P. Duelli
 S. Fink
 G. Friesinger
 A. Götz
 P. Gruber
 A. Grünhagen
 R. Heller
 W. Herz
 H. Irmisch (till 31.12.95)
 H. Kathol
 R. Kaufmann
 P. Klingenstein
 L. Lang
 O. Langhans

W. Lehmann
 W. Maurer
 I. Meyer
 G. Nöther
 U. Padligur
 K. Rietzschel
 G. Schleinkofer
 K. Schweikert
 Ch. Sihler (till 31.8.96)
 E. Specht
 H.-J. Spiegel
 H. Stiefel
 M. Süßer
A. Ulbricht
 D. Weigert
 G. Wiczorek (till 30.6.96)
 F. Wüchner
 G. Würz
 G. Zahn
 H.P. Zinecker
 V. Zwecker

MBAC High Field Operation of NbTi at 1.8 K

Subtask 1: He II Forced Flow Cooling: 1.8 K Test of the EC LCT Coil plus Development of Circulation Pumps

The 1.8 K cooling technique is indispensable, if technically applicable superconducting materials shall obtain their highest field levels. Therefore the task was started with a programme part containing the development of components included in such a cooling circuit and is continued with the operation of a large forced flow cooled fusion magnet, the Euratom LCT coil. The last experiment is an intermediate step in the sequence of upgrading the TOSKA facility for the ITER TF model coil test (Task MTOS). The experimental part of the task was successfully concluded in July 1996. The LCT coil achieved a quench current of 19.6 kA at 11 T at a temperature of 1.89 K. The quench current observed corresponds almost exactly (within 1 %) to the predicted value.

1. The 1.8 K Test of the Euratom LCT Coil [1]

The cryogenic and electrical supply system as it was used for the 1.8 K test of the LCT coil was already described in subtask MTOS-1. The operation was performed in two steps. First, the winding and case were cooled at 3.5 K by the forced flow circuit of the control cryostat B 250. Later, for superfluid supercritical operation, the winding was connected to the cooling circuit of the B 1000. The operation parameters, are given in Table 1.

Table 1: Cooling conditions

Operation mode		3.5 K	1.8 K	Standby at 1.8 K
Winding				
Mass flow rate	[g/s]	50	80	20
Pressure	[bar]	3.5	2.4	3.5
Pressure drop	[bar]	0.1	0.6	0.07
		10	27	25
Case & structure				
Mass flow rate	[g/s]	50	70	40
Pressure	[bar]	3.5	3.4	3.5
Pressure drop	[bar]	<0.1	<0.1	<0.1
Heat load	[W]	100	90	90
Currents leads				
Mass flow rate	[g/s]	2x1.6	2x2.0	2x0.3
Heat load to winding	[W]	2x5	2x8.5	2x12.5
Current per lead	[kA]	16	19	0

2. Test Results

2.1 Standard operation

After an idle time of nearly 9 years, the LCT coil with its reinforcement (total mass now 60 t) was cooled down again during 290 h to its operation temperature with about 1 K/h and a temperature difference of < 40 K between inlet and all

other temperature sensors. The leak rate at 4 K was less than 5×10^{-6} mbar/s. The coil was ramped up with 20 A/s in steps accompanied by dump tests up to its nominal current of 11.4 kA at an operation temperature of 4.6 K. The same procedure was repeated at 3.6 K. After a steady state operation at 16 kA the ramp up was started with 5 A/s. The coil showed a spontaneous quench at 16.5 kA in full agreement with the current sharing data measured earlier (Fig. 4). The dump was 2.5 s delayed caused by the impact of magnetic stray fields on relays of the quench detector. This was avoided for the following runs by a μ -metal screening. The estimated hot spot temperature was about 100 K in agreement with the expelled helium of about 80 K. After a quench of three pancakes, the cryogenic system handled the expelled gaseous helium without He losses and the recooling took place in less than 2 h.

2.2 He II operation at supercritical pressure

To proceed to 1.8 K forced flow cooling operation, roots blowers were started for subatmospheric operation until a pressure level of 16 mbar and a temperature of 1.8 K were reached in the assigned control dewar. The dewar was then filled with liquid helium. Thereafter, the winding was connected to the 1.8 K cooling loop and cooled down to its superfluid operation temperature while the coil case, reinforcement structure, and current leads remained on the 3.5 K cooling loop. The following procedure consisted of ramping up to different current levels (11.4, 16.3, 17.3, 19.0 kA), performing an inverter mode discharge, and, in a second step, a manual triggered dump. The ramp rate was 20 A/s up to 11.4 kA and above this level, 10 A/s. A ramp rate of 5 A/s was used for ramping the coil into the current sharing region.

2.3 Electrical properties

The coil was ramped up in its current sharing region, clearly visible on the resistive voltage. The quench started, as expected, in the center pancake. The inlet temperature was 1.89 K, the current 19.6 kA and the maximum field 11 T. This current is about 0.2 kA below the expected extrapolated quench current (Fig. 1). The coil and the dump circuit withstood a dump voltage of 2.45 kV with a peak power of 48 MW.

2.4 Thermohydraulic properties

The handling of the 4.5/3.5 K cooling system together with the 2 kW refrigerator was free of problems during computer controlled cool down, the coil cooling with the secondary pump loop, and also during recooling after quench or dump. Stable He II cooling of the winding with the piston and fountain pumps was demonstrated and the disturbance of the mass flow after a dump up to 14 kA was negligible. At a higher current, the pumps were switched off after dump or quench. The installed centrifugal pump could not be used because the inlet valve was blocked. For a continuous and equal mass flow through the 28 cooling channels, a rate of 80 g/s was necessary at 1.8 K. The mass flow instability occurred only during ramp up of the coil and is not completely

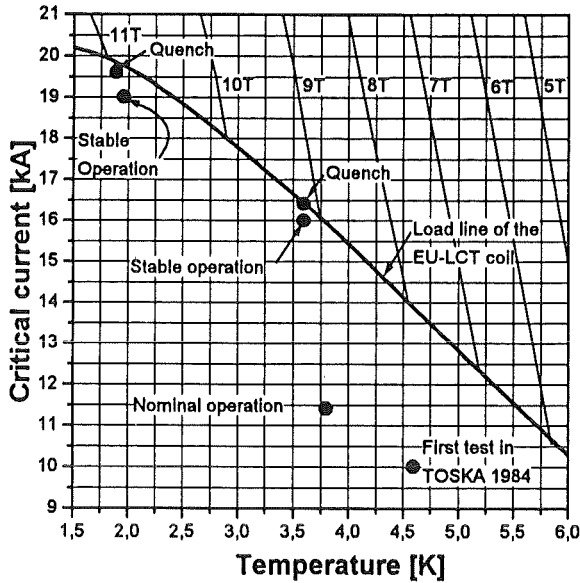


Fig. 1: Current sharing diagram for the EU-LCT coil derived from measured current sharing data and an extrapolation to the HE II range

understood up to now. No significant differences in pressure drop and heat losses between He I and He II cooling conditions after a dump or quench were observed (Tab. 1 and 2).

Table 2: Thermohydraulic properties after a dump or quench (peak values)

Operation mode D = Dump Q = Quench	3.5 K 16 kA D	1.8 K 19 kA D	1.8 K 19.6 kA Q
Winding			
Inlet temperature [K]	14.7	11.7	26.5
Outlet temperature [K]	8.8	11.0	17.4
Pressure [bar]	5.3	8.8	26.6
Heat load [MJ]	0.38	1.6	2.0
Case			
Inlet temperature [K]	12.5	17.5	24.3
Outlet temperature [K]	18.4	21.0	21.7
Pressure [bar]	5.6	18.1	13.4
Heat load [MJ]	1.1	1.3	1.65

2.5 Mechanical properties and FEM calculations

The LCT coil instrumentation was used as it was in the earlier tests. Additional 30 strain gauges were installed onto the reinforcement belts. A frame with displacement transducers was installed to measure the coil case deformation in the middle of the straight section. Also, the coil deformation across the apices was measured.

All the measured data like strain, displacement and equivalent stresses (v. Mises) at the coil case and reinforcement structure were in excellent agreement (< 10 %) with FEM calculations. The gap measured between winding and

case at the inner side of the straight part of the reinforced coil corresponds to measurements at the ORNL test facility where the LCT-coil was fixed to a bucking post. This confirms the quality of the design, the proper installation and the force transmission from the coil to the reinforcement structure.

3. Conclusions

- After 9 years idle time, was confirmed that the EU-LCT coil with all its components kept its full performance. Therefore, the coil is suitable to be used as background field coil for the ITER TFMC test.
- For the first time, it was demonstrated that a coil of this size can be cooled with forced flow He II at supercritical pressure.
- The ff cooling mode compensates the electrical insulation problems related to subatmospheric operation in liquid Helium.
- The test demonstrates the engineering standards of the design principles of the EU-LCT coil with fully predictable operation limits.

Literature:

[1] M. Darweschad et.al., Operation of the upgraded TOSKA facility and test results of the EU-LCT coil cooled with forced flow Helium II at supercritical pressure. Proc. 19th SOFT, Lisbon, Portugal, Sept. 16 - 20, 1996

Staff:

- H. Barthel
- M.S. Darweschad
- G. Friesinger
- A. Götz
- A. Grünhagen
- R. Heller
- W. Herz
- I. Meyer
- G. Nöther
- K. Rietzschel
- C. Sihler
- E. Specht
- H.-J. Spiegel
- F. Süß
- M. Süßer
- A. Ulbricht
- D. Weigert
- F. Wüchner
- G. Zahn
- V. Zwecker

M 27 Critical Current vs. Strain Tests on EU Strands and Subsize CICC's with Stainless Steel and Incoloy Jackets

Within this task the effect of axial strain (ϵ) on critical current (I_c) of various subsize "Cable in Conduit Conductors" (CICC) foreseen for TF and CS coils and their basic Nb₃Sn strands will be investigated. The CICC's consist of an outer jacket and an inner 36 strand cable. The jacket influences the I_c vs ϵ characteristic drastically. Therefore different jacket materials (stainless steel and Incoloy) and also various volume fractions of jacket material ("thin" and "thick" walled conduits) will be tested. For the cable Nb₃Sn strands will be delivered by the EU industry (VAC and LMI). The task will be performed as a collaboration between FZK/ITP, CEA and the EU industry. The samples will be delivered by CEA and measured in the high field test facility at FZK/ITP. The delivery of samples was scheduled for the end of 1995, and they arrived partly in July 1996.

First results of CICC's with VAC cable tested on "thin" and "thick" walled SS conduit samples (representative for TF and CS conductors, respectively) show the expected strong degradation of I_c due to prestrain (Figure 1). The decrease is about 10% smaller for the "thin" walled CICC in comparison to the "thick" walled one. Further tests are in progress.

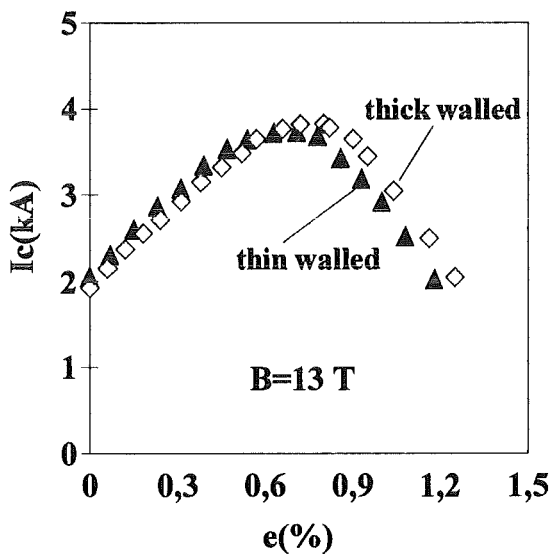


Fig. 1: Critical current versus axial strain of thick and thin walled stainless steel jacketed conductor

Staff:

H. Kiesel

W. Specking

M 31 Development of 60 kA Current Leads Using High Temperature Superconductors

The purpose of the program is to develop a 60 kA current lead for the ITER Toroidal Field Coil system using High Temperature Superconductors (HTSC), in a situation where d.c. operation is considered. The development will be done in collaboration with the Fusion Technology Division of the Centre Recherches en Physique des Plasmas (CRPP) of the Ecole Polytechnique Fédérale de Lausanne. The task has been started early this year. The development program is based on study and engineering work done during the last few years, both at FZK and CRPP, which demonstrate the capability (and the risks) of using HTSC's in current leads carrying several 10 kA.

Current leads for operation currents in the range of 10 - 60 kA are needed in the research community for fusion (ITER, W 7-X) or accelerator technology (LHC) applications. Most of the work presently done was concentrated on HTSC binary current leads for currents in the 1 to 2 kA range except the following ones: In the frame of the European Brite/EuRam programme, European industry is developing a 5 kA_{rms}/50 kV current lead, at Argonne National Laboratory, a 16 kA current lead has been designed for the Babcock&Wilcox Anchorage SMES project. Recently, Oxford Instruments and CERN have announced the successful test of an experimental 13 kA HTS current lead foreseen for the LHC.

As a result of study work done in the past, the following concept will be used: The current lead will be of the binary type, i.e., an HTSC part in the temperature range from 4 K to 70 K and a conventional copper part in the range from 70 K to room temperature (RT). A two-cooling circuit concept is foreseen, i.e., the HTSC part will be conduction cooled at 4 K and the copper part will be actively cooled with 60 K helium. The heat sink at 60 K will be realised using 60 K Helium from the refrigerator; this is in general available as shield cooling for e.g. transfer lines. It turns out that the reduction factor in refrigeration power will be in the order of 3 - 5, as compared to a conventional copper lead. The spread covers for example the uncertainties in refrigerator efficiency and contact resistance.

The development program is subdivided into three stages:

- A-1 Test of different materials and concepts in 1 kA modules for selection, i.e.,
- Bi-2212 bulk material (tubes),
 - Bi-2223 tapes with Ag/Au sheath in a straight stacked configuration,
 - Bi-2223 tapes with Ag/Au sheath twisted around a support GfK-tube, and
 - Y-123 bulk material (rod).

Each assembly is being tested separately in a test facility at CRPP. The tests cover the steady state as well as the transient behaviour with respect to temperature profile, heat load at 4 K level, mass flow of 60 K helium and safety behaviour in case of loss of coolant flow. The results of the tests will be compared to design calculations to qualify the numerical codes. In addition, the effect of thermal cycling on the behaviour of the leads will be measured.

At the end of stage A-1, one option will be chosen for the further development.

- A-2 Test of a 10 kA HTSC binary current lead using the material selected in stage 1. This will also be done at CRPP
- B Design and test of a 20 kA HTSC binary current lead to prove the modularity and scale-ability of the design. For this test, the STAR facility at FZK will be used.
- C After completion of stage B, a 60 kA current lead could be designed to replace an existing current lead in the TOSKA facility at FZK. This stage is an option, the decision will be made after completion of stage 3 depending on the results.

The task will be performed in stages A to B. After completion of stage B, a decision will be made whether to proceed with stage C.

Special emphasis will be given to safety. The safety requirements for the ITER TF-coil magnet system are such that the coil system has to be discharged with a time constant of 15 s of the exponential current decay without any damage. So, the current leads have to withstand a power discharge of the coils within approximately 60 s. The critical issue is the behaviour of the HTSC part of the current lead in case of a quench in the HTSC due to, e.g., a failure of the refrigeration system of the current leads.

Taking into account the fact that HTSC have a low thermal conductivity and generate large Joule heating in case of being normal conducting, a quench of HTSC bulk material would result in a burn-out during a very short time, if the energy will not be removed from the system very fast. As a consequence, a current lead design using HTSC bulk material requires a current stabilization for emergency situations. For the 1 kA current lead options using HTSC bulk material, no electrical bypass is foreseen because the power supply can be switched-off fast enough to prevent the HTSC material from damage. This has to be taken in mind if comparing the results of the different materials resp. concepts.

The design of the 1 kA current leads consists of a HTSC part and a copper part connecting the 4 K and 70 K resp. 70 K and RT regimes. The copper heat exchanger is of the bundle type, i.e., a large number of silver coated corrugated fine copper wires are bundled, compacted and put into a stainless steel tube to form a helium porous current carrying device. The

copper cross-section and length of heat exchanger is adapted to the operation current. The heat transfer area is very large although it is not exactly defined. This concept was been successfully applied to vapour cooled current leads up to a current of about 20 kA. The HTSC part consists of the HTSC bulk material resp. tapes and two copper adapters which are soft soldered to the copper heat exchanger and to the copper stabilized NbTi bus bar. The design allows the exchange of the HTSC part without changing the copper heat exchanger. The heat load on the 4 K level is determined by measuring the mass flow rate of the evaporating helium encapsulated in a separate volume to distinguish from cryostat losses. The mass flow rate of the 60 K helium, which cools the copper heat exchanger, is also measured. Temperature sensors as well as voltage taps are positioned along the HTSC and copper part to measure the temperature profile and the voltage drop along the HTSC and the copper heat exchanger resp. across the copper adapters to determine the contact losses. The conduction loss is measured at zero transport current by adjusting the upper temperature of the HTSC part to the same value as for nonzero current. The measurements are done for different mass flow rates and for different transport currents. The experimental results are compared with design calculations based on material property data.

As already mentioned above, four materials resp. concepts are being investigated. Melt-cast-processed (MCP) Bi-2212 bulk tubes fabricated by Hoechst AG, Frankfurt, are used having outer/inner diameters of 35/27 mm and a total length of 260 mm (including Ag-contacts). The current lead was tested at the end of last year.

B-2223 multifilamentary tapes sheathed by Ag(3at%)Au alloy fabricated by AmericanSuperConductor are currently tested.

At FZK, Bi-2223 tapes with Ag/Au sheath are currently fabricated. The tapes consist of seven Bi-2223 filaments embedded in a sheath made of Ag(8at%)Au, the tape dimensions are 0.20 x 2.4 mm². The volume fraction of superconductor is roughly 20 %. The critical current of the tape in self field at 77 K is 8 - 9 A (critical current density of 9000 - 10000 A/cm²). The choice of using 7 filaments was made to ease and fasten the fabrication although the critical current density is not as high as possible. For the next step of the program, it is planned to use tapes with 37 filaments, the expected j_c will be up to 2 times higher than for the current ones. Thirteen tapes are loosely put together to form a "stack". Ten of these stacks are equally-distanced mounted on a device which consists of two copper adapters which are needed to fit in the CRPP current lead device and a GfK tube which serves as mechanical connection and support. The stacks are twisted around a GfK support tube, the twist length is chosen to be twice the length of the tapes. The stacks are soldered in grooves and milled in the copper adapters. The length of the HTSC module is about 500 mm. Fig. 1 shows an artists view of the HTSC-module.

Without magnetic field correction, the critical current of the module should be 1100 A. at 77 K and zero magnetic field. Magnetic field calculations have been done using the code

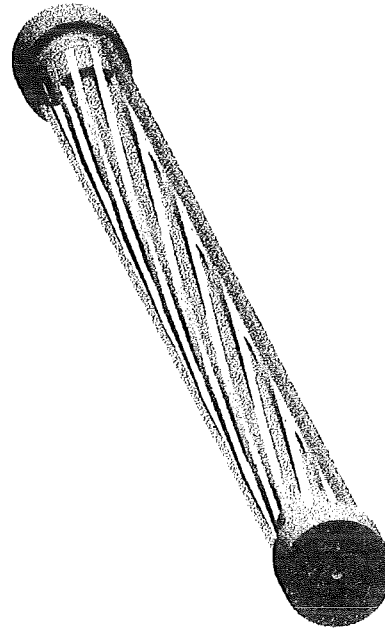


Fig. 1: Artist's view of the Bi-2223 tape (FZK version)

EFFI for the actual geometry. This results in an inhomogeneous distribution of critical current in the stack and in a total critical current of 800 A which is about 70 % of the uncorrected critical current. Because the maximum temperature at the upper end of the HTSC module in the current lead will be about 70 K, the critical current will be higher.

At FZK, Y-123 bulk rods are fabricated using a technique developed for the fabrication of pellets for a flywheel project. The rods are 14 x 9 mm² in cross-section and approximately 90 mm in length. Due to fabrication reasons, the rods consist of three Y-123 domains, so their critical currents are determined by weak links. The critical current measured in self-field at 77 K at one sample was 1800 A corresponding to a critical current density of 1400 A/cm². In the meantime, the fabrication of the rods have been further optimized to get higher critical currents.

In Table 1, the design parameters of the HTSC part of the 1 kA current leads are summarized. The calculations were done using the computer code CURLEAD which had been developed for optimization of forced-cooled conventional current leads. It also contains the Room Temperature Power Consumption (RTPC) normalized to a conventional copper current lead.

The calculated 4 K losses of option 1 (Bi-2212 bulk material) are lower by a factor of > 2.5 as compared to the other options (see Table 1). It should be reminded, however, that no electrical stabilizer was used in the design: for a current lead to be forseen in large magnet systems, such a stabilizer or safety lead is indispensable to minimize the operational risks. An electrical stabilizer, e.g. stainless steel, will lead to an increase of the total loss at the 4 K level.

Table 1: Design parameters of the 1 kA HTSC-modules

Material	Unit	Bi-2212 (bulk)	Bi-2223 (tape)	Bi-2223 (tape)	Y-123 (bulk)
I_c at $B=0, T=77K$	[A]	> 2000	1025	~1000	> 1800
B_{self} at 1 kA	[mT]	13	26	26	36
A_{sc}	[mm ²]	390	10.5	12.5	126
A_{stab}	[mm ²]	---	24.6	50	---
L	[cm]	26	50	50	9
$T_{top, HTSC}$	[K]	72.1	71.8	71.5	70.6
P_{cond} at 4 K	[mW]	97	375	314	240
ΔU for 1 kA	[mV]	31.7	31.2	30.8	31.3
Ideal RTPC	[%]	28	34	32	31

The 1 kA current leads are being tested at CRPP in a cryostat under vacuum conditions.

Table 2 contains the main results of options 1 and 2 for steady

Table 2: Test results of the 1-kA HTSC-modules

Material	Bi-2212 (bulk)	Bi-2223 (tape)
I [A]	1000	1000
mass flow [g/s]	0.08	0.08
$T_{top, HTSC}$ [K]	67.8	72.3
P_{cond} at 4 K	101	330
ΔU_{hex} [mV]	32	33
Total ideal RTPC [%]	29	34
ΔT [s]	540	n.a.

state operation as heat load and voltage drop. These results have to be compared to the design values of Table I. In addition it contains information about the transient behaviour in case of loss of coolant flow. Δt denotes the time difference between interruption of helium mass flow and exceeding a resistive voltage across the HTSC part of 100 mV. It turns out that the measured conduction losses as well as the temperatures at the upper end of the HTSC part agree well with the calculated ones.

In Fig. 2, the measured and calculated temperature profiles along the current lead using Bi-2212 bulk material resp. Bi-2223 tapes sheathed with Ag(3at%)Au alloy for 1 kA are

shown. The agreement between the measurement results and the calculations is good.

At the end of the year, the construction of the Bi-2223 (FZK-ITP) version as well as the Y-123 (FZK-INFP) version will be finished and the modules will be shipped to CRPP for testing.

In the meantime, the construction of the 10 kA current lead has been started. The test will also be done at CRPP.

Literature:

R. Heller et al., "Development Program of a 60 kA Current Lead Using High Temperature Superconductors", paper presented at 1996 Applied Superconductivity Conference, Pittsburgh, PA, Sept 25th - 30th 1996

Staff:

- R. Bußjäger
- G. Friesinger
- W. Goldacker
- R. Heller
- H. Kathol
- H. Orschulko
- B. Ullmann

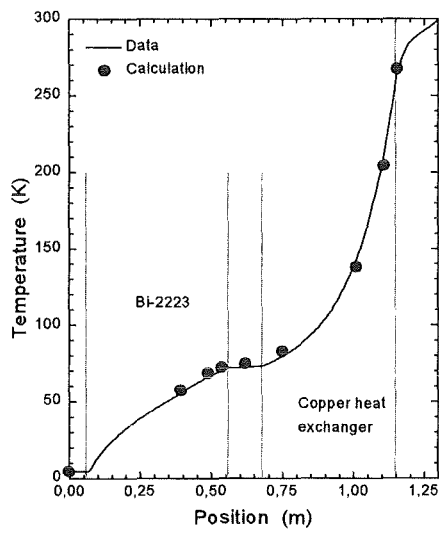
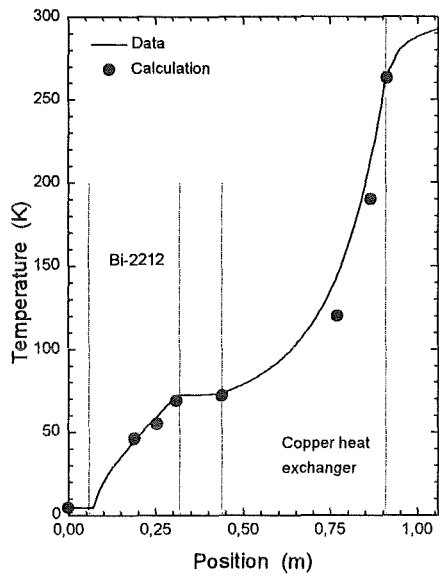


Fig. 2: Temperature profiles for the Bi-2212 bulk option (top) and for the Bi-2223 tape option (bottom) at 1 kA

N 11 TD 58 (SEA 3) Reference Accident Sequences - Magnet Systems

Subtask 2: Magnet System Safety

Within the subtask 3.2 FZK investigates the thermal and mechanical behavior of magnet systems during accidents.

In the period reported here code application and validation of MAGS have been major parts of the work. The work on structural analysis has been emphasized and is now focusing on the ITER TF coil test to be performed in TOSKA.

a) Thermal analyses for magnet systems

Analyses on arcs within coils have been performed using the module HEXAN (Helium EXPulsion ANalytical). First results showed the necessity to introduce also for this module the moving mesh option, being used for module GANDALF already. The module CRYOSTAT, thermo- and fluid dynamics in the cryostat, has been extended to be also applicable for small leaks. This development turned out to be difficult, because continuum mechanics are applied at very low pressures. This leads to very sensitive equation systems since volumes having small masses and small distortions from the boundary conditions can lead to oscillations. For a more general use of MAGS the GRID7 module was prepared. This allows for analyses of more complex coil shapes, e.g. stellarator coils.

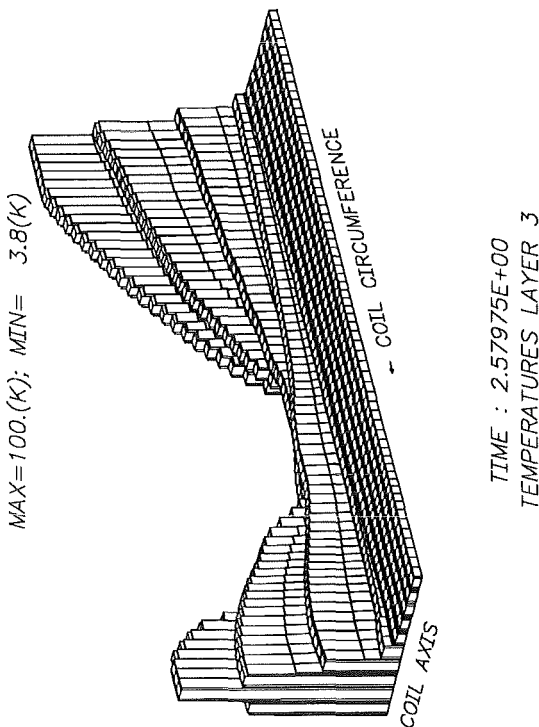


Fig. 1: Temperature due to quench propagation in a W7-X coil

Besides this some reprogramming of the code system was performed to improve the code performance and to ease the use of MAGS.

Investigations on shorts and arcs for the ITER coils have been performed. For the TF coils it turned out that the design is robust. Because the cable is located in grooves of the radial shear plates any insulation failure will lead to a current through the shear plate. These currents can be monitored and limited by appropriate selection of their 'grounding' resistors. In consequence, damages to the TF coils are not to be expected.

The central solenoid is wound with four cables in hand. Therefore shorts within one hand or between different hands have to be considered. For this coil it turned out that its electrical circuit is advantageous. Since all the four hands are connected in parallel, voltage difference between neighboring turns are small. Additionally, due to the almost perfect inductive coupling, current can be commuted to other hands so that the damaged area can be bypassed. Even with a short the coil can be safely discharged.

For the PF coils, the coil PF5 was investigated for reference. It was found that the present design and electrical circuit cannot exclude major damages to the coil. One reason for this result is the fact that the cables for this coil are connected in series, so that a short shortens many turns, the other is, that the cable has a high copper fraction so that even though quench is initiated the additional resistance does not help much to spread the energy on a larger fraction of the coil volume.

To test the GRID7 module, for a stellarator geometry, a quench analysis for a W7-X coil has been started. Three cables, i.e. 6 layers of conductor were investigated, a quench has been initiated at the transition between layer 1 and 2. Fig. 1 shows the temperatures in the third layer, in an circumferential - axial cut, 2.5 seconds after quench initiation. It is to be seen there that initially quench propagation via heat conduction between turns occurs, trapping cold slugs of helium. At the third turn, however, the quench propagation velocity along the conductor is higher than the transverse. The cold helium slug evaporates within 0.5s reducing the temperature gradient along the conductor.

b) Experiment to validate the MAGS code

As reported earlier, for validation of the MAGS code the 3d quench experiment Q3D is performed in the STAR facility in cooperation with ITP at FZK. The focus of this experiment is to examine the axial and transversal quench propagations in a coil having forced flow helium coolant. For the tests a one layer coil, wound with two conductors in hand, is used.

The coil is heavily instrumented, amongst others 10 taps have been drilled into the jacket to place measurement devices and the quench heaters. These taps as well as the cable feed-throughs between the helium conducting tubes and the cryostat vacuum are prone for leaks. At ambient

temperatures such leaks have been found and successfully tightened. But new leaks may show up during cooldown or during the experiments.

To protect the Q3D test apparatus as well as the STAR facility, an envelope was designed for the Q3D coil to provide a separate vacuum for it. This vacuum is tight against the vacuum of the STAR cryostat and can be pumped down separately. While a loss of vacuum for the STAR cryostat could lead to shorts or arcs, a leak in the separate vacuum of Q3D coil is no problem since this coil is non inductive, i.e. no arcs can be ignited.

The envelope is built and the Q3D coil was installed. Both are inserted in the STAR facility where helium and current supply are presently connected. The cabling of the measurement devices to the feed-throughs is in preparation, while the cabling from the cryostat to the control room is ready. First shake down tests of the measurement equipment and the power supply of the sensors are just done.

The software to prepare the experimental data is developed and adapted to the systems available. Tests are performed with simulated data.

In the framework of validation of MAGS comparisons with the QUELL (Quench Experiment on Long Length) have been performed. The QUELL-sample, built up at PSI, is based on a coil with two layers with 30 windings each and a connecting loop between the layers. The quench is initiated by an inductive heater located at the connecting loop.

For the first series of comparisons simulation data of the 1D-code GANDALF were used. The pressure profiles agree quite well. Temperature profiles are similar in shape but differ significantly in absolute values. The difference has to be investigated. Quench propagation computed with MAGS is slightly slower.

An important feature of the results of the 3D-code MAGS is the appearance of a transversal quench initiated by heat conduction from the outer to the inner layer, doubling the quench velocity. A slug of cold helium is trapped between the two quenched zones.

Calculations were performed using different discretisations of the cable cross section. The resolutions extend from 8 gridpoints in the cross section up to 48 gridpoints for the finest mesh. In the first case different lumped materials were used whereas in the latter only in the cable space, represented by 5 gridpoints, was mixed material. The overall agreement is quite good. Differences mainly arise from different heat conduction in the transversal direction due to lumped materials and due to the approximation of the circular cable with a coarse or fine mesh.

Differences between MAGS results and the given data also might be due to different initial conditions. Therefore the

boundary conditions leading to steady state have be properly defined.

Staff:

M. Biemüller

G. Bönisch

W. Kuhn

R. Meyder

CTA-EU-D 36 (SEP 2) Environmental Impact

Based on the knowledge gained with plant experiments, performed at FZK, Karlsruhe, the computer code 'Plant-OBT', for describing the OBT formation and translocation in wheat plants, has been developed. A first version of the stand alone program 'Plant-OBT' is described in [1]. The OBT formation is directly coupled to processes such as photosynthesis, respiration, metabolic exchange and maintenance of the plant. Comparative calculations, which were performed during the previous working period, with plant experiments carried out in the years 1993 - 1994 at FZK, showed that the photosynthesis process was not correctly taken into consideration. Therefore, the photosynthesis as well as the deposition submodules have been rewritten. New tests performed with experimental data from 1995 demonstrated the need for improvements in both processes, as the prior version of 'Plant-OBT' was not able to validate the data sufficiently correct. When completed, the model will be implemented into UFOTRI, the accident consequence assessment code for tritium releases [2].

Within BIOMOVs II (BIOSheric MOdel Validation Study - phase II) tritium models including UFOTRI and Plant-OBT were tested using three different scenarios. The first scenario was a model intercomparison study with an artificially derived release scenario. Important conclusions were, that the process oriented models are useful for understanding the processes of the tritium transfer in the environment, whereas compartment approaches are more suitable for dose assessments, but they are of minor help for describing the time dependency of tritium concentrations in the environment. Additionally, modelling of the soil and the dynamics of OBT proved to be the critical points of the models. The other two scenarios covered subprocesses such as the reemission process from soil and vegetation as well as the OBT formation during daytime and night-time conditions. The model results of UFOTRI for the reemission scenario were in rather good agreement with the calculations. However, the tritium flux out of soil and plants in the morning and in the evening were always overestimated. The results of UFOTRI for the OBT formation scenario showed the tendency to underpredict the OBT formation rate at night-time. The Plant-OBT model performed better in this case which supports the idea to replace the 'old' UFOTRI submodule by the 'new' Plant-OBT' code. Both model results showed a good agreement for the daytime scenario. The documentation of all scenarios will be finalized till the end of 1996 [3].

Starting with a series of small-scale field studies at FZK last year, scientists from the 'Zentrum für Strahlenschutz und Radioökologie' (ZSR), Hannover, have performed new reemission experiments this summer. Three experiments were carried out on reemission from grass covered soil after one-hour HTO deposition, one at sunrise (7:00 a.m.), one at sunset (9:00 p. m.) and one at noon. The aim of these experiments was to improve the UFOTRI submodel for estimating the reemission from bare soil and soil covered with vegetation.

For accidental and normal operation releases, dose assessments were performed in the frame of subtask SEP2 of the European Fusion Programme for the two sites of Greifswald and Cadarache, at the time of the investigations potential sites for ITER. Probabilistic calculations for accidental release conditions were carried out with the computer codes UFOTRI and COSYMA [4] for HT, HTO and activated steel, respectively. Two different release heights - 10 m with building wake effects and 100 m undisturbed stack release - were considered. Normal operation conditions were investigated for HT, HTO and activated steel by using NORMTRI [5] and COSYMA, respectively. For the normal operation scenarios, releases via a stack were assumed. The input parameters were adapted as far as possible to those used in the ITER-EDA study to allow a better intercomparison with the site independent dose assessments. No specific national criteria were applied in the calculations. The agreement between the results from the ITER study on accidental atmospheric releases and the two sites are rather good for tritium, whereas the ITER reference dose values for the activation product releases are often lower than the maximum doses for Cadarache and Greifswald. However, the percentile values fit better to the deterministic approach of ITER. Doses from site specific routine release scenarios were always lower than estimated within ITER [6]. Additionally, data from Stockholm, representing Forsmark and Studsvik (Sweden), were provided and the same assessments were repeated for this site. The resulting doses do not differ significantly from those of Greifswald and Cadarache [7].

The work on developing models for the assessment of doses to individuals and the public resulting from contamination of waterbodies after an accidental release of radionuclides has been progressed. The hydrological model chain which consists of the run-off model RETRACE-1 and RETRACE-2, the river models RIVTOX and COASTOX, the lake models LAKECO-B and COASTOX-lake and a simple dose model has been successfully coupled and demonstrated to a wide audience [8]. The model chain is undergoing test and validation studies on the Ilja river (Ukraine), the Pripjat river (Russia) and the Rhine catchment (mainly Germany). Individual models such as RETRACE and RIVTOX have been tested within the frame of the BIOMOVs-II study [8].

Literature:

- [1] Raskob, W., Diabaté, S. and Strack, S., A New Approach for Modelling the Formation and Translocation of Organically Bound Tritium in Accident Consequence Assessment Codes, in: Proc. of the International Symposium on Ionising Radiation: 'Protection of the Environment', Stockholm, Sweden, May 20 - 24, 1996, to be published
- [2] Raskob, W., Description of the New Version 4.0 of the Tritium Model UFOTRI Including User Guide, Report KfK-5194, Kernforschungszentrum Karlsruhe (1993)

- [3] Barry, P.J. Ed., Report of BIOMOV5 II Working Group on Special Radionuclides, in preparation, (1996)
- [4] COSYMA: A New Program Package for Accident Consequence Assessment. Joint report by Kernforschungszentrum Karlsruhe GmbH and National Radiological Protection Board, Commission of the European Communities, Report EUR-13028 EN (1991)
- [5] Raskob, W., Description of NORMTRI: a Computer Program for Assessing the Off-Site Consequences of Air-Borne Releases of Tritium during Normal Operation of Nuclear Facilities. Report KfK-5364, Kernforschungszentrum Karlsruhe (1994)
- [6] Raskob, W., Dose Assessment for Cadarache and Greifswald. Report FZKA-5753, Forschungszentrum Karlsruhe (1996)
- [7] Raskob, W. and Edlund, O., Comparison of Site Specific Probabilistic Dose Assessments with Deterministic Generic Dose Values Compiled Within the ITER-EDA, in: Proc. of the 19th SOFT Conference, Lisbon, Portugal, 16.9.96-20.09.96, to be published in Fusion Technology
- [8] Zheleznyak, M., Heling, R., Raskob, W., Popov, A., Borodin, R., Gofman, D., Lyashenko, G., Marinets, A., Pokhil, A., Shepeleva, T., Tklich, P., Modelling of Hydrological Pathways in RODOS. In: Proceedings of the Conference on Radiological Consequences of the Chernobyl Accident, Minsk, Belarus, March 1996, Report EUR 16544 EN, pp. 1139-1148, (1996)

Staff:

J. Ehrhardt
I. Hasemann
D. Meyer
W. Raskob

Vacuum and Fuel Cycle

Within task T 228 the copumping cryosorption pump concept has been selected for the ITER primary vacuum pumps, and in close collaboration with the NET as well as the ITER Team the design of a prototypical pump has been elaborated to match all operating requirements where high vacuum is involved. An integrated development program is under way to test novel design principles and critical components, to follow up the construction of a model pump and to carry out for the performance testing at FZK.

In order to meet the limitations related to the permissible tritium inventory of the cryopump system it had to be demonstrated that the pumping and regeneration cycles for the cryopanel can be kept extremely short. This comprised the development of both fast heating and fast cooling methods. The tests could successfully be carried out in the available cryostats TITAN and HELITEX after some modifications. In order to demonstrate that the proposed panel design for the ITER cryopump is able to withstand the high number of regeneration cycles, temperature cycling endurance tests are under way. Furthermore, requirements concerning advanced ITER operation modes and conditions (e.g. He-plasma) required further measurements especially for the "quilted panel" type in order to support the current baseline design and to provide a thorough understanding of the underlying mechanisms.

The supplementing task 234A is devoted to the objective of ascertaining the pump-out of the cryopumps during regeneration in the available short time frame by means of tritium-compatible, i.e. oil-free, forepump trains. The previously determined data set was used both for a calculation of the number of forepump trains necessary for ITER and for a variation in the number and size of forepump combinations. In addition experimental data were obtained on a novel, magnetically suspended turbo-hybrid pump. This pump shows a much better pumping speed especially in the low pressure range and may thus provide the starting-point for further forepump train optimization.

In the Fuel Cycle area a decision on an ITER reference design for plasma exhaust processing has been postponed by the ITER Team until the end of the EDA in favour of further parallel research and design work on competing fuel recycling processes in the respective tritium laboratories of the EU, JA and US Home Teams, while the centerpiece of the process as demonstrated by the technical facility CAPRICE has been retained as the basis for ITER cost estimates. The full recycling process CAPER as developed by FZK is being demonstrated on a technical scale after modification of CAPRICE in order to verify an overall decontamination factor of at least $2 \cdot 10^7$. Major accomplishments were achieved in the final decontamination ("polishing") step which is based on isotopic swamping in a counter current mode and extraction by permeation. Design work for an ITER Tritium Plant based on the CAPER process and including all safety features is well under way. Supporting experimental activities

were continued in the area of permeator endurance and tritium storage.

The PETRA permeator loop was operated with isotopic mixtures of hydrogen, and poisoning effects after the addition of tritiated hydrocarbons were studied. Concerning tritium storage the main effort was transferred to a fast releasing bed, and significant progress was achieved when heat was directly applied to the getter material via radiofrequency heating. For the ageing studies in ALTEX the analytical device for a quantitative detection of the decay product He-3 has been installed.

H.D. Röhrig

G 18 TT 22 (T 228) Cryopump Development

1. Prototype Pump Concept

1.1 Introduction

The primary vacuum pumps to be developed for ITER, shall accomplish torus pumping and maintenance of pressures specified during the various modes of reactor operation. The single pumps are included in the primary vacuum pump system consisting of sixteen identical batch regenerating cryosorption pumps, each located in one of the divertor ducts of the machine.

Having studied various alternatives [1, 2] the copumping cryosorption concept was selected as „point design“ for the prototype pump. The pump concept proposed embodies a number of novel design principles to meet the ITER requirements and an integrated development programme is under way in order to test critical components and to design, build and test a prototype pump.

1.2 Requirements

The primary vacuum pump has to meet the following operating requirements: Initial evacuation to high vacuum, following cross-over from the torus roughing pumps, pumping during bake out, pumping during conditioning, pumping during plasma burn and dwell periods and pumping during leak testing. The mass flows, pressures and composition of the exhaust gas vary considerably in the operation modes required [3]. The requirements for the plasma burn mode are presented in Table 1.

Table 1: Parameters for pump design

Total gas throughput	Pam ³ /s	200
He throughput	Pam ³ /s	2
Gas composition *Q ≅ H, D, T	Mole%	1.0 He, 1.0 H ₂ , 90 DT, 1.0 CQ ⁺ ₄ , 5.0 Ar or Ne or N ₂ or Kr. 0.25Q ⁺ ₂ O, 1.75 Air, CO, CO ₂
Divertor pressure	Pa	0.1 ≤ p ≤ 10
Net pumping speed	m ³ /s	adjustable between less than 2% and 100% of maximum in less than 5 - 10 s
Gas temperature at pump inlet	K	475 during burn mode
Maximum permissible Tritium inventory	g	100

To minimise conductance loss between the divertor and the pump, the pumps are installed in the divertor ducts at minimum distance from the torus. At this point, magnetic fields of 1 T are expected. The temperatures of the divertor duct walls increase to 450 K due to nuclear heating. The

tritium fraction in the exhaust gas does not allow any use of hydrocarbon-containing lubricants, insulating and bonding materials.

1.3 Prototype Pump Design

The pump concept selected is based on an intermittently working cryopump (s. Fig. 1) [4]. The gas to be pumped flows through the valve port into the cylindrical pumping chamber of 1500 mm diameter and 1500 length. The gas molecules first meet with the baffle rings, the shape of which is similar to that of conical spring washers. These baffles are kept at 80 K using GHe. Here, condensation of the high-boiling impurities of the exhaust gas mixture takes place. The 5 K cryopanel is completely surrounded by 80 K shields and baffles which form an optically tight enclosure with regard to the thermal radiation of the outer shell of the pump, the valve disc and shaft and the valve port. The plane shields are made of double walled stainless steel panels cooled by a forced flow of 80 K gaseous helium. Helium, the hydrogen isotopes and the low-boiling impurities pass this baffle structure into the 5 K pumping area. This consists of 20 double walled panels arranged to form a cylindrical array of 1 m length and 1126 and 1410 mm inner and outer diameter, respectively. Each panel is rectangular in shape with 200 x 1000 mm in dimension and inclined at 45° to the pump radius. The panels are cooled by a forced flow of supercritical helium (SCHe) supplied from a circular manifold. Pairs of panels are connected in series and the SCHe flow is returned by way of a second circular manifold. The panels are coated with activated charcoal on one or both sides.

The divertor pressure varies between 10⁻¹ and 10 Pa. Nevertheless, the pump is designed for operation in the molecular flow regime which exists at pressures lower than 10⁻¹ Pa at the pump inlet, to avoid high heat conduction which would occur in the gas under transition or viscous flow conditions. The throttling valve at the pump inlet also controls the throughput of the pump and is used to close the pump inlet during regeneration.

The valve stroke is 500 mm in order to achieve a lateral passage area of 2 times the front inlet area of 1 m diameter. To provide the necessary turn-down ratio in throughput, a small auxiliary valve may be incorporated in parallel to the main valve.

For a full valve opening the pumping speeds at the 1 m inlet port are 76 m³/s for DT and 42.5 m³/s for helium in the molecular flow regime. As the pressure increases above 10⁻² Pa, the flow conditions enter the transition regime, becoming fully viscous when the pressure reaches 1 Pa. For the maximum required throughput of 200 Pam³/s (0 °C) and 12 pumps in the pumping mode, the lowest possible total pumping pressure at the pump inlet was estimated to be 1.5·10⁻¹ Pa.

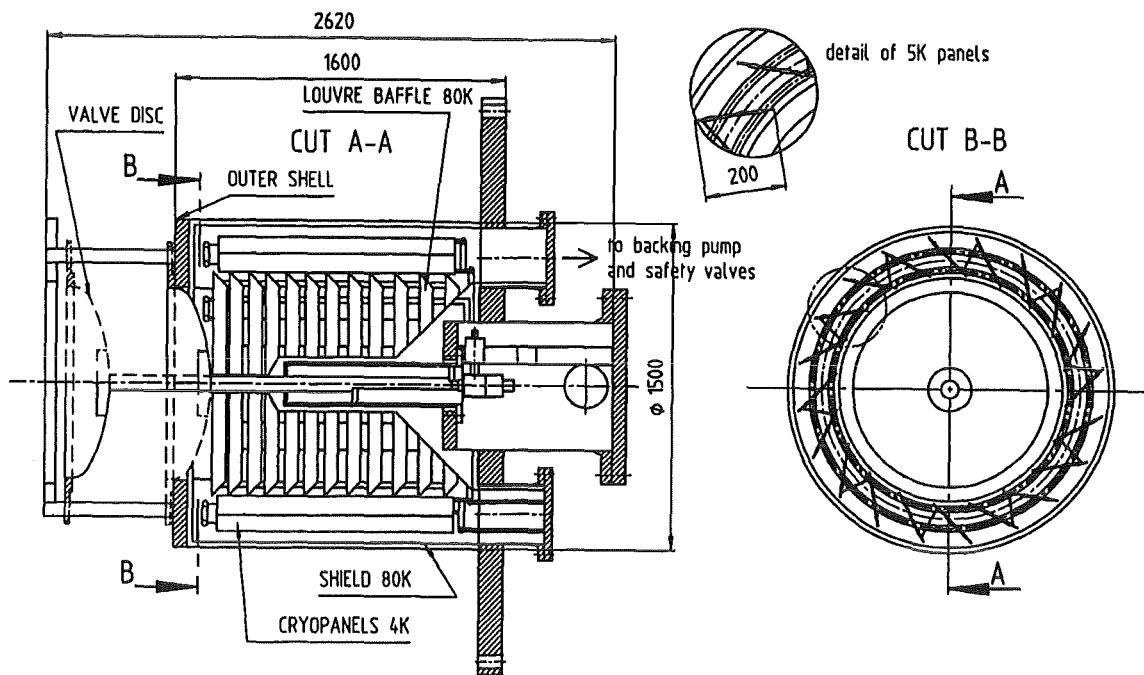


Fig. 1: ITER cryopump concept

1.4 Pumping Performance

For ITER operation, 16 pumps are planned to be used with 12 of them being in the pumping mode at any time. The remaining 4 pumps are regenerated by mechanical forepumps arranged outside the reactor cryostat. The pumping times are limited by the permissible tritium inventory of 100 g in the pumping system. The cryopumps are run in the cyclic mode, i.e. the pump that has reached its maximum permissible tritium inventory is valved off from the torus and regenerated. For the maximum permissible tritium inventory of 100 g pumping times of 750 s and regeneration times of 250 s are obtained.

1.5 Next Step towards the Prototype Pump

Prior to the construction of a prototype pump with 1600 mm length and 1500 mm diameter the concept is being tested on a reduced scale. For the model pump a 1:2 scale has been chosen for the surface of the cryosorption material. The linear dimensions of the cryopump have been reduced by the factor $\sqrt{2}$. The inlet valve is tested at full scale.

To test this model pump the TIMO-facility (Test facility for ITER model pump) is being built at FZK in which the cryogenic requirements can be satisfied during steady-state pumping, during partial regeneration between 5 K and 90 K, and during total regeneration between 5 K and 300 K. The flow scheme is shown in Fig. 2. The maximum 4.5 K cooling power is needed for the fast cooling down of the model pump panels forming a mass of 60 kg stainless steel from 90 K to 5 K after regeneration within less than 60 s. The cryogenic system is based on a 600 W He liquefier plant which supplies a control cryostat. The control cryostat serves both to set the supercritical He-state (SChE) and as a buffer tank for the remaining LHe from the He liquefier during steady state

pumping. In the control cryostat cold blowers for SChE are installed which allow mass flow rates of 50 g/s. With this available SChE supply system acceptance tests of the model pump will be performed.

To achieve the required cooling down times of < 60 s and temperature gradients of < 0.7 K along the cryopanel the presently available 850 l control cryostat is being upgraded. For the tests under ITER-relevant conditions a 3000 l control cryostat is planned including cold blowers delivering 250 g/s SChE flow.

For cooling the louvre baffle and the radiation shield a closed GHe-loop kept at 15 bar and thermostat controlled at 80 K by an LN-bath is used. A He gas flow rate of 50 g/s at room temperature is available for fast heating from 5 K to 90 K.

The model pump will be installed in a pressure vessel of 4400 mm length and 1800 mm diameter whose wall can be heated up to 200 °C, to simulate wall conditioning in ITER.

The model pump, the test vessel and the 80 K GHe-cooling system are presently manufactured by industrial companies.

2. Component Tests

2.1 Introduction

In component tests the pumping behaviour, fast regeneration methods, tritium compatibility and thermal shocks are studied. The results obtained serve as a basis for the final pump design.

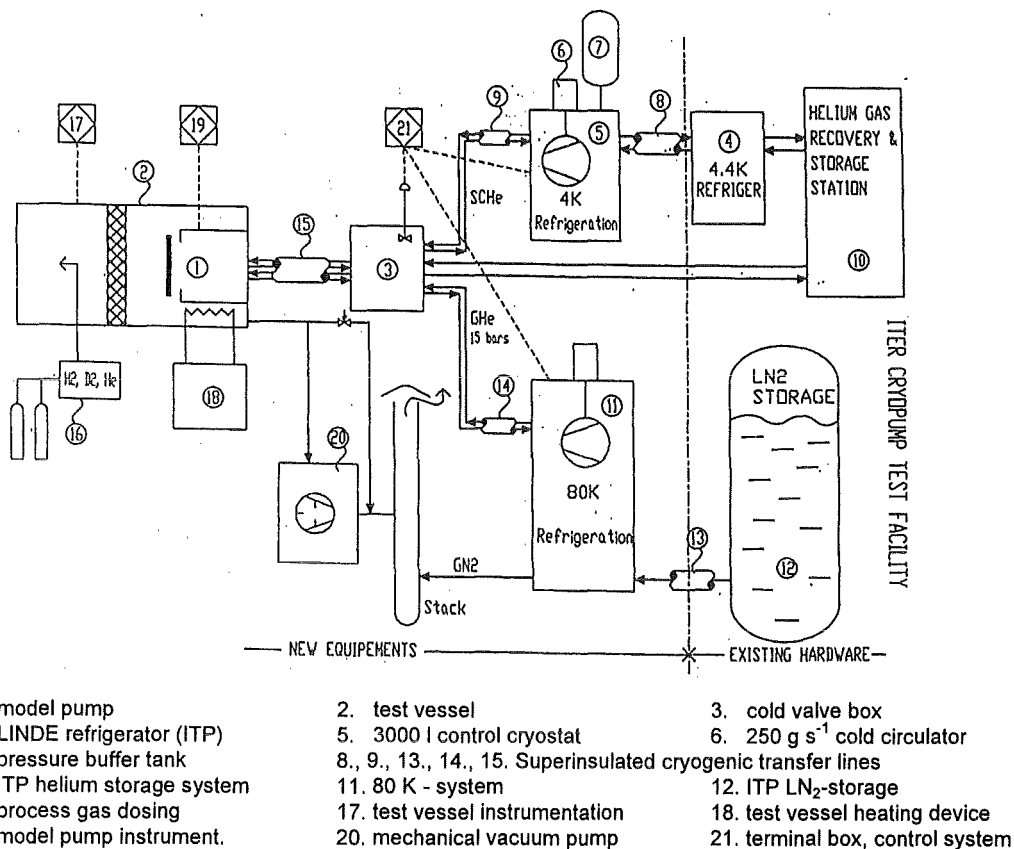


Fig. 2: TIMO - facility

2.2 Fast Regeneration Strategies

Contrary to the conventional cryopump performance, which is determined by the sorbent saturation capacity, the operation of the ITER cryopumps is limited to a gas load less than saturation in order to meet the condition of low tritium inventory (maximum allowable tritium inventory of 100 g in the whole cryopump system). This concept keeps the available cycle times very short, necessitating a large number of cycles. To cope with that, it is necessary to minimise by design measures the time needed for heating and cooling of the cryopanel within each regeneration phase. According to the pumping performance concept outlined above, only 120 s are left for fast heating and cooling. An experimental programme has been launched for detailed investigation and development of novel techniques.

2.2.1 Development of Fast Heating Methods at the TITAN Test Facility

At TITAN, the applicability of various fast heating methods of cryopanel has been investigated. The needed temperature rise is from LHe temperature to about 90 K. A screening study has been performed to check the potentials of various techniques. Within this procedure, various contactless methods, such as

- bare wire heating at a certain distance close to the panel surface,

- glow discharge heating,
- microwave heating and
- inductive heating

had to be rejected, because they turned out not to be feasible [5]. The final test programme comprised infrared heating as representative contactless technology and two direct heating methods, namely,

- forced flow of warm helium gas at elevated pressures inside the cooling channels of the panel and
- controlled electric heating, realized by attaching resistive heating elements (cables, o.d. 1.5 mm) on each side of the test panel, evenly distributed over the panel surface.

The experiments have been performed in the upgraded test facility [6], see Fig. 3. The test panel is installed in the centre of the cylindrical vacuum vessel of 0.7 m diameter and 2.2 m height. It can be baked up to 200 °C by trace heating.

The cryopump consists of two pumping stages. The first one is a LN₂ pool-cooled 106° chevron baffle. The baffle is screwed to the bottom of a cylindrical annular LN₂ recipient and thus kept at 80 K. Towards the top, the LN₂ volume is covered by a copper plate. The second stage is the LHe forced-flow cooled panel itself.

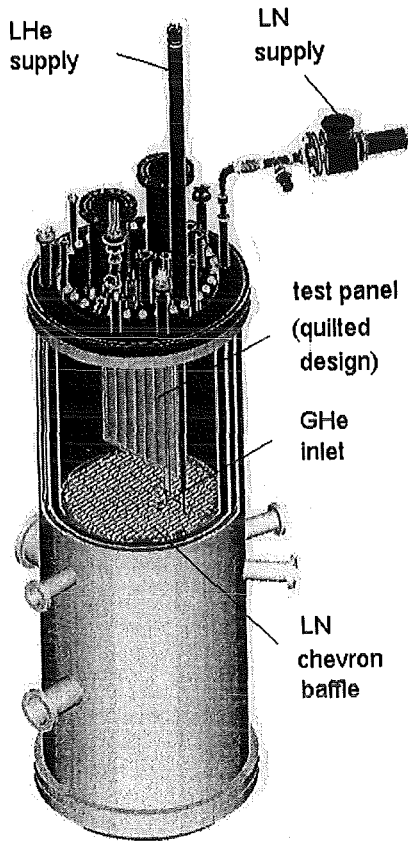


Fig. 3: TITAN test facility

The test objects with the length of 500 mm and the width of 350 mm were manufactured in quilted design, using SS plates. Two similar panels were used, both following the same geometry, consisting of seven flow channels (Fig. 4). Prior to

channels can be monitored. All sensors were shielded against thermal radiation using three layers of aluminium foil.

The first panel was used for the tests with IR radiation and forced warm He gas flow. The second panel, equipped with COAX electric heaters, was used for some reproducibility tests with GHe flow and all electric heating tests. The design was somewhat refined, incorporating experience gained from the first panel. For example, the panel was subjected to electrolytic copper coating (about 0.4 mm thickness) to ensure a homogeneous temperature profile. The central measuring position at the panel surface (denoted 144, see Fig. 4) was additionally equipped with a very fast responding silicon diode to be able to evaluate the influence of thermal response time of the sensors.

The test configuration for the individual methods was already described in last year's report.

Panels in quilted design shall be used as basic modules to achieve the total pumping area for ITER [8]. However, the detailed design study for the ITER vacuum system has meanwhile shown that a smaller number of channels per panel will be more feasible.

2.2.2 Test Results

2.2.2.1 Infrared Radiation (IR)

The required heating times could not be reached. This is possibly due to the fact that the absorption behaviour of solid deuterium is not sufficient at the wavelength of the IR transmitter. For a detailed evaluation more information on the absorption properties of frozen gas would be needed [9, 10]. Apart from that, the measurement results show a strong angle dependency of the thermal infrared radiation, causing a time lag of 10 min between the central position (144, see Fig. 4) and the edge position (147) to reach 90 K for an IR heater temperature of 400 °C. The thermal inertia of the IR heaters turned out to be too high. The fact that the energy could not be transported fast enough to the panel is typical for contactless heating methods.

2.2.2.2 Warm Gas Heating (GHe)

The warm gas was supplied via high-pressure bottles at ambient temperature. The heating tests were performed with a parametric variation of the GHe flow rate, covering laminar, turbulent and thermodynamically controlled (very high throughputs) flow regime. The flow rate was adjusted at elevated pressures up to 1.5 MPa. The TITAN panel yielded distinctive temperature differences across the panel surface during heating (e.g. a time lag of about 15 s between positions 146 and 147 to reach 90 K; conf. Fig. 4). This can be explained by a serious maldistribution problem of the total flow due to the large number of channels supplied by one unsymmetrically positioned feeder. This effect is emphasized by the rapid increase in volume caused by the evaporation of residual LHe in the panel. The delaying influence increases with increasing distance from the feeder position. However,

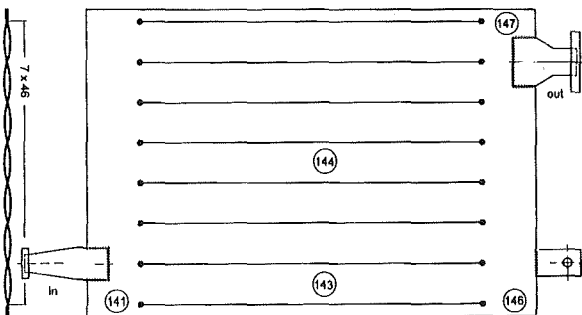


Fig. 4: TITAN test panel in quilted design. Reference positions for the location of temperature sensors are indicated

installation in TITAN, each panel was coated with activated carbon (mean particle diameter 1 mm mesh size) on both sides, according to the coating technique, which had been developed by FZK for use in ITER [7]. The panels were equipped with seven Fe-Rh temperature sensors at the surface. The temperature sensors are positioned in a way that both the panel edges, which are expected to have the greatest time lag, and the situation directly at the flow

this situation is not representative for ITER, as the panels used there will consist of less channels and the operation will be done with SCHe.

For this reason, we base our comparison of the TITAN results on that channel, which is the least affected by this situation, the one directly above the inlet, characterised by the two positions 141 (panel edge) and 143 (middle of channel). Fig. 5

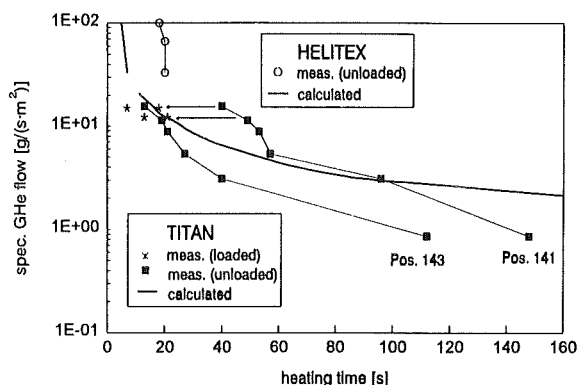


Fig. 5: GHe flow rates needed to reach 90 K vs. heating times

presents the results for heating times to reach 90 K as a function of the GHe flow related to the panel surface area. Also included are results for heating up the loaded TITAN panel (gas load scaled down to one typical ITER pumping cycle). The thermal gas release during the heating process causes a very steep pressure increase (from 0.1 Pa to some kPa in 2 s) and induces additional heat transfer from the LN₂ shielding to the panel which supports the heating and the temperature homogeneity. It becomes very obvious that the results taken at intermediate and high energy input fit very well. The experimental results are compared with calculated data based on a lumped system analysis model [6]. Fig. 5 also gives results, which have been measured at the HELITEX facility using a quilted panel with 3 flow channels (length of 1000 mm, width of 150 mm).

For turbulent flow conditions through the channels, heating times of less than 60 s were achieved. The GHe forced flow is a suitable method for establishing fast heating of cryopanel. However, as the heating process is not controlled primarily, difficulties are expected, if defined temperatures shall be reached and no overshooting can be tolerated. To minimise the temperature inhomogeneities, it is recommended to use panels with less flow channels.

2.2.2.3 Electric Heating

The second direct heating method investigated was surface bulk heating with electric heating elements. As for the GHe forced flow method, tests were carried out using both bare and loaded panels. The six COAX heaters were combined in three pairs, each of which was controlled within one heating loop using a thermocouple as controlling sensor. Prior to the test performance, an optimum controlling strategy was developed, which ensured the establishment of a rapid

temperature increase up to 90 K and almost instantaneous constancy at this temperature level without any overshooting.

Our measurements revealed that the temperature distribution across the panel surface is much more homogeneous than for GHe heating. Consequently, it is justified to characterise the panel temperature by the central position 144. In Fig. 6, the measured heating times are given

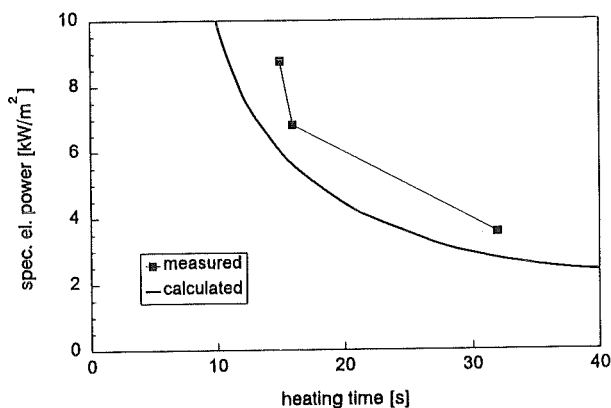


Fig. 6: Summarized results for electric heating

together with calculated results for different surface area related electric power inputs. Heating times of less than 30 s are reached without difficulty.

A major advantage of the electric heating technique is the excellent controllability. The temperature homogenizing effect of heating loaded panels is even more significant than for GHe heating. This is due to the fact that the heater is directly immersed into the charcoal (measured time lag of 4 s between positions 146 and 147 to reach 90 K, compared to 7 s for the unloaded panel).

2.2.2.4 Conclusions and Outlook

The experiments could demonstrate that fast heating and fast cooling within the regeneration process of ITER cryopumps is feasible. Two different methods were developed, which will ensure fast heating in less than 40 s at an acceptable expenditure of energy. Thus, it is possible to admit more than 60 s for the cooling process, which has higher energetic needs.

Electric heating appears to be most suited for ITER as it allows for precise temperature control and uniform temperature distribution. A final decision must also consider safety and economic aspects. The estimated heat input for a full size ITER cryopump (8 m² pumping surface) is the enthalpy related to about 70 g/s GHe mass flow or about 40 kW electric power.

As far as the temperature measurement strategy is concerned, we found out that fast responding silicon diodes are very well suited for the monitoring of dynamic fast processes. They have a thermal response time of some tens of ms, compared to some s for the Fe-Rh sensors. The thermal

contact situation is excellent due to their small size and the flat rectangular disk geometry (3x1.9x2.7 mm). Moreover, they are heatable up to 475 K, which is sufficient for usual vacuum bake-out processes. According to our experience, the choice of the most appropriate temperature measurement strategy is a very demanding question and needs a lot of practice. With the panel used for the electric heating tests we could compare a Si diode and Fe-Rh sensors and measured a time lag in the magnitude of up to 25 s.

The strong dependence of the experimental heating times on the pressure, i.e. the influence of molecular gas conductivity encouraged us to investigate the possibility of starting the heating process by gas puffing. In order to demonstrate that the proposed panel design is going to withstand the very large number of regeneration cycles, endurance testing of the cryopanel under temperature cycling is under way.

2.3 Pumping Characteristics of Cryosorption Panels

2.3.1 Objective

In early 96 the various operation modes foreseen for ITER have been fixed quantitatively [3]. New operation modes have been included, such as various shot conditions (hydrogen-, deuterium-, helium-shot). Consequently, the range of gas compositions to be pumped has been enlarged distinctively. Apart from that, the panel geometry has been fixed to quilted design [8]. Therefore, it was considered necessary to conduct pumping tests in order to obtain representative and reliable data for the new conditions and to support the current baseline design. The comparison with former pumping tests performed using the circular panel P12 (with the same sorbent material) [11, 12], which was positioned horizontally in the TITAN facility, will yield important information about the influence of panel geometry.

2.3.2 Test Programme and Results

As reliable literature information is scarce, a systematic test programme was developed, comprising pure gas species and mixtures. According to the new requirements, mixtures with high contents of noble gases (Ne, Ar, He) and/or nitrogen have to be investigated. The main constituent can be protium or deuterium. Quantitative pumping data are obtained by measurement of the pumping speed as a function of gas load and pumping pressure. The test series has already started and will extend until mid 97.

Until now, procured pure gases and two pre-defined gas mixtures have been investigated. The results obtained so far demonstrate that for the gases investigated the pumping characteristics will not be a limiting factor; the ITER requirement for a pumping speed of about 1 l/(s·cm²) at a specific gas load of 2 (mbar·l)/cm² and a pressure of 2.5·10⁻³ mbar is well achieved including a considerable safety margin. The saturation capacity will not be reached, except for the pure

helium-shot operation. But even in this case the ITER requirements are achieved.

The pure helium pumping results at approx. 6 K at the panel surface are shown in Fig. 7. The new measurements were

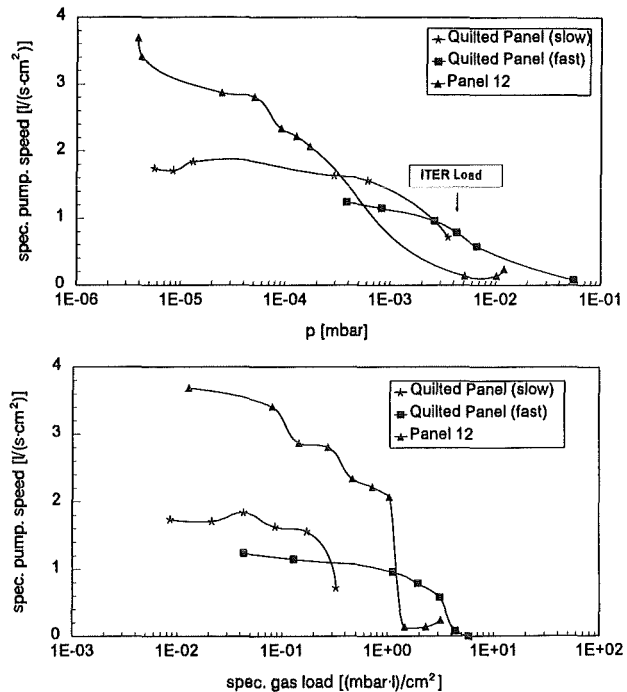


Fig. 7: Pumping characteristics for pure helium

performed at two different dosage programs. In the slow one, the dosage is varied from very low (1 SCCM) to maximum (1000 SCCM); in the fast one, the gas load is mainly built up by one fixed ITER relevant throughput (scale down to TITAN yields 530 SCCM). The agreement is satisfactory. The own results are compared with former results having been obtained with Panel P12. The agreement is within the expected range; the differences are due to the different geometrical situation, as discussed above.

The test programme is not only thought to provide the necessary information about pumping characteristics for special mixtures, but also to give a thorough understanding of the underlying adhesion mechanism for cryosorption processes. This is essential for further optimisation of the pumping process with respect to pumping time and operating temperature.

In preparation of the tests, we evaluated measurements of the equilibrium pressures for protium and deuterium at zero flow condition as a function of temperature and gas load.

The results for protium pumping with four circular panels, coated with different types of charcoal (thick and thin layers, [11]) are presented in Fig. 8. It becomes obvious that the equilibrium pressures are significantly smaller than the sublimation pressures, which indicates that adsorption is the ruling mechanism.

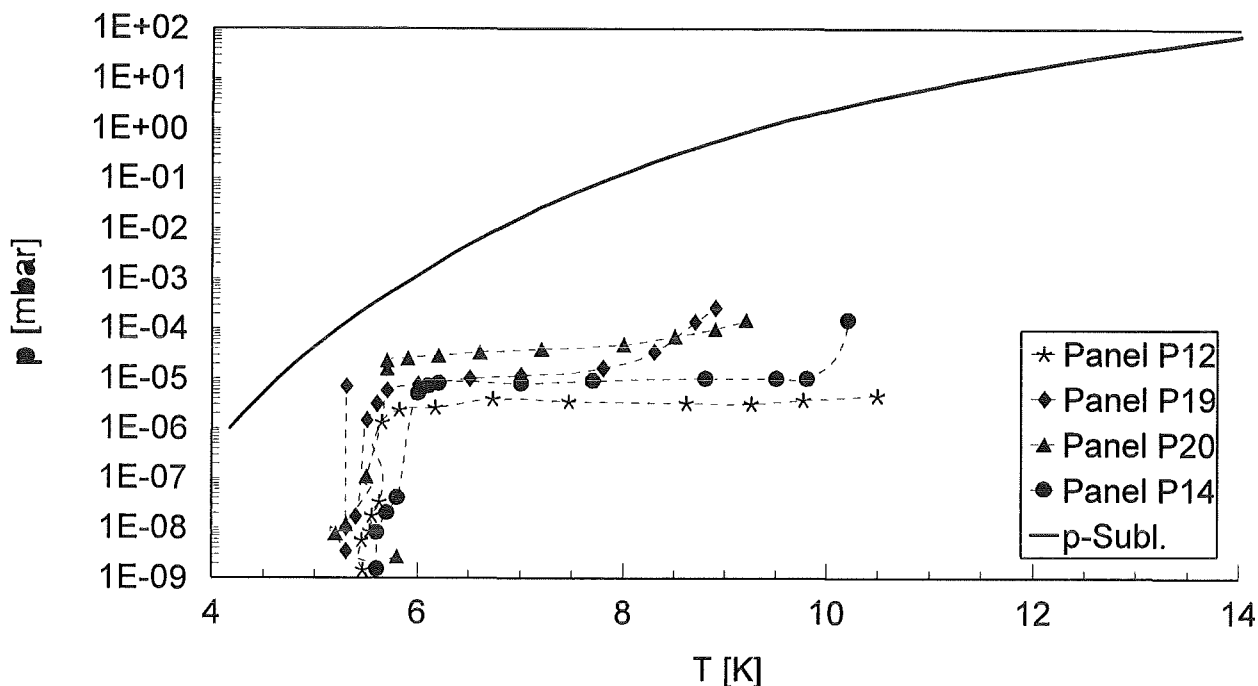


Fig. 8: Equilibrium points for protium pumping

The evaluation of the deuterium data revealed that deuterium is predominantly pumped by sublimation which causes higher equilibrium gas loads and a very fast thermal gas release within the regeneration phase of the cryopump.

Our results also show that the required pump ultimate pressure after partial regeneration of 10^{-8} mbar can be achieved for all gas species, including protium.

The valid adhesion mechanism determines the overall pumping behaviour. For adsorption, the dependence on temperature is quite weak over a broad temperature range (see Fig. 8) and the kinetics are slow (desorption times in the magnitude of tens of s), whereas a condensation mechanism is defined by the sublimation curve and very fast kinetics (less than 1 s). A steric influence has to be considered as well, because condensation happens at the surface, but adsorption is additionally influenced by the migration of the adhering particles into the charcoal pores. For the ITER gas mixtures, both mechanisms play a role at the same time. Thus, the growing of frozen gas layers on the surface may very much disturb the adsorption process and worsen the whole pumping performance. It is the objective of the present test campaign to gain more information about this kind of interaction.

In order to be able to investigate these phenomena in detail and very much to the point, a versatile gas mixing facility has been developed and constructed. This facility shall ensure the quick and reliable production of individual gas mixtures. The facility follows an easy principle. The wanted mixture composition can be adjusted gravimetrically and checked via monitoring of the partial pressures. First measurements during the set of operation of the facility yielded very promising results. All further investigations into pumping

characteristics will be based on mixtures produced in our own facility.

Literature:

- [1] Perinic, D. et al.: Proposal of a torus pumping and fuel recycling system for ITER. 18th SOFT, Karlsruhe, 1994
- [2] Mack, A., Perinic, D. : Conceptual study of the cryocascade for pumping, separation and recycling of ITER torus exhaust. Fusion Engineering and Design 28 (1995) 319 - 323
- [3] Ladd, P. : Torus Primary Pumping System. ITER-Specification No.: G31SP001W1.1, Draft 2, 23.4.96
- [4] Boissin, J.C.: ITER Model Cryopump Conceptual Design. FZK Contract 315/20 002 214/HIT 1.8.1995
- [5] Mack, A. : Fast heating tests for ITER cryopumps (Technical options and test facility). FZK Internal report HIT 14/1995
- [6] Day, Chr. et al. : Tests on fast heating for the regeneration process of ITER cryopumps. Report FZKA 5806, Karlsruhe, 1996
- [7] Perinic, D. et al. : Development of cryosorption panels for cryopumps. Adv. Cryogenic Engng. 39 (1994) 1553-1559
- [8] Mack, A. et al. : Primary vacuum pump concept, component testing and model pump development for ITER. 19th SOFT, Lisbon, Portugal, 1996

- [9] Souers, P.C. : Hydrogen properties for fusion energy. University of California Press, Berkeley, 1986
- [10] Tokaryk, D.W. et al. : Infrared emission spectra from cryogenic proton-irradiated helium gas. J. Chem. Phys.103 (1995)21, 10439-10444
- [11] Özdemir, I.; Perinic, D. : A comparison of thick and thin sorbent layers for plasma exhaust cryopumping. 18th SOFT, Karlsruhe, 1994
- [12] Illbruck, H.; Özdemir, I. : Cryopanel thick-layer tests at the TITAN test facility. FZK Internal report 310701P08A, 1993

Staff:

C. Day
A. Edinger
H. Haas
T. Höhn
W. Höhn
S. Horn
M. Jäger
B. Kammerer
U. Kirchhof
H. Knauß
J. Laier
A. Mack
N. Petersohn
R. Simon
D. Stern
U. Tamm
J. Weinhold
D. Zimmerlin

T 234 A Oil-Free Mechanical Pump Development

Mechanical Forepumps

The overall subtask goal is to select experimentally the best applicable oil-free pump types available and to specify the mechanical vacuum pump station for ITER. The most demanding objective of the mechanical pumps is the pump-out of the primary cryopumps during regeneration in about 60 s.

The FORTE facility has been constructed to test the possible candidates for the ITER vacuum system. Individual pumps (scroll and bellows oil-free forepumps) and trains of pumps connected in series have been investigated. It was shown experimentally that the compression ratio for light gases, especially protium, has improved substantially with the pumps operated in series in comparison to individual pumps [1, 2]. For this reason, a forepump train consisting of three positive displacement oil-free scroll pumps (type 1300 m³/h + type 600 m³/h + type 60 m³/h, supplied by NORMETEX, France) was chosen as the reference roughing unit for a scale-up to ITER. The pump characteristic is given in Fig. 1; for the calculation we used the results for the ITER relevant mixture M7.

Starting from the mass balance between the volume V, which has to be pumped down in a required time range t by a pump unit with given pumping speed S, the following equation can be derived for the needed number of pump units n:

$$n = -\frac{V}{t} \cdot \int_{p_1}^{p_2} \frac{dp}{p \cdot S(p)}$$

For integrating, the functional dependency of the pumping speed on the pressure has to be considered. The volume comprises the cryopump volume (2.7 m³) and the total volume of the duct and piping system between the divertor port and the place where the backing pumps are located. As this number is still unknown, we used 5 m³ as approximate estimation. The starting pressure results from the gas load, which accumulates during pumping operation of the cryopumps and also depends on the duct and piping volume. According to the numbers discussed above, we obtain about 16 mbar starting pressure. The cross-over end pressure p₂ is specified to be 10⁻¹ mbar.

Starting from these assumptions, we calculate a theoretical number of necessary forepump trains of n=3.6. For further optimisation, we are in the process of extensive re-evaluation of the measurement results to extract the general pump characteristics as a function of throughput and variable suction and back pressures. This will enable us to theoretically design pump trains with more than one pump of the same

type and thus to compose the optimum forepump train configuration.

As illustrated in Fig. 1, a minimum pumping speed is reached for pressures of less than 10⁻² mbar. To check the potentials of lowering this operating suction pressure to the UHV range, a turbo-hybrid pump with a magnet-suspended rotor has been added. The resulting pumping characteristic is shown in Fig. 2 for the ITER relevant exhaust gas mixture M7 and the pure gases N₂, H₂, D₂ and He.

Literature:

- [1] Kirchof, U. et al. : Tests of dry mechanical forepumps for use in the ITER vacuum pumping system. Report FZKA 5578, Karlsruhe, 1995
- [2] Perinic, D. et al. : Selection of mechanical pumps for ITER. Combined technical meeting tritium plant and fuelling&pumping systems. ITER Naka JWS, Dec 1995

Staff:

C. Day
 A. Edinger
 H. Haas
 T. Höhn
 W. Höhn
 S. Horn
 M. Jäger
 B. Kammerer
 U. Kirchof
 H. Knauß
 J. Laier
A. Mack
 N. Petersohn
 R. Simon
 D. Stern
 U. Tamm
 J. Weinhold
 D. Zimmerlin

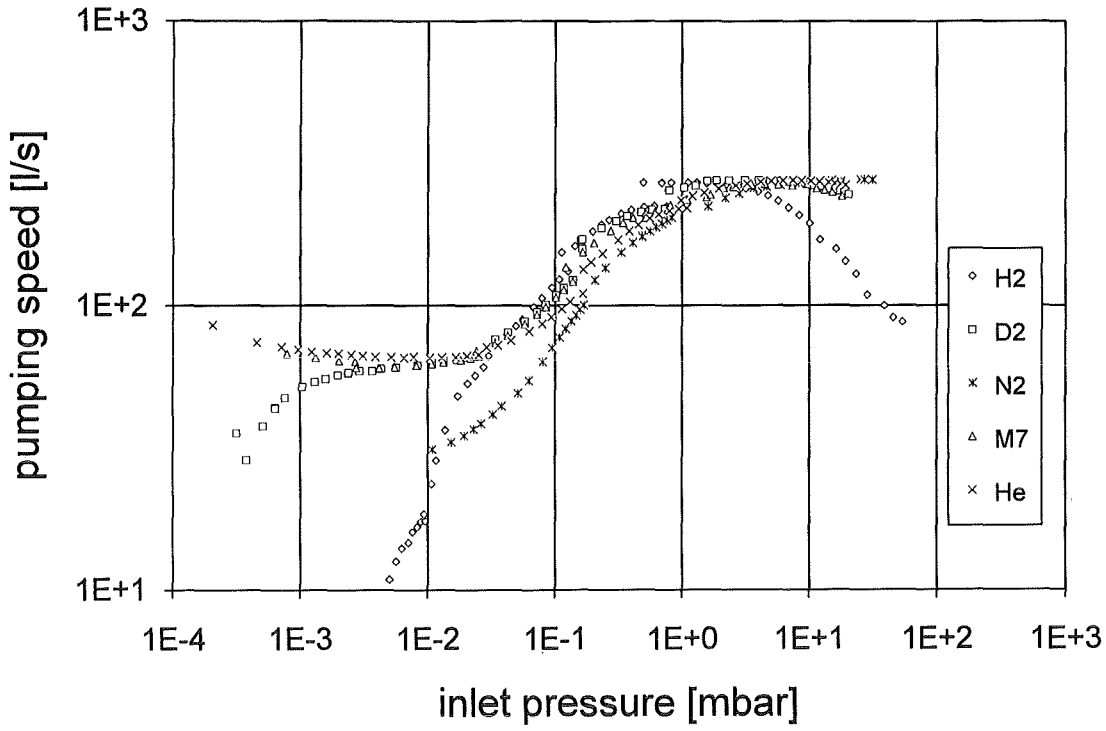


Fig. 1: Pumping speed of the combined NORMETEX 1300+ 600+60 pumps for various gases at 1200 mbar back pressure

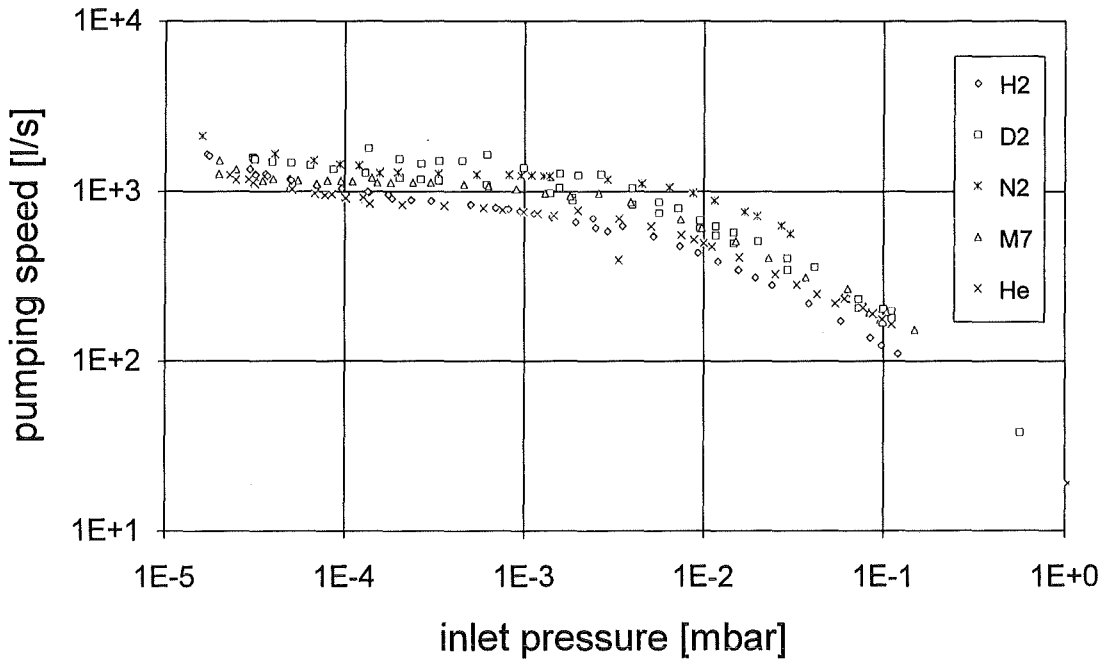


Fig. 2: Pumping speed of BALZERS TMU1600 + NORMETEX 60 + METAL BELLOWS-6 for various gases at 1200 mbar exhaust pressure

**N 32 TT 06 (T 299/T 332 b)
Plasma Exhaust Processing Technology**

**1. Performance Tests of Palladium/Silver Permeators
with Tritium at the Tritium Laboratory Karlsruhe**

Permeators are crucial components of the plasma exhaust clean-up system of a fusion reactor. A battery of permeators has been proposed at the front-end of the fuel clean up system to effectively recuperate unspent fuel from the exhaust gas. Permeators are also main components of impurity processing loops such as the CAPRICE facility, in operation at the Tritium Laboratory Karlsruhe (TLK). While much experience has been gained on the performance of permeators under a tritium environment, tests were mostly carried out with protium, deuterium and helium as the only other additional gas phase constituents. Endurance tests under conditions that closely simulate the singularities of the fuel clean-up process of a fusion reactor are thus still needed.

At the TLK permeation studies with protium, deuterium, and deuterium tritide were carried out in a closed loop (PETRA facility) housed in a glove box of approx. 6 m³. The PETRA permeator has a permeation area of 0.12 m² and is operated in/out (feed gas injection to the inside of the permeation tubes and pumping of the permeated hydrogen isotopes at the tubes outside) at a temperature of about 360 °C. The facility PETRA is equipped with a Normetex scroll pump type PV12/Siemens oil-free double containment metal bellows pump combination to pump the permeate and a Siemens metal bellows double containment pump to pump the bleed gas. Polytritiated deuterio methane was synthesized by passing DT containing 3 % CD₄ through a Ni catalyst bed heated to 300 °C. Radio gas chromatography was used for gas analysis. The parameters varied included the permeate pressure; the feed and bleed flow rate; and the feed gas composition, i.e. helium, Q₂, and CQ₄ (Q = H, D, T).

When hydrogen isotopes are fed into a permeator at progressively increasing flow rates while pumping the permeated gas, a sharp gas flow break-through at the bleed exhaust is observed after the maximum possible permeation has been attained. At feed flows above that, the bleed gas pressure is equal to or higher than that of the permeate gas and essentially no gas flow takes place. Once the saturation permeation is exceeded, a bleed gas flow sets in, that is always equal to the incremental feed gas flow rate.

To measure the achievable decontamination factors and to evaluate the magnitude of isotope effects bleed gas flow break-through curves as a function of the feed gas flow of protium, deuterium, and deuterium tritide were determined with the PETRA permeator. In these experiments the feed gas pressures of hydrogen and deuterium were held constant at 900 mbar and those of deuterium tritide at values of 820, 830 and 850 mbar (900 mbar were not achievable because of limited availability of DT). A plot of the pumping supported max. achievable permeate flow rate against the difference

between the square root of the feed pressure and the square root of the permeate pressure is depicted in Fig. 1

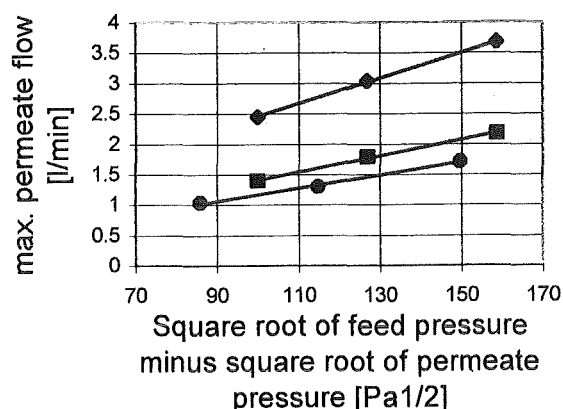


Fig. 1: Max. permeate flow rate of \blacklozenge = H₂, \blacksquare = D₂, and \bullet = DT as function of the difference of the square root of the feed pressure and of the permeate pressure

for the permeation of H₂, D₂, and DT at constant permeate pressures of 200, 300, and 400 mbar. The straight lines covering a broad range of feed and permeate pressures demonstrate that the \sqrt{p} -law is obeyed at least within the examined permeate pressure ranges.

The observed isotope effects were larger than estimated from a simple „square root of the atomic weight ratios“ approach. The break-through (BT) ratios of hydrogen with respect to deuterium and deuterium tritide were estimated to be BT(H₂)/BT(DT) = 2.08, 2.07, and 2.03, and BT(H₂)/BT(D₂) = 1.76, 1.71, and 1.66 at 400 mbar, 300 mbar, and 200 mbar, respectively. It is seen that the H₂/D₂ and H₂/DT break-through ratios are practically constant over the investigated feed/permeate pressures. Under the assumption that the employed gases are pure, the isotope effects, i.e. H₂/D₂ = (1.72 ± 0.03) and H₂/DT = (2.06 ± 0.03), are dominated by the different specific permeation rates of the various hydrogen isotopes and, to a much lesser extent, by the prevailing gas dynamics.

To investigate the effect of methane and polytritiated methane (CD_xT_y) on the palladium/silver permeator, the permeator was first conditioned by repeated treatment with laboratory air at the operation temperature and then a deuterium tritide permeation break-through curve was determined at a constant permeate pressure of 200 mbar. The deuterium tritide used contained either 3 % helium or 3 % helium and 3 % polytritiated methane (27 mbar) as impurities. The deuterium tritide/impurity mixture was then circulated through the permeator kept at 360 °C and new break-through curves were periodically determined for periods of time totaling 144 hours. It was found that under these experimental conditions a low tritiated methane partial pressure in DT carrier gas has practically no influence on the break-through curves. From the results it is concluded that polytritiated methane and for that matter methane do not

cause poisoning of Pd/Ag membranes when diluted in a hydrogen isotope carrier gas.

After completion of the CD_xT_y/DT runs, the permeator was again fully reactivated and a series of break-through curves with deuterium at constant permeate pressures of 200, 300 and 400 mbar were determined. The deuterium was then pumped off and the palladium/silver exposed to deuterated methane diluted in helium. Following a certain period of recirculation deuterium was again added and a new set of break-through curves determined. This time a slow, progressive poisoning of the permeator observable at the three investigated permeate pressures became apparent. The break-through feed flow rate (l/min) was found to decrease with a rate of 0.05 % per hour of exposure to pure deuterated methane.

Runs in which the permeator held at 360 °C was exposed to a gas mixture consisting of 0.8 mbar deuterium tritide, 5.2 mbar polytritiated deuterio methanes, and 0.5 mbar polytritiated deuterio ethanes (all species containing approx. 50 % tritium and 50 % deuterium) diluted in 253 mbar helium a rapid and very marked decrease in permeability for deuterium tritide was noticed. The feed flow at which break-through took place was reduced to 7 % of its original value in 144 hours and the isotope effect almost completely vanished (see Fig. 2). Typical for the occurrence of surface reactions the square root

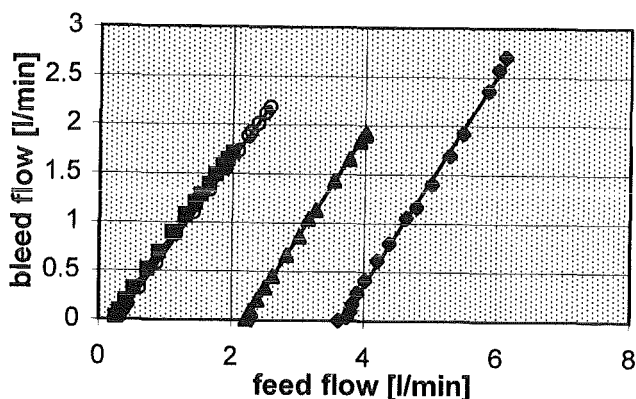


Fig. 2: Break-through curves of H_2 and D_2 through a conditioned and through a poisoned permeator after exposure to CD_xT_y at 360 °C. The symbols denote: \blacklozenge = H_2 , 200 mbar permeate pressure, 0 hours exposure, \blacktriangle = D_2 , 200 mbar permeate pressure, 0 hours exposure, \circ = H_2 , 200 mbar permeate pressure, 144 hours exposure, and \blacksquare = D_2 , 200 mbar permeate pressure, 144 hours exposure

pressure dependency was no longer found to hold after this exposure time.

Further tests to examine whether radiation-induced reactions influence the rate of palladium/silver poisoning were performed with polytritiated methane in an analogous way to that described above. As in previous runs, the series was started with several DT break-through curves through the reactivated palladium/silver permeator of the PETRA

experiment at constant permeate pressures of 200, 300, and 400 mbar. The test gas was a nearly equimolar D/T mixture. After each breakthrough curve determination the deuterium tritide was again gettered on the ZrCo bed and the permeator once more exposed to polytritiated methane alone. Subsequently deuterium tritide was again released from the bed into the primary system and a new set of break-through curves determined. This procedure, i.e. exposure of the permeator to tritiated methanes and evaluation of the poisoning via break-through curves was carried out until an integral exposure time of 288 hours was reached. The data show that, after an initial induction period, poisoning progressively sets in until the permeator becomes practically impermeable to hydrogen isotopes. The rate of poisoning by polytritiated methane was found to be much faster than that by deuteromethane. Poisoning by hydrocarbons can be reversed by a chemical treatment. To completely reestablish the original permeation properties of the permeator it is necessary to expose the permeator repeatedly to laboratory air at 350 °C.

The permeator of the PETRA experiment has now been discontinuously in operation with mainly deuterium tritide and to a lesser extent with protium and deuterium for now more than one and a half years without contingencies or loss of integrity. During most of this period the temperature of the permeator was held at approx. 360 °C. From the results obtained to date, it can be concluded that permeators are components suitable for use in the ITER Tritium Plant.

Staff:

- U. Berndt
- S. Grünhagen
- K. Günther
- R.-D. Penzhorn
- E. Kirste
- J. Wendel

2. Catalytic Cracking Process

The technical facility CAPRICE (Catalytic Purification Experiment) was industrially designed and fabricated to demonstrate and to optimize the catalytic clean-up process concept, developed at the Research Center Karlsruhe for the processing of torus exhaust gases specified for ITER. During the initial tritium campaign of Caprice the facility was regularly operated for more than one year with up to 90 % of tritium in deuterium and a relevant spectrum of plasma exhaust impurities. The main objectives were to measure the achievable integral and partial decontamination factors and to determine the tritium inventories in the various process components.

The first step of CAPRICE is based on continuous impurity separation by a main palladium / silver permeator at a target

throughput of about 10 mole/h of DT and about 1 mole/h of tritiated and non-tritiated impurities. In a second, batch type step the impurities and remaining molecular hydrogen isotopes are processed by catalytic hydrocarbon cracking reactions and the water gas shift reaction in combination with another palladium / silver permeator.

The tritium inventories in the two different catalyst beds of the impurity processing loop of CAPRICE were determined by a technique based on mass balance and radio gas chromatography. In each test the catalysts were exposed to a well defined amount of gas with known tritium concentration. The gas phase and the catalyst immediately became equilibrated and the tritium hold-up of the catalyst beds were calculated after the overall tritium content in the gas phase was again measured. The quantities of tritium reversibly adsorbed in the catalysts were found to be dependent mainly on the operation temperature, the concentration ratio of tritium to total hydrogen isotopes and the moisture content of the gas. Under design operating conditions and 50 % of tritium in deuterium the inventory was measured to be 0.12 g per kg of nickel catalyst and 1.6 g per kg of water gas shift catalyst. The overall tritium inventory of an ITER sized catalytic torus exhaust clean-up system would then be less than 15 g.

Tests of the main palladium / silver permeator used to separate the impurities from molecular hydrogen isotopes have shown, that the target throughput was achieved even at the highest tritium concentration and in the presence of moisture. However, after almost one year of short-term, but frequent operation with gases like tritiated methane, tritiated water and carbon oxides mixed with tritium, the apparent permeability progressively decreased. In Fig. 3 the feed and bleed flow rates of a mixture of deuterium with moist helium are compared with the flow rates for deuterium / tritium, also mixed with moist helium, nearly 2 years later.

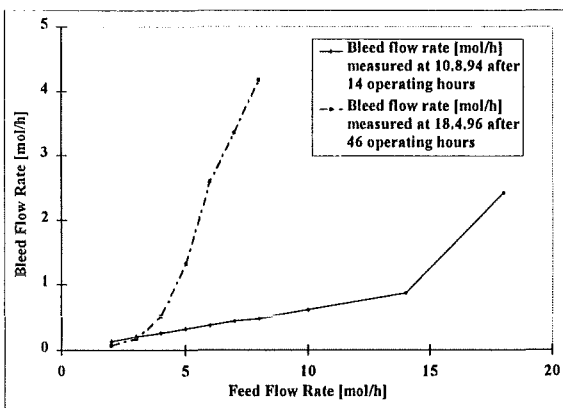


Fig. 3: Reduction in apparent permeability due to long-term operation with tritiated impurities

The substantial reduction of the throughput was attributed to regular exposure of the palladium / silver membrane to mixtures of tritium with carbon oxides at elevated partial pressures. Regeneration of the permeator by heat treatment

under air atmosphere completely restored the original permeability.

Since permeators are common to any fuel processing concept considered for ITER, regular regeneration of permeators will have to be foreseen within the ITER tritium plant.

The performance of the impurity processing loop of Caprice was quantified. Concentration profiles for total tritium, tritiated methane, tritiated water and carbon oxides were measured with the nickel cracking catalyst, the water gas shift catalyst and the impurity processing loop permeator on and off line. Typical results are depicted in Fig. 4.

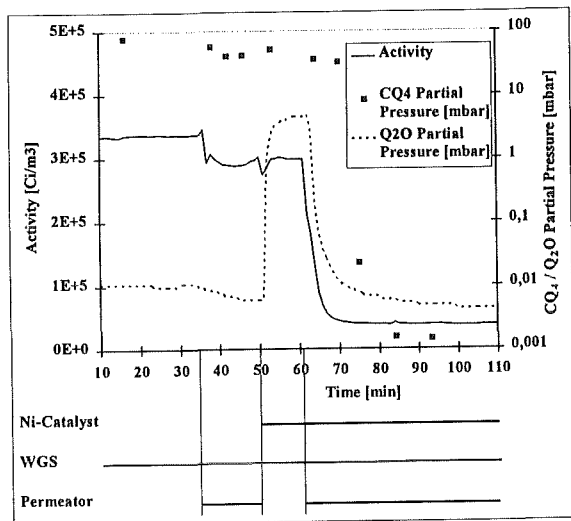


Fig. 4: Concentration profiles and tritium activity with different components of the impurity processing loop on and off line

With the water gas shift catalyst and the permeator on line water is converted with carbon monoxide to carbon dioxide and hydrogen / tritium, the latter being removed by the permeator. Therefore the total tritium concentration in the loop, followed with an in line ion chamber, drops accordingly, but remains high due to the presence of tritiated methane. An immediate decrease of the overall tritium concentration is observed as soon as both the catalysts and the permeator are on line. Because of substantial memory effects of the in line ion chamber, the final true tritium concentration in the gas phase can only be measured with a 'clean' ion chamber.

The feed gas composition of the impurity processing loop of Caprice never needed to be adjusted. Due to simple side reactions within the heterogeneously catalyzed system the gas phase was all the time detritiated.

In a number of runs the overall tritium decontamination factors (DF's) of the impurity processing loop as well as the partial DF's for tritiated water and tritiated methane were determined at different tritium levels employing gases with a variety of compositions. Tritium concentrations were measured at the beginning and after 20 min of gas processing and the concentration ratios calculated. Some decontamination factors measured with different methods

employing DT (50 % T) mixed with water, tritiated methane and carbon oxides are summarized in Table 1. While for example for methane DF's of higher than 40.000 were determined, the overall DF was found to be about 5.300 or 6.000, depending on the method employed.

Table 1: Overall and partial DF's as measured with the Caprice impurity processing loop

	Clean Ion Chamber	Radio Gas Chromatography	Moisture Meter
Overall DF	5.300	6.000	not applicable
DF for Water	not applicable	not applicable	> 1.000
DF for Methane	not applicable	> 40.000	not applicable

The results of the initial tritium campaigns and data from tritium experiments with a permeator / catalyst combination (PERMCAT) for isotopic swamping are used to develop CAPER, an advanced torus exhaust clean-up process. CAPER will be a completely continuous, three step process comprising a front end permeator battery, a once through impurity processing loop and a Permcatal for final clean-up. The overall decontamination factor of the process, given by the product of the DF's of the three consecutive steps, is determined to be at least $2 \cdot 10^7$, thus meeting ITER specifications for clean-up of plasma exhaust gases.

Staff:

- M. Glugla
- K. Günther
- T.L. Le
- W. Leifeld
- R.-D. Penzhorn
- K.H. Simon
- D. Taylor (guest scientist)

Not only the CAPRICE process, but also the overall technical system was shown to perform satisfactorily. The safety concept and the interlocks worked as designed and the pressures and temperatures were all the time kept within the operation margins.

CAPRICE was mostly on hot standby during the night and on weekends. The frequent supply and return of tritium from and to the infrastructure of the laboratory was via double walled tubing. The maximum overall tritium inventory was 7g.

Non of the major components failed during the current test program. The only problem encountered was the necessity to replace the carbon brushes of the motor of a Metal Bellows 601 pump; it required removal of a glove box window for repair.

The steady state concentration of tritium in the CAPRICE glove boxes were normally below $1 \text{ Bq} / \text{m}^3$. This could be achieved by using vacuum jackets for all heated components like catalytic reactors or permeators. Depending upon the temperature of the heated unit and the partial pressure of tritiated hydrogen fairly high permeation rates into the interspace were occasionally observed. This demanded regular evacuation of the jackets into the impurity processing loop to maintain thermal insulation and to avoid excessively high temperatures of the outer mantle of the component.

The tritium from other sources, e.g. sampling for radio gas chromatography, was not transferred to the waste treatment system of the Tritium Laboratory, but fed into a CAPRICE buffer vessel and recovered with the impurity processing loop. Thereby the amount of tritium discharged to waste could be kept to an absolute minimum.

TEP 3 Tritium Storage

A tritium storage bed with the capability for a fast release of hydrogen isotopes is needed particularly in the fuel supply section of a fusion reactor. Another potential application of a fast releasing bed is seen in the area of hydrogen isotope dosage. Basically, with a fast releasing bed the use of tritium in gaseous form can be minimized or even avoided. In principle, shortening of the release time of tritium from a storage bed can be associated with less tritium permeation losses through the outer containment wall and smaller inventories of free molecular tritium handled in a tritium facility.

Conventional uranium tritide storage beds require more than an hour of heating to attain the temperature, at which a tritium dissociation pressure of approx. 1 bar is established, i.e. 450 °C. Hydrogen can be extracted faster and at lower temperatures from a uranium hydride bed when the released gas is pumped while the bed is heated. Fig. 1 shows release data obtained with a uranium storage bed containing 200 g of uranium. It is seen that in about one hour all the hydrogen immobilized in the bed can be pumped off with a 15 m³/h Normetex scroll pump/two stage Siemens pump combination (achievable vacuum less than 1 mbar), when the temperature of the bed is held at a constant temperature of 300 °C. At lower temperatures considerably longer times are required.

Experimentally it was shown that the period of time required to extract hydrogen from a uranium storage bed can be reduced considerably if the bed is first preheated up to a temperature of about 300 °C, at which the uranium tritide dissociation pressure is still low, e.g. < 1 mbar, and

subsequently heated rapidly up to 450 °C. Under these conditions the time required to pump-off the gas with the pump combination mentioned above is of only half an hour.

If ZrCo is used instead of uranium as the getter material, the preheating temperature of the bed should not exceed 150 °C if the dissociation pressure is to remain below 1 mbar. The time required to heat the bed preheated to 150 °C up to the temperature at which a dissociation pressure of 1 bar is attained, i.e. 350 °C, was found to be of the same order of magnitude as for uranium. From these results it is apparent, that from the point of view of heating rate, there is no advantage in replacing uranium by zirconium/cobalt. The minimum heating time to reach a dissociation pressure of 1 bar, i.e. ½ hour, with either preheated uranium or zirconium/cobalt, is taken as reference case for improvements of the release rates.

With the purpose of accelerating the release rate of gettered hydrogen isotopes from a tritium getter material a different heating concept was explored. Instead of conventional heating with an electrical resistance radio frequency heating of the getter material placed inside of a ceramic vessel was chosen. The ceramic vessel used is provided with an ultra high vacuum-tight metal flange. The ceramic vessel is connected to a four liter SS vessel provided with a pressure sensor. For evacuation purposes a turbo molecular pump is available. With radio frequency heating the outer wall of the ceramic vessel remains at comparatively low temperatures because it is only heated by the radiation heat emitted by the metal core. Since the permeation rate of tritium through ceramics is

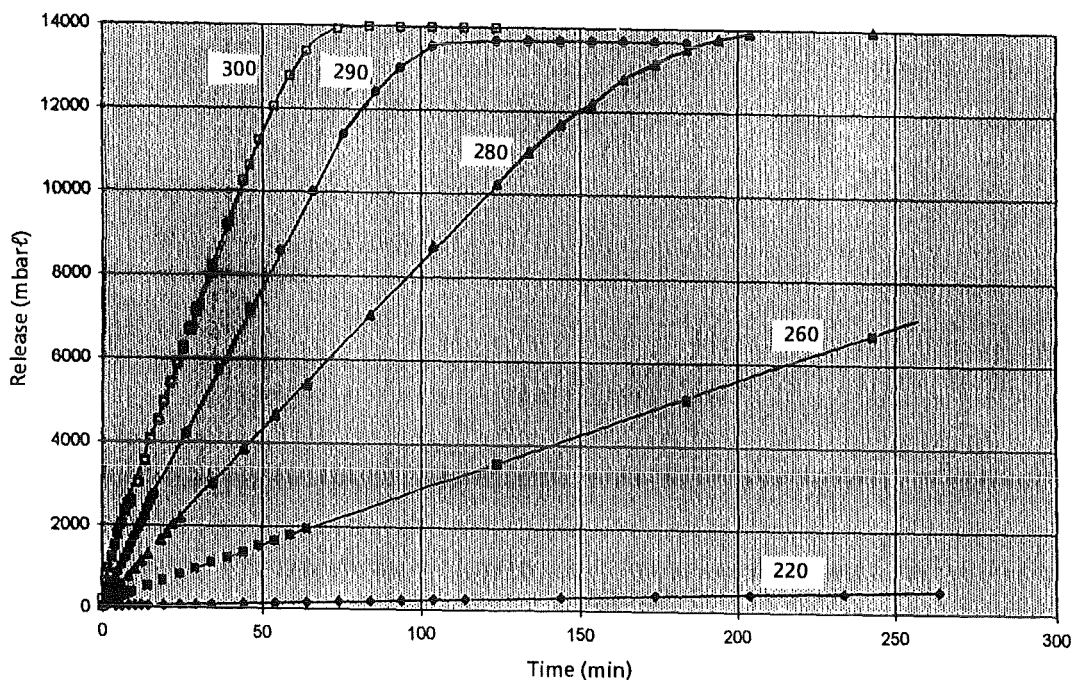


Fig. 1: Release rate of hydrogen from a uranium bed installed in the Storage System of the Tritium Laboratory Karlsruhe. The bed was preheated to constant temperatures in the range 220 - 300 °C (indicated in the Figure) and pumped with a Normetex scroll pump/two stage Siemens metal bellows pump combination

very slow even at elevated temperatures, tritium losses from this device into a glove box are expected to be very minor.

First screening runs were performed with titanium powder as hydrogen getter. Since attempts to couple the titanium powder to the radio frequency source were unsuccessful, the getter material was placed inside of a thin platinum vessel. Under these conditions temperatures of more than 1000 °C could easily be attained in a very short time. Titanium was abandoned, however, after these preliminary experiments, because of the very high temperature, i.e. > 700 °C, that was necessary to release the bulk of the gettered gas. Furthermore, while platinum could be heated very quickly to high temperatures, heat transport from the platinum to the metallic powder was not fast enough. In addition, damage to the ceramic containment by the large generated temperature gradients was feared.

Staff:

U. Besserer
W. Jung
R.-D. Penzhorn
M. Sirch
T. Vollmer

The next getter material tested was ZrCo. In these runs a previously activated sample of the intermetallic compound powder was placed in the platinum containment inside of the ceramic vessel. 0.0133 mol of hydrogen were then introduced into the 4 l vessel and this gas expanded into the ceramic vessel. As expected hydrogen was quantitatively gettered by ZrCo down to a pressure of < 0.1 mbar in a few minutes. When the radio frequency power necessary to reach 550 °C was instantly applied (without preheating), 91 % of the gettered gas was released in approx. 6-7 minutes. The necessary power value was obtained from previous calibration tests. Gettering/release cycles of this kind could be repeated several times with good reproducibility. Heat transport was influenced by the prevailing gas pressure. In view that the release was achieved without pumping of the gas, it is possible to conclude that heating by radio frequency may constitute a significant progress. In future experiments the transport of heat within the platinum vessel shall be improved to further accelerate the hydrogen release rate.

A first conceptual design of a storage bed based on the release of hydrogen isotopes by a radio frequency heating technique has been developed together with industry. In a next step it is planned to build a smaller version of this bed to further optimize the technique.

In preparation of experiments with tritium, the quadrupole mass spectrometer of the ALTEX facility has been calibrated with isotopes of neon and with He-3/He-4 mixtures. About 15 ppm of He-3 (the decay product of tritium) in He-4 could still be detected with the mass spectrometer. Presently the dissociation pressure of ZrCo hydride at room temperature and temperatures slightly above that is being measured with a Vicovac gauge. This gauge has a magnetically suspended rotating ball, whose deceleration in a viscous medium is used to determine the pressure of a gas.

G 16 TT 82 (T 218) Shielding Neutronics Experiments

The experimental validation of the nuclear performance of the ITER shielding system is one of the tasks in the Engineering Design Activities. A mock-up at the Frascati Neutron Generator simulates the inboard shield, including first wall, blanket, vacuum vessel and toroidal field coils. Nuclear responses of the assembly are determined in a joint effort of European and Russian groups [1].

The assembly is shown in Fig. 1. It consists of a combination of

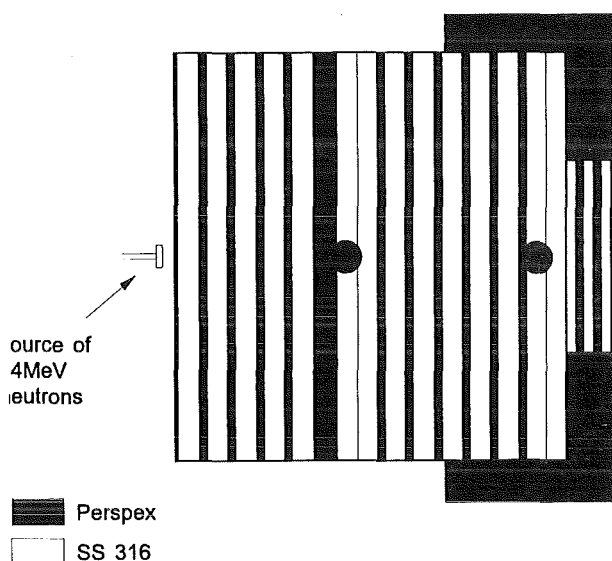


Fig. 1: Experimental arrangement of the bulk shield assembly

slabs made from the water equivalent material PERSPEX (2 cm thickness each) and SS316 (about 5 cm thickness each) and has a front area of 100 x 100 cm². The total thickness of the assembly is 94.26 cm including a 1 cm thick Cu layer in front. Behind this assembly a block of Cu and SS316 plates is arranged simulating the coils for the toroidal magnetic field. The rear part of the assembly is surrounded with a polythene shield covering also the last 30 cm of the PERSPEX/SS316 block in order to reduce room-return background.

The investigation started with measurements of spectral neutron and photon fluxes by the group of TU Dresden because the fluxes are the basic weighing functions for the other integral quantities to be determined (such as reaction rates, activation, heating). Measurements were carried out at two positions in the centre of the mock-up corresponding to the backsides of the shielding blanket and of the vacuum vessel, respectively.

Gas-filled proton recoil proportional counters and a stilbene scintillation spectrometer were applied for the neutron spectra measurements between about 30 keV and 3 MeV. A NE213 scintillation spectrometer was used for simultaneous measurement of the neutron flux spectrum between about 1 MeV and 15 MeV and of the photon flux spectrum for $E > 0.2$

MeV [2]. The results are presented on an absolute scale as fluences per one source neutron.

The experimental results were analysed by means of Monte Carlo transport calculations with the MCNP-4A code [3] and nuclear data from advanced versions of the European Fusion File EFF-2 [4], the Japanese Fusion File JENDL-FF [5] and the ITER reference nuclear data library FENDL-1 [6]. The MCNP calculations were performed taking into account the precise geometry of the mock-up and its mechanical support, the neutron generator with target and drift tube as well as the experimental hall with concrete walls [7].

The comparison of measured and calculated neutron fluence spectra for the two positions A and B is shown in Fig. 2. The experimental spectra are corrected for material and size of the different detectors by MCNP/FENDL calculations and represent the spectral fluences in an SS316 sphere with a radius of 2 cm in correspondence with the calculations. All results are normalised to one source neutron. Integrated values of the neutron fluence are given in Table 1. The calculation-to-experiment ratios C/E show that the experiments are well described by the calculations in position A where the discrepancies are within a 10 % limit for all data libraries. The best agreement is obtained with EFF-2 data. Also in position B EFF-2 data describe the experiment within a 15 % range with the exception of the lowest energy interval where the discrepancy increases to 25 %. For the energy range 5 ... 10 MeV the spectra are overestimated in all calculations, in the other ranges they are underestimated. Measured and calculated photon fluences are presented in Fig. 3, their integral values for $E > 0.4$ MeV are shown in Tab. 2. The calculated integral fluences using EFF-2 and FENDL-1 data agree well with the experiment in pos. A whereas they underestimate the experiments by 5 ... 10 % in pos. B.

Literature:

- [1] P. Batistoni, M. Angelone, W. Daenner, U. Fischer, L. Petrizzini, M. Pillon, A. Santamarina, K. Seidel, Neutronics shield experiment for ITER at the Frascati Neutron Generator FNG, Proceedings of the 19th Symposium on Fusion Technology, Lisbon, 1996, in print.
- [2] H. Freiesleben, W. Hansen, D. Richter, K. Seidel, S. Unholzer, Report on detailed design of neutron and gamma spectra measurements, Report TUD-IKTP/95-02, Dresden, April 1995.
- [3] J.F. Briesmeister (ed.), MCNP - A general Monte Carlo n-particle transport code, Version 4A, Report LA-12625-M, Los Alamos, 1993.
- [4] J. Kopecky, H. Gruppelaar, Status of the European Fusion File (Revision EFF-2.3), EFF-DOC-203, 1993.
- [5] S. Chiba, B. Yu, T. Fukahori, Report JAERI-M94-027, 1992.

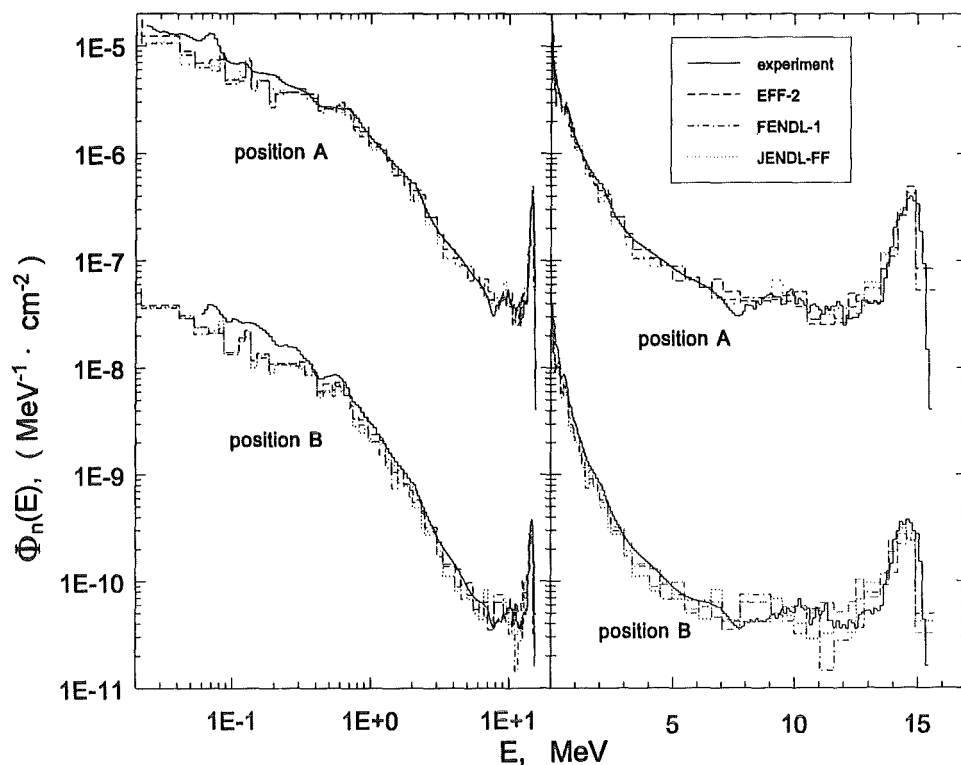


Fig. 2: Measured and calculated neutron fluences per one source neutron at position A and position B (left hand side: logarithmic energy scale, right hand side: linear energy scale)

[6] S. Ganesan and P. K. Mc Laughlin, FENDL/E - Evaluated nuclear data library of neutron interaction cross-sections, photon production cross-sections and photon-atom interaction cross-sections for fusion applications, Version 1.0, Report IAEA-NDS-128, Vienna, 1994.

[7] U. Fischer, P. Batistoni, M. Pillon: Three-dimensional Neutronics Analyses of the ITER Bulk Shield Experiment, Proceedings of the 19th Symposium on Fusion Technology, Lisbon, 1996, in print.

Staff:

H. Freiesleben
 W. Hansen
 K. Merla
 D. Richter
K. Seidel
 S. Unholzer
U. Fischer
 Y. Wu

Table 1: Integrated neutron fluence per cm² and per source neutron for different neutron energy ranges and calculation-to-experiment ratios

	E / MeV	0.1 ... 1	1 ... 5	5 ... 10	> 10
Pos. A	Experiment	(2.76±0.28)E-06	(1.43±0.08)E-06	(2.47±0.13)E-07	(5.42±0.14)E-07
	Calc(EFF-2)	(2.54±0.04)E-06	(1.38±0.03)E-06	(2.66±0.12)E-07	(5.05±0.23)E-07
	Calc(FENDL-1)	(2.39±0.03)E-06	(1.28±0.02)E-06	(2.56±0.09)E-07	(4.88±0.18)E-07
	Calc(JENDL-FF)	(2.51±0.03)E-06	(1.29±0.02)E-06	(2.62±0.12)E-07	(5.05±0.22)E-07

	C(EFF-2)/E	0.92±0.09	0.97±0.05	1.08±0.07	0.93±0.05
	C(FENDL-1)/E	0.86±0.09	0.90±0.05	1.04±0.07	0.90±0.04
	C(JENDL-FF)/E	0.91±0.09	0.91±0.05	1.06±0.07	0.93±0.05
Pos. B	Experiment	(8.78±0.89)E-09	(2.37±0.13)E-09	(2.69±0.14)E-10	(5.79±0.15)E-10
	Calc(EFF-2)	(6.59±0.11)E-09	(2.03±0.06)E-09	(2.83±0.22)E-10	(4.90±0.35)E-10
	Calc(FENDL-1)	(6.00±0.08)E-09	(1.81±0.04)E-09	(2.93±0.15)E-10	(4.56±0.25)E-10
	Calc(JENDL-FF)	(6.09±0.09)E-09	(1.86±0.05)E-09	(2.69±0.15)E-10	(4.94±0.33)E-10

	C(EFF-2)/E	0.75±0.08	0.86±0.05	1.05±0.10	0.85±0.06
	C(FENDL-1)/E	0.68±0.07	0.76±0.04	1.09±0.08	0.79±0.05
	C(JENDL-FF)/E	0.69±0.07	0.78±0.05	1.00±0.08	0.85±0.06

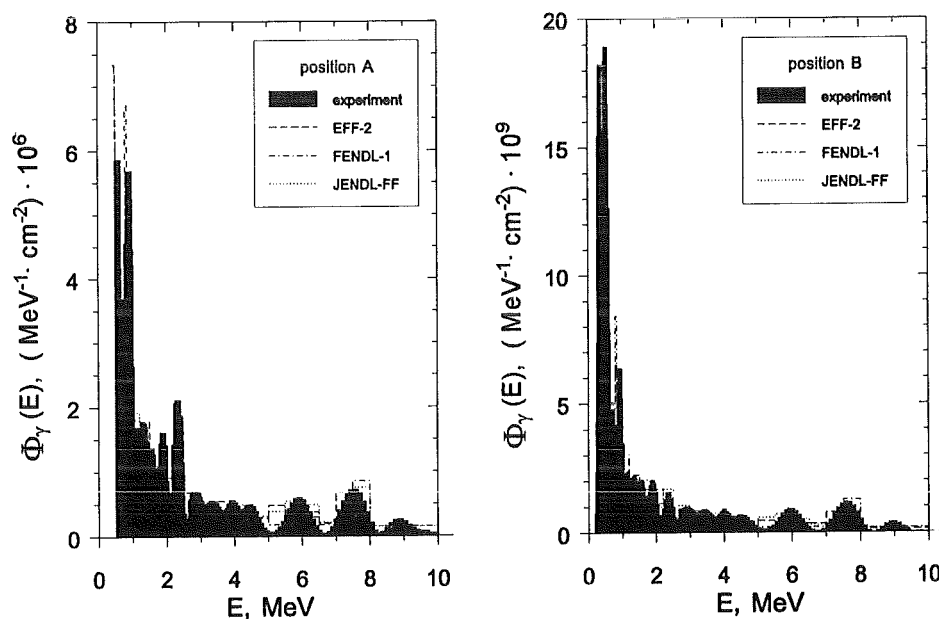


Fig. 3: Measurement and calculated photon fluences per one source neutron at position A (left hand side) and position B (right hand side)

Table 2: Integrated photon fluence for $E > 0.4$ MeV per cm^2 and per source neutron and calculation-to-experiment ratios

		E > 0.4 MeV
Pos. A	Experiment	$(7.47 \pm 0.19)E-06$
	Calc(EFF-2)	$(7.83 \pm 0.17)E-06$
	Calc(FENDL-1)	$(7.63 \pm 0.15)E-06$
	Calc(JENDL-FF)	$(8.31 \pm 0.20)E-06$
	C(EFF-2)/E	1.05 ± 0.04
	C(FENDL-1)/E	1.02 ± 0.03
	C(JENDL-FF)/E	1.11 ± 0.04
Pos. B	Experiment	$(1.07 \pm 0.03)E-08$
	Calc(EFF-2)	$(1.02 \pm 0.04)E-08$
	Calc(FENDL-1)	$(9.55 \pm 0.28)E-09$
	Calc(JENDL-FF)	$(1.07 \pm 0.04)E-08$
	C(EFF-2)/E	0.95 ± 0.05
	C(FENDL-1)/E	0.89 ± 0.04
	C(JENDL-FF)/E	1.00 ± 0.05

G 16 TD 21 (D 203) ITER Breeding Blanket Development and Design

Introduction

At the end of the BPP of ITER it is intended to exchange the shield blanket modules against a breeding blanket with the objective to generate in the plant a significant fraction of the tritium needed during the EPP. The breeding blanket consists of modules of the same size and shape as the shielding modules. The dimensions of the modules are about 1800 mm (poloidal), 800 mm (toroidal), and 300 mm (radial). According to the present design the breeding blanket will use Li_2ZrO_3 pebbles as breeder material arranged in poloidal/toroidal layers of 10 mm thickness. The breeder pebble beds are canned by a thin SS sheath and enclosed by Be blocks and cooling plates.

Heat Transfer Correlations

One of the FZK contributions to the ITER breeding blanket development was the provision of correlations for the thermal analysis, in particular the Li_2ZrO_3 pebble bed with pebble diameters of 1.2 and 0.165 mm, respectively (binary bed). The effective thermal conductivity of the binary bed was determined according to the extended Schlünder formula, which includes as primary parameters the equivalent particle diameter, the thermal conductivity of the ceramic material and of the helium in the pores of the bed, and the void fraction. In the temperature range from 300 to 900 °C the thermal conductivities of the binary pebble bed calculated according to this model are between 1 and 1.35 W/mK (see Fig. 1).

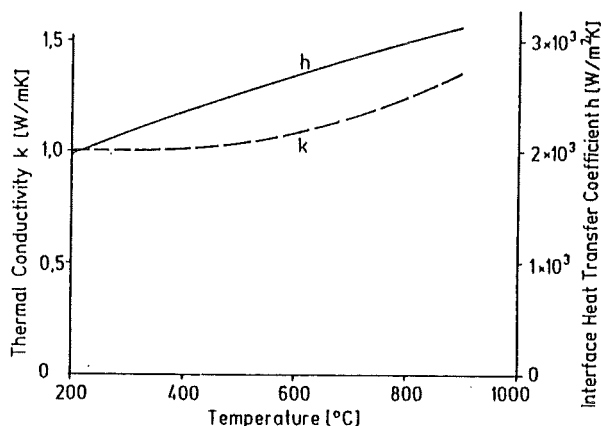


Fig. 1: Thermal conductivity and interface heat transfer coefficients of a binary Li_2ZrO_3 pebble bed (1.2/0.165 mm pebble diameter)

The bed to wall heat transfer coefficients were determined by combining the Schlünder correlation with experimental results available for a homogeneous Li_2ZrO_3 pebble bed. At first, the Schlünder model was applied to the homogeneous bed. The pebble surface roughness was used to adjust the calculated results to the measurements. Then, the same

assumptions were applied to the binary bed using an estimated surface covering degree of 90 %. The resulting heat transfer coefficients (surface roughness 25 μ) are in the range of 2200 to 3100 W/m² K, and are likewise represented in Fig. 1.

The calculated values of the thermal conductivity as well as of the heat transfer coefficients are significantly above those for the homogeneous bed with a pebble diameter of 1.2 mm.

Thermal Calculations

To verify the correlations suggested in the previous section and to investigate the sensitivity of the temperature distribution to the gap size between the Be blocks and the SS surfaces, thermal calculations have been carried out for the primary wall and the neighbouring breeder zone using the FE codes ABAQUS and FIDAP. The geometrical data and the internal heat generation rates have been chosen according to the present JCT outboard blanket design.

For the gap between the Be blocks a size of 10 and 200 μm was assumed. For the heat transfer coefficient, the thermal conductivity of helium was used.

Consideration of the calculated temperature distribution led to the following conclusions:

- The temperature distribution is strongly affected by the gaps between the Be blocks and the SS structures. Assuming a gap size of 200 μm leads to Be and ceramic temperatures which are 280 to 300 K higher than in the case of good contact.
- In the case of a good thermal contact between the Be blocks and the SS structures (10 μm gap), the calculated temperature distributions are in reasonable agreement with the JCT results.
- The temperature of the stiffening ribs at the inner surface of the FW is affected significantly by the thermal resistance between the Be blocks and the SS plates. For the 10 μm gap, the maximum rib temperature is 440 °C, whereas for the 200 μm gap, the temperature attains 510 °C.

Studies of Alternative Designs

Besides the uncertainties of the temperature distribution resulting from the possible gap between the Be blocks and the SS plates, the large poloidal extension of the ceramic pebble bed of the present breeder module design is of concern because it may cause thermal ratcheting effects. This gave rise to the search for alternatives. One of the studied solutions is a concept similar to the HCPB blanket (see B 1.1.1 and 1.2.1). This concept is characterized by a radial/toroidal arrangement of breeder and multiplier pebble beds and the separating cooling plates (see Fig. 2). Such a concept has the following advantages:

distribution was determined at the plasma-side and the back-side of the breeder zone

The minimum and maximum temperatures are as follows:

temperature [°C]	plasma-side	back-side
max. multiplier (Be pebbles)	450	300
min. ceramic (Li_2ZrO_3 pebbles)	525	365
max. ceramic (Li_2ZrO_3 pebbles)	855	465

Literature:

K. Schleisiek et al.: FZK Contribution to ITER Task D203 Stage I: Breeding Blanket Development and Design. FZK Internal Report IRS-Nr. 1/96 (1996).

Staff:

K. Gabel
 H. Gerhardt
 S. Gordeev
 P. Norajitra
K. Schleisiek
 I. Schmuck

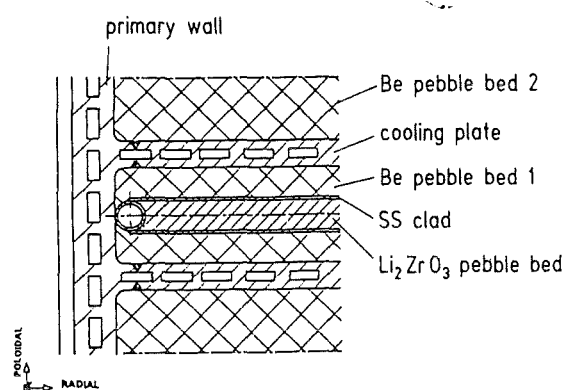
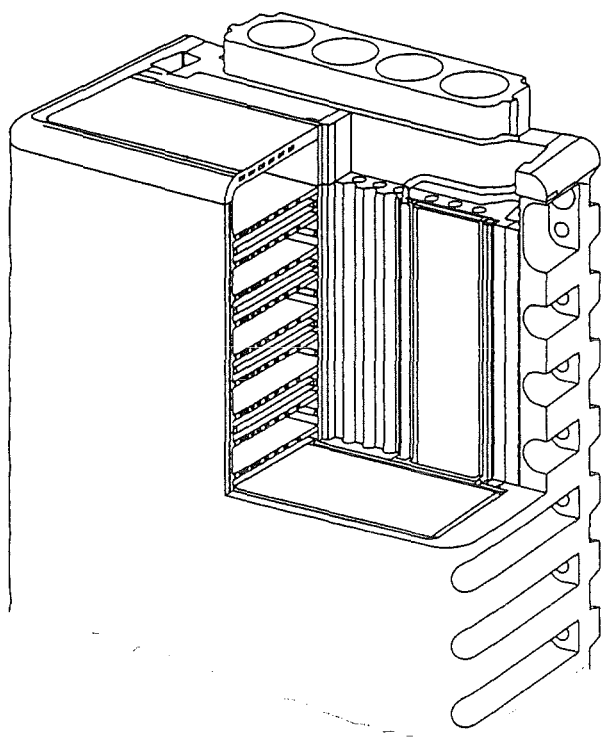


Fig. 2: Perspective view and toroidal structure of an ITER breeding blanket module with radially/toroidally layered configuration

- The Be pebble bed can be filled from the backside i.e. the filling height is small. Ratcheting problems are not to be expected.
- The cooling plates can be welded to the module box, i.e. they serve at the same time as stiffeners.

Other features of the present breeder blanket design can be retained.

The Be pebble bed 1 with a thickness of about 10 mm assures the breeder temperature needed for adequate tritium release. The thickness of the Be pebble bed 2 (about 40 mm) can be adjusted to obtain an optimum breeding ratio.

To verify that the concept leads to reasonable temperatures in the Be and breeder material, preliminary one-dimensional thermal calculations have been carried out using the FE code ABAQUS. In these calculations the poloidal temperature

Studies for ITER / NET

Introduction:

By granting study contracts to FZK, the ITER Home Team draws upon special expertise available in the laboratory. In contrast to the technology tasks which extend over a longer period of time and consist in most cases of experimental work, study contracts are agreed on short notice and are of limited duration. Most of the contracts support the ITER design.

J.E. Vetter

ERB 5000 CT 95 0064 NET (NET/95-384) ITER Magnets and TFMC Stress Analysis

The stress analysis for the conceptual design of the Toroidal Field Model Coil (TFMC) test configuration has been continued.

In addition to the simple shell-beam model reported in [1], a more detailed shell-solid global model (Fig. 1) was established to get a better stress and displacement resolution for the advanced design (Nov. 95). This model aims at a rather detailed simulation of the intercoil structure (ICS). The models for the TFMC and the LCT-coil are less detailed and intend to give the adequate stiffness behavior needed for the analysis of the ICS. In addition, this global model allows for a determination of the required boundary conditions for the detailed analysis of the LCT- and the model coil, being performed by our partners [2].

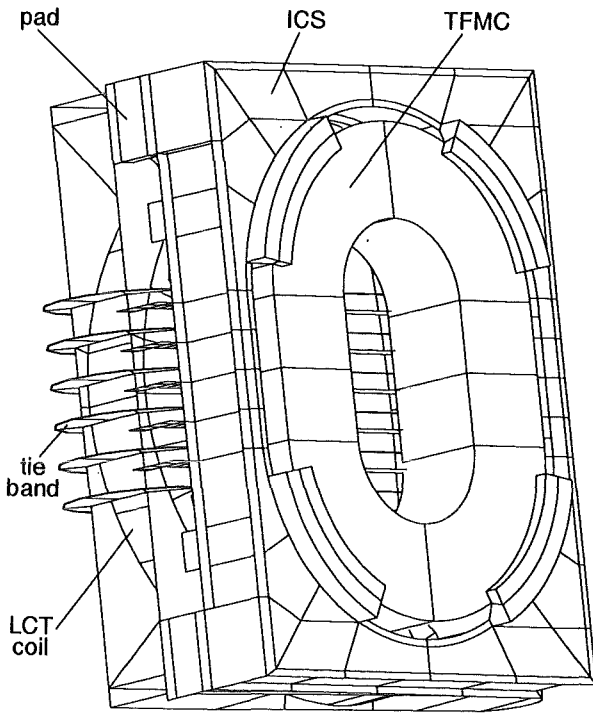


Fig. 1: Geometry of the global model with intercoil structure and the two coils

The analysis with the new global model revealed some highly stressed parts of the ICS. Some details of the results are shown in Fig. 2. The side wedges, which have to overtake the high attracting forces of the coils, are nonuniformly distributed, leading to a rather high stress peak at one edge. In addition, locally high stresses occur at the horizontal plates and at the supporting pads of the ICS.

In order to reduce these high stresses, some modifications have been proposed (Fig. 3). To lower the mean stress and to get more uniformly distributed stresses the wedges have been elongated and their position has been better adapted to the load distribution of the coil. The elongation of the pads

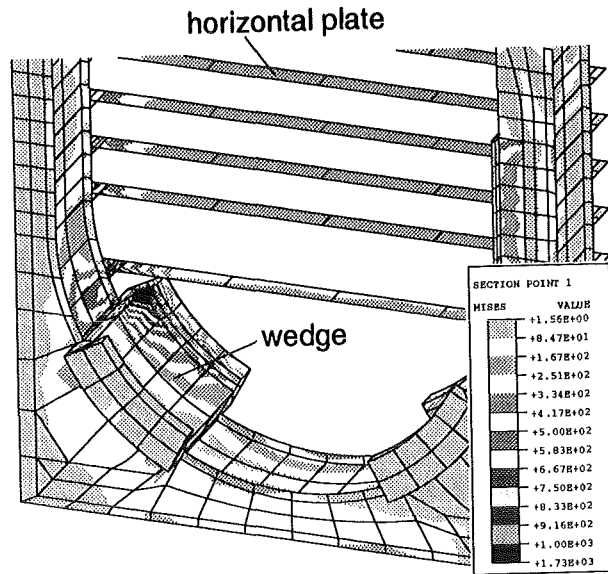


Fig. 2: ICS - v.Mises stresses (values in MPa)

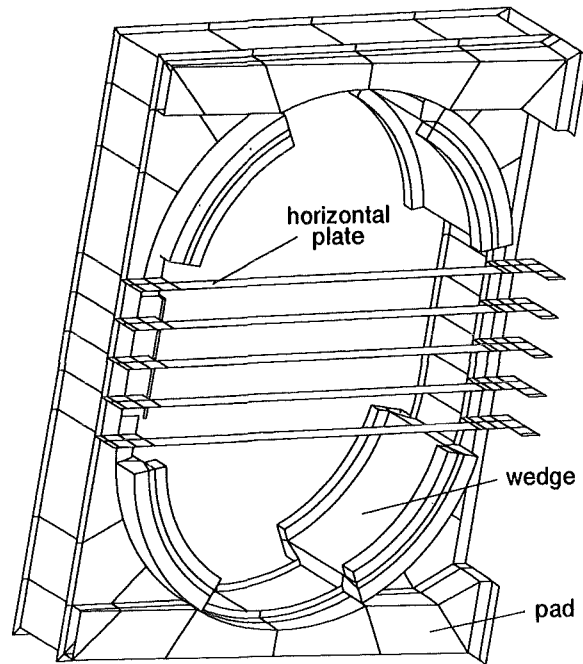


Fig. 3: ICS with horizontal plates, longer wedges and continuous supports (pads)

over the whole ICS width avoids stress concentrations at the pads and, as a side effect, reduces the LCT coil displacements. Some reinforcement of the horizontal plates (not visible in Fig. 3) was done at the cost of some reductions in the tie bands of the LCT.

The engineering design will now be performed by an industrial consortium (AGAN). During this period we will still be in charge of some additional analyses concerning critical

structural parts. However, our main activities will then concentrate on the stress analysis for the ITER coils.

Literature:

- [1] 'Nuclear Fusion Project Annual Report of the Association Forschungszentrum Karlsruhe/EURATOM', October 1994 - September 1995, FZKA 5688, EUR 16749EN
- [2] EU Home Team 'ITER TF Model Coil - Finite Element Analysis of the Conceptual Design of the TFMC Test Configuration', June 1996

Staff:

B. Dolensky
R. Meyer
S. Raff

**ERB 5004 CT 960050 (NET/96-405)
(Subtask of ITER Task MD9 for 1996)
Transient Voltage Behaviour for the ITER TF Coil**

The aim of the contract is the investigation of the ITER toroidal field coil according to its behaviour under transient voltages like they can occur during the operation of counteracting current switches for removal of the stored energy after a quench.

It was experimentally found and theoretically confirmed by a network model in the test of the POLO coil that overvoltages can appear inside the winding during the switching process. Since the shear disk pancake design represents a different type of winding (Fig. 1) the effect of surges had to be

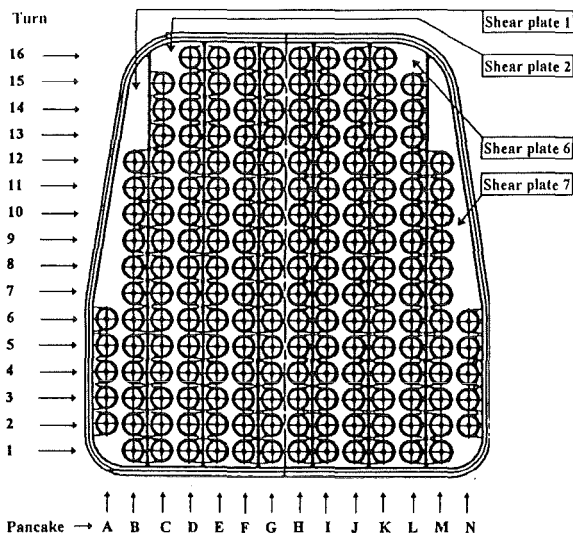


Fig. 1: Cross-section of the straight part of the D-shaped ITER TF Coil

investigated in order to get design criteria for the insulation coordination.

Considering the shear plate design and the size of the ITER TF coils it has to be expected that the coils have natural frequencies of oscillation below 5 kHz which would probably have consequences for the switchgear design. It was therefore proposed to develop a detailed network model of the ITER TF coil in order to determine its transient properties. The object of this work is to identify the allowable voltage rise rate of the switching system, to act as specification to the power supply designers. A network model was elaborated by calculating the internal capacitances and the inductance matrix of the winding (Fig. 2) [1]. In order to reduce the computational effort involved with the network model, only four turns of the TF coil were modelled with separate inductances. All other turns were modelled in combining two turns in replacing them by one single inductance in the network model. The result is an electrical network model with 98 self inductances being coupled by 9506 mutual inductances. The mutual inductances in the network model of

the TF coil are considered by 4753 ($M_{ik} = M_{ki}$) magnetic coupling factors k

$$(k = \frac{M_{ik}}{\sqrt{L_i L_k}})$$

In taking advantage of magnetic symmetries in the winding not all of the self and mutual inductances had to be calculated numerically. The calculated values for the self inductance of single windings of the TF coil vary from 48.98 μ H to 55.84 μ H for single turns and from 181.1 μ H to 208.9 μ H for combined turns. The corresponding magnetic coupling factors k have values between 0.32 and 0.84. These values lead to a total inductance of the network model of 0.94 H. The winding, ground, and plate-to-plate capacitances (see Fig. 2) were calculated analytically from the construction drawings. Values ranging from 74.6 nF to 168 nF were calculated for the winding capacitances. Accordingly the plate-to-plate capacitances have values between 360 nF and 373 nF and the ground capacitances of shear plate 1 and 7 have a capacity of 102 nF, whereas all other plate to ground capacitances have only about 32 nF.

The high voltage tests performed with the POLO coil showed that the superconducting filaments in the cable do not show an influence on internal overvoltage oscillations at the beginning of a high voltage pulse. This can be explained by the natural time constants of superconducting strands which are typically higher than the period of internal high voltage oscillations.

Therefore, only the copper, bronze, chrome, and Incoloy portions of the TF cable were considered in calculating the values for the serial ohmic resistances which represent the damping (caused by eddy current losses) in the network model at the beginning of the pulse. These resistances account for both, the skin and proximity effects. Since the TF conductor has a complicated compound structure, a simplified electromagnetic finite element model has been used to get an approximate solution for the skin effect in this type of cable at room and cryogenic temperature. The model has the same dimensions and cross-sectional portions of copper, bronze, chrome, and Incoloy as the original TF conductor.

The Finite Element Method (FEM) calculations performed for the first to fourth eigenfrequency of the network with the simplified model of the TF conductor resulted in the following ratios for the resistance rise due to the skin effect:

The values of the ohmic resistances in the network model can be derived by superposing these values to the resistance rise values being caused by the proximity effect. A numerical investigation of the proximity effect by means of a different FEM model was executed in order to find out which influence the eddy current barriers in the TF conductor cross-section have.

Frequency/Hz	1740	4000	7600	11000	49000
$R(f) / R(0 \text{ Hz})$	59	200	583	1080	7425

During the pulse, part of the current propagates capacitively through the winding respectively the network model. Therefore, and also because of the complex compound structure of the TF cable, the values for the ohmic damping being caused by the skin and proximity effects are only approximate values. But in earlier investigations it could be shown that the ohmic damping caused by the skin and proximity effects does not influence the calculated transient voltage oscillations inside a winding as long as only the order of magnitude of the damping values is correct.

In order to find the optimum grounding conditions for the TF coil, its transient behaviour will be calculated for the following grounding conditions of the shear plates (see Fig. 3):

- Case 1: Floating shear plates.
- Case 2: The shear plates are tied to the potential of the high field joints in Fig. 2 by a current limiting resistance R ($R = 1 \Omega$).
- Case 3: The shear plates are directly tied to the potential of the high field joints in Fig. 2.

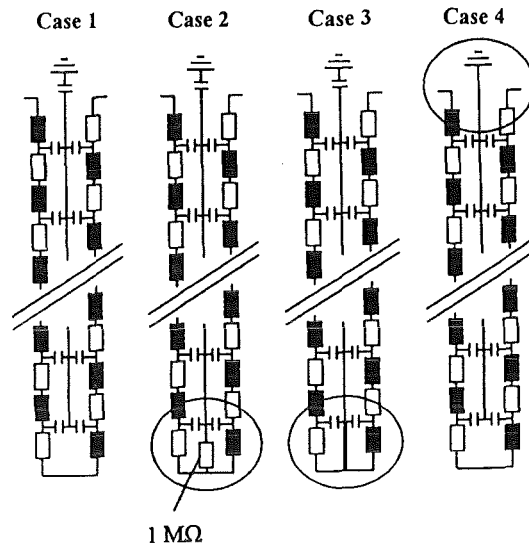


Fig. 3: Investigated grounding conditions of the shear plates

- Case 4: Grounded shear plates.

For investigating the transient behaviour of the winding under different grounding conditions five surges were applied across the winding terminals (risetime: 500 μs , 250 μs , 100 μs , 50 μs , 20 μs).

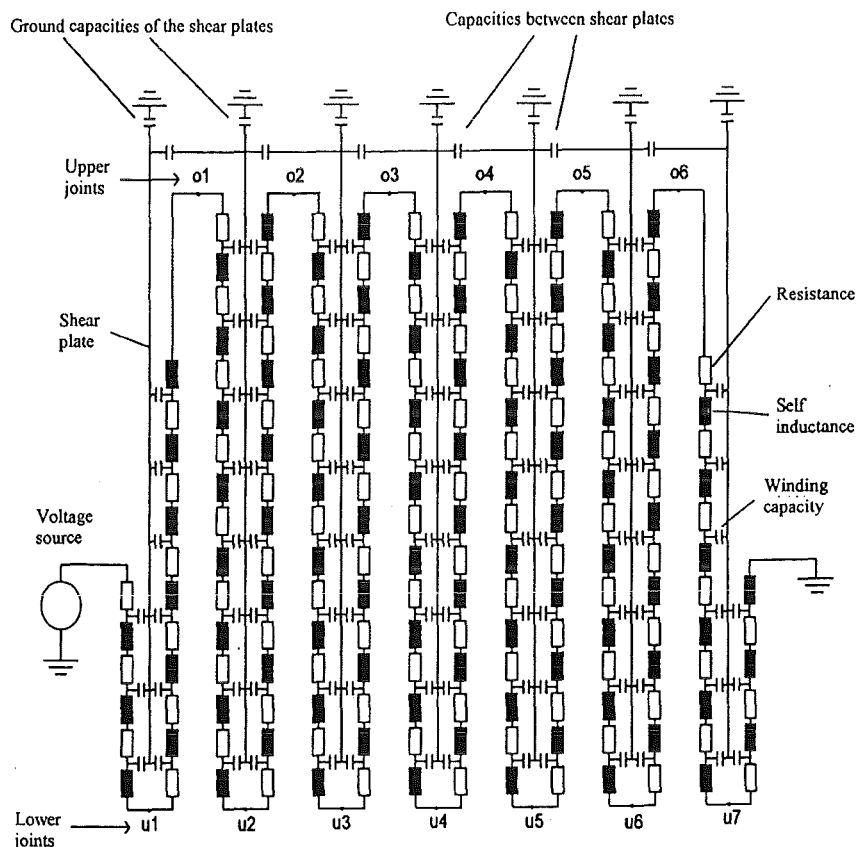


Fig. 2: Electrical network model of the TF coil

First simulations performed with the model described above, under the assumption that the shear plates are floating lead to the following results:

- Oscillations and overvoltages inside the winding of the TF coil must be expected at surges with a risetime below 300 μ s. The magnitude of the transient electrical stresses increases with shorter risetimes and reaches values of more than twice the nominal electrical stress in most locations of the winding for a surge with a risetime of 20 μ s.
- Although the insulation system of the TF coil seems to have large safety margins, the generation of fast rising surges and surges with oscillating components should be avoided by the power supply designers.
- The amplitudes of the transient electrical stresses might be lower at a different grounding condition of the shear plates (see Fig. 3).

This will be investigated in future simulations which will also include a parametrical study of the behaviour of the TF coil assuming higher damping values (although this assumption does not seem to be justified). A survey of internal electrical stresses at the optimum grounding conditions for the TF coil will be presented in the final report.

Literature:

- [1] A.M. Miri, J. Gruber; Erstellung eines detaillierten Netzwerkmodells der ITER TF-Spule zur Untersuchung ihres transienten Verhaltens zur Isolationskoordination, Forschungsbericht, Institut für Elektroenergiesysteme und Hochspannungstechnik Universität Karlsruhe Juni 1996.

Staff:

C. Sihler (till 31.8.96)
A. Ulbricht

**ERB 5004 CT 960053 (NET/96-408)
Characterization of Jacket Material**

This report covers the efforts with respect to materials characterization of an industrial manufactured jacket material, designed for the use as a conduit for the ITER CS-model coil. Candidate materials for the jacketing were 316LN (Valinox) and a newly developed γ' -prime precipitation hardened Ni-base alloy by Inco. Company, Incoloy 908. The jacket with overall sizes of 50x50 mm² and a central bore of a 37.5 mm diameter was manufactured by hot tube extrusion process. 14 samples of ca. 400 mm length consisting of both materials including orbital welds were provided to FZK by Ansaldo company, Genova at the end of 1995. Samples of ca. 70 mm length were cut for the 200 h/650°C heat treatment process, thus simulating the later aging process for the superconducting A15 phase formation. The stress / oxygen partial pressure / temperature sensitivity of the Incoloy 908 material demanded a careful heat treatment process performed at vacuum under clean conditions. For these reason a standard oxygen potential measuring probe (EMF-cell) was used to monitor continuously at the reaction site. The high sensitivity of the used probe allowed to determine oxygen partial pressures in the range of 10⁻³⁰ bar. Tensile and fracture tests were performed at 295 K and at 7 K in as received and in aged condition, respectively.

Material and specimens

A small quantity of the material 316LN in as received condition was chemically analyzed to verify the vendor's analysis. Special attention was paid on carbon content which was in past taken as the major responsible element of the embrittlement process (grain boundary sensitization) during the long aging process. The chemical analysis was performed by a commercial certificated chemical laboratory. Table 1 gives the results of the chemical analysis of the 316LN material and Table 2 shows the chemistry of the material Incoloy 908.

For tensile tests several round bar specimens of the length 65 mm, 30 mm reduced length of 4 mm diameter were machined out of the corner position of the jacket section. To

characterize the centrally located thinnest wall position (ca. 4 mm thickness) specimens having test section diameters of 3.5 mm were also machined. For fracture toughness measurements a major problem in this case was the small wall thickness which allowed only a machining of small ASTM proportional (45 x 43 x 4) mm compact tension (CT) specimens.

Besides, several round bars of 6 mm diameter were machined with a severe notch around the girth by the EDM (Electro-Discharge Method) technique to determine the toughness with a newly developed method. The net diameter of these specimens were 1-2 mm with a notch tip radius around 0.1 mm (Fig. 1). These samples were used to assess the jacket

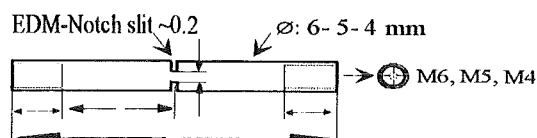


Fig. 1: RB-specimens (round bar)

materials toughness by using the J-Rice relation (Some Further Results of J-Integral Analysis and Estimates, J. R. Rice et al, ASTM STP 536, 1973, pp. 231-245) for the circumferentially notched round bars. Especially, this technique has been developed under the viewpoint to determine the toughness level of 2 mm thick specimens machined out from aged tubes used for the jacketing of ITER TF-superconducting cable.

Tensile and fracture tests

The results of the cryogenic tensile tests (Table 3) show that both candidate materials fulfill the yield strength requirements of >1000 MPa.

The above given results confirm that the jackets corner was heavily cold worked as compared to the mid position where

Table 1: Chemical composition of Valinox in wt%

C	Si	Mn	Ni	Cr	Mo	N	V	Co	W	Cu	Fe
0.015	0.25	1.66	11.9	17.2	2.44	0.18	0.04	0.11	0.03	0.35	bal.

Table 2: Chemical composition of Incoloy 908 in wt%

C	Al	Mn	Ni	Cr	Co	N	Ti	Nb	Fe
0.001	0.93	0.041	49	3.98	< 0.1	0.002	1.74	2.94	bal.

Table 3: Tensile properties of the two candidate materials at 7 K after 200 h heat treatment (vacuum, 650°C)

Material	Yield strength mid position/ corner position MPa	Ultimate tensile strength MPa	Elongation %
Valinox	1167 / 1226	1673	~ 40
Incoloy 908	1141 / 1216	1706	~ 22

the wall thickness is the smallest. Besides, the material Incoloy exhibits nearly a factor of two smaller elongation at fracture.

The determination of the fracture toughness, however, caused problems owing to the small sample dimensions. The ASTM standards E 813-81 and the revised version of -88 were initially the only applicable test method, whereas the limiting size criterion of the used compact tension specimens were at the border of the allowable thickness size ($B > 3.5$ mm). Therefore, with the elasto plastic J-test technique the difficulty arose owing to the limited specimen thicknesses of $B = 3.8-4.0$ mm. For this reason several bench mark tests were necessary with similar materials having different specimen sizes.

In addition to the standard J-tests, round bars (6-4 mm dia.) having an EDM-notch around the girth were uniaxial (tensile) loaded to obtain the fracture energy by using the load displacement curve. This newly developed test method allowed to give a fair empirical correlation between a variety of different aged and non aged materials. This type of specimens have the advantage contrary to the small size CT specimens of behaving fully plane strain under loading. The application of the J-integral solution for circumferentially cracked round bars resulted a ca. 0-20% (depending on toughness and yield level) higher J-values for aged and non aged materials as compared to the known critical J-data. The possible increase of the J-values by this test method can be attributed to the absence of the bending component during the uniaxial loading of the round bar specimen.

The circumferentially notched round bars require, therefore, a higher input energy as compared to the CT specimens where the bending of the CT in mode I facilitates the crack extension.

Fig. 2 and Fig. 3 show the J-test results obtained so far using 4 mm thick CT specimens machined from the aged original provided jacket sections of both materials Incoloy 908 and Valinox. In addition, in Fig. 1, results of aged plate and bar materials from different batches are also given. In this figure significant differences owing to the type of production can be seen. The validity criteria of the ASTM standard E 813 also limit the reliability of the obtained J-results considering the

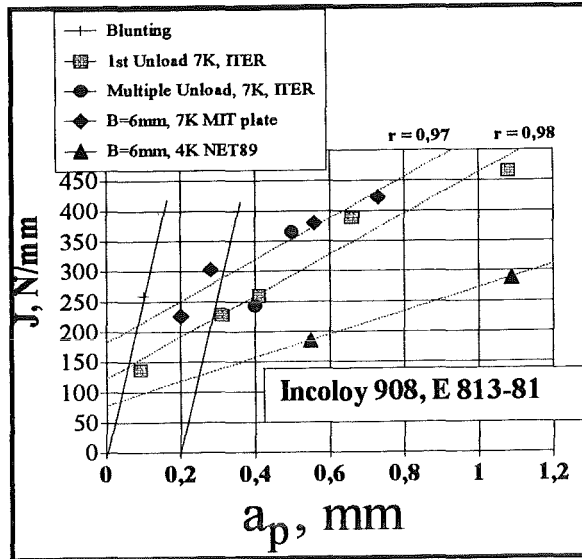


Fig. 2: Resistance curves of the aged Incoloy 908 obtained with 4 mm and 6 mm thick ASTM proportional CT specimens at 7 K and in LHe by using E 813-81 standard. The square and round points refer to 4 mm thick specimens. The given r-values are the correlation coefficients of the 1st order regression analysis of the evaluated points.

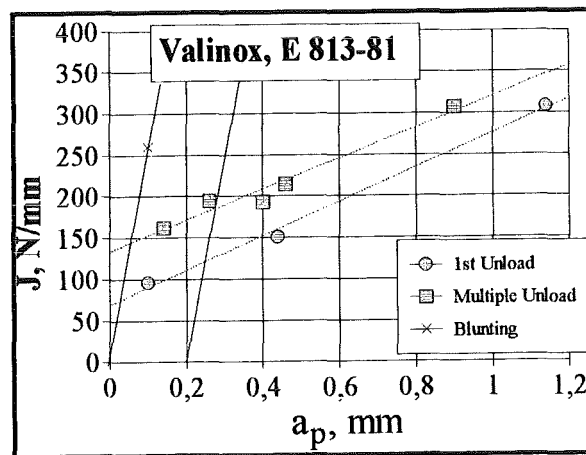


Fig. 3: Resistance curves of the aged 316LN, Valinox obtained with 4 mm thick ASTM proportional CT specimens at 7 K by using E 813-81 standard. The round points refer to J-data of the first loading/unloading of the specimen in its virgin state.

obtained crack front profile. Besides, the critical values of J-tests depend on the used standards E 813-81 or 88. This is one of the reasons for the data uncertainty. However, taking the lowest possible critical values of J, the aged jacket materials (excluding the 89 NET batch) exhibit a critical J-value approximately of 140 N/mm for both materials Incoloy 908 and Valinox.

The calculated J_c values of the Fig. 2 are according to the standard E 813-81. The use of the revised standard 88 resulted

in J_c values with negligible difference to the above evaluated values. However, the critical J value in case of -88 standard obtained by the intersection of the logarithmic regression line and the 0.2 mm offset shift delivers significantly high critical JIC values as compared to standard 81. The linear regression line and the intersection of this with the 0-offset blunting line according to the 81 standard result so far in critical J -values which are reasonable. Especially, the MIT (provided by Plasma Fusion Center, MIT, Cambridge, USA) plate material tested in the past in various labs yield a critical value around ~ 220 N/mm. In Fig. 2 the intersection of the regression line with the blunting line give also a value of ca. 220 N/mm (bold diamond plots). This means in this context, the 88 standard in case of small size specimens owing to the high plastic constraints during the loading simulates a non existing high toughness behaviour for the material under test. Besides, the 0.2 mm offset line of the 88 standard has no fundamental physical meaning. Therefore, the assessment of the J - test results obtained with these small size CT specimens (Fig. 4) were performed by the standard E 813-81.

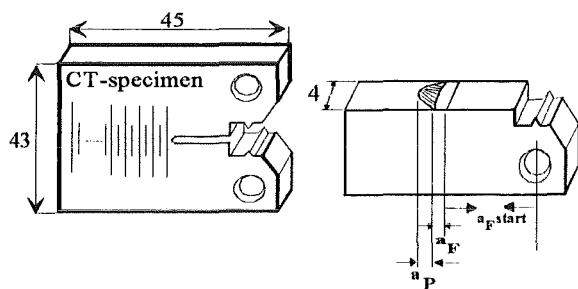


Fig. 4: Used 4 mm CT-specimens (compact tension). a_F refers to the fatigue crack growth extension prior the physical crack a_P extension. $a_{F-start}$ is the difference between the load line and notch position

The obtained J -test results for the Valinox show also a similar toughness level of this material at 7 K. Only the first loading/unloading test of the virgin CT specimen results in a comparable smaller J_c value. This phenomenon will be further investigated in near future. The circumferentially notched round bar specimens of these aged materials yielded also similar J - values for both Incoloy 908 and Valinox. These confirm that both materials have toughnesses covering the design requirements. In addition, the fatigue crack growth rate measurements of the aged jacket materials will be the main subject of the next task.

Staff:

A. Nyilas

H. P. Raber

T. Rusli (since June 1996)

Gyrotron and Window Development

Introduction:

Gyrotrons are generators of mm-wavelength power suited to heat plasmas confined by strong magnetic fields. Additional functions of plasma shaping and control are envisaged. Frequencies of today's applications are 70 to 120 GHz, ITER plans for 140 to 170 GHz, whereas the Wendelstein project intends to use 140 GHz systems. Development of gyrotron tubes with continuous wave power outputs of ~ 1 MW are underway in industry.

The FZK programme aims at major improvements on the classical gyrotron, it is intended to

- increase to output power
- to achieve frequency tunability
- to increase the overall efficiency.

Progress of these activities is described.

The transmission of MW power from a vacuum sealed gyrotron into a waveguide and, from the waveguide, into the plasma containing vacuum chamber of a tokamak or stellarator, has been looked upon as a feasibility issue. Only recently advanced materials, sophisticated mode optimization and improved cooling concepts have paved the way to successfully transmitting up to 2 MW of 170 GHz cw power through such windows. Under several alternatives proposed for ITER and Wendelstein solutions are followed by FZK that allow for flexible experimental conditions and for easy operation.

J.E. Vetter

Gyrotron Development (includes ITER Tasks T 24 and T 245/6)

1. Introduction

The FZK Electron Cyclotron Wave (ECW) source development is based on the conventional cylindrical cavity gyrotron [1,2] and the novel coaxial cavity gyrotron [3,4]. The cylindrical cavity gyrotron for 1 MW, CW operation seems feasible at the W7-X frequency of 140 GHz, whereas this type of gyrotron works close to its performance limits at the higher frequency of 170 GHz foreseen for ITER. These performance limits are imposed by mode competition and ohmic wall loading. Coaxial cavity gyrotrons designed for operation at frequencies of 140 GHz and 165 GHz with an rf-output power of 1.5 MW are under investigation at FZK. The recent experimental results let expect that this advanced development line could result in a tube well capable of operating at 1.5 to 2 MW, 170 GHz, CW.

Important development goals of a cylindrical cavity W7-X gyrotron, such as the depressed collector technology, the advanced built-in quasi-optical converter and the window concept are also prerequisites for the coaxial cavity gyrotron development, and therefore in these areas the development of a cylindrical cavity gyrotron will be able to provide an important input for the development of a 2 MW, 170 GHz, CW coaxial gyrotron for ITER.

2. Coaxial Gyrotron at 140 GHz (TE_{28,16}-mode)

A 4.5 MW (90 kV, 50 A) inverse magnetron injection electron gun for a 1.5 MW, 140 GHz coaxial gyrotron was designed, manufactured and successfully tested earlier [5]. In a first step, operated at short pulses (≤ 0.5 ms) the coaxial gyrotron had an axial waveguide output for mode purity studies. In a second step a tube design relevant for CW operation with a radial rf output will be investigated. Especially because of the present power limit of rf output windows the mm-wave power will be split into two beams and coupled out radially through two windows. In addition, a single stage depressed collector will be used in order to enhance the total efficiency and to reduce the power on the collector surface.

The first coaxial gyrotron had an axial waveguide output (Fig. 1a) with a fused silica window of 100 mm diameter and a thickness of 4.61 mm corresponding to $9\lambda_e/2$ of the TE_{28,16} mode at 140 GHz. The electron beam collector with the same diameter is a part of the output waveguide. The estimated electron beam power density at the collector surface is as high as 50 kW/cm² thus limiting the maximum allowable pulse length to about 0.5 ms at the design beam parameters.

The schematic layout of both coaxial gyrotron versions is shown in Fig. 1.

The TE_{28,16} mode was found to work stable in a wide parameter range. This proves the suppression of possible competing modes by a tapered and corrugated inner rod [6]. A maximum rf output power of 1.2 MW with an efficiency of

27.2% has been measured [7] in the TE_{28,16} mode in single mode operation at $U_b = 86$ kV, $I_b = 50$ A and $B_{cav} = 5.63$ T. The measured frequency of 139.96 GHz is close to the calculated value. The internal losses in the cavity, the output taper and window are estimated to be 5.5%.

Fig. 2 shows as an example the measured and the calculated rf output power versus the beam voltage for a magnetic field of $B_{cav} = 5.62$ T and a beam current between 50 A and 52 A. The calculations have been performed with a multi mode code using the operating parameters and the geometry of the cavity without any fitting and with an assumed velocity spread of 6 %. As expected from the numerical calculations the azimuthal neighbours TE_{29,16} at 142.02 GHz and TE_{27,16} at 137.86 GHz, which are the remaining competitors, are limiting the stability region of the working mode in the U_b - B_{cav} parameter space. The experimentally observed regions with single and multi-mode oscillation are indicated at the top of Fig. 2. At a given magnetic field, the TE_{29,16} mode oscillates at a voltage below and the TE_{27,16} above the oscillating range of the TE_{28,16} mode. Single mode oscillation of the TE_{28,16} mode is found within several kV of U_b . The regions of oscillations of the 3 measured modes agree well with the numerical predictions. Only the transition region is wider in the experiment than expected. According to calculations the rf power should rise up to $U_b = 87$ kV while the measured values reach a maximum around 84 kV and above about 86 kV the TE_{27,16} mode is oscillating. In the region between $U_b = 84$ to 86 kV there is a small amount of the TE_{27,16} mode present simultaneously with the TE_{28,16} mode. This gives an explanation for the reduced efficiency and output power in that region. However, this multimoding is not predicted by the numerical calculations. The discrepancy is thought to be caused mainly by window reflections which support the competing TE_{27,16} mode, since the rf window is optimized for 140 GHz and has a reflectivity of 10% at the frequency of the competitor. Another reason for the loss of single mode stability at higher voltages is a 4 % overshooting of the accelerating voltage (up to 3 - 4 kV) during a pulse. At the peak of the voltage the competing mode starts oscillations, and after the voltage dropped again these oscillations may remain. Both of these problems will disappear in the tube with radial output.

The possibility of step tuning has been proven over a range from 115.6 GHz to 164.2 GHz using the same experimental configuration (Fig. 3). Frequency tuning was performed by changing the magnetic field with constant magnetic compression. Output powers around 1 MW and efficiencies above 25% have been achieved near frequencies where the window reflection is minimal (122 GHz, 140 GHz and 158 GHz). With high window reflections the gun could not be operated at the desired voltage because of beam instabilities, probably due to leakage of reflected and converted rf power towards the gun. However, these reflections will vanish in the tube with radial output. It is therefore expected that in the radial version any of the possible oscillating modes shown in Fig. 3 will have an output power and efficiency similar to modes at frequencies without window reflections. Tab. 1 gives some examples for excited modes. At frequencies above

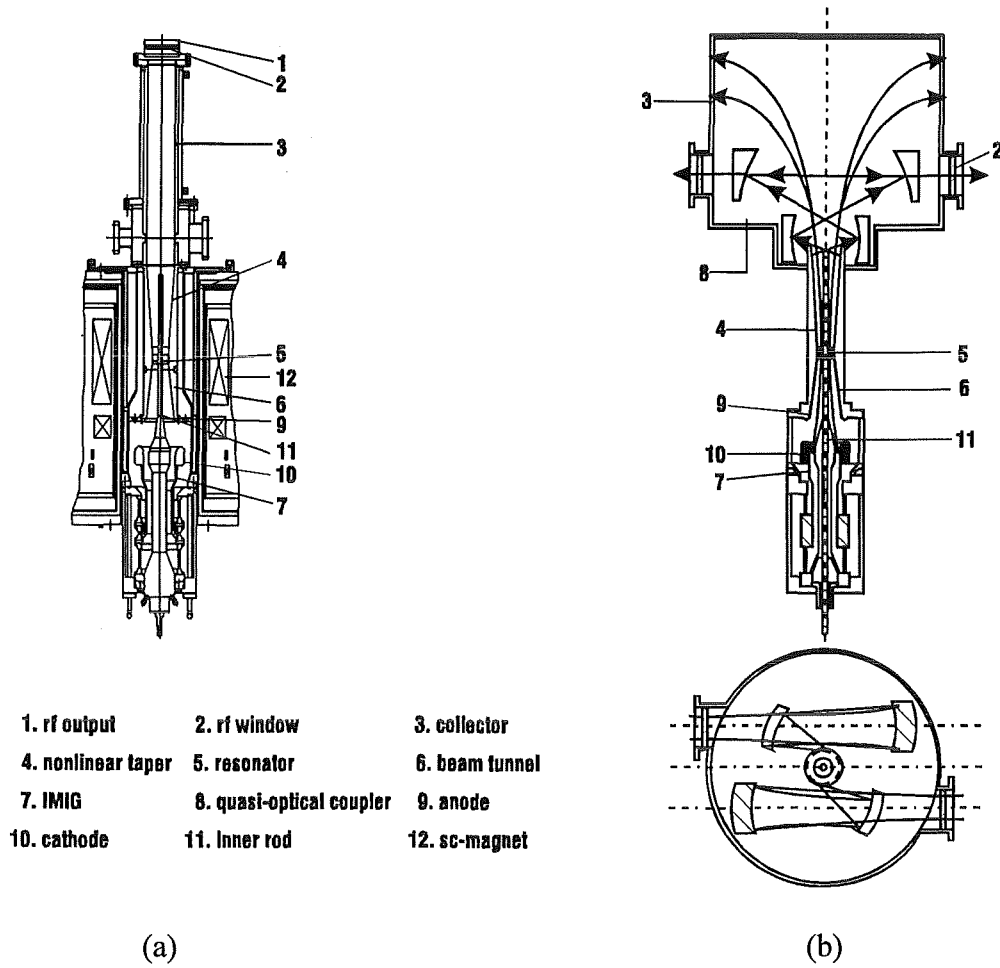


Fig. 1: Schematic layout of the coaxial cavity gyrotrons: (a) with axial rf-output, (b) with a dual-beam radial rf-output with two output windows

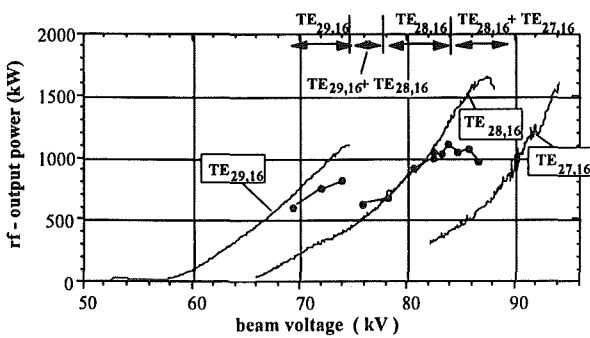


Fig. 2: RF output power versus beam voltage U_b , $I_b = 50 - 52$ A, $B_{cav} = 5.62$ T. Experimental results are given as points, with oscillating modes indicated to atop. Solid lines are possible stable single mode operation points from multi mode calculations

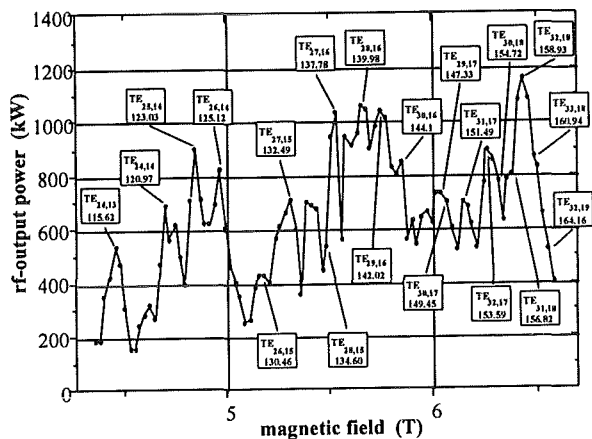


Fig. 3: RF output power versus magnetic field. $I_b = 50 - 52$ A, beam radius $r_b = 10$ mm. Each point represents stable single mode operation

the design value the maximum achievable velocity ratio decreases below the design value due to the need of a higher magnetic field and owing to the diode type of the gun.

3. Coaxial Gyrotron at 165 GHz (TE_{31,17} Mode)

A coaxial cavity gyrotron operating in the TE_{31,17} mode at 165 GHz has also been tested [8,9]. The selection of the operating frequency and mode are based on limitations imposed by the

Table 1: Oscillating modes of the step tuning experiments at low window reflections

P_{out}/MW	f /GHz	mode	B_{cav}/T	$\eta_{out}/\%$
0.9	123.03	TE _{25,14}	4.84	24.9
0.71	132.49	TE _{27,15}	5.31	17.6
1.17	139.98	TE _{28,16}	5.63	27.2
1.16	158.93	TE _{32,18}	6.43	26.2
0.83	160.94	TE _{33,18}	6.50	19.4

maximum magnetic field of the existing superconducting magnet at FZK and the use of the inverse magnetron injection gun (IMIG) of the 140 GHz, TE_{28,16} coaxial gyrotron, and a possibility of transforming the cavity mode to a whispering gallery mode appropriate for the dual-beam quasi-optical output coupler and the two output windows, which are foreseen for the lateral output version of the tube. For performing the experiments, the cavity of the 140 GHz-TE_{28,16} coaxial gyrotron of FZK has been replaced by a new coaxial cavity with tapered and corrugated inner conductor designed to oscillate at 165 GHz in the TE_{31,17} mode. The rf output window has also been replaced by a new boron nitride single-disk edge-cooled window with minimum reflections at the operating frequency. The rest of the tube (IMIG, beam tunnel, collector, etc.) remained unchanged. The tube with axial output has been tested [10] and delivered a maximum power of 1.2 MW in the designed TE_{31,17} mode with 26.7 % efficiency at 164.98 GHz. Maximum efficiency of 28.8 % was achieved at 0.9 MW output power. As in the case of the 140 GHz coaxial gyrotron the design operating point with an output power of 1.36 MW and an efficiency of 36.7 % is not accessible in the axial output version of the tube because of enhanced mode competition due to window reflection and beam instabilities developed at high beam current and high electron velocity ratio. Power at higher frequencies was also detected: 1.02 MW at 167.14 GHz in the TE_{32,17} mode with 26.8 % efficiency, 0.63 MW at 169.46 GHz in the TE_{33,17} mode with 18.0 % efficiency, and 0.35 MW at 171.80 GHz in the TE_{34,17} mode with 13.3 % efficiency.

4. Quasi-Optical Mode Converter for Coaxial Gyrotrons

Due to power limitations of gyrotron rf windows, the mm-wave output power of a 2 MW coaxial cavity gyrotron must be split into two linearly polarized wave beams and coupled out radially through two 1 MW windows. Beam splitting can be performed either by a quasi-optical 3 dB splitter (e.g. special phase correcting mirror or a diffraction grating), or by a dual-beam launcher of a quasi optical (q.o.) mode converter.

The advantage of the second solution is that an improved dimple-type launcher, generating two output beams, is much shorter than a single-beam launcher. If one employs, as in

conventional cylindrical cavity gyrotrons, a q.o. mode converter for the operating volume mode of the cavity, the dimensions of the mirror system are excessively large for a dual beam output since the azimuthal spread angle of the radiation is quite large, e.g. $\phi = 2 \arccos(m/\chi_{mp}) \approx 143^\circ$ for the TE_{28,16} mode (Fig. 4b).

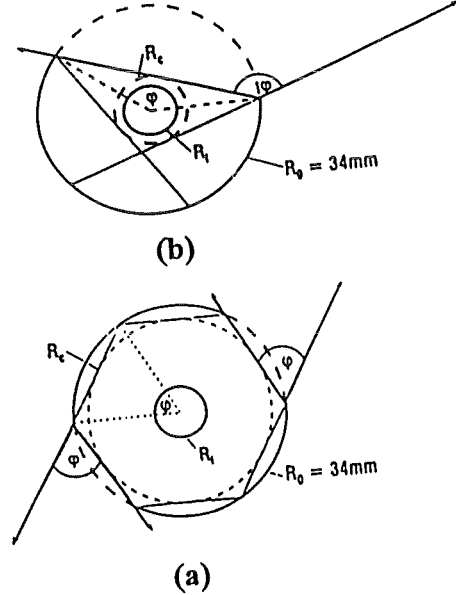


Fig. 4: Azimuthal angle of radiation (a) for the TE_{76,2} mode foreseen for use in the double-beam q.o. mode converter and (b) for the TE_{28,16} cavity with single-beam q.o. mode converter. The caustic radius $R_c = (m/\chi_{mp}) \cdot R_0 = 29.6$ mm and 10.9 mm for the TE_{76,2} and TE_{28,16} mode, respectively.

This is not the case for a high-order whispering gallery mode (WGM) of the type TE_{m,2} since here the caustic of the mode is close to the waveguide wall, e.g. $\phi = 2 \arccos(m/\chi_{mp}) \approx 59^\circ$ for the TE_{76,2} mode (Fig. 4a) so that a double-cut q.o. launcher can generate two diametrically opposed narrowly-directed output wave beams.

The actual design of a q.o. mode converter compatible with the constraints of a coaxial gyrotron dual beam output concept for operation with two outputs employs the two-step mode conversion schemes

$$TE_{-28,16} (\chi_{mp} = 87.36) \rightarrow TE_{+76,2} (\chi_{mp} = 87.38) \rightarrow TEM_{00} \text{ at } 140 \text{ GHz} \quad (1)$$

$$TE_{-31,17} (\chi_{mp} = 94.62) \rightarrow TE_{+83,2} (\chi_{mp} = 94.69) \rightarrow TEM_{00} \text{ at } 165 \text{ GHz} \quad (2)$$

which both generate two narrowly directed (60° at the launcher) output wave beams [11,12].

The conversion of the co-rotating cavity mode to its degenerate counter-rotating WGM is achieved in a rippled-wall waveguide mode converter. The q.o. WGM to TEM₀₀

mode converters employ improved dual-beam dimple-type launchers with $\Delta m_1=2$ and $\Delta m_2=6$ perturbations for longitudinal and azimuthal bunching, respectively. High conversion efficiencies are expected (94 % and 92 %, respectively).

Fig. 5 shows the unrolled theoretical intensity contour map of an advanced double beam launcher for the $TE_{76,2}$ mode at 140 GHz.

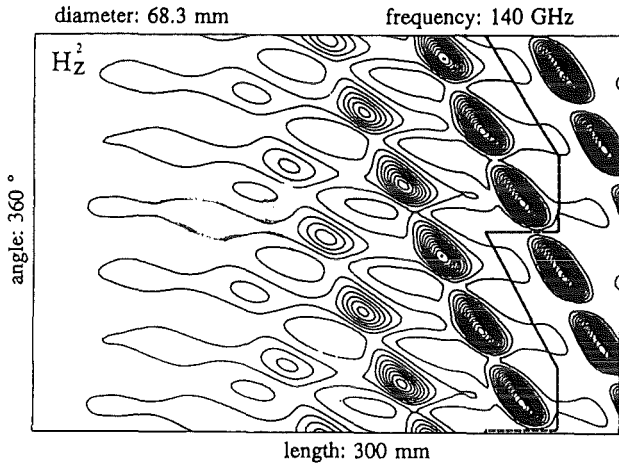


Fig. 5: Theoretical intensity contour map (unrolled) of a dimple-type double beam launcher for the $TE_{+76,2}$ mode at 140 GHz

5. Conventional Cylindrical Cavity Gyrotron

The development of conventional cylindrical cavity gyrotrons at FZK concentrates on four important items of high-power gyrotrons for various ECW applications on ITER: improved q.o. mode converters, high efficiency by energy recovery via a single-stage depressed collector (SDC), frequency tunability and multi-pass-band or broadband high-power mm-wave windows for the gyrotron and the plasma torus. An improved 1 MW, 140 GHz, $TE_{22,6}$ -gyrotron with q.o. mode converter, depressed collector and Brewster angle window is under construction.

A 0.5 MW, 118 GHz, $TE_{22,6}$ gyrotron (210 ns pulse length) with cryogenically-edge-cooled single disk sapphire window has been developed and tested in collaboration with CEA Cadarache, CRPP Lausanne and Thomson Tubes Electroniques [13]. Up to now, 0.5 MW pulses with a duration of 5 ns have been achieved at an efficiency of 30 %.

Literature:

[1] E. Borie, O. Braz, G. Dammertz, C. Iatrou, S. Kern, M. Kuntze, G. Michel, A. Möbius, B. Piosczyk, G. Soudée, M. Thumm, Proc. Jahrestagung Kerntechnik, Mannheim, 1996, 593-596.

[2] Kuntze, B. Piosczyk, G. Soudée, Proc. 20th Int. Conf. Infrared and Millimeter Waves, Lake Buena Vista (Orlando), Florida, USA, 1995, 199-200.

[3] V.A. Flyagin, V.I. Khishnyak, V.N. Manuilov, A.B. Pavelyev, V.G. Pavelyev, B. Piosczyk, G. Dammertz, O. Höchtl, C. Iatrou, S. Kern, H.-U. Nickel, M. Thumm, A. Wien, O. Dumbrajs, Proc. 19th Int. Conf. on Infrared and Millimeter Waves, Sendai, 1994, JSAP Catalog No.: 941228, 75-76.

[4] B. Piosczyk, O. Braz, G. Dammertz, S. Kern, A. Möbius, M. Thumm, A. Wien, S.C. Zhang, V.A. Flyagin, V.I. Khishnyak, A.N. Kuftin, V.N. Manuilov, A.B. Pavelyev, Pavelyev, A.N. Postnikova, V.E. Zapevalov, Proc. 20th Int. Conf. Infrared and Millimeter Waves, Lake Buena Vista (Orlando), Florida, USA, 1995, 423-424.

[5] V.K. Lygin, V.N. Manuilov, A.N. Kuftin, A.B. Pavelyev, B. Piosczyk, Int. J. Electronics 79, 1995, 227-235.

[6] S. Kern, C.T. Iatrou, M. Thumm, Proc. 20th Int. Conf. Infrared and Millimeter Waves, Lake Buena Vista (Orlando), Florida, USA, 1995, 429-430.

[7] B. Piosczyk, O. Braz, G. Dammertz, C.T. Iatrou, S. Kern, M. Kuntze, A. Möbius, M. Thumm, Proc. 21th Int. Conf. Infrared and Millimeter Waves, Berlin, 1996, AM2.

[8] C.T. Iatrou, O. Braz, G. Dammertz, S. Kern, B. Piosczyk, M. Thumm, A. Wien, S.C. Zhang, Proc. 20th Int. Conf. Infrared and Millimeter Waves, Lake Buena Vista (Orlando), Florida, USA, 1995, 415-416.

[9] C.T. Iatrou, 1996, IEEE Transactions on Plasma Science 24(3).

[10] C.T. Iatrou, O. Braz, G. Dammertz, S. Kern, M. Kuntze, B. Piosczyk, M. Thumm, Proc. 21th Int. Conf. Infrared and Millimeter Waves, Berlin, 1996, Ath15.

[11] A. Wien, and M. Thumm, Proc. 20th Int. Conf. Infrared and Millimeter Waves, Lake Buena Vista (Orlando), Florida, USA, 1995, 469-470,

[12] M. Thumm, C.T. Iatrou, A. Möbius, D. Wagner, Proc. 21th Int. Conf. Infrared and Millimeter Waves, Berlin, 1996, AM6.

[13] S. Alberti, O. Braz, P. Garni, E. Giguët, M. Pain, P.H. Thouvenin, M. Thumm, C. Tran, M.Q. Tran, Proc. 21th Int. Conf. Infrared and Millimeter Waves, Berlin, 1996, AF1.

Staff:

W. Baumgärtner

E. Borie

O. Braz (Uni Karlsruhe)

H. Budig

G. Dammertz

P. Grundel

C. Iatrou (Guest Scientist)

S. Illy

M.V. Kartikeyan (from 1.1.96, Guest Scientist)

S. Kern (to 31.7.96, Uni Karlsruhe)

M. Kuntze

G. Michel (Uni Karlsruhe)

A. Möbius

N. Münch

B. Piosczyk

G. Soudée (to 31.3.96, Guest Scientist)

M. Thumm

R. Vincon

S.C. Zhang (to 31.12.95, DAAD-Fellowship)

High Power ECW Windows (includes ITER Tasks T 25, T 245/6 and D 321)

1. Introduction

High unit power, in excess of 1 MW, and high-efficiency gyrotrons significantly lower the cost of Electron Cyclotron Wave (ECW) systems by reducing the size of the auxiliary support equipment (power supplies, cooling system, number of sc magnets, ...). CW operation is required for some of the anticipated ITER applications: 3 s for start-up, 100 s for heating to ignition and 100-1000 s for current drive. In order for the ECW system to perform these functions a window has to be developed to serve as both the tritium containment barrier on the torus and as the output window on the tube. The former application is technically more demanding as a torus window must also serve as a high pressure barrier during off-normal events (5 bar overpressure capability), should not use FC-cooling liquid, must not degrade unacceptably under modest neutron and γ irradiation (and X-rays), and, in the case of cryo-cooling, must be prevented by a cold trap from cryo-pumping.

Starting from the previously examined concept [1,2] of a liquid nitrogen edge cooled sapphire single-disk window, at FZK, a number of alternative concepts have been considered in additional field studies related to the coolant (LNe, 27K; H₂O, 293 K), window material (diamond, silicon) and the window geometry (circular, elliptical, rectangular), by which concepts the potential could be enhanced of achieving 1 MW transmission power. Furthermore, the frequency (140 GHz, 170 GHz) and the power profile (Gaussian, flat, annular) have been taken into account as sub-parameters.

2. Sapphire Window with Edge Cooling by Liquid Neon

The FZK LNe window design is based on a single circular sapphire disk of 110 to 140 mm diameter and 1.74 mm thickness ($6\lambda/2$) in a short cylindrical waveguide structure of about 60 to 90 mm diameter [3]. The microwave energy absorbed in the window disk is removed by nucleate boiling of liquid neon at atmospheric pressure (27.15 K) in a rim around the edge of the disk ("bath" cooling). Using the measured power absorption factor of $\tan\delta = 1.48 \cdot 10^{-11} (f/\text{GHz}) \cdot (T/\text{K})^2$ for Ti-doped sapphire and a relatively low value ($\approx 1500 \text{ W/mK}$) for the thermal conductivity, the maximum calculated CW power transmission for a Gaussian/HE₁₁-power distribution is 2.8 MW, 2.3 MW and 1.8 MW at 140 GHz, 170 GHz and 220 GHz, respectively. At 1 MW, 170 GHz, CW the power absorbed by the window disk is 67 W and the maximum and minimum temperatures would be $T_{\text{max}} = 34 \text{ K}$ and $T_{\text{min}} = 29 \text{ K}$ (for a diameter of 90 mm), respectively. Computations and design studies on realistic window assemblies have been done. Special care has to be taken in order to minimize the static liquid neon consumption. The closed-cycle neon refrigeration system "Philips Cryogenerator PH 110" (refrigeration capacity: 150 W) available at FZK could be used for first experimental tests on such a liquid neon

cooled single-disk sapphire window at 118 GHz, 0.5 MW, 210 s using the European TTE gyrotron at CEA Cadarache.

3. Medium Aspect Ratio Elongated Sapphire Window with Edge Cooling by Liquid Nitrogen

A liquid nitrogen edge cooled single disk sapphire window for 1 MW, 170 GHz, CW operation has been investigated [3]. Detailed calculations and design studies on the temperature and thermomechanical behavior for a realistic window assembly employing a racetrack or elliptical geometry and a flexible brazing collar have been performed using the finite element code ABAQUS supported by the pre-processor code FEMGEN for preparation of the discretization mesh. The use of elliptical windows with a flattened elliptical beam with an aspect ratio of 8:1 (window aperture $a = 252 \text{ mm} \times b = 32 \text{ mm}$, disk thickness $d = 1.74 \text{ mm}$) or of a ring-shaped elliptical beam with an aspect ratio of 3:1 (window aperture $156 \text{ mm} \times 52 \text{ mm}$, disk thickness $d = 1.74 \text{ mm}$) allows for a power transmission capability of 1 MW at 170 GHz without thermal runaway. The absorbed power at 1 MW beam power is 340 W and 285 W, respectively. Calculations on stress distribution and overpressure capabilities have shown that all stresses are well below the admissible limit (at 5 bar pressure difference) since the measured bending tensile strength of HEMEX sapphire is around 500 MPa and the compressive strength is approximately 2800 MPa.

4. Large Aspect Ratio Rectangular Torus Window System with Edge Cooling by Water

As an alternative to the distributed window concept under development by the US Home Team, the EU Home Team considers a high-aspect-ratio rectangular waveguide window inclined at the Brewster angle [3]. This broadband concept will use water edge cooling of a single disk made out of Au-doped silicon or PECVD (Plasma Enhanced Chemical Vapor Deposition) diamond. The window assembly consists (Fig.1) of an open-ended corrugated circular HE₁₁ waveguide, radiating into a dog-leg configuration consisting of a defocusing and a focusing reflector which generate the highly elongated HE₁₁ mode of a corrugated rectangular (200 mm x 12 mm) waveguide that houses the Brewster window. The reflectors are contained in an evacuated box. Behind the window, the back conversion to the circular HE₁₁ waveguide is achieved by applying the reflectors in the inversed sequence. In the final design the total losses of the assembly (7.3 %) can be reduced to approximately 3 % by using periodically rippled wall mode converters to generate the 90 % HE₁₁/10 % HE₁₂ (in phase) mode mixture for optimum coupling to the free-space Gaussian mode. Finite element calculations on the temperature and stress distributions at 170 GHz and $\Delta p = 5 \text{ bar}$ show that Au-doped silicon ($\tan\delta \approx 1/f$) and PECVD diamond ($\tan\delta \approx 1/\sqrt{f}$) are possible candidates. Diamond is preferable since there is no danger of enhanced losses due to thermal excitation of charge carriers at temperatures higher than 350 K.

In any case, a conventional circular, water cooled diamond window would have a much simpler mechanical structure

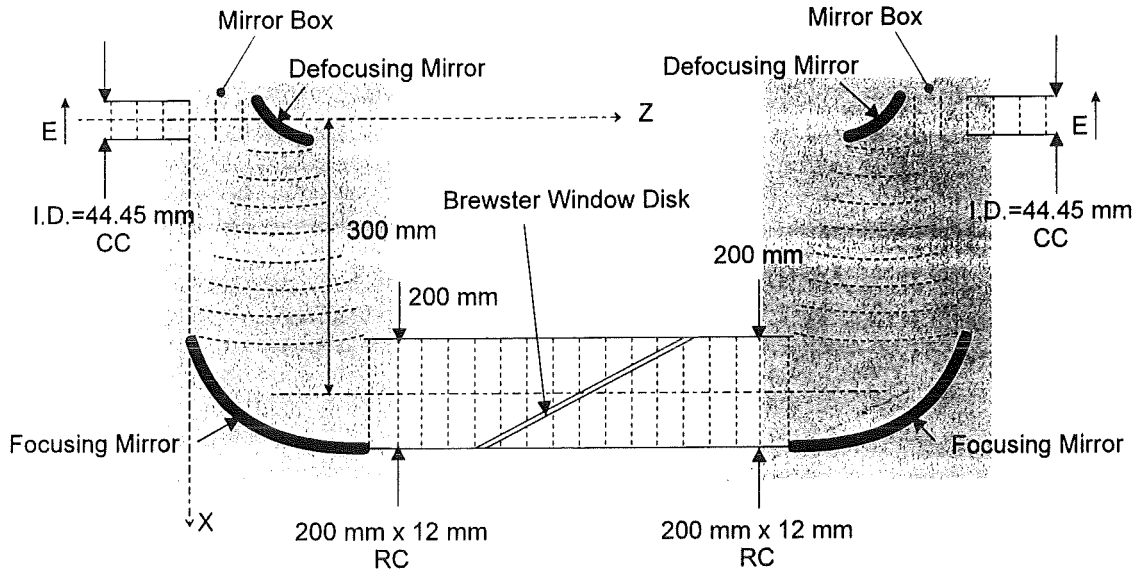


Fig. 1: Large aspect ratio rectangular Brewster angle window

compared to the present large-aspect ratio rectangular window. Additionally, there would be much lower losses.

5. Design and Specifications of the ITER Window Block

The window block consists of the window assembly together with a maintenance and an isolation valve. We are considering two major options that can easily carry 1 MW CW power at 170 GHz: (1) Edge-cooled twin PECVD-diamond window (water, 293 K) and (2) edge-cooled single-disk cryo-sapphire-window (LNe, 30 K).

5.1 Twin-PECVD-Diamond Window (Gaussian Power Distribution)

Through the use of a double window, window failures can be easily detected (as on the JET LH system). A very low vacuum pressure ($\approx 10^{-9}$ Torr) can be achieved within the interspace between the two window disks. Since the total volume is small, vacuum pumping can be done with only one Vac-Ion pump. Any failure of either window is detectable as a pressure rise on the ion pump even in the case in which a lower grade vacuum ($\approx 10^{-5}$ Torr) is present on the opposing surfaces. Bandwidth calculations show, that the disk distance should be e.g. $52.9 \text{ mm} = 30 \lambda$. The rf-power absorption in the window is approximately 100 W. With a heat transfer coefficient of $12 \text{ kW/m}^2\text{K}$ to the cooling water (flow velocity = 3 m/s) the central window temperature will not be higher than approximately 330 K. The design of the window assembly is under way.

During the last months we performed additional cold measurements on PECVD diamond (diameter = 40 mm, thickness = 1.03 mm, 145 GHz). Loss tangent and permittivity proved to be constant in the temperature range 200-360 K: $\tan\delta = 2 \cdot 10^{-5}$, $\epsilon_r = 5.665 \pm 0.005$. Since the thermal expansion of diamond is negligible, we have also constant reflection features of the diamond disks, so that there will be

no problems of trapped power between the two window disks.

In collaboration with EU industry we are preparing first metallization and brazing/bonding tests on cheap (grey) diamond samples with about 25-30 mm diameter.

5.2 Cryo-Sapphire-Window (Gaussian Power Distribution)

This much more complicated torus window option (see 2.) is kept as a back-up solution.

Literature:

- [1] P. Norajitra, H.E. Häfner, M. Thumm, Proc. 20th Int. Conf. Infrared and Millimeter Waves, Lake Buena Vista (Orlando), USA, 1995, 475-476.
- [2] H.E. Häfner, P. Norajitra, K. Müller, Thumm, M., Proc. 18th SOFT, Karlsruhe, 1994, Fus. Tech. Vol. 1, 505-508.
- [3] M. Thumm, O. Braz, H.E. Häfner, R. Heidinger, A. Möbius, P. Norajitra, G. Soudée, FZKA Report 5808, Karlsruhe, 1996.

Staff:

- O. Braz
- H.E. Häfner (to 31.12.95)
- R. Heidinger
- A. Hofmann
- N. Münch
- P. Norajitra (to 31.12.95)
- G. Soudée (to 31.3.96, Guest Scientist)
- M. Thumm

Long-Term Technology Programme

The long-term technology programme addresses those fields which are part of the development of fusion power reactors including DEMO, but which are not covered by the R&D accompanying the ITER-EDA.

These fields are:

- Blankets
- Materials
- Neutron Source (IFMIF)
- Nuclear Data Base
- Safety and Environment (SEAL)

None of these is entirely independent from ITER: test modules of the DEMO-blanket will be built, which the structural material developed in the long-term programme, and tested in ITER. The development of the material requires a high-energy intense neutron source, such as the International Fusion Materials Irradiation Facility (IFMIF). The safety and environmental issues of power reactors are closely connected to similar issues for ITER.

Nuclear Data Base is new as an area, but the work proposed is a continuation of old activities which in the past were included in other fields.

Blanket Development Programme

Introduction:

Within the European Fusion Technology Programme originally four different blanket concepts have been developed for the future demonstration reactor DEMO:

A water-cooled Pb-17Li liquid metal (WCL) concept, a self-cooled Pb-17Li liquid metal-cooled concept with helium-cooled first wall (the dual coolant (DC) concept), a helium-cooled solid breeder-in-tube (BIT) concept, and a helium-cooled solid breeder-out-of-tube (BOT) concept.

The blanket development programme was started in 1989 and carried out mainly by CEA, ENEA and FZK, with smaller contributions from JRC Ispra, SCK Mol and ECN Petten. The work was coordinated by the Blanket Coordination Group (BCG).

A key milestone in the blanket programme during 1995 was the selection of the two most promising concepts for inclusion in the future European Long-Term Programme. A decision on the blanket concepts to be selected was taken by the FTSC-P at the meeting on 24 November 1995. Of the four concepts which had been under development in the Associations, the following two concepts were selected:

- A.) a water-cooled lithium-lead blanket concept (WCLL) (based on the former WCL concept), and
- B.) a helium-cooled pebble bed blanket concept (HCPB) (based on the former BOT concept).

During the FTSC-P meeting in November 1995 it was also decided to form a new Blanket Management Committee (BMC) to manage the future European Blanket Programme (EBP) with the task of developing the breeder blankets for DEMO and the corresponding modules to be tested in ITER.

In preparing the subtasks for the new blanket programme, the BCG was requested by the FTSC-P to concentrate in 1996 on basic issues and not to pre-empt decisions of the BMC for 1997/98. Consequently the programme described in this report covers only the transition period 1996. Milestones were set in October 1996. They enable the BMC to conduct a revision of the programme and to generate, by the end of 1996, a detailed integrated programme addressing both blanket and structural materials related tasks for 1997 and 1998.

The R&D programme 1996 for both concepts was divided into work packages (WP) with tasks and subtasks. These work packages and tasks are:

Concept A: Water-cooled Lithium-Lead Blanket (WCLL)

WP-A-1: Design and Analysis

- A1-1 Demo blanket segments and system
- A1-2 ITER test module and external circuits

- A1-3 Analysis and modelling
- A1-4 Reliability/availability analysis

WP-A-2: Fabrication, Assembly and Development Studies of the Blanket Segment

- A2-1 Segment-box and headers
- A2-2 Double wall tubes fabrication and testing
- A2-3 Nuclear qualification for licensing of components and fabrication procedures

WP-A-3: Pb-17Li Physico-Chemistry Experiments

- A3-1 Purification from corrosion products, impurities, and activation products
- A3-2 Products redeposition within the blanket system
- A3-3 On-line monitoring and stabilisation of the Li-content

WP-A-4: MHD

- A4-1 Evaluation of MHD effects
- A4-2 MHD-related experiments

WP-A-5: Tritium Control including Permeation Barriers

- A5-1 Pb-17Li-side and water-side permeation barrier development
- A5-2 In-pile testing of permeation barriers
- A5-3 Out-of-pile testing of permeation barriers

WP-A-6: Tritium Extraction

- A6-1 Experiments and evaluation of T-extraction from Pb-17Li
- A6-2 Experiments and evaluation of T-extraction from water

WP-A-7: Safety related Activities for DEMO and ITER Test Module

- A7-1 Blanket system safety-assessment
- A7-2 Definition of safety-related devices
- A7-3 Water-Pb/17Li interaction - Large-leak experiments
- A7-4 Water-Pb/17Li interaction - Small-leak experiments
- A-5 Water-Pb/17Li interaction - Reaction products behaviour experiments

WP-A-8: ITER Test Module System and Testing

- A8-1 Small-size test-object system out-of-pile
- A8-2 External circuit components testing
- A8-3 Pb-17Li-circuit instrumentation and minor components development

Concept B: Helium-Cooled Pebble Bed Blanket (HCPB)

Most of the FZK work was concentrated on concept B. The FZK contributions to concept A refer to the work packages WP-A-1, A-3, A-4 and A-5.

WP-B-1: Design and Analysis

- B1-1 Design optimisation and modifications of present design incl. first wall box
- B1-2 ITER test module and external circuits
- B1-3 Analyses and modelling
- B1-4 Reliability/availability analyses

A. Fiege

WP-B-2: Fabrication, Assembly and Development Studies of the Blanket Segment

- B2-1 Fabrication, assembly and development studies of segment box and blanket cooling plates

WP-B-3: Ceramic Breeder Pebbles

- B3-1 Pebble characterization and optimization of industrial production
- B3-2 Reactor irradiation

WP-B-4: Beryllium Pebble Development

- B4-1 Characterization and optimization of mechanical properties
- B4-2 Behaviour under irradiation

WP-B-5: Tritium Control including Permeation Barriers

- B5-1 Calculations of tritium permeation losses from purge system and first wall
- B5-2 Permeation tests in martensitic structural material and Incoloy 800 as a function of temperatures and H₂O/H₂ ratio
- B5-3 Permeation barriers and compatibility with ceramic breeder pebbles

WP-B-6: Tritium Extraction

- B6-1 Ancillary loops incl. helium purification plant and tritium purge flow system

WP-B-7: Safety related Activities for DEMO and ITER Test Module

- B7-1 Safety studies

WP-B-8: ITER Test Module System and Testing

- B8-1 Out-of-pile tests in HEBLO and HEFUS-3
- B8-2 In-pile tests of small submodules in BR2 or HFR

WP A 1 Design and Analysis

A 1.1.1 Design and Fabrication Alternatives for the Blanket Box

The following manufacturing techniques developed by FZK for the HCPB blanket (and previously also for the Dual Coolant blanket) have been considered with respect to their applicability to the DEMO-WCLL blanket box:

- Diffusion bonding of plates
- Bending of thick plates with internal cooling channels
- Electron beam (EB) welding of FW plates or box sections as double weld with intermediate leak detection gap in a single step.

Three proposals have been elaborated for the manufacturing of the FW plates with cooling tubes which are partly mixed applications of CEA and FZK techniques. The main advantage of these proposals is that deep hole drilling of the FW plates and brazing of the FW cooling tubes could be avoided.

The two-dimensional bending of the thick plates to obtain the box structure of the outboard blanket segment is a difficult fabrication step. An alternative design solution is the manufacturing of straight FW sections including the side walls. Several proposals have been elaborated for the design of the EB welds between the sections which take into account the variable thickness of the WCLL blanket box side wall.

Additionally, the routing of the poloidal cooling tubes in the breeder zone of the DEMO outboard blanket segment was investigated with the help of three-dimensional CAD modelling. A solution was found which is free of collisions between the tube, the box, and the stiffeners. At some locations the distances between the tubes and the FW are larger than anticipated so far. This necessitates additional thermal analyses.

Staff:

S. Gordeev
T. Heider
K. Schleisiek

A 1.4.1 Availability Analysis and Data Base

The availability or unavailability (equal to 1 minus availability) of the Pb-17Li system of the WCLL-DEMO blanket was analysed. A measure for the unavailability is the probability for the system to be unavailable on demand. This occurrence is termed the top event. It is assumed that a single failure in the system leads to the top event. The data base for the analysis are the component failure rates used in the blanket selection exercise. The system considered consists of 4 circuits, each serving 12 outboard and 8 inboard segments (with their associated divertor segments). Each circuit in turn consists of the external loop with piping, recirculating pump, valves, and burst discs. Also included in the analysis are the extraction columns and part of the purge gas circuit as the link between the Pb-17Li system and the tritium recovery system. The latter has not been considered, since it is at a premature state. Problems are not expected here, if similar maintenance and repair strategies can be applied as for the tritium recovery system of the HCPB blanket for which a high availability was obtained.

The analysis yields an unavailability of the whole Pb-17Li system of 0.27, corresponding to an availability of 73 %. This result is determined by more than 82 % by the rupture discs, for which a failure rate (rupture or leakage) of $1.9 \times 10^{-4}/h$ was used. Relatively small contributions come from the active components of the main circuit, i.e., valves with 8.3 % and pumps with 6.2 %. The passive components like pipes, bends, and collectors contribute by only 1.36 %. The contribution of the purge gas components is almost negligible.

The study has shown that the unavailability of the Pb-17Li system affects strongly the overall availability of the whole blanket system. Therefore, design alternatives should be investigated. In order to explore the potential for improvements, a modified Pb-17Li system was analysed consisting of 5 liquid metal circuits (instead of 4) in a 4 out of 5 logic. The unavailability would then be reduced from 0.27 to about 0.006, giving a high availability of the Pb-17Li system of 99.4 %.

Staff:

H. Schnauder

WP A 3 Pb-17Li Physico-Chemistry Experiments

A 3.1.1 Radiological Important Impurities and Nuclides

During operation of a Pb-17Li blanket a number of radioactive nuclides are formed. Most important because of their volatility and toxicity are Po-210, Hg-203 and Tl-202. Because polonium is formed from bismuth, also this element has to be considered.

The investigations of the behavior of Hg and Tl have started. A thermodynamical consideration showed a very high volatility of mercury from Li-Pb mixtures. The compound LiHg is not stable at higher temperatures. Radioactive Hg-203 will be used in the experiments. It is produced by irradiating a mixture of lead with 0.1 % Hg in the TRIGA reactor of DKFZ. For thallium a first test in a thermal gradient capsule was performed. Tl was found completely in the liquid phase, contrary to the behavior of Bi, Fig. 1.

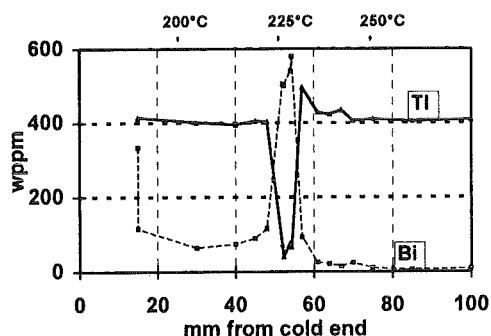


Fig. 1: Distribution of Tl and Bi in thermal gradient capsule No.21

To minimize the Po-210 content bismuth has to be removed to concentrations below 8 appm [1]. Solubility functions for Bi were published before [2]. A diffusion type cold trap with a solid phase was successfully tested in thermal convection loop No.8. After adding Bi in form of Li3Bi the concentration in the eutectic mixture decreased with time, Fig. 2. Bi was deposited in the solid phase of the cold trap, as shown for a capsule in Fig. 1. The final concentration was in the requested range. Also excess Li was deposited there. This effect was observed before in loop TRITEX, where a freeze valve acted as cold trap with a solid phase.

It can be concluded that Po-210 will cause no problems in a fusion reactor. The volatility of Po-210 is low [3] and Bi can be removed with a simple cold trap. Because such 'cold traps' are in each loop system, e.g in form of a freeze valve, no special device is required.

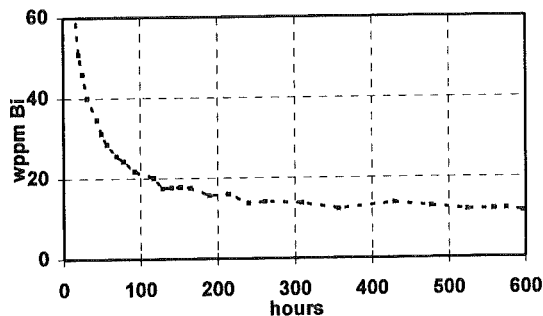


Fig. 2: Removal of Bi in thermal convection loop No. 8

Literature:

- [1] H. John et.al. (editor) KfK 4908 (1991)
- [2] Bucké et.al., Fusion Technology 1996, to be published
- [3] H.Feuerstein et.al., J.of Nucl.Materials 191-194 (1992) 288

Staff:

- J. Beyer
- S. Bucké
- H. Feuerstein
- A. Holzmann
- L. Hörner
- S. Horn

A 3.1.2 Behavior and Removal of Corrosion Products

Corrosion products in a liquid metal system form particles. The deposition of these particles in narrow gaps causes the risk of blocking. Therefore corrosion products have to be removed from the liquid metal. For the study of the behavior of corrosion products and the possibility of removal, loop TRITEX is used [1]. It is a pumped loop with about 80 kg Pb-17Li circulating, fabricated from ferritic steel 4922. The loop surface of 1 m² is the source of corrosion products. TRITEX has operated so far in 6 experimental phases with a main loop temperature of 450°C for 8000 hours. A total of 150 grams corrosion products are produced.

Different kinds of cold traps and magnetic traps were tested in TRITEX. So far no enrichment of corrosion products were found in these traps [2]. However the electro magnetic pump acted as an effective magnetic trap, 25% of the particles were deposited there after phase 5. More than 60% of the particles were deposited in crusts at the covergas interface. Because of the density difference, particles float to liquid metal-covergas interfaces.

For experimental phase 7, a magnetic trap similar to the EMP, as well as a special particle deposition device were installed. The loop has started in October 1996. It will run for 4 months. Then it will be dismantled and analyzed.

Literature:

[1] H. Feuerstein et al., J. of Nucl. Mater. 155-157 (1988) 520

[2] KFK-5288 (1993), p.119

Staff:

J. Beyer

S. Bucké

H. Feuerstein

L. Hörner

S. Horn

A 3.3.1 Li Behavior and Adjustment

The Li concentration in a blanket has to be kept constant at the eutectic concentration of 15.8 at.%. During operation lithium may be lost by burnup, oxidation or segregation effects [1]. A reduced Li concentration gives lower tritium breeding rates and increases the melting point of the mixture. If the system contains a diffusion type cold trap, lead may deposit in the solid phase at the eutectic temperature. On the other hand an excess of Li above the eutectic composition causes the deposition of the compound LiPb in the cold trap. Fig. 1 shows this in a thermal gradient capsule [1].

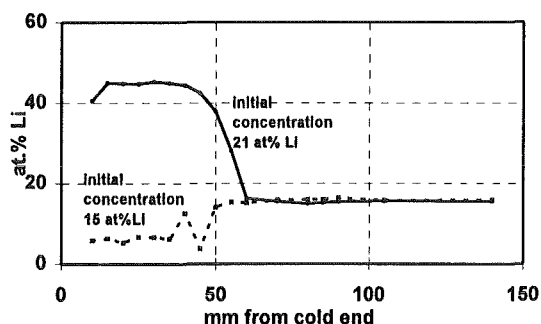


Fig. 1: Distribution of Li in thermal gradient capsules

These effects were observed also in loops. TRITEX was even blocked by the formation of LiPb at a cold spot at the end of experimental phase 6. The initial concentration was near 17 at.% Li, the final one the eutectic concentration of 15.8 at.%, excess Li was deposited.

As shown before [2] Li-adjustment is possible by adding LiPb, Li₃Pb or lead. From observations in loops it might be possible to have a kind of self-adjustment. A diffusion type cold trap with a solid phase should be sufficient for this. Thermal convection loop No. 9 is designed especially to study this possibility. The experiment is planned for early next year.

Literature:

- [1] H. Feuerstein et.al., Liquid Metal Systems, Plenum Press 1995, 357
- [2] H. Feuerstein et.al., Fusion Technology 1994, 1257

Staff:

J. Beyer
 S. Bucké
H. Feuerstein
 L. Hörner
 S. Horn

WP A 4 MHD

A 4.1.1 / 4.2.1

Theoretical and Experimental Investigations on Natural Convection in WCLL under MHD Conditions

Experimental Investigations

Heat transfer improvement by natural convection in a horizontal flat box with an aspect ratio 2cm x 20cm x 40cm heated from below and cooled on the top wall will be conducted at the beginning of 1997. This test section can also be used by slight modification in a vertical turned position within the solenoid magnet of the MEKKA laboratory (see attached schematic Fig. 1). These experiments with the

frame made of nickel and this nickel frame was afterwards welded with the stainless steel parts. In the meantime we succeeded to tighten the leaks in the welding seams.

Theoretical Studies:

Modelling work to investigate heat transfer improvement by natural convection and the corresponding suppression of convection by MHD-effects are under way.

During these investigations the influence of the height of the magnetic field (expressed by the Hartmann-number) and of the electrical conductivity will be studied.

Two-dimensional (2D) formulation of the problem

In three-dimensional (3D) magnetohydrodynamic flows the energy of vortices whose axes are inclined to the direction of the magnetic field is immediately removed by Joule's dissipation and the vortices will be strongly damped. Vortices whose axes are aligned with the direction of the magnetic field are not affected by the field as long as fluid is of infinite extend in the direction of the magnetic field. So if the magnetic field is strong enough a 2D pattern of convective rolls aligned with the direction of the magnetic field will evolve.

If the fluid is of finite extend in the direction of the magnetic field, electric currents induced by the fluid motion can close in the viscous Hartmann layers and in the electrically conducting Hartmann walls. Thus, the fluid motion is damped by an additional Lorentz force. Integrating along magnetic field lines, taking into account symmetry conditions and the thin wall condition, this 3D currents can be taken into account and the problem can be described by 2D equations (B is parallel to the x-axis):

Results:

Fig. 3 shows the Nusselt number describing the heat transfer from a vertical heated wall to a parallel cooled wall as a function of the damping parameter τ . The parameter τ characterizes the damping of the convection cells by the magnetic field. Fig. 4 demonstrates how the convective flow pattern between the parallel walls changes for different τ -regimes.

Heat Transfer Improvement in MHD Flow

Magnetohydrodynamic (MHD) flows even at high magnetic fields typical for fusion reactor applications reveal features which improves significantly the heat transfer from the highly heat loaded plasma facing first wall. One of these features is the so-called two-dimensional (2D) turbulence. This kind of turbulence, appearing inherently in inflection point velocity profiles exceeding a certain parameter constellation does not lead to a measurable increase of pressure drop in contrary to ordinary hydrodynamic flows. However, 2D-turbulence leads to an improved heat transfer behaviour even without additional turbulence promoters compared to the laminar

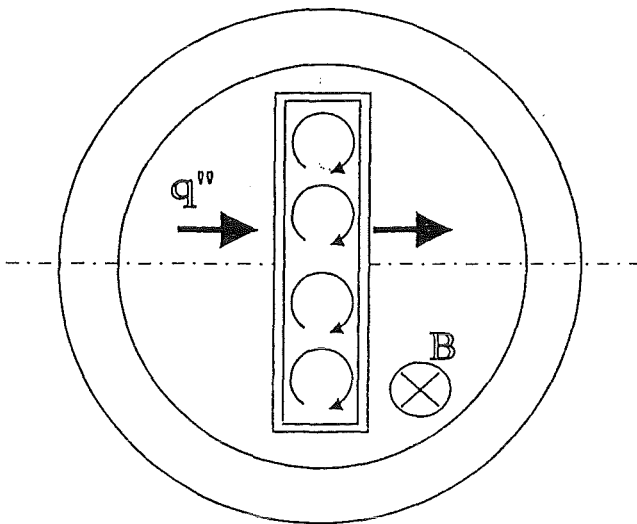


Fig. 1: Schematic view of the experiment in MEKKA to study heat transfer by natural convection and MHD-conditions

modified test facility could be started mid of 1997.

Design and fabrication of the test section:

The design of the whole test apparatus has been finished. Fig. 2 shows a cross section of the test facility and gives an overview about the technical specifications:

There are five thermocouples in each copper plate to measure the temperature gradient over the liquid metal layer. Their positions are as close as possible to the liquid - containment interface to enable the measurement of time dependent signals. The average temperatures at the upper and the lower fluid - wall interface will be determined by averaging in time and between the five positions.

The manufacturing of the test section has been almost completed. Unfortunately severe problems arised of welding the copper plates with the other components of the apparatus made of stainless steel. Copper can not be welded directly with stainless steel. Therefore, it was welded with a

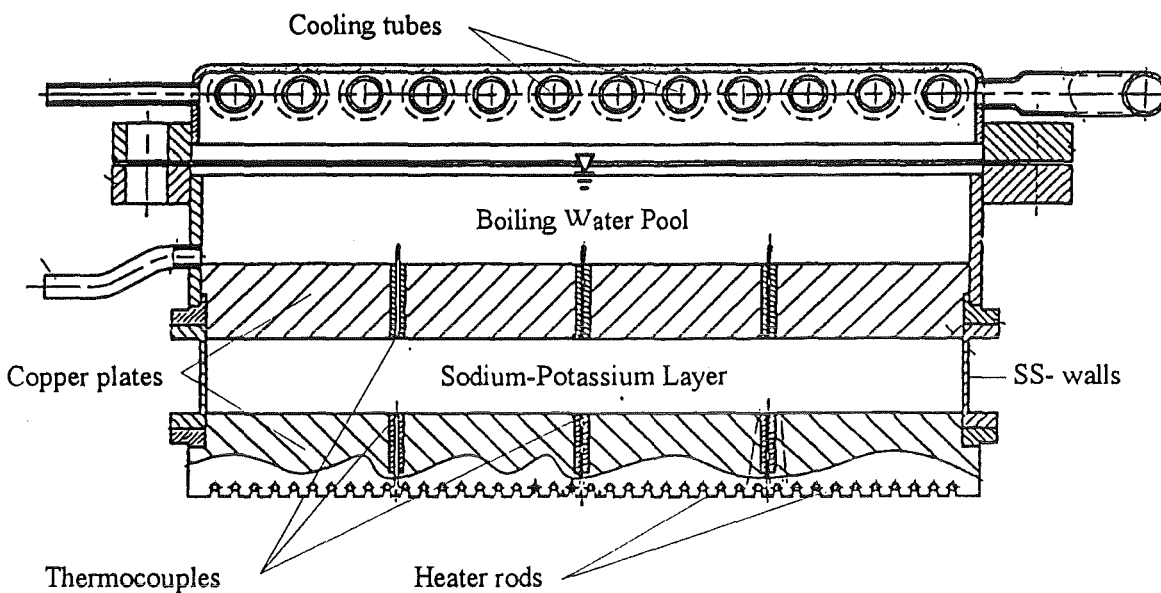


Fig. 2: The test facility WUEMAG

flow assumptions used in previous design calculations. both theoretical and experimental investigations of the heat transfer of a MHD flow in a rectangular electrically conducting channel at fusion relevant parameters have been conducted. Besides, that rectangular ducts appear quite often in technology this design has been chosen, because a MHD flow in an electrically conducting duct exhibits an M-shaped

velocity profile which is characterised by high velocity jets at the walls parallel to the magnetic field B . The main results are:

- At high magnetic fields for hydraulic Reynolds numbers Re larger than 6000 the heat transfer is strongly improved due to the formation of 2D vortices. These

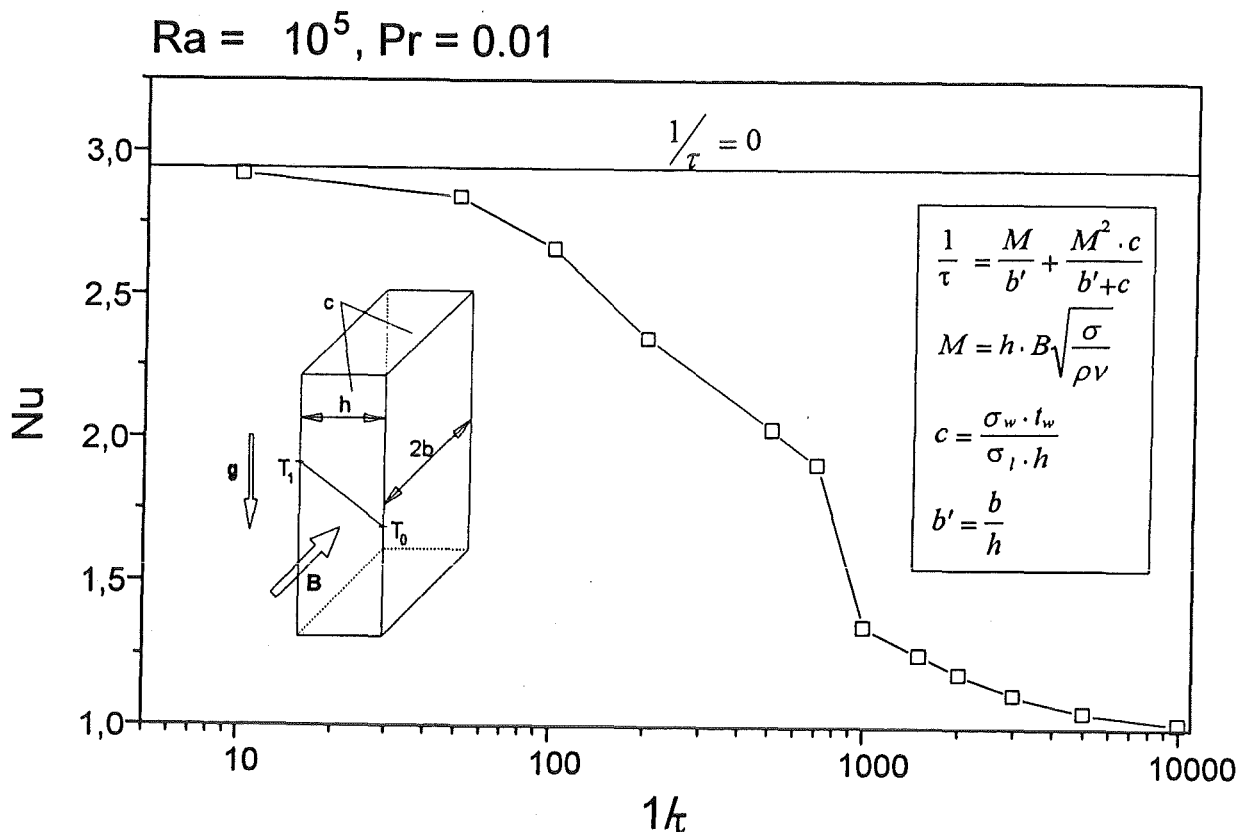


Fig. 3: Nusselt-number as a function of the damping parameter τ

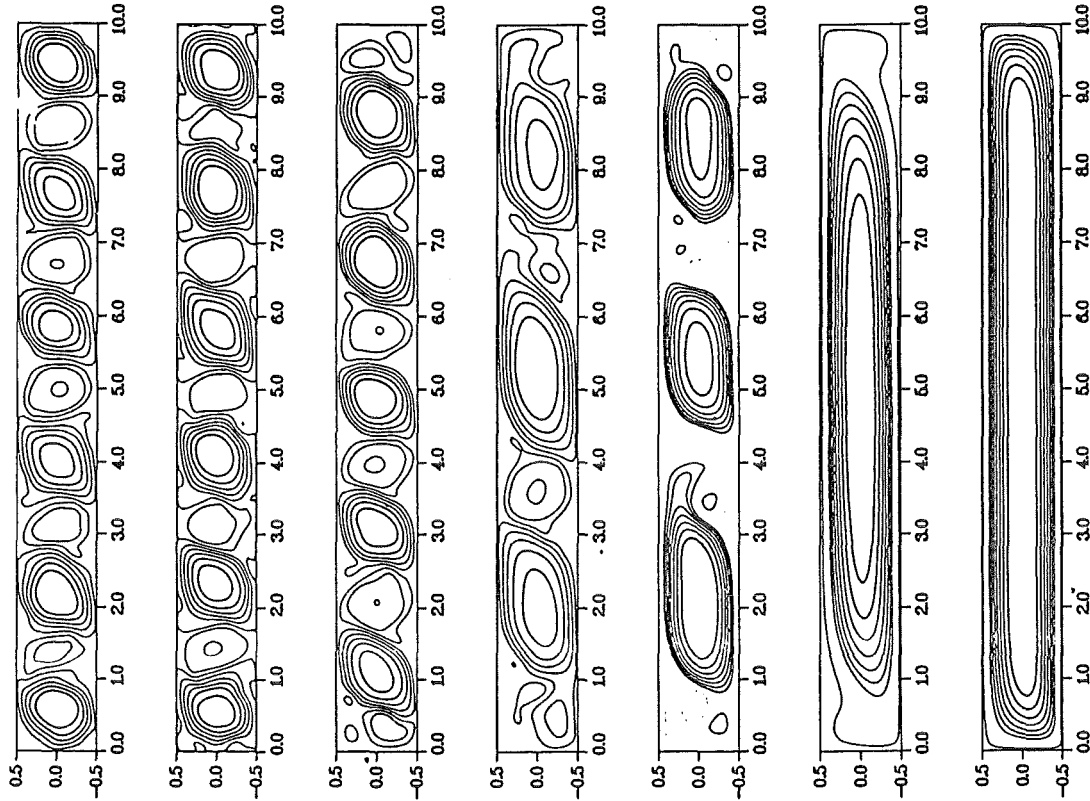


Fig. 4: Convective Flow patterns for different τ -Regimes

vortices are not damped by B and persist quite long downstream. The experiments demonstrated that the onset of turbulence and the 2D-turbulent flow is not accompanied by additional pressure losses.

- The improved heat transfer shows a lateral distribution. For reactor typical Re numbers the heat transfer improvement in the midplane expressed by the Nusselt number Nu is 3 times larger than in laminar flow.

In a second experimental campaign the additional improvement of the heat transfer characteristics has been investigated by means of inserting electromagnetic obstacles (Turbulence Promotions (TP)) on the ducts surface.

- The insertion of electromagnetic obstacles leads to a further improvement of the heat transfer, which is significantly higher than the additional pressure drop caused by the promoters. The additional pressure drop due to the turbulence promoters is about 30 %. Here, also the laminar-turbulent transition is not expressed by an increase of the dimensionless pressure drop.

The Fig. 5 shows how the velocity distribution can be controlled by means of turbulence promoters in order to enhance the heat transfer from the wall. The resulting dimensionless temperature distribution for the controlled flow (TP) compared to the uncontrolled is shown in Fig. 6.

Literature:

- [1] R. Stieglitz, L. Barleon, L. Bühler and S. Molokov: Magneto-hydrodynamic flow in a right-angle bend in a strong magnetic field, Journ. Fluid Mech., Vol. 326, 10 Nov. 1996
- [2] L. Barleon, K. J. Mack, R. Stieglitz: The MEKKA-facility a Flexible Tool to Investigate MHD-flow Phenomena, FZKA 5821
- [3] L. Barleon, K. J. Mack, R. Kirchner and R. Stieglitz: Heat Transfer in MHD-Flow at High Hartmann Numbers and Improvement by Turbulence Promotion, Magneto-hydrodynamics, Vol. 31, No. 3, (1995)

Staff:

- L. Barleon
- L. Bühler
- U. Burr
- W. Hartmann
- K. J. Mack
- (R. Stieglitz)
- R. Vollmer

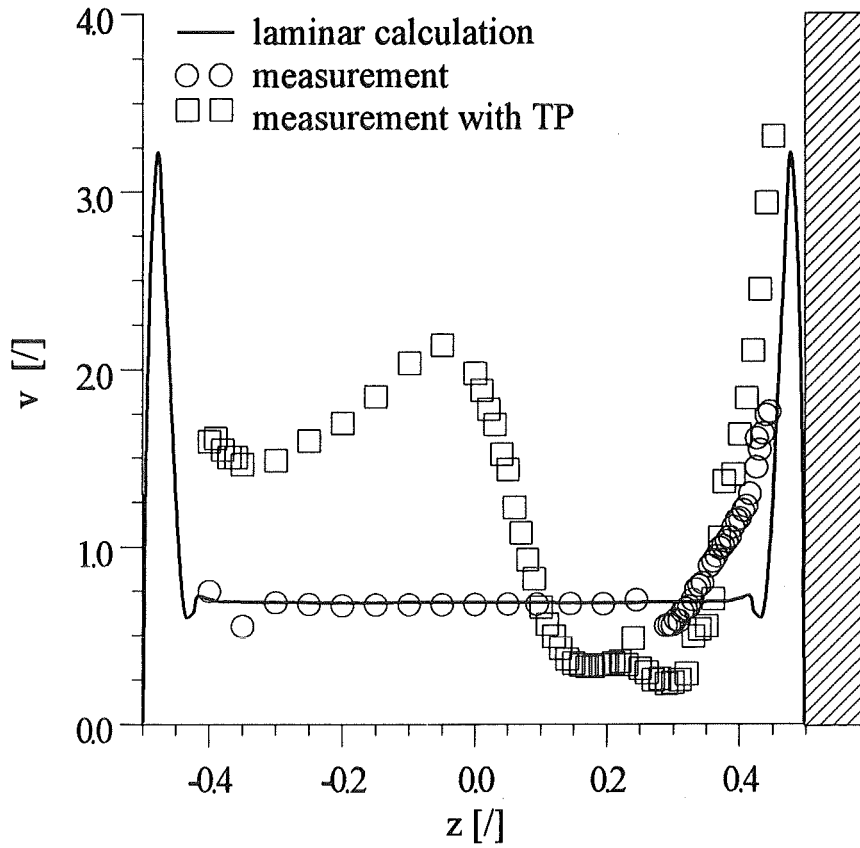


Fig. 5: Velocity distribution in the midplane of the duct for $M=4970$, $Pe=980$ and $Re=38\,000$

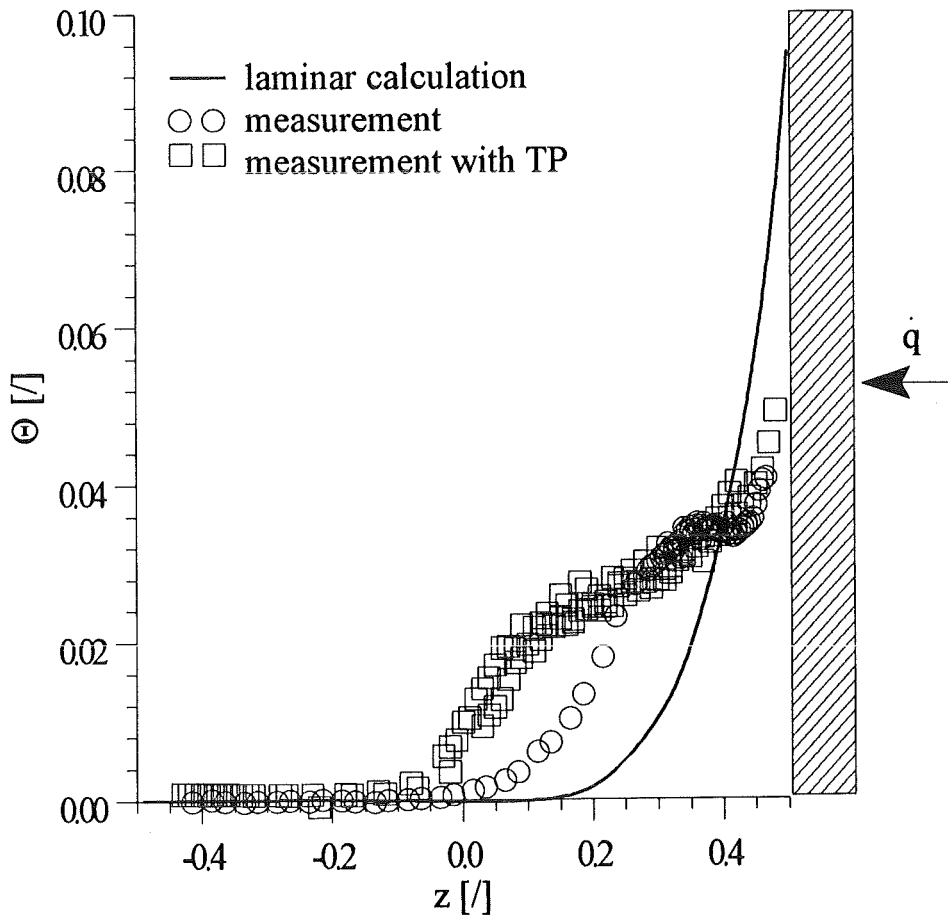


Fig. 6: Dimensionless temperature distribution for the same parameters as in Fig. 5

WP A 5 Tritium Control including Permeation Barriers

A 5.1.1 Coating and Tritium Barrier Development

In the water-cooled lithium-lead blanket concept, Pb-17Li serves only as a breeder and a neutron multiplier. A low flow rate of the Pb-17Li and a low tritium solubility result in a significant tritium partial pressure in the liquid metal. The tritium permeation from the melt through the structural material MANET into the cooling water has to be strictly minimised for safety and economic reasons. Therefore, the necessity of a tritium permeation barrier is fundamental for this blanket concept. One possible technique of reducing the diffusion rate of tritium is the coating of MANET with a material with a low tritium permeation rate. The positive influence of aluminide and/or alumina coatings on the permeation rate is well established [1-2]. Hence, the development of Al-based coatings on MANET seems to be very promising for the reduction of the tritium permeation rate.

The hot dip aluminising is an encouraging technique for the formation of aluminide coatings on MANET [3]. In FZK, a new pilot facility was developed for the coating of samples with a length up to 250 mm. The samples can be pre-heated prior to aluminising in a reducing Ar-5% H₂ atmosphere.

The steel sheets were pre-heated above the Al melt at 760 °C for 5 min and then hot dipped for immersion times between 5 and 900 s. Following aluminising, the specimens were cooled down slowly to room temperature under Ar-5% H₂.

After hot dipping, all specimens were uniformly covered with Al. Only the 5 s and 10 s-samples showed some small unwetted spots. After aluminising, solidified Al remained on the MANET surface. The metallographic cross sections showed, that the scale on the aluminised steel consisted of two different layers. Fig. 1 shows a cross section of a sample

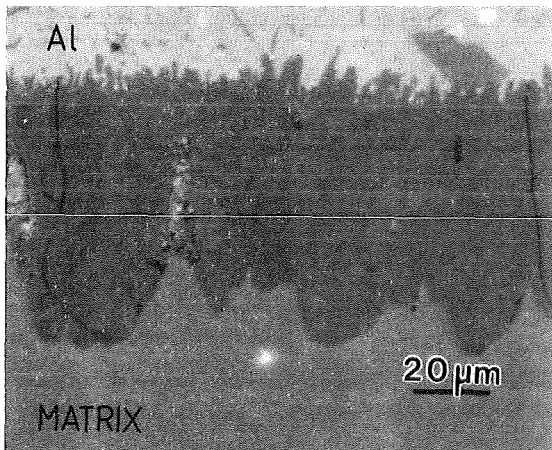


Fig. 1: Cross section of specimen, hot dipped in Al at 750 °C for 120 s

hot dipped for 120 s. By EDX analysis it could be shown, that the main part of the scale, which was adjacent to the MANET matrix, corresponded to the (Fe,Cr)₂Al₅ phase. Point analysis of the outer area revealed a phase with a composition similar to (Fe,Cr)Al₃.

The scale growth rate law has been determined from a graph of scale thickness versus immersion time (Fig. 2). Assuming the rate follows a function

$$s^n = kt,$$

where S is the scale thickness, k the reaction constant, t the dipping time and n the rate law exponent, a value of 2.75 for n could be calculated. This was an indication that a subparabolic rate was valid.

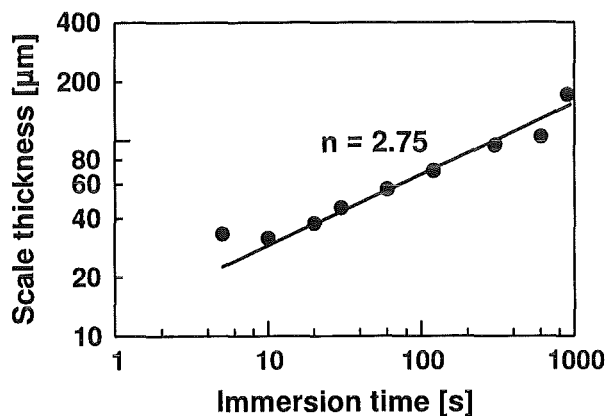


Fig. 2: Scale thickness versus immersion time for specimens, hot dipped in Al at 750 °C

To determine the growth direction of the intermetallic phases on MANET in an initially pure Al melt, a method described in [4] was used. For each specimen the thicknesses before hot dipping (d_0) and after immersion including (d_1) respectively excluding (d_2) the formed intermetallic phases, were measured. By using the equations $(d_1 - d_0)/2$ and $(d_0 - d_2)/2$ it could be shown that the scales grew into the steel by inward diffusion of Al. The total thickness (steel plus intermetallic phase) has slightly decreased after aluminising.

Vickers microhardness (HV 0.05) of the intermetallic phases and the steel matrix was measured. The hardness of the MANET (250 - 280 HV 0.05) remained unchanged after hot dipping, compared to the final heat treatment. The microhardness obtained for the (Fe,Cr)₂Al₅ phase was between 1000 and 1200 HV 0.05. Due to the small thickness of the (Fe,Cr)Al₃ phase, no hardness measurements were possible.

A comparison of microstructures and formation of intermetallic phases on MANET, F82-H and an unalloyed steel revealed, that the thickness of the (Fe,Cr)₂Al₅ phase depended on the Cr content and was lower for F82-H than for MANET. X-ray analysis showed that the transformation of (Fe,Cr)₂Al₅ phase into FeAl-solid solution seemed to be

slightly preferred for F82-H, because of thinner intermetallic scale thickness. The homogeneity of the scales was strongly influenced by the post-heat treatment. F82-H steel showed a reduced porosity in near surface regions, compared to MANET.

Literature:

- [1] H. Glasbrenner, A. Perujo, E. Serra, Fusion Techn. 28 (1995) 1159
- [2] A. Perujo, T. Sample, E. Serra, H. Kolbe, Fusion Techn. 28 (1995) 1256
- [3] H. Glasbrenner, H.U. Borgstedt, J. Nucl. Mat. 212-215 (1994) 1561
- [4] G. Eggeler, W. Auer, H. Kaesche, Z. Metallk. 77 (1986) 239

Staff:

H. Glasbrenner

M. Green (bis 31.08)

J. Kony

K. Stein (ab 05.02)

Z. Voß

O. Wedemeyer

Neutron Irradiations of Insulating Al₂O₃ Coatings

To investigate the so-called Radiation Induced Electrical Degradation (RIED) effect as a function of the n-dose, performance of a n-irradiation test using polycrystalline Al₂O₃ at HFR-Petten was proposed. After performance and evaluation of the preceding gamma irradiation tests, which were reported last year, the design of the n-irradiation capsules and the irradiation rig was completed. Two irradiation capsules have been manufactured and electrically examined [5].

Fig. 3 shows the principal experimental setup for the measurement of the electrical resistances between the lead wires of the triaxial cables and the electrodes of the irradiation probe. All measurements were done as current-voltage-measurements, the voltage was permanently 40 V. By changing the connections between the I-, U- and common-wires on the one hand and between the wires of the triaxial cables on the other hand and by omitting parts of the common connections or not it was possible to measure all interesting resistances. Resistances were measured as a function of the capsule temperature between room temperature and 600 °C.

With two exceptions the measured resistances were at room temperature higher than 100 MΩ. As expected at capsules temperatures higher than 400 °C all measured resistances were lower than at room temperature. Between 400 °C and

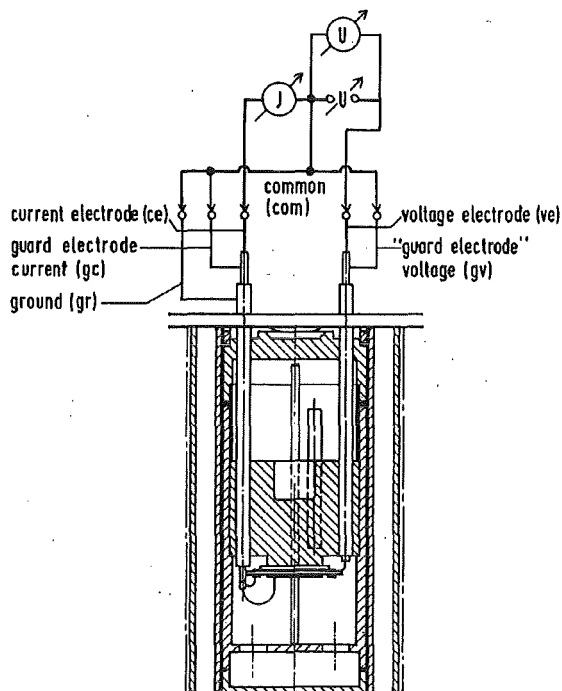


Fig. 1: Experimental setup for the measurement of cables and probe electrodes electrical resistances

500 °C the most interesting combinations had resistances higher than 10 GΩ. These values have to be compared with the equivalent values caused by gas ionisation (0,83 MΩ) and by radiation induced conductivity (RIC, 2,5 MΩ). The result is, that the accuracy and sensitivity of measurement is determined by RIC and gas ionisation. The maximum admissible RIED effect causes a reduction of the resistance to 250 Ω. This is orders of magnitude below the resistances caused by the other effects. This comparison shows that blanket relevant changes of the electrical resistance due to the RIED effect can reliably be detected in the HFR experiment.

As a result of the blanket selecting exercise it was decided to stop all works concerning the dual coolant blanket concept. Therefore the n-irradiation will not be performed.

Literature:

- [5] G. Schmitz: "Konstruktion und Bau einer Kapsel zum Bestrahlen von Keramiken mit schnellen Neutronen bei gleichzeitig anliegenden elektrischen Feldern"; FZK Int. Br. IRS-Nr. 10/96, to be published

Staff:

K. Schleisiek

G. Schmitz

A 5.3.2 Influence of the Magnetic Field on the Self-healing of Tritium Permeation Barriers in Flowing Pb-17Li

The self-healing of coatings for tritium impediment between Pb-17Li and the structural material is an important issue for the WCLL. The magnetic field might influence significantly the diffusion of oxygen due to the specific MHD features (laminarized MHD flow, velocity distribution). Furthermore, a significant influence of electrochemical mechanisms might exist due to the electric potential gradients and very high local electric currents.

Tritium permeation experiments in a set-up with liquid metal circulation and a high magnetic field would be very costly. A much simpler experiment is proposed which uses the similarity of the self-healing mechanisms of defected Al_2O_3 coatings needed for tritium permeation reduction and that for the reduction of electric currents entering the structural material. Although the quantitative extrapolation of the results to tritium permeation conditions is difficult, it is believed that the experiments are a valuable step to improve our understanding of fundamental MHD effects on tritium permeation.

Two different types of containers are used:

Pump electrode = aluminized probe: Here, the container (inner diameter 55 mm, height 100 mm) contains a cylindrical outer electrode made of an inoxidizable metal (V, Nb) and the inner cylindrical electrode consisting of a MANET cylinder aluminized at the surface. The electrodes are connected to a power supply which keeps the electric current constant. The radial electric currents within the liquid metal result in a circumferential velocity.

The diffusion of oxygen atoms from the Pb-17Li bulk to the Al-rich surface of the MANET gives rise to the formation of an oxide layer which causes an additional electric resistance which is directly measured. At the end of the experiments the probe surface will be analyzed in order to correlate the time dependent electrical resistance with the kinetics of the oxide layer formation.

Separate probes: Here, an Al_2O_3 container with an annular flow duct is used where inoxidizable pump electrodes provide the volume flow and the self-healing effect is investigated with separate probes.

This system is specially suited for investigating the healing of defects in Al_2O_3 coatings on MANET probes.

Characteristic probes consist of metal sheets covered with an Al_2O_3 layer, each of them provided with a defined line defect in the vertical direction (simulating a crack in the Al_2O_3 layer).

Parallel to the experiments, theoretical investigations will be performed to describe the velocity and electric current distribution and to model the kinetics of self-healing.

Fig. 1 shows the experimental set-up for the first type of experiments. The components have been fabricated and are presently mounted. An important feature in these experiments with a liquid metal interface and a gas atmosphere above is the avoidance of a liquid metal film by condensation at the ceramic lid by appropriate heating. In first operational experiments this effect will be investigated.

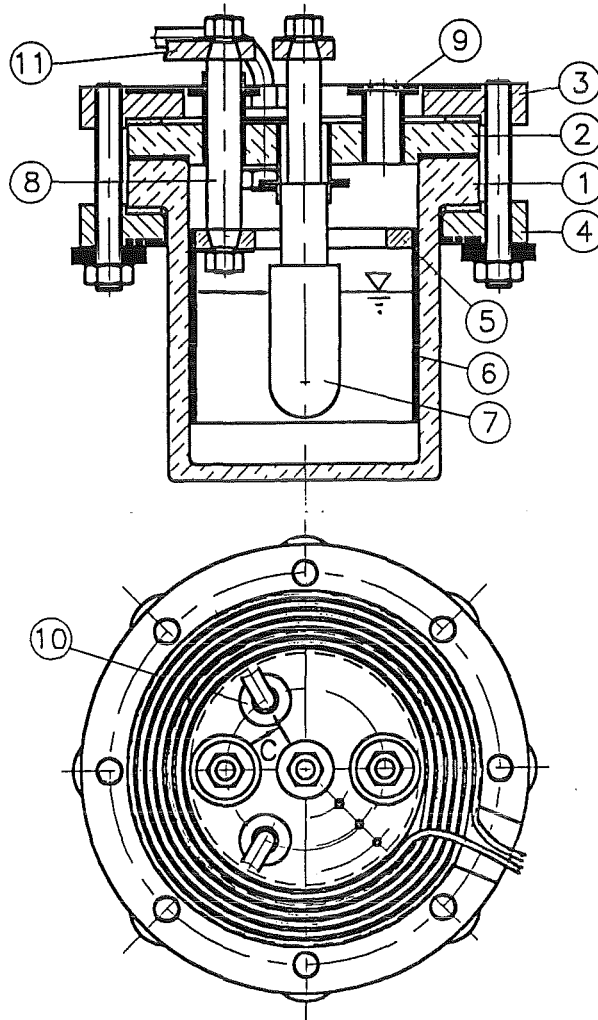


Fig. 1 Test section with $D_1 = 55$ mm: 1) Al_2O_3 pot; 2) Al_2O_3 lid; 3)+ 4) electrically heated flanges; 5), 6) + 8) outer electrode; 7) inner electrode; 9) + 10) connection to vacuum and gas system; 11) connection to power supply

Staff:

J. Reimann
E. Eggert

WP A 7 Safety related Activities for DEMO and ITER Test Module

A 7.1.1 Safety Studies for DEMO Blanket and ITER Test Module

The afterheat removal capability by natural convection of the pressurised water in the first wall (FW) cooling system after occurrence of a loss of flow accident (LOFA) was investigated [1, 2]. Seven cases under different boundary conditions were analysed. Special attention was directed towards the FW cooling channels located in the lower part of the blanket which have an unfavourable geometry with respect to natural convection. The calculations were performed with the thermal-hydraulic computer code RELAP5/MOD3.1.

The following conclusions have been drawn from the study. Generally, afterheat removal from the FW of the WCLL blanket concept by natural convection of the FW cooling water in case of a LOFA is assured by the present design. In particular, no stagnant steam plenum in the lower blanket part evolves during the LOFA. The natural convection flow in the main loop is accompanied by an internal circulation in the segment box channel system with flow reversal in the upper part. Attention has to be directed towards the transition region from normal to reverse flow, since the highest void fractions and structure temperatures occur in this blanket region during the LOFA. Even in the hypothetical case without plasma shutdown the natural circulation flow is sufficient to provide for heat removal from the blanket to the heat sink, disregarding the thermo-mechanical implications connected with the elevated structural temperature level.

Literature:

- [1] K. Gabel, FZK internal report, April 1996.
- [2] K. Gabel, K. Kleefeldt: Analysis of loss of flow transients in the first wall cooling system of the water-cooled Pb-17Li blanket concept for the European DEMO fusion reactor, 19th Symposium on Fusion Technology, September 16-20, 1996, Lisbon, Portugal.

Staff:

K. Gabel
K. Kleefeldt

WP B 1 Design and Analysis

B 1.1.1 Design Optimization/Adaptation to Updated DEMO Conditions

As a result of the DEMO blanket selection exercise carried out in 1994/95 it was decided to continue the development of a Helium Cooled Pebble Bed (HCPB) breeder blanket as one of the two DEMO blanket concepts to be pursued in the frame of the European Blanket Development Programme. Reference concept of the HCPB blanket is the BOT solid breeder blanket concept developed at FZK.

Because of the priority of the development of the HCPB test module for ITER, the design of the HCPB-DEMO blanket was continued with reduced effort. Work was concentrated on the optimization of the design with the objective to reduce the stresses and to improve the fabricability. Several design concept were developed for the rear part of the blanket box where the primary stresses are maximum in the case of a coolant system leak inside the box. The possibility of replacing the massive coolant header with drilled helium channels by a welded box structure was studied. A choice between the different variants can only be made when stress calculations have been carried out.

Besides the design work, investigations of special effects and the development and qualification of tools was continued. A FE analysis of the deformation behaviour of Be spheres was carried out using the ABACUS code. The results were compared with tests carried out in the FZK Hot Cells where Be spheres of 2 mm diameter were compressed between two plates up to deformations of 100 μm or 5 %. The forces measured at the maximum deformation varied between 200 and 400 N. The reason for this scatter is the heterogeneous structure of the spheres. In the FE analysis an elastic-idealplastic model was used with a yield strength of 200 and 400 MPa, respectively. The results with the higher yield strength are well within the scatter band of the experimental data, whereas the results with the yield strength of 200 MPa represent the lower limit. The calculated force/deformation characteristics are independent on whether the Be spheres are pressed against each other or against a steel plate. Because of the low Poisson number of Be, the lateral expansion of the Be spheres is negligible.

Considering the high cyclic thermal fluxes and the high pressures inside the cooling channels of the First Wall it seemed necessary to investigate the possibility of thermal ratcheting in this structure. In the early phase of the blanket design, however, it is neither feasible nor appropriate to make detailed numerical analyses. Therefore a simplified method was developed, which will yield a first qualitative result. In this charge the wall between the cooling channels and the plasma is considered as a beam with both ends fixed. Now it is possible to reduce the whole problem to a one-dimensional case. A closed form solution is achieved, resulting in a Bree-like diagram, which makes it possible to predict the behaviour of the structure simply by assuming the thermal and mechanical loadings in each loading-cycle. The analytical

solution yields that under the assumed service conditions with the proposed loadings, geometry and material no thermal ratcheting will occur in the plasma facing wall. Finite-Element calculations show, that the assumptions of a perfectly plastic material and an one-dimensional state of stress yield conservative results with respect to the net displacements and to the number of cycles to achieve a shakedown state. However, only the local loadings - the pressure in the cooling channels and the heat flux in the plasma facing wall - are considered. Loads caused by events outside the normal service conditions, like plasma disruptions, have been neglected so far. These may cause larger plastic deformations than those, which occur during the normal service and have to be computed separately.

The main tool used for the thermo-hydraulic analysis of the blankets is the FE code FIDAP. Work has focused on refining the representation of blanket boundary conditions in the FE model. In particular, the periodicity in the poloidal heat flux that is inherent in the layer geometry of the breeding blanket has been implemented. Also, the linking of FW and BZ channels through temperature conditions has improved modelling.

In parallel to the qualification of FIDAP, the development of a second thermohydraulic code has been started which is based on the computer code MAGS developed for thermal analyses of superconducting magnets. Several blanket-relevant modules have been provided which allow the calculation of local heat transfer coefficients and pressure losses, and the treatment of complex flow schemes with separations, conjunctions, and parallel channels with alternating flow directions [1].

Fig. 1 shows the result of an application to a first wall cooled by two helium systems in two passes with four cooling channels each. The temperature distribution clearly reflects the alternating flow directions.

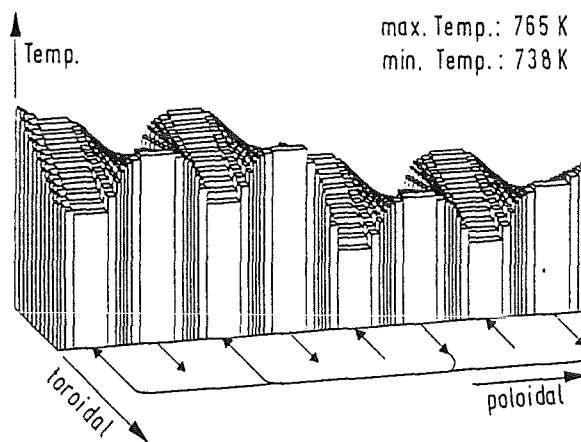


Fig. 1: Temperature distribution at the plasma-facing surface of a blanket box cooled by two independent helium systems

Literature:

- [1] I. Acalovschi: Entwicklung eines Computerprogramms für die thermohydraulische Analyse von Fusionsreaktor-Blankets. Forschungszentrum Karlsruhe, unpublished report 1996

Staff:

I. Acalovschi
St. Böhmer
M. Dalle Donne
H. Gerhardt
Th. Heider
St. Hermsmeyer
P. Norajitra
G. Reimann
K. Schleisiek

B 1.2.1 Design, Layout and Integration of ITER Test Module and Internal Circuits

General

The Helium-Cooled Pebble Bed (HCPB) Blanket is one of the two European DEMO blanket concepts proposed for testing in ITER. It uses a martensitic steel (present investigations: MANET II) as structural material. The testing includes the demonstration of a breeding capability that would lead to tritium self-sufficiency in a reactor and the extraction of high-grade heat suitable for electricity generation. To accomplish these goals, the ITER horizontal ports will be used to provide a relevant fusion plasma and the appropriate nuclear environment.

The purpose of the tests is to validate the design principles and the operational feasibility for the demonstration blanket system. This includes the basic support functions like tritium extraction, helium cooling and heat transport, and helium purification. In addition, the basic properties and operating characteristics of the system's materials will be validated. To assess these qualities and characteristics, the test blanket systems are to be exposed directly to the ITER plasma for relatively long, continuous operation periods. The European and the Japanese have collaborated in their approach for testing their helium-cooled solid breeder test modules. During the ITER Basic Performance Phase (BPP) the European HCPB Blanket Test Module (BTM) shall occupy half of the test port allocated to the helium-cooled blankets, the other half being occupied by the Japanese helium-cooled ceramic breeder blanket module. The tritium subsystems for the two BTMs will be separate and placed in the pit immediately adjacent to the test port. The helium coolant loops (heat transfer, heat transport and helium purification) will also be separate and will be placed outside the pit, probably in the tritium building. To facilitate handling operations, the two BTM's together with their shield shall be bolted to a water cooled frame.

Design of the Test Module

The arrangement of the Blanket Test Modules inside the horizontal port of ITER is shown in Fig.1. The BTMs are provided with a mating flange mounting system (support frame and shield) around the perimeter to transmit the internal loads to the ITER shielding system. The support frame is bolted to the ITER back plate; the shield with the BTMs attached to it is bolted to the support frame. The lower position inside the frame is occupied by the European HCPB-BTM, while the upper position is reserved for the Japanese helium-cooled BTM (not present in the figure).

Both support frame and shield are massive steel structures cooled by water at a temperature of about 150°C. They must contribute to the fulfilment of ITER requirements (neutron shielding, electrical resistance, temperature differences, etc.) when integrated into the system.

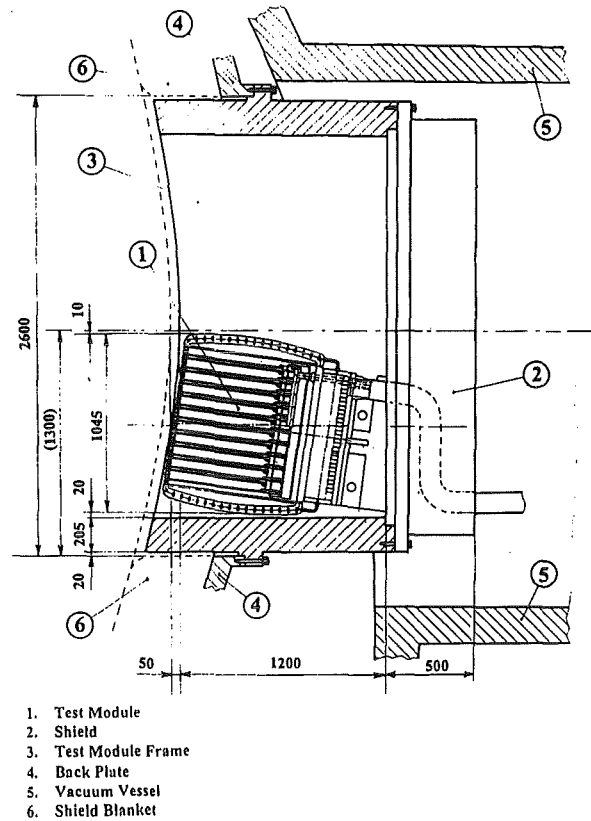


Fig. 1: Arrangement of HCPB Blanket Test Module in a horizontal ITER test port (dimensions in mm)

The ITER port dimensions and the presence of the 205mm-thick support frame determine the physical size of the BTMs. Assuming a gap of 20 mm between the frame and the BTMs it yields a maximum BTM size of 1045 high and 1010 mm wide.

The HCPB-BTM for ITER exhibits the same basic design features as the European HCPB DEMO blanket, which is based on the use of separate ceramic breeder and beryllium pebble beds placed between radial toroidal cooling plates. It represents a poloidal portion of the HCPB DEMO blanket (see Fig. 2). As in the DEMO the radial toroidal plates and the first wall are cooled by helium at 8 MPa flowing first in the first wall and then in the cooling plates. For safety reasons the helium flows in two completely separated loops. The coolant is flowing alternately in opposite directions in the first wall and in the adjacent cooling plates. In this way the BTM temperature distribution is more uniform. In the reference module (BTM-I) design there are alternately 11 mm thick ceramic breeder pebble layers and 45 mm thick beryllium pebble layers between the cooling plates. The tritium purge gas is helium at about 0.1 MPa flowing in radial direction from the first wall to the back of the module. The plasma side of the first wall is protected by a 5 mm beryllium layer and recessed from the shield blanket contour by a minimum of 50 mm. At the upper and lower ends the BTM is closed by covers capable to sustain a pressure of 8 MPa. During normal operation the space in the BTM (other than in the cooling plates and in the FW) is at the purge gas pressure of 0.1 MPa.

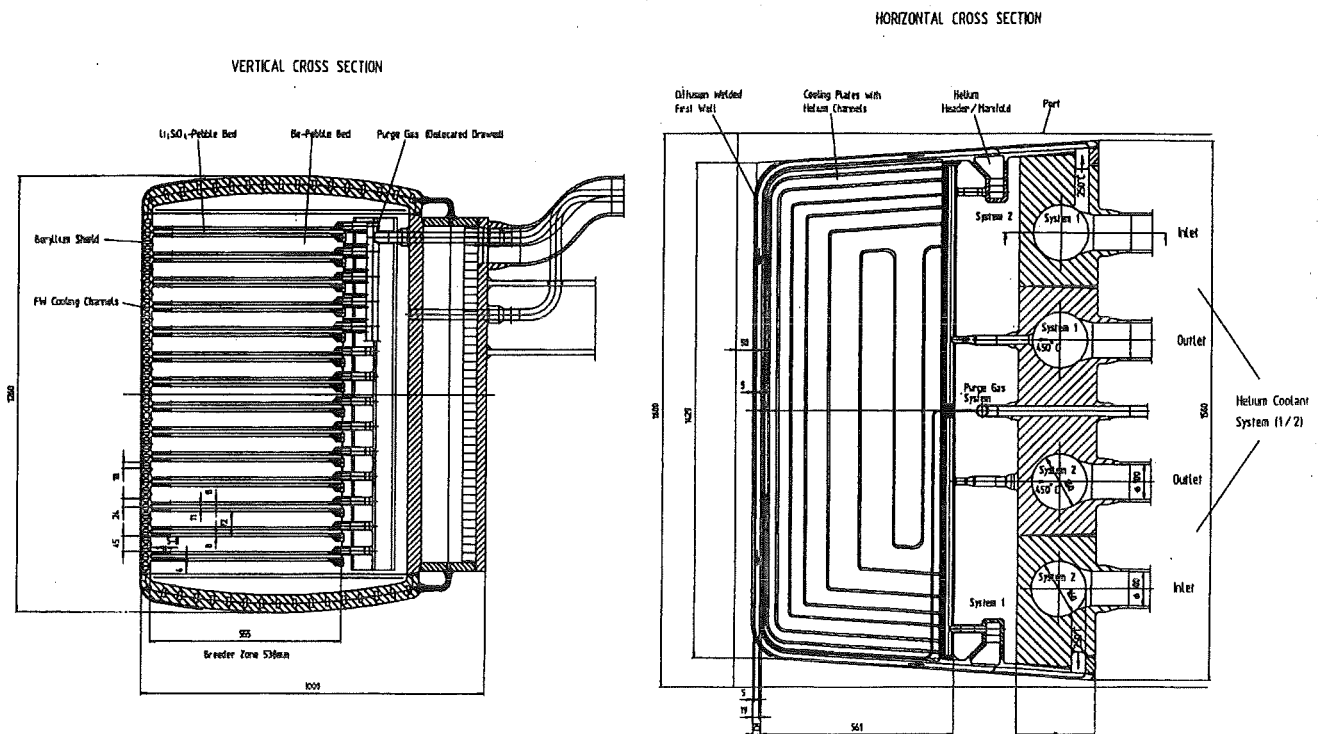


Fig. 2: Vertical and horizontal cross sections of the HCPB blanket module to be tested in ITER (preliminary)

However, in case of a leak from a cooling plate, it can be pressurized up to 8 MPa. Thus the blanket box, and the helium purge system have been designed to sustain the full pressure of 8 MPa. This is a double barrier against helium leakage from the cooling plates and would allow, in case of need, to wait for the next planned period for the exchange and repair of the module.

The second version of the test module with a modified flow scheme in the FW and an increased thickness of the ceramic pebble bed (BTM-II) allows a significant increase of the helium outlet temperature and of the maximum ceramic bed temperature at about the same FW temperature. BTM-II will be tested in ITER after the BTM-I during BPP. Calculations have also been performed for a third test module (BTM-III) to be tested during the EPP. These calculations have been performed to size the ancillary loops for the HCPB-BTM, so that the same ancillary loops could be used during the EPP period as well.

Neutronic Analysis

The nuclear design analysis for the HCPB blanket test module has been performed on the basis of a 9° ITER torus sector model equipped with a horizontal outboard blanket port containing the water-cooled steel support frame and two test modules of the HCPB-type (Fig. 3). Three-dimensional Monte Carlo transport calculations were performed with the MCNP-code and nuclear cross-sections from the FENDL-1 data library to obtain the nuclear heating and the tritium production in the lower test blanket module and to assess its shielding

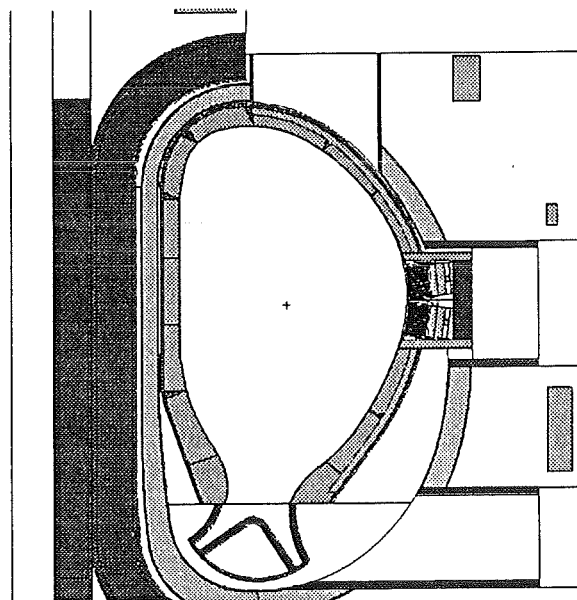


Fig. 3: Vertical cross-section of the MCNP torus-sector model

performance with regard to the radiation loads on the TF-coil and the vacuum vessel adjacent to the test blanket port.

There is a strong albedo effect of the ITER shielding (BTM-I, -II during BPP) and breeding blankets (BTM-III during EPP) on the nuclear performance of the HCPB test blanket modules. The local tritium breeding ratios are 0.99, 1.01, and 1.19 for BTM-I, -II and BTM-III, respectively. The total nuclear power

production in the HCPB test blanket module amounts to 1.52 MW for both BTM-I and -II, and 1.84 MW for BTM-III corresponding to energy multiplication factors of 1.24 for the BPP and 1.50 for the EPP. The power generated in the steel frame is 2.2 MW for the BPP and 3.2 MW for the EPP.

The shielding efficiency was assessed by calculating the radiation loads to the vacuum vessel and the TF-coil adjacent to the test blanket port. The required radiation limits can be safely met assuming 3 FPY operation at a fusion power of 1500 MW. This is mainly the result of optimising the test blanket module and the steel frame configuration in the blanket port for a maximum shielding efficiency by reducing void gaps and designing the steel frame as efficient radiation shield. The accumulated helium production in the SS-316 front plate of the vacuum vessel amounts to about 0.39 appm which satisfies the joint reweldability criterion within a safety factor 2.

Thermal-Mechanical Analysis

Table 1 shows the results of the 2D steady-state temperature calculations performed with the FE computer code ABAQUS in comparison with corresponding DEMO values [1]. In case of the module BTM-I, with DEMO blanket geometry, the maximum FW temperature approaches that of the DEMO blanket. However, the temperatures in the breeding zone are considerably lower than in DEMO. This is due to the fact that the neutron load, and thus the power densities, are smaller than in the DEMO, while the maximum heat flux on the first wall is the same. The BTM-II is proposed to obtain higher, and thus more DEMO relevant, temperatures in the breeding zone. In this case, however, the flow scheme is slightly different from that in the DEMO. Namely the coolant helium flows in series through two FW coolant channels before entering the blanket region, rather than in one pass as in the DEMO blanket. Furthermore the thickness of the ceramic pebble layers has been increased from 11 to 14 mm.

Two and three-dimensional stress calculations have also been performed with the FE computer code ABAQUS. The results of the two-dimensional stress calculation for the first-wall region are shown in Table 2 (BTM -I and II) and Table 3 (BTM-III). The admissible stresses according to ASME and RCC-MC are likewise included. The comparison of the results in both tables shows that all calculated stresses are below the admissible limits.

In the 3D ABAQUS calculations a full radial/toroidal section of the BTM with a poloidal height of 48 mm including two FW channels and two cooling plates was investigated. In a preliminary analysis rather high stresses were obtained for the side wall of the box between the breeder zone and the helium manifold in the case of full helium pressure in the whole blanket box. For this reason two radial/poloidal stiffening ribs were introduced which connect the manifold with the cooling plates. With this modification the stress in the side wall of the box is reduced to 210 MPa. The stress in the stiffening ribs amounts to 233 MPa. Both values are below

the admissible stress which is - because of the lower local temperatures - above 300 MPa.

Stress analysis of the plasma facing beryllium coating shows that use of solid beryllium coating would result in the failure of the coating due to fatigue. Thermal stresses can be significantly reduced by cutting a square mesh of slots in the beryllium layer (castellation), thus avoiding beryllium failure.

Additionally, three-dimensional thermal calculations have been carried out with the FE code FIDAP to determine the temperature distribution in the BTM-I during operational transients. In these calculations a section of the blanket box with three FW cooling channels and the neighbouring breeding zone with two cooling plates and two cooling channels each was analysed. The length of the model corresponds to the length of the FW cooling channels, i.e. the FW and the side walls of the box. The alternating flow directions of the two helium systems were taken into account. The input data correspond to the steady-state temperature calculations, with the exception that for the surface heat flux a value of 0.5 MW/m² was assumed for the whole plasma-facing surface of the box. Two cases were considered with a constant helium inlet temperature of 250 °C:

- a) The cyclic operation of ITER with the following power history (for surface heat flux and internal heat sources): Linear power ramp-up within 50 s; full power burn time 1000 s; linear power ramp-down within 100 s; pulse repetition time 2200 s.
- b) An instantaneous power excursion (surface flux and internal heat sources) to 120 % of nominal with a duration of 10 s.

The results of the FIDAP calculations can be summarized as follows:

- The specified power cycling times are sufficient to reach steady state conditions: e.g. 110 s after establishing full power, the breeder material has reached 590 °C, that is 90 % of the temperature rise under steady-state conditions (see Fig. 4).
- The time constant of the plasma-facing side of the box is much shorter: The 90% temperature rise is attained 25 s after reaching the full power level.
- The maximum temperature ramp rate of the breeder material is 4.5 K/s during ramp-up, and 3.0 K/s during ramp-down.

Electromagnetic Analysis

The mechanical design of the test blanket subsystem components (blanket test modules, support frame and shield) is strongly influenced by the magnitude of electromagnetic loads due to plasma disruptions. As these components are

Table 1: Results of the thermal-hydraulic calculations for the three BTMs*

	BPP		EPP	DEMO
	BTM-I	BTM-II	BTM-III	Blanket
Li ⁶ -enrichment	75 %	75 %	75 %	25 %
Total Power [MW]	1.9	1.9	2.3	2500
Total helium mass flow [kg/sec]	3.7	2.1	3.7	2400
Helium pressure [MPa]	8	8	8	8
Helium pressure drop in BTM [MPa]	0.19	0.22	0.19	0.24
Helium inlet/outlet temp. [°C]	250/350	250/420	250/370	250/450
Max. power density [MW/m ³] in				
structural material	10	10	15	25
beryllium pebble bed	5	5	5	15
ceramic pebble bed	19	19	30	37
Maximum temperatures [°C]				
structural material	507	506	522	520
beryllium pebble bed	410	464	423	637
ceramic pebble bed	622	777	779	907

* based on preliminary nuclear calculations

Table 2: Results of the first-wall stress calculation for BTM-I and BTM-II (Basic Performance Phase)

- a) Maximum von Mises primary stresses [MPa]: occurs at the corners of the plasma side of the FW cooling channels (T = 400 °C):

	p = 8 MPa	1.2 p = 9.6 MPa	Admissible limit by ASME (Class 1) and RCC-MC (Class A) for 1000 hours*
Normal operation (pressure only in cooling channels)	56	67	300
Leakage from cooling plates (pressure in the whole blanket box)	131	157	300

- b) Maximum von Mises primary plus secondary stresses [MPa]: occurs at the FW interface between FW and plasma facing beryllium layer (T = 507 °C):

	p = 8 MPa	1.2 p = 9.6 MPa	Admissible limit by ASME (Class 1) and RCC-MC (Class A) for 1000 hours*
Normal operation (pressure only in cooling channels)	360	363	463
Leakage from cooling plates (pressure in the whole blanket box)	407	421	463

* During the Basic Performance Phase the operation of one BTM will be less than 1000 full power hours.

Table 3: Results of the first-wall stress calculation for BTM-III (Extended Performance Phase)

a) Maximum von Mises primary stresses [MPa]: occurs at the corners of the plasma side of the FW cooling channels (T = 413 °C):

	p = 8 MPa	1.2 p = 9.6 MPa	Admissible limit by ASME (Class 1) and RCC-MC (Class A)
Normal operation (pressure only in cooling channels)	56	67	290* for 3600 hours
Leakage from cooling plates (pressure in the whole blanket box)	131	157	292* for 1000 hours

b) Maximum von Mises primary plus secondary stresses [MPa]: occurs at the FW interface between FW and plasma facing beryllium layer (T = 522 °C):

	p = 8 MPa	1.2 p = 9.6 MPa	Admissible limit by ASME (Class 1) and RCC-MC (Class A)
Normal operation (pressure only in cooling channels)	365	368	403* for 3600 hours
Leakage from cooling plates (pressure in the whole blanket box)	410	424	427* for 1000 hours

* If operation foreseen for the whole EPP (3 MWa/m² ≈ 20000 h), the first wall should operate at a lower temperature (higher helium cooling mass flow)

** Within 1000 full power hours operation is very likely possible to change the leaking module during a planned plasma shut-down.

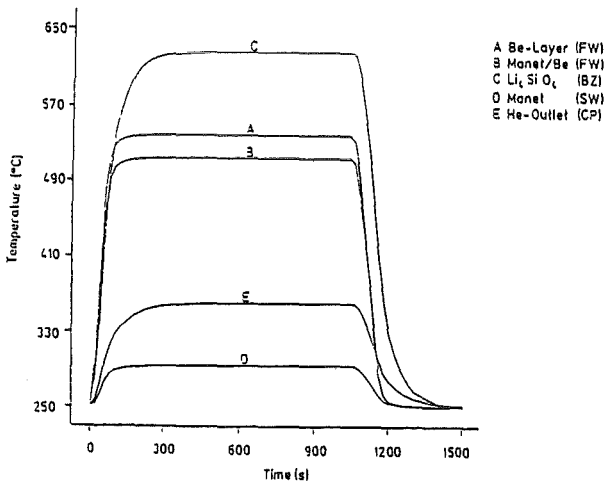


Fig. 4: Blanket temperatures during cycling operation (normal operation)

supported by the ITER back plate, their electromagnetic loads affect also the design of this ITER component.

A preliminary electromagnetic analysis for a centered disruption has already been performed (see also section B 1.3.1-2). The resultant forces and torques acting on the BTM at end of disruption (t=10 ms) are summarized in Table 4. The values are given for the HCPB-BTM, the Japanese BTM

(placed in the upper position inside the support frame) and for the total subsystem. The resultant torques are calculated at the geometric center of the corresponding component. The total torque is calculated at the back plate location.

Helium Cooling Subsystem

The cooling subsystem (see Fig. 5) includes the primary helium heat removal loops with all components, and the pressure control subsystem. The secondary water loop subsystem with the ultimate heat sink is part of the ITER cooling system providing water flow at low temperature. A further interface to the cooling subsystem are the connections to the helium purification subsystem, taking a bypass flow of about 0.1 % of the main mass flow rate. Two separate primary heat removal loops of 2 x 50 % heat capacity are foreseen for redundancy purposes in accordance with the DEMO blanket design. The cooling subsystem will be housed in the tritium building, next to the helium purification subsystem at a floor level about 20 m above the test module, requiring a space of about 700 m³.

The thermal-hydraulic design parameters are as follows: The maximum heat to be removed from the test module amounts to 2.3 MW. Nominal primary helium coolant conditions are 250 °C and 350 °C (later on 250 °C and 450 °C) at module inlet and outlet, respectively, and 8 MPa of pressure. The total flow rate in both primary helium loops is 3.7 kg/s. The secondary

cooling water has a temperature of 35/60 °C at the heat exchanger inlet/outlet, a pressure of 0.5 to 1.0 MPa, and a maximum mass flow rate of 22 kg/s.

Main components in each loop are the heat exchanger, circulator, electrical heater, dust filter, and pipework. The total helium mass inventory in one loop amounts to 22 kg and the overall pressure loss is about 0.27 MPa, most of which occurring in the test module proper. The heat exchanger is assumed to be a straight tube bundle heat exchanger, or alternatively consisting of U-tubes, with high pressure helium flowing inside the tubes. The design specification for the circulator is as follows: temperature 300 °C, pressure 9.6 MPa,

mass flow rate 1.9 kg/s at a pumping head of 0.28 MPa at 80 % of maximum speed and at 250 °C inlet temperature, speed variation max/min of at least 4. The heater with an electrical power of 100 kW which is installed in a bypass to the heat exchanger is needed for baking the test module first wall at 200 °C and for heating the whole cooling subsystem. A filter unit is installed in the hot leg of the main loop, accumulating residual dust and particles from fabrication, and erosion particles down to a size of typically 10⁻⁶ m. For the main pipework an outer diameter of 168.3 mm and a wall thickness of 10 mm have been chosen for the part external to the cryostat. Inside the cryostat smaller pipes are foreseen (114.3 mm outer diameter, 8 mm wall thickness) to limit the pipe

Table 4: Forces and torques resulting from electromagnetic analysis

	HCPB BTM	JA-BTM	Frame and Shield	Total
x-coordinate (*) [m]	11.768	11.768	12.291	11.658
y-coordinate (*) [m]	0.000	0.000	0.000	0.000
z-coordinate (*) [m]	0.823	1.887	1.355	1.355
Force x [MN]	-0.035	0.029	-1.975	-1.981
Force y [MN]	0.200	-0.085	0.229	0.344
Force z [MN]	0.693	-0.201	1.108	1.600
Torque x [MNm]	2.007	2.010	-0.243	3.927
Torque y [MNm]	-0.104	0.377	-0.409	-1.085
Torque z [MNm]	-0.961	1.164	-1.742	-1.869

(*) According to the torus Coordinate System

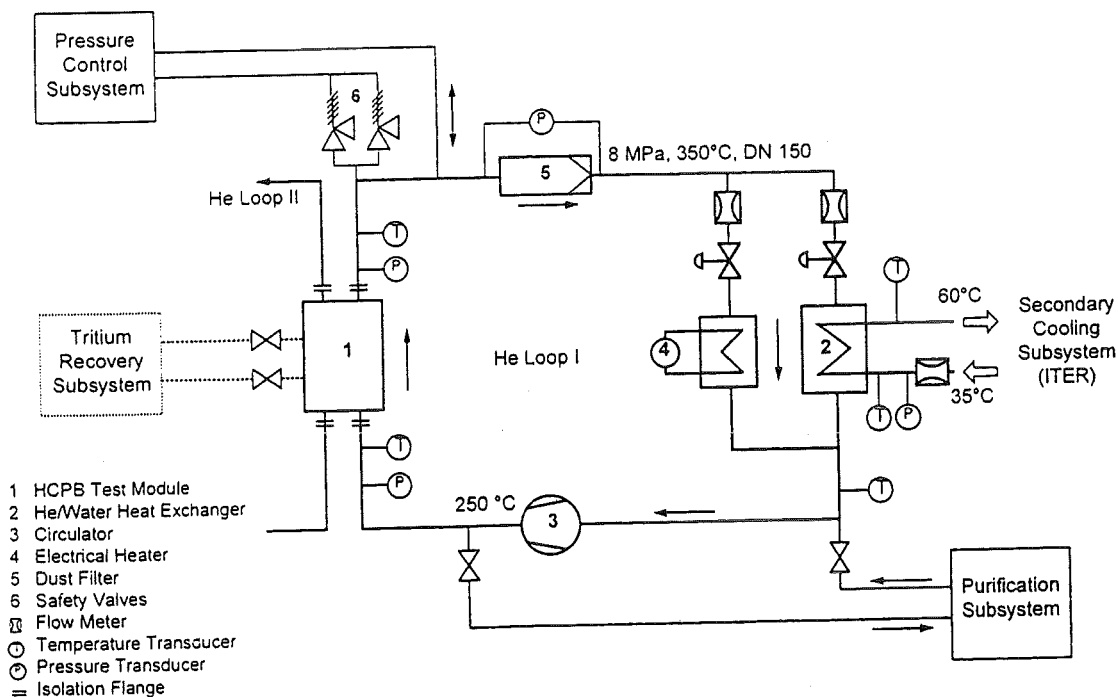


Fig. 5: Helium Cooling Subsystem Flow Diagram

penetrations to 130 mm. This results in flow velocities between 15 and 41 m/s.

The total pipe length sums up to 120 m per loop. The number of valves in the main loops has been kept at a minimum to avoid inadvertent closure which would mean loss of heat sink. All of the piping and components in the primary cooling subsystem will be constructed of austenitic steel.

The pressure control subsystem is needed for evacuation, helium supply, pressure control, and overpressure protection. The components are conventional and of relatively small size, except for the storage and dump tanks.

The following preliminary control scheme is proposed for pulsed operation where the principal objective is to keep the test module inlet temperature at 250 °C: The secondary cooling water inlet temperature is kept at 35 °C, the circulator is operated at rated speed, the electrical heaters are turned off, and flow partition through the heat exchanger and heater bypass is controlled as to maintain the inlet temperature close to 250 °C. During longer shutdown periods afterheat removal is achieved at reduced circulator speed, or by natural convection.

Other Work

The activities related to manufacturing, helium purification, tritium extraction, safety, and reliability are reported under Subtask Nos. B 1.4.1, B 2.1.1, B 6.1.1, and B 7.1.1.

Literature:

- [1] P. Norajitra, Thermohydraulics Design and Thermo-mechanics Analysis of Two European Breeder Blanket Concepts for DEMO, FZKA 5580 (1995)

Staff:

L. Boccaccini
M. Dalle Donne
U. Fischer
S. Gordeev
H. Gerhardt
St. Hermsmeyer
K. Kleefeldt
P. Norajitra
G. Reimann
R. Ruprecht
K. Schleisiek
I. Schmuck

B 1.3.1 Electromagnetic Effects with a Ferromagnetic Structural Material

1. Effect of the presence of ferromagnetic structural material on the DEMO Helium Cooled Pebble Bed Blanket during plasma disruptions (L.V. Boccaccini, P. Ruatto)

Martensitic steels, like MANET and F82H, have been proposed as structural material for the DEMO fusion reactor in view of their better swelling behaviour under high neutron irradiation. Such steels show a non-linear ferromagnetic behaviour so that distribution and magnitude of the magnetic flux are significantly modified outside and inside the plasma facing components. When a plasma disruption occurs, as eddy currents are induced in the conducting structures, electromagnetic forces rise which can be greater and differently distributed than those for the case with non-magnetic structural material.

In order to assess the capability of the structure to withstand the mechanical effects of a major plasma disruption a computer code - named AENEAS - that allows electromagnetic analyses in presence of non-linear ferromagnetic materials has been developed at the Karlsruhe Research Center (FZK). By means of AENEAS the electromagnetic behaviour of the DEMO Helium Cooled Pebble Bed (HCPB) Blanket [1] during a centered reference plasma disruption has been investigated and on the basis of the calculated electromagnetic load distribution a static and dynamic stress analysis have been performed.

In the following the basic formulation of AENEAS is described and the results of the calculations are discussed pointing up the importance of considering the ferromagnetic properties of the structural material.

1.1 Problem formulation

The transient eddy current problem for a conducting body Ω with a ferromagnetic subdomain Ω_M is described in AENEAS extending an integral formulation for non-magnetic materials [2] to take into account the contribution of magnetization density M to the magnetic vector potential A

$$\eta(\mathbf{r})\mathbf{J}(\mathbf{r},t) + \frac{\mu_0}{4\pi} \int_{\Omega} \frac{1}{|\mathbf{r}-\mathbf{r}'|} \frac{\partial \mathbf{J}(\mathbf{r}',t)}{\partial t} d\tau' = -\frac{\partial \mathbf{A}(\mathbf{r},t)}{\partial t} - \nabla\phi(\mathbf{r},t) - \frac{\mu_0}{4\pi} \int_{\Omega_M} \frac{\partial \mathbf{M}(\mathbf{r}',t)}{\partial t} \times \nabla' \frac{1}{|\mathbf{r}-\mathbf{r}'|} d\tau' \quad (1.1)$$

where η is the electrical resistivity tensor, \mathbf{J} current density, \mathbf{A}_e the magnetic vector potential of external fields, ϕ the scalar electric potential and the apices distinguish the source points from the field ones. Solenoidality conditions for \mathbf{J} are also considered.

As the new unknown M is introduced, the relation between M and magnetic field strength H in Ω_M is considered to solve the

problem:

$$\mathbf{M}(\mathbf{r},t) = \chi(|\mathbf{H}(\mathbf{r},t)|) \mathbf{H}(\mathbf{r},t) \quad (2.2)$$

where H is calculated by the Biot-Savart law and the scalar magnetic susceptibility χ is a function of the module of H .

An iterative procedure is applied to the finite element approximation of (1.1) and (1.2) to determine the time evolution of \mathbf{J} and \mathbf{M} . In particular, \mathbf{J} is approximated by using edge elements, while zero-order elements are used for \mathbf{M} : it means, \mathbf{M} is taken uniform in the interior of an element and zero outside.

The contributions of \mathbf{J} and \mathbf{M} to force and torque acting on Ω can be computed by

$$\mathbf{F} = \int_{\Omega} \mathbf{J}(\mathbf{r},t) \times \mathbf{B}(\mathbf{r},t) d\tau \quad (2.3)$$

$$\mathbf{C} = \int_{\Omega} \mathbf{r} \times (\mathbf{J}(\mathbf{r},t) \times \mathbf{B}(\mathbf{r},t)) d\tau \quad (2.4)$$

$$\mathbf{F} = \int_{\Omega} (\nabla \times \mathbf{M}(\mathbf{r},t)) \times \mathbf{B}(\mathbf{r},t) d\tau + \int_{\partial\Omega} (\mathbf{M}(\mathbf{r},t) \times \mathbf{n}) \times \mathbf{B}(\mathbf{r},t) dS \quad (2.5)$$

$$\mathbf{C} = \int_{\Omega} \mathbf{r} \times [(\nabla \times \mathbf{M}(\mathbf{r},t)) \times \mathbf{B}(\mathbf{r},t)] d\tau + \int_{\partial\Omega} \mathbf{r} \times [(\mathbf{M}(\mathbf{r},t) \times \mathbf{n}) \times \mathbf{B}(\mathbf{r},t)] dS \quad (2.6)$$

where \mathbf{B} is the total magnetic flux density and the magnetic material is described in terms of volume and surface Amperian currents $\mathbf{J}_M = \nabla \times \mathbf{M}$ and $\mathbf{K}_M = \mathbf{M} \times \mathbf{n}$. Due to the assumption made for \mathbf{M} , only currents \mathbf{K} are present. Further details on the mathematical and numerical formulation of the code are in [3].

1.2 Electromagnetic analysis

The finite element model used for the calculation consists of a complete outboard blanket segment and vacuum vessel segment (Fig. 1.1). It includes 1084 8-node brick elements (972 of which belong to the ferromagnetic structure) giving 1239 degrees of freedom for \mathbf{J} and 2916 for \mathbf{M} . Magnetic interaction with the other 47 outboard segments is taken into account. Each blanket segment is considered electrically insulated from the other segments and components of the reactor. The electrical resistivity of the different parts of the model has been calculated considering temperature distribution and possible anisotropy due to the presence of cooling channels in the structure. The effect of the saddle loop is considered too. The vacuum vessel - with non-

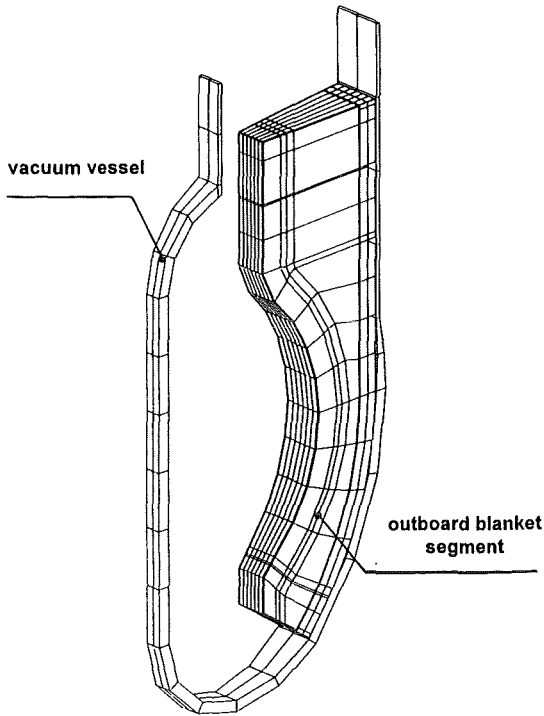


Fig. 1.1: Finite element model of the DEMO reactor

magnetic SS 316 as structural material - has a resistance of $20 \mu\Omega$.

The plasma model consists of a filamentary conductor; a current of 19.8 MA decreases linearly to zero in 20 ms. The external toroidal magnetic field is considered to vary inversely to the torus radius with a value of 6 Tesla at a radius of 6.3 m. A poloidal magnetic field configuration of equilibrium has been also included in the calculation. The ferromagnetic properties of MANET are taken into account by a magnetization curve [4] as shown in Fig. 1.2. MANET is fully

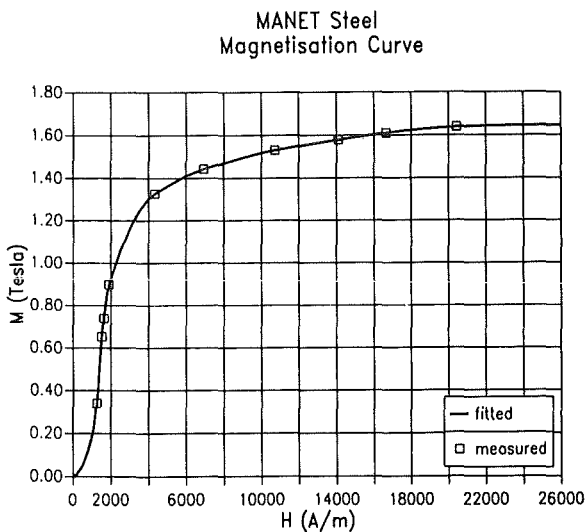


Fig. 1.2: Magnetization curve of MANET

saturated for low applied magnetic fields with a saturation magnetization of 1.64 Tesla.

The results of the electromagnetic analysis can

be summarized as follows:

- As the structure is fully saturated by the strong toroidal magnetic field, M is directed almost entirely toroidally causing a thickening of the toroidal component of B (Fig. 1.3), whereas the influence of M on the poloidal

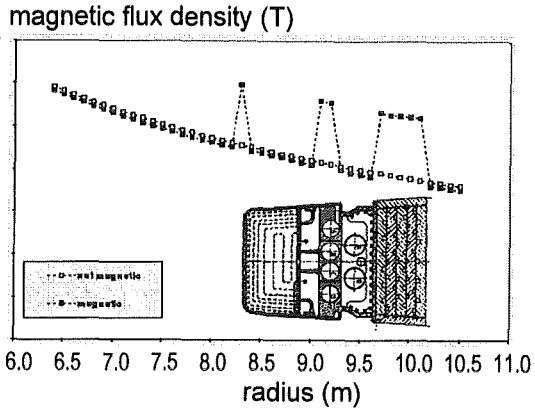
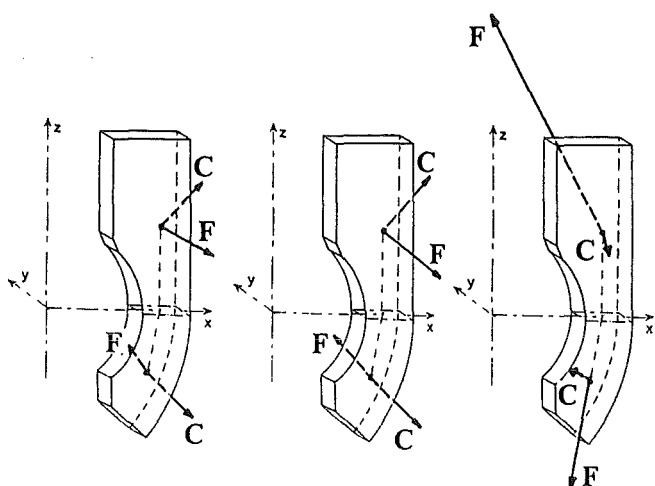


Fig. 1.3: Toroidal component of the magnetic flux density B as function of the torus radius

component of B is slight. The magnitude increases in connection with the toroidally continuous MANET structures.

- A direct consequence of the first point is that the varying poloidal magnetic field of the plasma caused by a disruption "sees" the same situation as the structure would be non-magnetic. That means, behaviour and distribution of the eddy currents induced in the structure are approximately the same with or without ferromagnetic structural material.
- In comparison to the non-magnetic case the electromagnetic forces (1.3) (and torques (1.4)) caused by interaction between J and B increase only their magnitude due to the contribution of M to the toroidal component of B , whereas their direction remains practically unchanged. In the most stressed part of the outboard segment box, like the side walls, the increase is about 11%. Resultants of forces and torques for upper and lower half of the structure are shown in Fig. 1.4 for a non-magnetic structure (left) and a structure of MANET (center): both cases show a large torque acting on X-axis and a torsion in Z-direction. For the ferromagnetic the values are higher.
- Additional forces (1.5) (and torques (1.6)) are present in the structure caused by direct interaction between M and B . As shown in Fig.1.4 the resultant of such forces and torques stretches the structure. This contribution, which is present only in ferromagnetic structures,



	Nichtmagnetischer Stahl		MANET			
	Lorentz-Kräfte		Lorentz-Kräfte		Magnetisierungskräfte	
	F_x	C_x	F_x	C_x	F_x	C_x
O	1.1	30.4	0.8	38.0	-3.9	-10.4
	-2.4	7.1	-3.6	10.2	3.8	-16.1
	-0.2	22.6	-0.7	25.8	13.7	-0.6
U	1.0	24.0	0.7	27.5	-2.4	0.5
	2.5	-4.9	2.8	-6.1	-1.5	9.8
	-0.1	-23.0	0.9	-25.1	-5.7	-0.8

Fig. 1.4: Resultant forces (1.3) F and torques (1.4) C are shown for a non-magnetic structure (left) and a structure of MANET (centre). Results of additional forces (1.5) and torques (1.6) acting on the magnetized structure are shown on the right. The resultants for the two halves of the structure are calculated on the geometrical centre of the equatorial horizontal section

produces a completely different electromagnetic load for the DEMO outboard blanket segment with MANET in comparison to a non-magnetic one.

Finally, a stress analysis [1] has been performed for the outboard blanket segment on the basis of the calculated electromagnetic load distribution. The resulting stresses have been compared with the allowable stresses according to ASME norms (Section III, "Design Conditions"); in Fig. 1.5 are shown the surfaces (in per cent) of the segment where the primary stresses lie between different intervals determined by fractions of the maximum allowed stress. Values are reported for a non-magnetic structure and a structure with MANET. Even if the stress of the structure is increased due to the presence of ferromagnetic material, it can be concluded that the outboard segment of the DEMO HCPB Blanket can withstand the mechanical stress caused by a major plasma disruption.

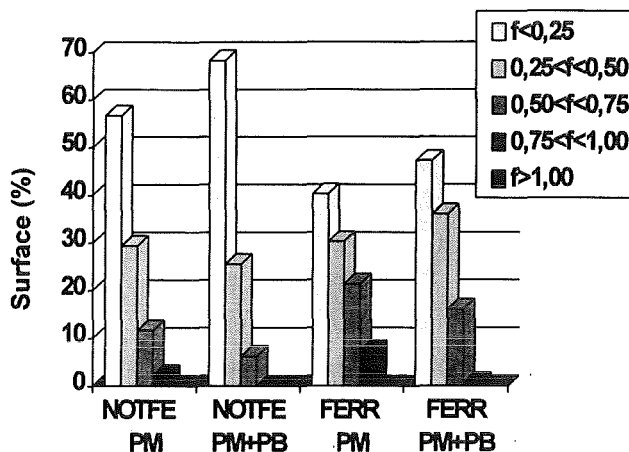


Fig. 1.5: Comparison of the calculated stresses with allowable limits according to ASME norms. The results are given for a structure with MANET (FERR) and a non-magnetic structure (NOTFE)

1.4 Conclusions

AENEAS is a new computer code developed for electromagnetic analyses in presence of non-linear ferromagnetic materials.

The code has been applied to study the electromagnetic behaviour of the DEMO HCPB Blanket during a major plasma disruption. The results show that the electromagnetic load of the structure increases and is differently distributed due to the presence of ferromagnetic structural material. A stress analysis of the outboard blanket segment shows that the structure can withstand the mechanical effects of a plasma disruption; the calculated stresses are lower than the allowable limits according to ASME norms.

Literature:

- [1] M. Dalle Donne et al., KfK 5429, Karlsruhe, 1994
- [2] R. Albanese and G. Rubinacci, IEE Proceedings, 135A (1988) 457
- [3] P. Ruatto, FZK 5683, Karlsruhe, 1996
- [4] K.A. Hempel, personal communication, RWTH Aachen, 1995

2. Electromagnetic Forces in the Test Module for ITER (L.V. Boccaccini, P. Ruatto)

The mechanical design of the Test Blanket Subsystem components (Blanket Test Module, Support Frame and Shield) is strongly influenced by the magnitude of electromagnetic loads due to plasma disruptions. As these components are

supported by the ITER back plate, their electromagnetic loads affect also the design of this ITER component.

In this section a preliminary electromagnetic analysis in case of a centered disruption is presented. The magnetic forces acting on the Test Blanket Subsystem components have been calculated.

2.1 Analysis Method

Eddy currents and electromagnetic forces have been calculated by means of the 3D Finite Elements Code AENEAS [1], which allows electromagnetic calculations in presence of nonlinear ferromagnetic materials.

2.2 Materials

The electrical and magnetic properties of the materials taken into account in the electromagnetic calculation are listed in Table 2.1. In particular the martensitic steel MANET is a

Tab 2.1: Electrical and magnetic properties

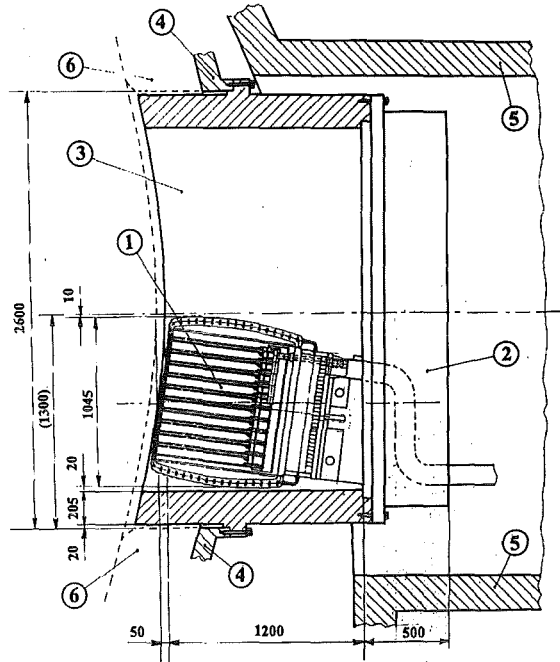
	electrical resistivity [$\mu\Omega\text{m}$]				magnetic permeability
	100°C	200°C	300°C	400°C	
MANET	0.657	0.732	0.806	0.881	[2]
316LN	0.915	0.884	0.949	1.002	vacuum (μ_0)

ferromagnetic magnetic material. The magnetic properties of MANET have been measured at the RWTH Aachen [2]. For 316LN steel the vacuum permeability is assumed in the calculation.

2.3 Model Description

Fig. 2.1 show the geometrical model on the basis of which the electromagnetic calculation has been performed. The HCPB Blanket Test Module (BTM) is placed in the lower half of the frame. The upper half is reserved for the Japanese BTM. In default of a detailed description of the Japanese BTM, the upper position is supposed to be occupied by another HCPB-BTM.

Fig. 2.2 shows the electromagnetic FEM model used in the calculation. 1/20 of the ITER reactor has been modelled. Vacuum vessel, back plate, PF-coils and Test Module System are taken into account in the model. The electrical resistivity of the vacuum vessel has been chosen in order to achieve a toroidal resistance of $13.2 \mu\Omega$. The back plate is assumed to be electrically insulated from the vacuum vessel. Its electrical resistivity results in a toroidal resistance of $7.4 \mu\Omega$. This value takes into account the contribution of the shield blankets supported by the black plate and electrically connected to it.



- 1. Test Module
- 2. Shield
- 3. Support Frame
- 4. Back Plate
- 5. Vacuum Vessel
- 6. Shield Blanket

Fig. 2.1: Vertical cross section of the Support Frame with the European HCPB-BTM

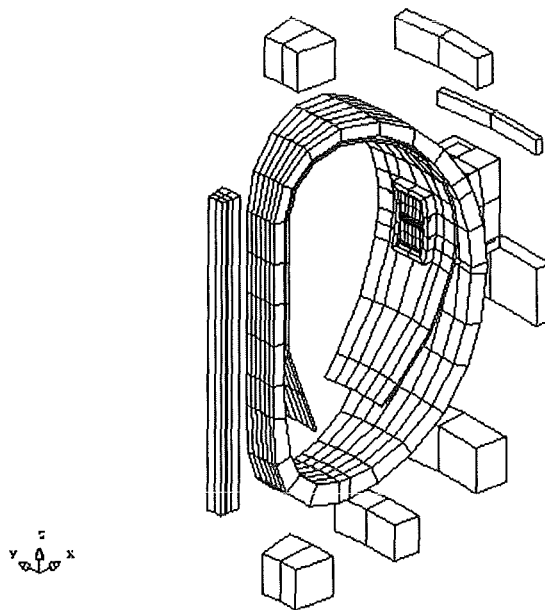


Fig. 2.2: Electromagnetic FE model of ITER with Test Modules

The model of the Test Blanket Subsystem is shown in detail in Fig. 2.3. The Support Frame is electrically connected to the back plate with a toothed-flange. The shields are both

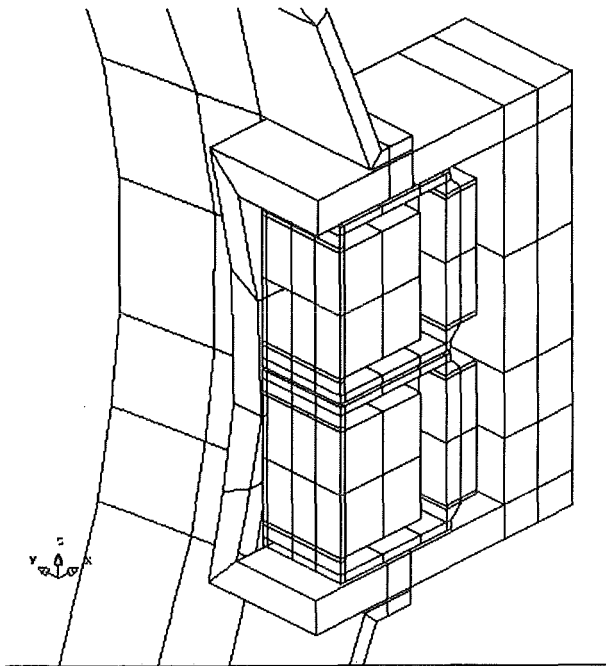


Fig. 2.3: Electromagnetic FE model of ITER: detail of the Test Modules

electrically connected to the Frame by means of a flange bolted to the back side of the Frame. The structural material of the Support Frame and Shield is 316LN steel at an average temperature of 150°C. The Test Modules are electrically insulated from the other components of the Test Module Subsystem. The structural material MANET has been considered at an average temperature of 350°C.

In Table 2.2 the most important parameters of the FEM model are summarized. The calculation has been performed with a relatively small amount of degrees of freedom (d.o.f.) 2482 (964 for the description of the current and 1464 of the magnetization, i.e. vector). A relatively rough mesh has been used for vessel and back plate; a finer mesh has been used for the test port region.

For the centered disruption a filamentary model derived from the plasma equilibrium is used. The plasma current center has a radius of 8.2 m and a height above the equatorial plane of 1.47 m. The plasma current of 21 MA decays to zero linearly in 10 ms. The poloidal field coil currents are considered at end-of-burn (EOB). The Pf-coil dimensions and current values are summarized in Table 2.3.

A toroidal field of 5.7 T at a radius of 8.1 m is also included.

2.4 Analysis Results

The resultant forces and torques acting on the BTM at end of disruption (t= 10 ms) are summarized in Table 2.4. The values are given for the Lower BTM, the Upper BTM, the Support Frame (together with the Shield) and for the total Subsystem. The resultant torques are calculated at the geometric center

Table 2.2: Mesh parameters

Component	Node No.	Element No.	current d.o.f.	magnetic d.o.f.
Lower BTM	511	268	301	732
Upper BTM	511	268	301	732
Vessel	414	176	172	---
Back plate, Frame and Shield	503	230	239	---
PF-coils	120	20	10	---
Total	2059	962	1023	1464

of the corresponding component. The total torque is calculated at the back plate location.

The results represent a basis for the structural analysis of the connection between BTM and Shield, and between the whole Test Blanket Subsystem and the ITER back plate. Nevertheless, in view of a complete structural analysis of the ITER back plate for load conditions caused by the presence of the Test Blanket Subsystem, a more accurate analysis of the force distribution acting directly on the back plate has to be performed. These forces are due to the distortion of the eddy current patterns on the back plate.

2.5 Conclusions

A preliminary electromagnetic calculation has been performed to evaluate the magnetic forces acting on the various components of the Test Blanket Subsystem.

The analysis has been performed with the three-dimensional code AENEAS, which allows calculations of eddy currents and magnetic forces in presence of ferromagnetic materials.

Literature:

- [1] P. Ruatto, FZKA 5683, Forschungszentrum Karlsruhe (1996).
- [2] K.A. Hempel, W. Salz, personal communication, RWTH Aachen, (1995)

3. Integration of a dynamic plasma model

The dynamic model of the plasma was accomplished and integrated in the 3d eddy current code CARIDDI - now called CARIDDI-P. Thus the important coupling effects between the

electrically conducting structural boundary, the plasma current and the plasma motion can be taken into account.

The plasma model is based on reduced magneto-hydrodynamic (MHD) equations, which are appropriate for the dense fusion plasma. Assuming toroidal symmetry of the plasma current the plasma itself can be represented in a 2D radial-poloidal symmetry plane. The balance of internally produced ohmic heat and edge radiation during the disruption allows to treat the plasma isothermal.

The MHD description consists of a electromagnetic and a fluiddynamic part. For the electromagnetic part a FEM formulation of the plasma was chosen to simplify the coupling with the 3D electromagnetics of the solid structures. For the fluidmechanic part a Volume Of Fluid (VOF) method on a spatially fixed grid is applied. The plasma is assumed to keep its shape during vertical displacement until it contacts the structure. Due to the wall contact the associated part of the plasma, the scape-off layer, is cooled down immediately. The trigger for the simulation of the plasma disruption in CARIDDI-P are small perturbations of the temperature, resistivity profile, respectively, or small deflections or initial velocities disturbing the MHD equilibrium.

With CARIDDI-P two types of calculations were conducted with the general intention to verify the complex code.

3.1 Computations with spatially fixed plasma

Some first simple calculations were conducted to control the formulation of the mutual inductivity. They dealt with current loops fixed in space. This simplification allowed to compare the CARIDDI-P results with analytical solutions of the loop currents. The results were nearly identical.

An analysis on the influence of the first wall toroidal electrical resistance was conducted. It turned out that an intermediate resistivity of the first wall yields the best compromise concerning the loading of the blankets and the first wall during the plasma disruption [1].

3.2 Computations with plasma motion

Most of the plasma disruptions observed are linked to a vertical displacement event (VDE). CARIDDI-P is now capable of reproducing this motion with its various contributions to the electromagnetics and structural dynamics.

It should be emphasized that the plasma behavior actually is determined by the electromagnetic properties of the surrounding structure. That means a fixed prescribed plasma behavior as used in the conventional eddy current codes will not be compatible with varying the design of the components adjacent to the plasma.

So the extension of CARIDDI with the dynamic plasma turned out to be very important. Especially it will be needed for analyses of design parameters which will change the electromagnetic properties of the vessel or in-vessel components of tokamaks.

To verify the fluiddynamic part of the plasma model the bot #1500 of the ASDEX experiment [2] was computed. The results of CARIDDI-P reproduced the observed plasma behavior to a satisfying degree. So here no advantage arises from applying very specialized plasma physics codes, like TSC. In contrary, these codes do not have the ability to model the complicated 3D structural boundary as CARIDDI does.

At last a realistic model of ITER consisting of high order FEM elements was developed. It includes the mutual mechanical support originated in the toroidal continuity of the back wall

Table 2.3: PF-coils

Coil	R (mm)	Z (mm)	DR (mm)	DZ (mm)	Current (MA)
CS Module 1	2038,0	0,0	224,0	12071,0	-37,55
CS Module 2	2263,5	0,0	205,0	12071,0	-40,33
CS Module 3	2531,1	0,0	308,0	12071,0	-61,20
PF-2	5868,0	9981,0	1553,0	1528,0	-5,76
PF-3	12892,0	7389,0	657,0	1186,0	-7,05
PF-4	15364,0	-2090,0	587,0	2222,0	-13,15
PF-5	13198,0	-7943,0	1236,0	1743,0	-4,55
PF-6	9703,0	-9583,0	1035,0	1385,0	4,47
PF-7	5859,0	-9981,0	1553,0	1528,0	8,68
PF-8	15177,0	3691,0	273,0	556,0	0,00

Table 2.4: Resultant forces and torques

	Lower BTM	Upper BTM	Frame and Shield	Total
x-coordinate (*) [m]	11.768	11.768	12.291	11.658
y-coordinate (*) [m]	0.000	0.000	0.000	0.000
z-coordinate (*) [m]	0.823	1.887	1.355	1.355
Force x [MN]	-0.035	0.029	-1.975	-1.981
Force y [MN]	0.200	-0.085	0.229	0.344
Force z [MN]	0.693	-0.201	1.108	1.600
Torque x [MNm]	2.007	2.010	-0.243	3.927
Torque y [MNm]	-0.104	0.377	-0.409	-1.085
Torque z [MNm]	-0.961	1.164	-1.742	-1.869

(*) According to the torus Coordinate System

and vacuum vessel. The possible contact of the back wall and the vessel is taken into account with the help of gap elements. Figures 3.2a and 3.2b show remarkable differences in the maximum loading as a result of a CARIDDI-P calculation (a) and as a result of a conventional analysis with a prescribed plasma behavior (b). Both computations start from the same initial conditions.

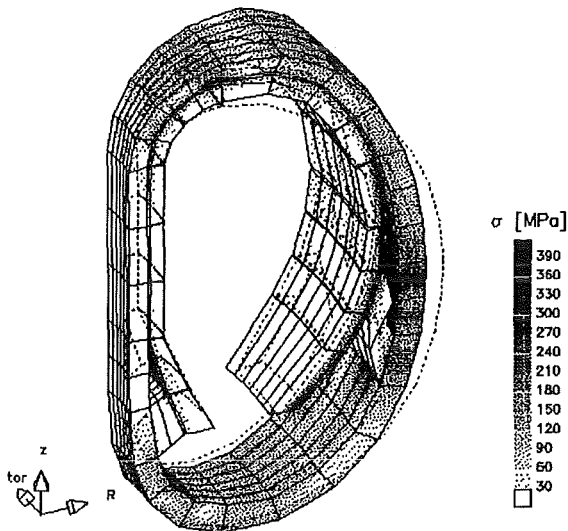


Fig. 3.2a: Maximum von-Mises stresses and deformation in ITER at t=40 ms calculated with the dynamic plasma of CARIDDI-P

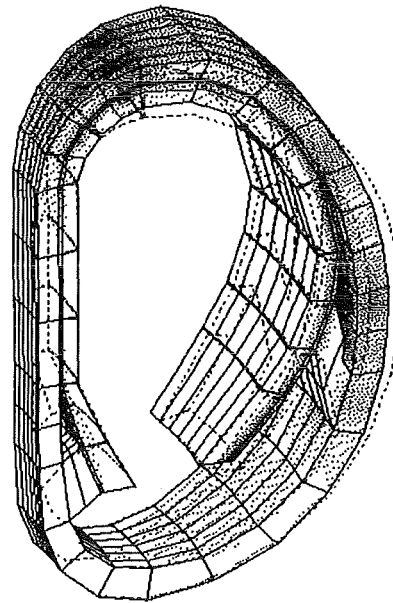


Fig. 3.2b: Maximum von-Mises stresses and deformation in ITER at t=30 ms calculated with a prescribed plasma behavior

Literature:

- [1] T. Jordan, D. Schneider: Minimizing the first wall and blanket loading caused by plasma disruptions by tuning first wall's resistivity, SOFT '96, Lisbon

- [2] O. Gruber, G. Pautasso et al.: Disruptions in vertically elongated ASDEX-Upgrade plasmas, Plasma Physics and Controlled Nuclear Fusion Research 1994, IAEA, Seville

Staff:

L.V. Boccaccini

T. Jordan

P. Ruatto

D. Schneider

B 1.3.2 Calculation of the Combined Stresses in the Blanket and Test Module

For the Helium Cooled Pebble Bed Blanket (HCPB) a finite elements (FEM) structural analysis has been performed in order to be able to account for the radiation-induced stresses in the blanket structure. The analysis refers to steady-state operating conditions of the outboard blanket segment, since loads arising during an accidental situation have been not yet considered.

Radiation induced loads arise mainly due to both beryllium and Li_4SiO_4 swelling. These dimensional changes, caused by both helium production and neutron damage, can result in large mechanical stresses on the blanket structural material, especially at the reactor End-of-Life.

According to the temperature distribution from ref. [1], the beryllium swelling as a function of temperature and neutron fluence has been evaluated with the code ANFIBE [2]. However, since experimental evidence has shown that the temperature of the beryllium pebbles varies quite considerably during the irradiation [3], more realistic calculations of the beryllium swelling have been performed. A special computer program has been developed to solve the heat conduction differential equation, accounting for the variations of temperature caused by beryllium volume swelling and relative thermal expansion pebble bed/containing wall.

The maximum beryllium temperature decreases from 637 °C at the blanket Beginning-of-Life (BOL) to 501 °C at the blanket End-of-Life (EOL) and the EOL temperature distribution in beryllium is smoother than the BOL one. As a consequence of the decreased EOL beryllium pebble bed temperature, also the EOL swelling distribution will be smoother and the peak beryllium swelling decreases to 8.3% (Fig. 1).

The pressure exerted on the blanket cooling plates as a consequence of the beryllium swelling has been calculated using an elasto-plastic model and it is shown, as a function of the radial distance, in Fig. 2.

As first approximation it has been assumed that, due to the presence of the lithium orthosilicate pebble beds, the cooling plates do not bend under the effect of the radiation induced beryllium loads. Under this assumption the stress analysis performed with the FEM code ABAQUS leads to a maximum von Mises equivalent stress of 118 MPa in the front part of the blanket module near the first wall, where the maximum swelling occurs (Fig. 3). The resulting maximum stress is far below the tolerable limit imposed by the ASME norms.

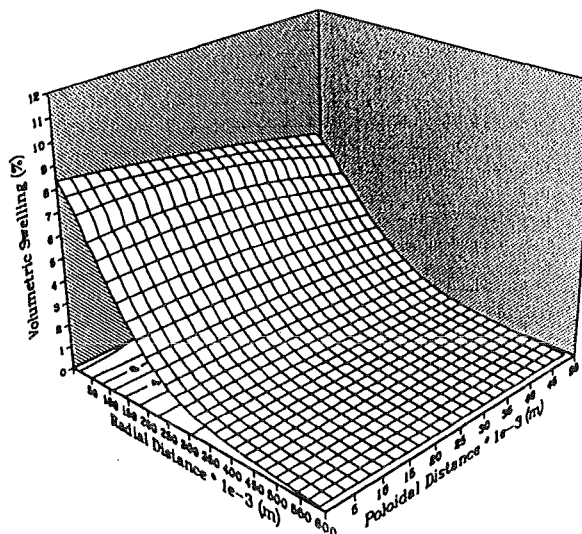


Fig. 1.: EOL swelling distribution in the beryllium pebble bed

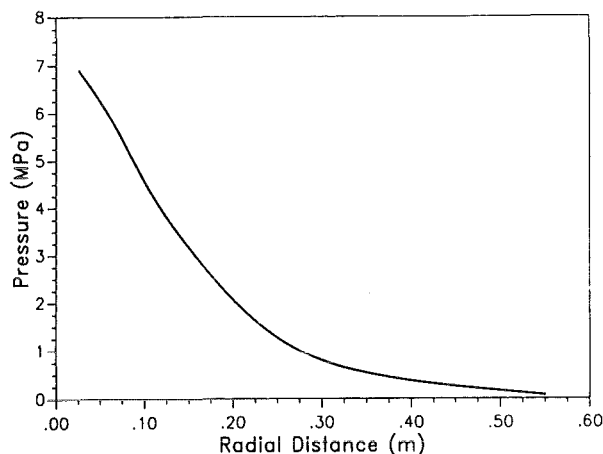


Fig. 2: Pressure due to beryllium swelling at the blanket EOL

Literature:

- [1] P. Norajitra, "Thermohydraulics Design and Thermomechanics Analysis of Two European Breeder Blanket Concepts for DEMO", FZKA Bericht 5580, Karlsruhe, Juni, 1995.
- [2] F. Scaffidi-Argentina, "Modellierung des Schwellens und der Tritium-Freisetzung von bestrahltem Beryllium", FZKA Bericht 5632, Karlsruhe, October, 1995.
- [3] M. Dalle Donne et al., "European DEMO BOT Solid Breeder Blanket", KfK Bericht 5429, Karlsruhe, November, 1994.

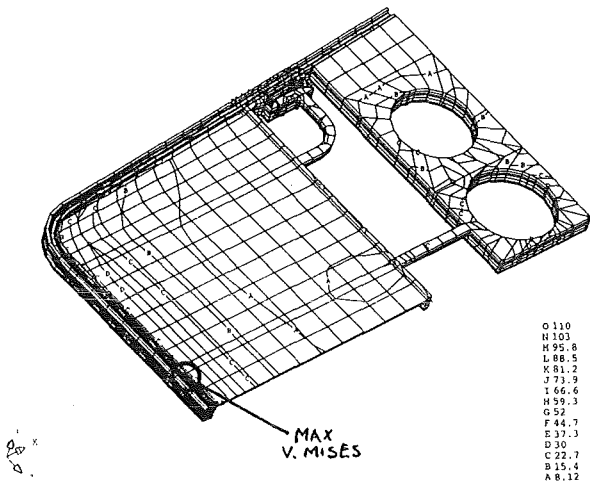


Fig. 3: Von Mises stress distribution due to beryllium swelling at the blanket EOL

Staff:

M. Dalle Donne

F. Scaffidi-Argentina

B 1.4.1 Reliability Assessment including Ancillary Systems

The availability/unavailability had been investigated for the European DEMO blanket concepts, comprising the blanket proper [1] and the associated cooling systems [2] in the frame of the blanket selection exercise. In recent studies similar assessments were made for ancillary subsystems pertaining to the HCPB DEMO blanket, i.e., for the tritium recovery system and the helium purification system. Also a first availability analysis was performed for the ITER blanket test module.

In all studies the fault tree methodology was applied. It comprises the definition of the system, break-down of the system into components (e.g., pipes, pumps, valves, heat exchangers, etc.) and subcomponents (e.g., welds of different types, bends, tube sections, etc.), defining the top event and designing the related fault tree, assigning failure rates to components and subcomponents, estimating repair or replacement times for components, and finally computing the unavailability, that is the probability of occurrence of the top event. The top event is defined as the case that the system under consideration is unavailable (in the sense that the plant must be shut down) on demand. The most critical points in the analysis are the failure rates and mean time to repair/replacement. Here the data base established during the blanket selection exercise has been adopted where applicable. The systems investigated, the basic assumptions, and the results are summarised below.

Tritium Recovery System (TRS) of the HCPB DEMO Blanket

The system layout is based on the work performed in Task B 6.1.1. The main components are the blanket segments (here the blanket internals related to the purge gas system), and the purge gas circuits with heat exchangers, filter, vaporiser, adsorber, compressor, tubes, and valves. Also the adjoined Q₂O and Q₂ loops (Q=H, D, T) with their components have been taken into account.

As to the repair/replacement times of failed components in the external circuits, a mean time to repair/replacement of 3-6 hours was assumed. This is considered reasonable because the components are small and are located outside the cryostat. Any failure inside the blanket segments has been neglected for several reasons: The nominal purge gas pressure is low (0.1 MPa), the purge gas distribution pipes are perforated so that small cracks, entailing some redistribution of the flow, could be tolerated, and finally the circuits are designed to temporarily operate at full coolant pressure (8 MPa) in case of an internal leak from the primary side.

An overall unavailability of 0.002 has been obtained for the TRS by fault tree analysis. This is small compared to typical values of 0.1 - 0.2 calculated earlier for the blanket system. It could even be further improved by providing redundancy for selected components. For instance, redundant loops for the Q₂ and Q₂O subsystems would lower the unavailability to

about 3×10^{-4} . This would leave margin for uncertainties in the assumed failure rates.

Coolant Purification System (CPS) of the HCPB DEMO Blanket

The fault tree analysis is based on the system layout and flow diagram described in the last annual report. It is essentially a series of oxidiser, several coolers, filter, water separator, adsorber, and compressor. The coolers are arranged as recuperative heat exchangers to regain the energy from the cool-down process from 720 K to 80 K. Ancillaries to the CPS are not yet elaborated and have been ignored.

To get an idea of the size of the coolers for failure rate estimation, a first layout has been performed resulting in a typical coolant tube bundle diameter of 0.7 m at bundle lengths of between 0.5 and 2.7 m. In Table 1 are listed the components and the resulting component unavailability. The latter is approx. the product of the number of components, component failure rate and mean time to repair/replacement (MTTR). Again, a short MTTR of 10 hours was assumed, for valves MTTR=5 h was chosen.

The total unavailability of the system adds up to 4.6×10^{-4} (here approx. equal to the sum of the last column in Table 1). The main contributors are the compressor and the numerous valves. Of some relative importance are also the filters, whereas the heat exchangers and coolers contribute with only 1 % to the total unavailability. It is obvious that underestimation of failure rates or MTTR of the main contributors impact directly the total unavailability.

Table 1: Components of the CPS and their unavailability

Component	Quantity	Unavailability
Oxidiser	1	7.1×10^{-6}
Heat exchanger 1	1	1.0×10^{-6}
Filter	2	5.4×10^{-5}
Heat exchanger 2	1	1.0×10^{-6}
Water separator	1	1.0×10^{-6}
Helium pre-cooler	1	1.0×10^{-6}
Helium cooler	2	2.0×10^{-6}
Adsorber + 2 filters, cooler	2x2	1.42×10^{-5}
Compressor	1	2.2×10^{-4}
Tubes	500 m	5.0×10^{-7}
Bends	100	5.0×10^{-6}
Valves	30	1.5×10^{-4}

HCPB Blanket Test Module (BTM) for ITER

Staff:

H. Schnauder

The basis for the unavailability analysis is the HCPB-BTM design as described under Task B 1.2.1. The principal configuration consisting of blanket box, cooling plates, pebble beds, and manifolds is the same as for DEMO. Hence, identical subcomponents, i.e., electron beam welds, diffusion welds, butt welds, pipes, and bends appear and the same failure effects can occur in the BTM proper. These are (a) helium leakage into the vacuum vessel, (b) cooling disturbance, (c) purge gas flow disturbance, and (d) loss of structural integrity. The cooling circuits and the interface to the vacuum vessel were not yet considered. A mean time to repair/replacement for the BTM of 8 weeks has been assumed.

Fault tree analysis yielded a small overall unavailability of the BTM of 0.006. The paths leading to the failure effects (a) to (d) above contribute as displayed in Table 2. The most probable occurrence is the helium leakage into the vacuum vessel, contributing with 93 %, followed by the cooling disturbance with 4 %. The other two paths (c) and (d) are in the 1 % range. Table 2 shows also the occurrence rates per year for the different failure paths. Accordingly, the top event, i.e., the unavailability of the BTM (without any ancillaries) on demand, is expected to occur at a frequency of 0.004 per year.

Table 2: Results of the BTM reliability analysis

Failure Effect	Occurrence rate (1/y)	Unavailability	
		absolute	%
Helium Leakage into VV	3.7×10^{-3}	5.8×10^{-4}	93
Cooling disturbance	1.6×10^{-4}	2.5×10^{-5}	4
Purge gas flow disturbance	2.6×10^{-5}	2.6×10^{-5}	1
Loss of structural integrity	6.1×10^{-5}	6.1×10^{-5}	2
Total	4.0×10^{-3}	4.0×10^{-3}	100

Literature:

- [1] H. Schnauder, C. Nardi, M. Eid: Comparative availability analysis of the four European DEMO Blanket Concepts in view of the selection exercise, to be published.
- [2] C. Nardi, H. Schnauder, M. Eid: Reliability & availability analysis as a decisional means at early stages of the new machines design, 19th Symposium on Fusion Technology, September 16-20, 1996, Lisbon, Portugal.

WP B 2 Fabrication, Assembly and Development Studies of Blanket Segments

B 2.1.1 Fabrication, Assembly and Development Studies of Segment Box and Cooling Plates

Introduction

The design of the European Helium-Cooled Pebble Bed (HCPB) blanket (see subtask B 1.1.1 and B 1.2.1) makes it necessary to investigate, develop and qualify fabrication and inspection techniques which enable the manufacturing and assembly of the DEMO blanket segments and in particular the blanket test module to be tested in ITER. The work of the past year was concentrated on the following four fabrication steps:

- Diffusion bonding of the FW sections and the cooling plates, both with milled grooves to produce plates with integrated cooling channels
- Bending of the diffusion bonded first wall (FW) plates to obtain a section of the U-shaped segment box.
- Electron beam welding between the FW sections to build up the FW box of one complete blanket segment.
- Welding of the cooling plates to the FW at the inside of the segment box.

The results of these investigations are described in the following [1]:

Diffusion Bonding of Plates with Internal Cooling Channels

The diffusion bonding tests made on cooling plates of MANET 2 - consisting of a structural plate with thin webs and a cover plate (Fig. 1, Version A) - have shown that the joining zone, despite the high degree of deformation, is not sufficiently deformed with this non-symmetric buildup of the welded joint [2].

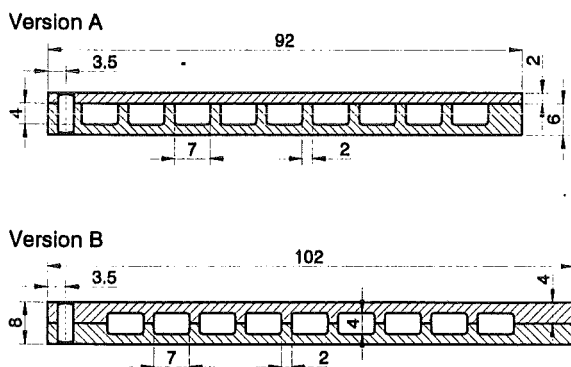


Fig. 1: Diffusion bonded Cooling Plates

Symmetric parting of the structure (Fig. 1, Version B) is more expensive in terms of manufacture but it seems to offer more advantages with respect to the safe optimization of the welded joint avoiding the risk of web buckling. This design was investigated in another test series, again conducted jointly with the Institut für Kerntechnik und Energiewandlung, Stuttgart. The post-test examinations yielded good welding results. The microsections of all specimens exhibit the flawless pattern of the joining zone. The bending test showed full bending without rupture, with strength values corresponding to those of the parent material [3].

Bending of First Wall Plates with Internal Cooling Channels

To obtain the U-shape of the blanket box diffusion bonded FW plates with internal cooling channels have to be bent with angles of about 96° for the inboard and 86° for the outboard blanket segments. To investigate and qualify this fabrication step plates with FW geometry and four internal cooling channels (Fig. 2) have been bent in cooperation with the

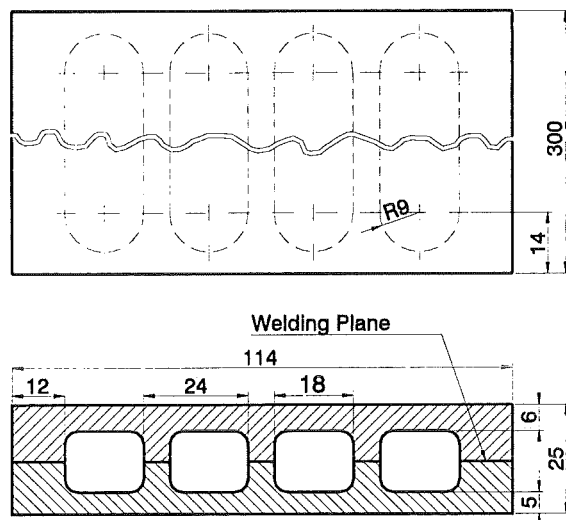


Fig. 2: Specimens for the bending tests

Institut für Kerntechnik und Energiewandlung and the Forschungsgesellschaft für Umformtechnik, both in Stuttgart [4]. The bending tests have been carried out at room temperature with a bending radius of 75 mm.

During the first test without filling material in the cooling channels a crack arose in the elongated plane because the bending radius did not follow the radius of the bending punch so that the real bending radius was much smaller than intended (approximately 25 mm).

To avoid this effect two counter-measures have been initiated: a) bending of the specimen together with a sandwich plate, a second steel plate, which presses the specimen against the bending punch, b) use of a filling material in the cooling channels to obtain a plate behaviour comparable with the solid plate. Accordingly, the next two bending tests with diffusion welded specimens have been

carried out using a sandwich plate. Additionally, one of the plates has been filled with a tin-bismuth-eutectic alloy.

Both bending tests have been successful, i.e. no surface cracks could be detected, and the bending radius was approximately 75 mm as intended. The deformation of the two central channels was relatively small; the channel height with and without filling material was reduced by 8.3% and 10.5%, respectively (Fig. 3).

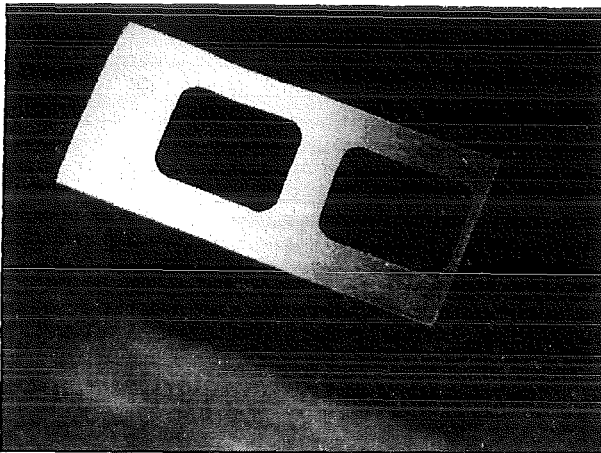


Fig. 3: Channel geometry after bending without filling material

To ascertain specific bending parameters like the location of the neutral plane, the maximum and local stress, and the geometry variation during bending, the tests have been accompanied by FEM calculations. According to these calculations maximum elongation of approximately 50% is bearable.

In a next step a plate only with filling material and without a sandwich plate will be bent using a bending radius of 75 mm. Afterwards all tests will be repeated with a bending radius of 50 mm to explore the bending limits of the material.

US Inspection of Electron Beam Welded Double Welds

In cooperation with the Siemens Company the investigations were continued on qualification of an ultrasonic (US) inspection method on electron beam (EB) welded double welds with inspection gap of a first wall specimen made from MANET 2. Test flaws differing in size, in the form of slots simulating crack-like defects and drilled holes simulating volumetric defects, were machined in the welded specimen according to Fig. 4.

The US measurement runs yielded good detectability down to 0.5 mm test flaw depth in case of the slots on the weld surface and 1 mm on the side of the inspection gap (inner side of the weld); for the holes the detectability was good up to 1 mm diameter on the inner side. Fig. 5 shows by way of example one of the ultrasonic scans of the slot reflectors. A conclusion

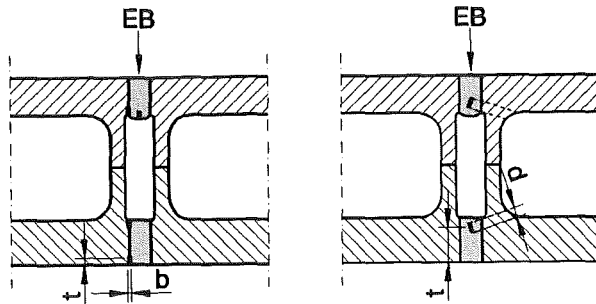


Fig. 4: Location of the test flaws in the EB specimen: left: slots, right: drilled holes.

Test flaw	length	5	5	5	5
[mm]	width	0.2	0.2	0.2	0.2
	depth	0.5	1	2	3
		↓	↓	↓	↓

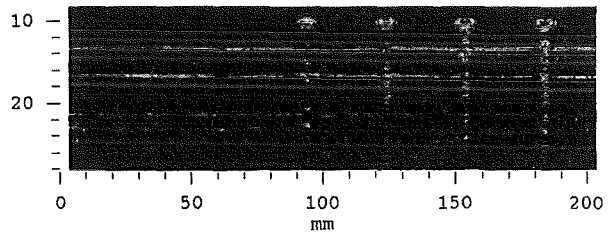


Fig. 5: US-scan, slot reflectors, surface of weld

with respect to the sizing of flaws is possible with limitations only [5].

Therefore, it is proposed to analyse in more detail the sizing capability by application of a specifically developed US detector which will allow better detectability and subsequent probabilistic analysis of the weld [6] taking into account the results of the ultrasonic inspections.

Welding of Cooling Plates to the FW Box

The cooling plates separating the Li₄SiO₄ and the Be pebble beds (Fig. 1) have to be welded to the bent FW-box. This weld has been investigated with the objective to avoid preheating during welding, to reduce the heat affected zone, and to minimize distortions. Prior to testing, two studies have been carried out to investigate the feasibility of this joint, to make proposals for the weld seam design, the welding processes, weld seam testing methods, repair concepts and to review the state of the art of these aspects [7], then to discuss the advantages and disadvantages of the proposals with the objective to elaborate an experimental program [8]. For the weld seam design the most favourable proposal is shown in Fig. 6.

By the use of the channel between the two welds the weld thickness has been reduced to a value of 2 mm each. This leads to a small heat affected zone and hence, a reduction of stresses in the structure. Another advantage of the 2 mm wall

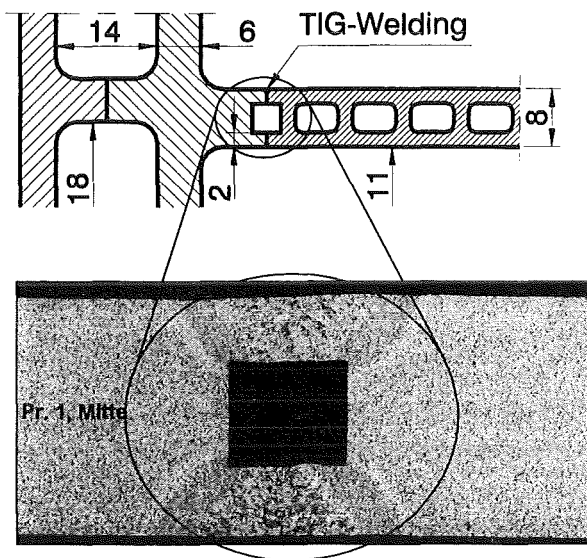


Fig. 6: Weld seam between FW and cooling plates and first result of a metallographic examination

thickness is that the welds can be carried out without preheating. TIG- and laser-beam welding can be used for these joints, and the inspection can be made by US, eddy current, leak detection or visual methods.

In a current test program the TIG-welding process, the US and the eddy current testing methods are being applied with very encouraging results, i. e. no cracks have been observed in the welds and the distortions are very small. After this test series it is planned to weld one complete cooling plate (without cooling channels) into a U-shaped plate.

Literature:

- [1] T. Heider, G. Reimann, H. Riesch-Oppermann, K. Schleisiek: Development of Fabrication Techniques for the European Helium Cooled Pebble Bed Breeder Blanket, 19th Symposium on Fusion Technology, September 16-20, 1996, Lisbon, Portugal.
- [2] G. Haufler: Diffusionsschweißen von Platten aus MANET 2 mit Kühlkanälen unterschiedlicher Geometrie, Forschungsinstitut für Kerntechnik und Energiewandlung, Stuttgart, 1-TB-244/95 (1995).
- [3] G. Haufler: Diffusionsschweißen von Kühlplatten aus MANET 2, Forschungsinstitut für Kerntechnik und Energiewandlung, Stuttgart, 1-TB-248/96 (1996).
- [4] G. Haufler, D. Kolev: Biegen von Platten mit internen Kühlkanälen, KE / FGU Stuttgart, 1-TB-245/95, (1995).
- [5] K. Gemmer-Berkbilek: Arbeitsprogramm zur quantitativen Bestimmung von Schweißfehlern in EB-Doppelschweißnähten mittels Ultraschall - Teil A

"Qualitativer Testfehlnachweis" -, Siemens (KWU), Erlangen, KWU NPP2/96/033 (1996).

- [6] S. Zhang, H. Riesch-Oppermann: Probabilistic Analysis of Non-destructively Determined Flaws in Welds, Fusion Engineering and Design, 31 (1996), 1-8.
- [7] G. Engelhard: Machbarkeit des Einschweißens und Prüfen der Kühlplatten in die U-förmige Outboard- und Inboard Blanketbox, Siemens / KWU, NR-A/95/046, (1995).
- [8] G. Engelhard: Fertigungstechnische Untersuchung für das Einschweißen der Kühlplatten in die U-förmige Outboard- und Inboard Blanketbox, Siemens / KWU, KWU NR-A/95/82, (1996).

Staff:

- T. Heider
- G. Reimann
- H. Riesch-Oppermann
- K. Schleisiek

WP B 3 Ceramic Breeder Pebbles

B 3.1.1 Li_4SiO_4 Pebbles Characterization and Optimization of Large Scale Production

The European Helium Cooled Pebble Bed (HCPB) blanket is based on the use of slightly overstoichiometric lithium orthosilicate ($\text{Li}_4\text{SiO}_4 + 2.2\text{wt}\% \text{SiO}_2$) pebbles [1]. The pebbles are fabricated by the firm Schott Glaswerke by melting and spraying with a gas jet. The chosen pebble diameter range is 0.25-0.63 mm.

To improve the mechanical properties of the pebbles a small amount of TeO_2 has been added to the orthosilicate. The TeO_2 increases the surface tension of the molten phase, results in pebbles with smaller crystals and reduces drastically the presence of cracks and the gap thickness at the grain boundaries, thus improving considerably the mechanical and thermomechanical properties of the pebbles. Annealing at 1030°C , required by the pebbles without TeO_2 , which would have been expensive in an industrial production, is not necessary anymore.

The effect of adding TeO_2 on the radioactivity after irradiation in the blanket is small. Also the effect of the foreseen amount of TeO_2 on the blanket tritium breeding ratio is negligible.

Results of crush tests on single pebbles and of thermal cycle tests on pebble beds are presented [2]. Tritium release behaviour during annealing of irradiated pebbles without and with TeO_2 is discussed in section B3.2.1.

Mechanical strength of single pebbles

The mechanical strength is examined by continuously increasing the load imposed by a piston to a single pebble until it breaks. The pebble is placed on a glass plate to avoid plastic deformation of the supporting surface, so that the Hertz's equations can be applied. By means of these equations the breaking stress, i.e. the tensile stress at the border of the contact surface between pebble and support plate can be calculated. The breaking tests were performed for many pebbles of the same type and correlated by means of the two-parameter model of the Weibull statistics [3]. Fig. 1 shows the derivative of the pebble breaking probability with respect to the breaking stress versus the breaking stress for pebbles with and without TeO_2 . Before the tests, the optimum thermal annealing for each of the materials was applied (1030°C for 5 minutes for the pebbles without TeO_2 and a treatment at considerably lower temperatures for the pebbles with TeO_2). The improvement in the mechanical stability due to the TeO_2 is evident from the figure.

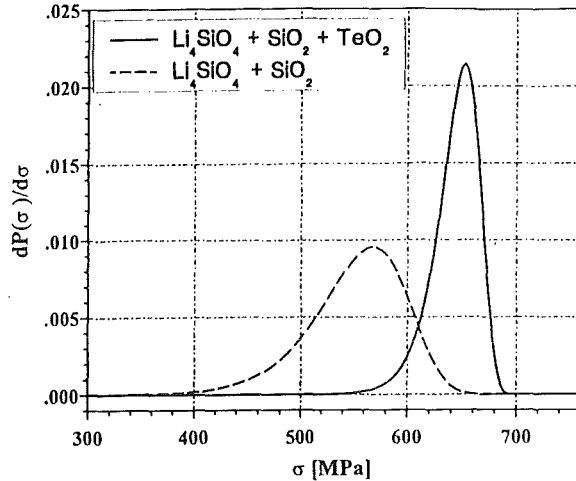


Fig. 1: Pebble crush tests. Derivative of pebble breaking probability with respect to the breaking stress versus the breaking stress.

Thermal cycling tests on pebble beds

The beds were contained in a straight horizontal tube (20 mm \varnothing , 110 mm length), the principle and technical details are described elsewhere [4].

Two types of tests were performed. The objective of the first type is to determine the thermal shock resistance of the pebbles by applying very fast temperature transients. In this case the beds are not densified to avoid stresses caused by the relative dimensional variations between pebble bed and container during the temperature transients. Fig. 2 shows

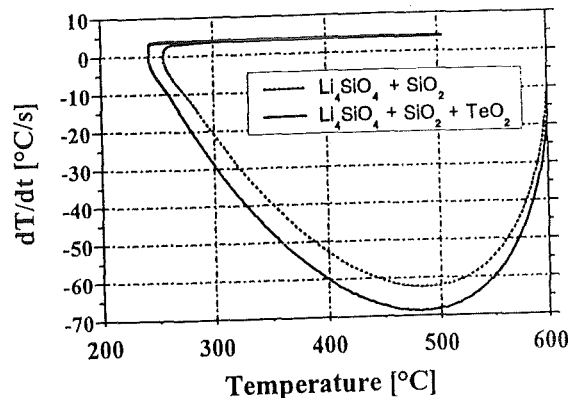


Fig. 2: Comparison of the curves dT/dt versus T at $R = r_{cri}$; r_{cri} = radius beyond which the pebbles are broken.

that both kind of pebbles (without and with TeO_2) can sustain very high thermal shocks (more than 60°C/s), the pebbles with TeO_2 being slightly better.

A second type of thermal cycle test was performed in view of irradiation tests of HCPB test modules in ITER. Contrary to the DEMO, frequent temperature cycles in the blanket are foreseen in ITER due to the limited length of the plasma pulses (≤ 1000 sec). Calculations show that the maximum

temperature gradient is 3°C/sec. On the other hand, however, because the blanket tests modules would be subjected to a few thousands thermal cycles in ITER, even these relatively small temperature gradients could lead to failures of pebbles, especially due to the stresses caused by the different thermal expansions of the pebble bed and of the containing walls. Thus the tests were performed with beds with the maximum packing factor. This was obtained by thoroughly vibrating the pebble bed. A temperature rate of change of 5°C/sec was obtained by cooling the pebble bed container with uniformly distributed air jets. Fig. 3 shows the increase of the pressure

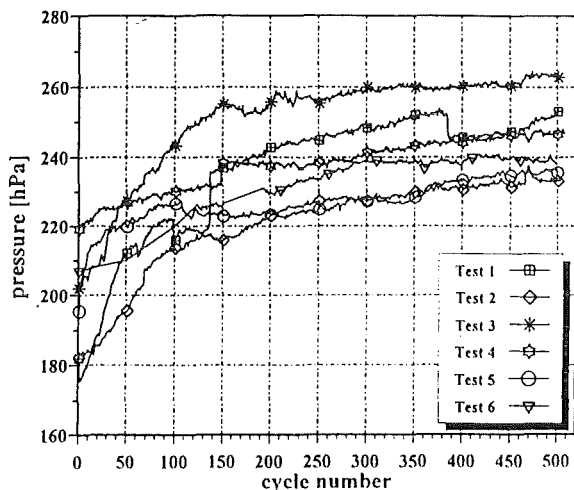


Fig. 3: Pressure drop of helium flowing through the pebble bed versus thermal cycle number (for the meaning of the curve numbers, see Table 1).

drop of the helium flowing through the pebble bed versus the number of cycles. The tests were performed up to 500 cycles, as the pressure-drop variations indicate that beyond this value the pressure increase is negligible.

Table 1 shows the maximum pressure drop variations and the amount of broken particles for the various types of tested pebbles. The amounts of broken particles and the differences between pebble types are quite small. Preliminary tests, where the pebble bed was, after the test, filled with epoxy resin and then cut, showed that the broken particles were evenly distributed in the bed, rather than being at the bed walls as in the thermal shock tests [4].

To summarize, the mechanical and the thermal cycling tests indicate that the addition of TeO₂ to the overstoichiometric Li₄SiO₄ improves considerably the mechanical stability of the pebbles. The mechanical stability as well as tritium release will be checked in the EXOTIC-8 experiment to be started fall 1996 in the HFR reactor at Petten.

Literature:

[1] M. Dalle Donne et al., KfK 5429, Nov. 1994.
 [2] M. Dalle Donne et al., "Development work for lithium orthosilicate pebbles ", SOFT-19 Lisbon, 1996.

Table 1: Results of thermal cycling tests with ramp = 5 °C/s

Test Nr.	Te addition	Enrichm.	Anneal.	Broken (%)	Δpf - Δpi [hPa]
1	No	Natural	No	3.5	71.0
2	No	Natural	Yes	1.8	51.5
3	Yes	Natural	No	2.8	61.2
4	Yes	Natural	Yes	2.1	27.7
5	Yes	50 % Li ⁶	No	3.9	40.1
6	Yes	50 % Li ⁶	Yes	2.6	31.0

[3] W. Weibull, J. Applied Mech, 18 (1951).
 [4] M. Dalle Donne et al., in Proc. 18th SOFT, Karlsruhe 1994, Elsevier Science, B.V., p. 1229.

Staff:

- M. Dalle Donne
 R. Huber
 G. Piazza
 A. Weisenburger

B 3.2.1 Irradiation of $\text{Li}_4\text{SiO}_4 + \text{TeO}_2$ pebbles

Slightly overstoichiometric lithium orthosilicate ($\text{Li}_4\text{SiO}_4 + 2.2$ wt% SiO_2) pebbles with diameters between 0.25 and 0.63 mm are used as breeder material in the European Helium Cooled Pebble Bed (HCPB) blanket. Recent tests demonstrated that an addition of a small amount of TeO_2 increases the mechanical stability of the pebbles [1] (see section B3.1.1). To get a first idea on the tritium release characteristics annealing tests were performed with the reference (OSi, 7.5 % Li^6) and the new pebbles (OSi (Te), two charges: 7.5 and 50 % Li^6).

The pebbles (0.25 - 0.63 mm diameter) were dried (at different temperatures between 300 and 1030 °C), loaded under He atmosphere into dried quartz glass ampoules and irradiated in the HFR reactor at Petten to a tritium activity of about 4×10^8 Bq/g. The irradiation temperature was specified to be ≤ 150 °C. The tritium release was studied by out-of-pile annealing (purge gas He + 0.1 % H_2 , temperature ramp 5 °C/min to 850 °C).

The release behaviour depends on the drying temperature. The behaviour of well-dried (≥ 900 °C) samples is considered to be blanket - representative and is shown in Fig. 1 for OSi

Literature:

- [1] M. Dalle Donne et al., "Development work for lithium orthosilicate pebbles", SOFT-19, Lisbon, September 1996.
- [2] H. Kwast et al., J. Nucl. Mater. 212 - 215 (1994) 1010.

Staff:

E. Damm
 M. Dalle Donne
 R. Huber
 D. Knebel
 F. Scaffidi-Argentina
H. Werle
 H. Ziegler

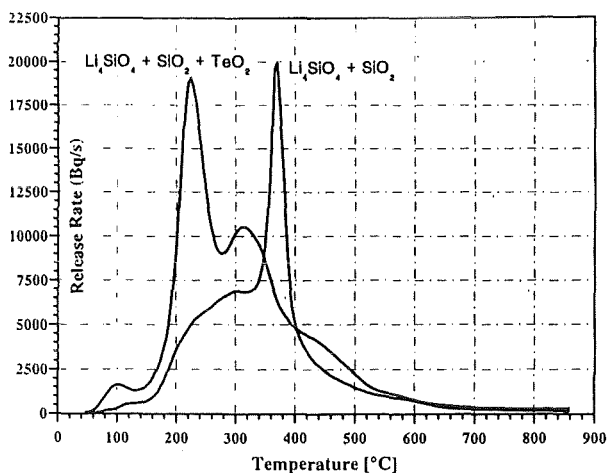


Fig. 1: Comparison of tritium release for reference OSi and OSi (Te) pebbles.

and OSi (Te, 50 % Li^6). The release rate as function of temperature during the 5 °C/min ramp is plotted. The release maximum is achieved for the OSi (Te) sample at lower temperature than for the reference OSi pebbles. Therefore it is expected that the inpile tritium release behaviour of the new OSi (Te) pebbles is better than that of the reference OSi pebbles, which have been carefully tested in EXOTIC-6 [2]. The new pebbles OSi (Te, 50 % Li^6) will be tested in the next European inpile experiment EXOTIC-8.

WP B 4 Beryllium Pebble Development

B 4.1.1 Characterization and Optimization of 2 mm and 0.1-0.2 mm Beryllium Pebbles

For the Helium Cooled Pebble Bed (HCPB) Blanket, which is one of the two reference concepts developed within the European Fusion Technology Programme, the neutron multiplier consists of a mixed bed of about 2 mm and 0.1-0.2 mm diameter beryllium pebbles [1]. The main structure of the pebble bed is given by the larger pebbles with a packing factor of 63%. In the space between them are placed the smaller beryllium pebbles with a packing factor of 18%.

Both kinds of pebbles are fabricated by melting, however for the larger ones a relatively inexpensive intermediate product of the beryllium fabrication route (Brush-Wellmann Company) has been chosen [2]. The present paper deals with the metallographic and mechanical tests performed for the bigger pebbles. Beryllium has no structural function in the blanket, however, microstructural and mechanical parameters are important, as they might influence the behavior of beryllium under neutron irradiation. Because of the poorly defined production conditions, the bigger pebbles are characterized by a quite large scatter in the microstructural and mechanical data. Therefore, a relatively large number of pebbles have been analyzed from both the metallographic and the mechanical point of view to get statistically representative data.

Metallographic analysis

For the metallographic analyses, 20 pebbles with a mean diameter of 2.1 mm and 20 pebbles with a mean diameter of 1.6 mm were selected. The pebbles show a relatively large number of indentations on their external surface. This is probably due to the fact that during the fabrication process very hot (or still partially molten) beryllium pebbles come in contact with cold and already solidified ones. With optical microscopy, a quite strong variation of coarse pores was observed. Some pebbles show big voids which seemed to be generated during the cooling phase of the fabrication process. Relatively often a coarse porosity with a pore size of 0.1-0.2 mm has been observed. It appears to be heaped up in "nests" and might have arisen from interconnected shrink holes. On the other hand, most of the pebbles reveal a very small micro-porosity usually oriented along the crystal axis showing a very fine dendritic or cellular structure. In general, it has been observed that the porosity of small pebbles is always smaller than that of the bigger ones, which clearly confirms that coarse porosity is generated during the cooling phase of the fabrication process. Furthermore, a large number of pebbles presents, near the external surface, a dense region the depth of which usually reaches 0.2-0.3 mm. A typical porosity distribution in a beryllium pebble is shown in Fig. 1.

The metallographic structure of both smaller and bigger pebbles shows the presence of large grains, in some of the

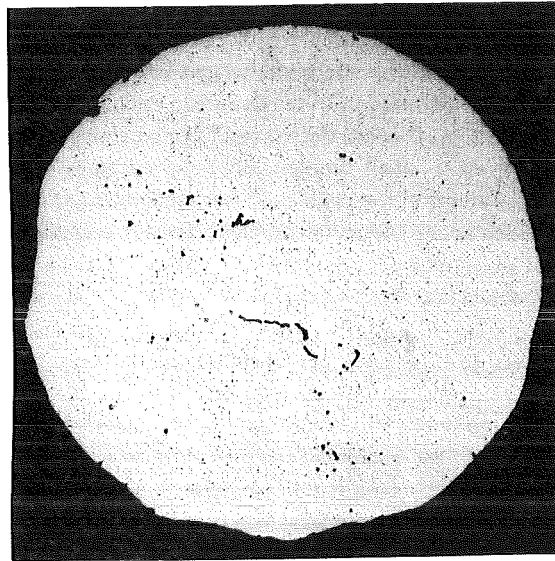


Fig. 1: Porosity distribution in a beryllium pebble

smaller pebbles as large as the pebble diameter as is clearly indicated in Fig. 2.



Fig. 2: Grain size distribution in the beryllium pebbles (polarized light)

Insoluble impurities have been usually observed on the grain boundaries, while iron and chrome are almost exclusively present in solid solution in the beryllium-matrix. The external surface of the large Be pebbles is usually covered by a $2\mu\text{m}$ thick SiO_2 layer and/or a fluorine layer (probably BeF_2) the thickness of which is generally lower than $2\mu\text{m}$. Two extraneous phases are present in almost all the analyzed pebbles as shown in Fig. 3. Mostly a round bright phase looking like an eutectic stored in the beryllium matrix and

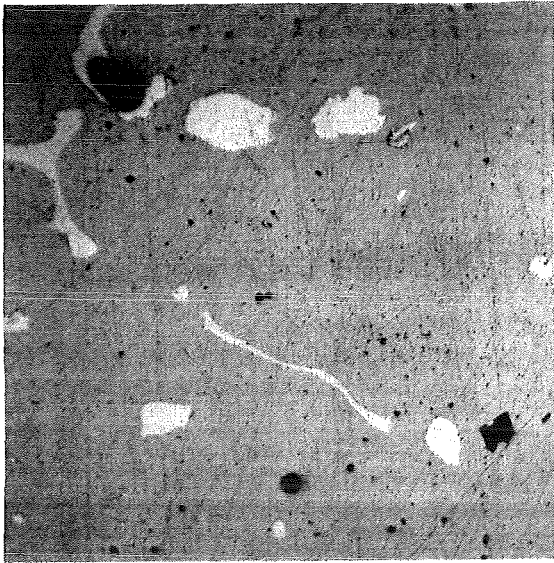


Fig. 3: Extraneous phases in the beryllium matrix

occasionally a dark square phase which appears as a primary precipitated phase has been observed. The dominant precipitated phases are Be_{13}Mg , $\text{Be}_{13}(\text{Mg}, \text{Zr}, \text{U})$, Mg_2Si and Al_2O_3 [3].

Mechanical behavior

The mechanical behavior of a significant number of pebbles with the larger diameter has been investigated by submitting them to compressive loads up to 1600 N at room temperature. The plastic deformations of the pebbles have been measured and correlated with the applied loads as shown in Fig. 4.

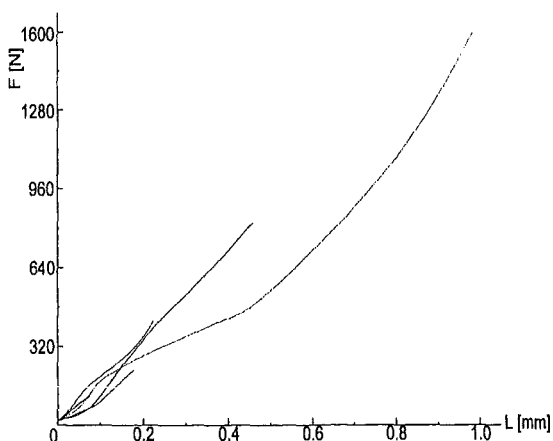


Fig. 4: Deformation of the Be-pebbles for various applied mechanical loads

As for the microstructure, relatively large variations have been observed in the mechanical response of the pebbles. However, probably due to the very small amount of BeO impurities ($\text{O}_2 < 0.2 \text{ wt\%}$), all the pebbles showed a high ductility at room temperature. Pebbles loaded up to 400 N

show diameter reductions up to 13% but, in spite of evident large plastic deformations, no fracturing or crack formation was registered as clearly shown in Fig. 5.

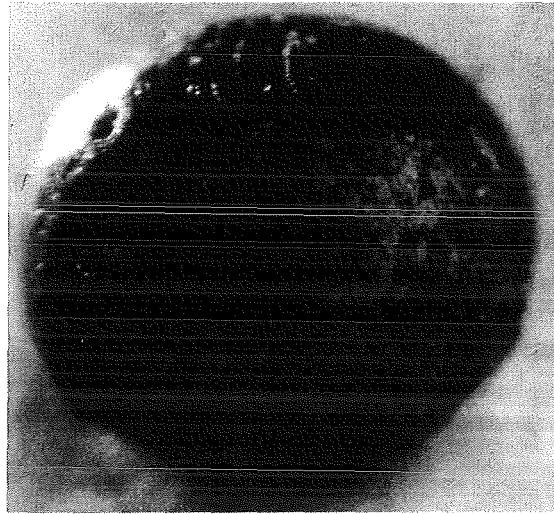


Fig. 5: Be-pebble after loading at 400 N

On the other hand, pebbles loaded with 800 N (diameter deformation up to 25%) or more, reveal cracks on their "meridian" planes as shown in Fig. 6.

Conclusions

A significant large number of beryllium pebbles with a mean diameter of 1.6 mm and 2.1 mm made by Brush-Wellman as an intermediate product in the beryllium production route has been analyzed from both the metallographic and the mechanical point of view. Because of the poorly defined production conditions, the pebbles are characterized by a large scatter in the microstructural and mechanical data.

A quite strong variation of coarse pores has been observed. Some pebbles show big voids which seem to be generated during the cooling phase of the fabrication process. On the other hand, most of the pebbles show a very small micro-

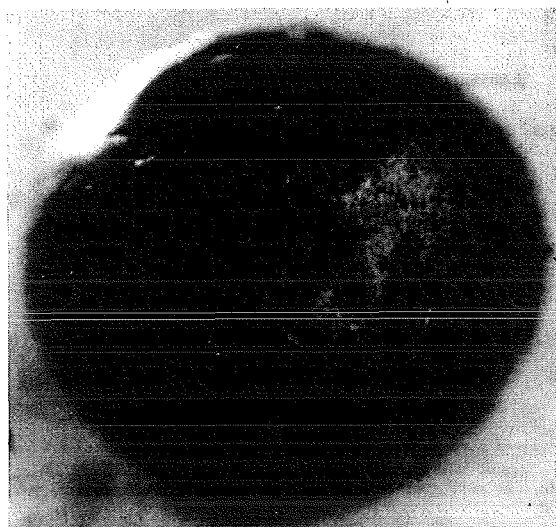


Fig. 6: Be-pebble after loading at 800 N

porosity usually oriented along the crystal axis. The metallographic structure of both smaller and bigger pebbles show the presence of large grains, in some of the smaller pebbles as large as the pebble diameter.

The mechanical behavior of pebbles with the larger diameter has been investigated by submitting them to compressive loads up to 1600 N at room temperature. After the compressive tests the pebbles have been analyzed by means of optical microscopy. Similar as for the microstructure, large variations have been observed in the mechanical response of the pebbles. However, probably due to the very small amount of BeO impurities, all the pebbles show a high ductility at room temperature: with evident large plastic deformations no fracturing of the pebbles was registered for diameter reductions up to 13%.

Literature:

- [1] M. Dalle Donne, et al., European DEMO BOT Solid Breeder Blanket, KfK Bericht 5429, Kernforschungszentrum Karlsruhe, November 1994.
- [2] Brush-Wellman, Private Communication.
- [3] H. Kleykamp, Private Communication.

Staff:

M. Dalle Donne

E. Kaiser

O. Romer

F. Scaffidi-Argentina

P. Weimar

H. Werle

H. Kleykamp

Chemical Analysis on Unirradiated Beryllium Pebbles

Beryllium is fabricated by dressing of the raw beryl resulting in Be hydroxides which react with gaseous HF to BeF_2 and H_2O by a modified Kroll process. The metal is reduced by Mg according to the reaction $\text{BeF}_2 + \text{Mg} = \text{Be} + \text{MgF}_2$ between 1300 and 1400°C. Both phases are immiscible and liquid at these temperatures. Slow cooling of the lighter phase results in Be spheres in the 2 mm diameter range on the liquid MgF_2 surface. This solid material is an intermediate product of the beryllium processing.

The spheres were used for the irradiation experiments CORELLI-2, Be/Pe irradiation and EXOTIC-7. Unirradiated samples were investigated by X-ray microanalysis. The instrument was equipped with a synthetic multilayer crystal of the lattice spacing $2d = 20$ nm to analyse the electron beam induced, extremely soft characteristic $\text{BeK}\alpha$ radiation of the wavelength $\lambda = 11.4$ nm by diffraction of a wavelength dispersive X-ray spectrometer. The total impurity concentration is 0.7%. Precipitates of the impurities less than $10 \mu\text{m}$ in diameter were observed predominantly in the grain boundaries of the Be grains. The main precipitates are Be_{13}Mg , $\text{Be}_{13}(\text{Mg}, \text{Zr}, \text{U})$, Mg_2Si and Al_2O_3 . Fe and Cr are nearly exclusively dissolved in the Be matrix. The Be surface is coated by a $2 \mu\text{m}$ thick discontinuous SiO_2 layer and partly by a less than $2 \mu\text{m}$ thick fluoride layer. The analysis reveals further the maximum solubilities in Be at its melting point $T_m = 1289^\circ\text{C}$: 0.010 at. % Si, 0.008 at. % Fe, 0.002 at. % Cr.

Further analysis on unirradiated 2 mm diameter Be pebbles of the heat Be MS1-EMC-171 with 0.4 % total impurities results in the following precipitates in the Be matrix: MgBe_{13} , Mg_2Si and a two-phase Al-Mg alloy. The main impurities are Mg, Al and Si. The phase Mg_2Si is the primary precipitate ($T_m = 1085^\circ\text{C}$) in this ternary sub-system. The residual Al-Mg melt contains nearly no Si and solidifies between 460 and 437°C . The Be pebbles contain some cavities, their surfaces are covered with Fe-Cr phases. A supposed phase AlFeBe_4 was not observed.

A heat treatment did not change significantly the number density and composition of the precipitates in both Be heats.

Staff:

H. Kleykamp

H. D. Gottschalg

B 4.2.1 Evaluation of Beryllium Irradiation Experiments and Improvements of ANFIBE

1. Evaluation of the "Beryllium Irradiation Experiment" in HFR/Petten

For the Helium Cooled Pebble Bed (HCPB) Blanket [1], which is one of the two reference concepts studied within the European Fusion Technology Programme, the neutron multiplier consists of a mixed bed of about 2 mm and 0.1-0.2 mm diameter beryllium pebbles (packing factor 63% and 18% respectively) to achieve a high bed density ($\approx 1.5 \text{ g/cm}^3$).

In the fast neutron field of a fusion reactor tritium is produced in beryllium which, due to the relatively slow tritium release at normal blanket temperatures is accumulated but may be released during an uncontrolled temperature increase. Therefore, for safety considerations a good knowledge of tritium inventory and release kinetics is important.

In this paper the results of the first tritium annealing studies with the two types of beryllium pebbles are presented and compared with previously investigated beryllium samples and with predictions by the ANFIBE code [2].

Samples and irradiation conditions

Both types of pebbles are fabricated by Brush-Wellman. The large pebbles are an intermediate product, which results after separation of molten beryllium and MgF_2 . The small pebbles are produced from molten beryllium either by the rotating electrode method (REP) or by spraying with an inert gas. The main characteristics are summarized in Tab. 1.

Table 1: Main characteristics of the pebbles [3]

Type	Diameter (mm)	Closed porosity (%)	BeO (wt%)	Other impurities (wt%)
Large pebbles	1.5-2.3	0.57	0.3	Fe 0.18 Mg 0.12 others < 0.1
Small pebbles (REP)	0.08-0.18	0.86	0.08	Each < 0.1

The small pebbles are characterized by a smooth surface and no open porosity, whilst the large pebbles by dimples on the surface and some open (big and small) porosity [4].

Mixtures of large and small pebbles were dried by purging them with helium at 650 °C for 3 hours and filled into steel capsules.

The capsules were evacuated, then filled with 1.1 bar helium and closed by welding. The capsules were irradiated from

April to August 1994 over four reactor cycles in the HFR-Petten reactor (irradiation "Beryllium") at a temperature of about 420 °C (capsules 2 and 3) and 510 °C (capsules 5 to 8) to a fast neutron fluence ($E > 1 \text{ MeV}$) of about $1.0 \cdot 10^{21} \text{ cm}^{-2}$ (capsules 2 and 3) and $1.2 \cdot 10^{21} \text{ cm}^{-2}$ (capsules 5 to 8) [5]. After irradiation the samples were handled under inert atmosphere before annealing.

Tritium release annealing tests

For the tritium release annealing tests the two types of pebbles were first separated by sieving. Release kinetics and total amount of released tritium were determined by annealing the pebbles with 5 °C/min up to 850 °C, keeping constant this temperature for about 3 hours and purging them with 50 SCCM He+0.1 vol% H_2 .

A series of tests showed that the release characteristics of each type of pebbles is reproducible and essentially the same for all the capsules. In Fig. 1 representative release curves for

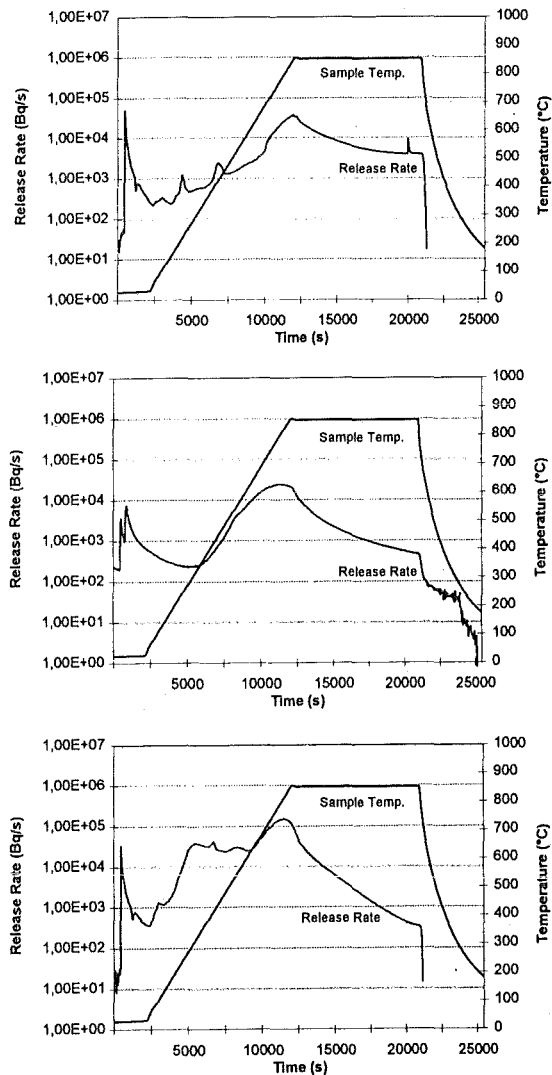


Fig. 1: Tritium release kinetics for large beryllium pebbles (top), pieces from crushed large pebbles (middle) and for small pebbles (bottom).

large pebbles, pieces ($\Phi < 0.7$ mm) from crushed large pebbles and for small pebbles (all from capsule 2) are shown.

Useful parameters to characterize tritium release kinetics are the fractional release (release R/production P), the temperature T_{max} corresponding to the maximum release rate (during the 5 °C/min temperature ramp) and the factor DF by which the release rate decreases (at 850 °C within 3 hours). For the pebbles investigated in the frame of the present work and for previously investigated beryllium samples these parameters are given in Tab. 2.

From Fig. 1 and the data of Tab. 2 the following conclusions concerning tritium release kinetics can be drawn:

- Release from 0.7 mm diameter pieces from the large pebbles is faster than that from the whole pebbles ("particle size" effect). A further decrease of the particle size to ≤ 0.5 mm diameter indicated no further release improvement.
- Release from the small pebbles is faster than that from 0.7 mm diameter pieces from the large pebbles.
- Release from previously investigated Brush-Wellman samples (B-26, S200-HIP) [6-8] is comparable with that from the large pebbles. Therefore, it can be assumed that the experimentally determined tritium residence times of beryllium B-26 [7] apply also to the large pebbles.
- Release from "old" beryllium (Kawecki Berylco) irradiated with moderate fluences is slow. However, if it is irradiated with high neutron fluences, the release is pretty fast, probably due to the formation of porosities caused by the migration of helium bubbles [7].

Comparison of experimental data with ANFIBE predictions

In order to better understand the physical mechanisms governing tritium release behaviour, the performed annealing experiments have been simulated with the ANFIBE code [2]. The different tritium release kinetics between small and large beryllium pebbles is essentially due to the different helium release kinetics during the annealing tests. Calculations indicate in fact that, for both small and large pebbles, most of tritium produced during in-pile irradiation is trapped into relatively small intragranular helium bubbles ($r \approx 7$ nm). During the annealing at high temperature these bubbles move into the lattice and tend to coalesce, thus forming bigger bubbles the radius of which will reach about 20 nm. Because the bubble diffusion coefficient decreases strongly with the bubble radius ($\propto 1/r^4$) the integral migration distance

$$x(t) = \sqrt{6D_b(r)t}$$

covered by a growing bubble will attain rapidly an asymptotic value which is determined by the distance migrated during the early bubble lifetime.

Therefore, tritium trapped in helium bubbles will reach the sample free surfaces much easier in the case of small pebbles than in the case of larger ones. This "particle size" effect explains why tritium release from larger pebbles is slower than that from smaller ones. The calculated fractional release for the large beryllium pebbles, for the pieces from crushed large pebbles and for the small pebbles is 32%, 60% and 95% respectively, which is in good agreement with the experimental data reported in Tab. 2.

Conclusions

Tritium release kinetics of a variety of beryllium samples was studied and was found to be pretty similar. A common

Table 2: Tritium release characteristics of various beryllium samples

Irradiation	Material	Φ [cm^{-2}] ($E > 1$ MeV)	P [Bq/g]	R [Bq/g]	R/P [%]	T_{max} [°C]	DF
"Beryllium" Capsule 2	Large pebbles	$1.0 \cdot 10^{21}$	$2.1 \cdot 10^9$	$8.0 \cdot 10^8$	40	> 850	10
	Large pebbles (pieces)	$1.0 \cdot 10^{21}$	$2.1 \cdot 10^9$	$1.4 \cdot 10^9$	70	800	50
	Small pebbles	$1.0 \cdot 10^{21}$	$2.1 \cdot 10^9$	$2.0 \cdot 10^9$	100	400, 800	$5 \cdot 10^2$
SIBELIUS [6,7]	Brush-Wellman, B-26 BeO < 300 ppm pellets $\Phi 8 \times 2$ mm	$\approx 7.0 \cdot 10^{20}$	$\approx 1.0 \cdot 10^9$	$8.0 \cdot 10^8$	≈ 80	> 850	20
Mol F-BSBE1 [8]	Brush-Wellman S200-HIP BeO = 0.9 wt% pieces $\Phi \approx 2$ mm	$1.6 \cdot 10^{21}$	$4.0 \cdot 10^9$	$2.0 \cdot 10^9$	50	600 > 850	20
Mol BR2 core [7]	Kawecki Berylco vacuum hot pressed BeO < 2 wt% pieces $\Phi \approx 2$ mm	$8.0 \cdot 10^{21}$	$4.0 \cdot 10^{10}$	$4.0 \cdot 10^9$	10	> 850	5
		$2.8 \cdot 10^{22}$	$1.5 \cdot 10^{11}$	$1.4 \cdot 10^{11}$	90	840	10^3
		$3.9 \cdot 10^{22}$	$2.2 \cdot 10^{11}$	$2.2 \cdot 10^{11}$	95	≈ 800	10^4

feature of all samples during annealing with 5 °C/min up to 850 °C is that the maximum release rate is achieved at temperatures higher than 800 °C. Nevertheless, the following differences exist:

- The release for 0.7 mm diameter pieces from the large pebbles is faster than that from the whole pebbles ("particle size" effect).
- The release for small pebbles is faster than that from 0.7 mm diameter pieces from the large pebbles.
- The release for previously investigated Brush-Wellman beryllium (B-26, S200-HIP) is comparable with that for the large pebbles.
- The release for "old" beryllium (Kawecki Berylco) irradiated with moderate fluences is slower than that for "modern" beryllium (Brush-Wellman).

Literature:

- [1] M. Dalle Donne, Status and Further Development of the European Ceramic Breeder Blanket, Jahrestagung Kerntechnik, Mannheim, 1996.
- [2] F. Scaffidi-Argentina, Modellierung des Schwellens und der Tritium-Freisetzung von bestrahltem Beryllium, FZKA Bericht 5632, Karlsruhe, Oktober 1995.
- [3] M. Dalle Donne, et al., European DEMO BOT Solid Breeder Blanket, KfK Bericht 5429, Karlsruhe, November 1994.
- [4] P. Weimar and H. Werle, Irradiation Behaviour of Lithium Orthosilicate and Beryllium Pebbles, Proceedings of the Fourth International Workshop on Ceramic Breeder Blanket Interactions, Kyoto, 1995.
- [5] R. Conrad and R. May, Project D282.01, Beryllium, Final Irradiation Report, Report HFR/95/4262, Petten, May, 1995.
- [6] W. Dienst, D. Schild, H. Werle, Tritium Release of Li_4SiO_4 , Li_2O and Beryllium and chemical compatibility of Beryllium with Li_4SiO_4 , Li_2O and Steel (SIBELIUS Irradiation), KfK Bericht 5109, Karlsruhe, December 1992.
- [7] F. Scaffidi-Argentina and H. Werle, Tritium Release from Neutron Irradiated Beryllium: Kinetics, Long-Time Annealing and Effect of Crack Formation, Proceedings of the Second IEA International Workshop on Beryllium Technology for Fusion, Jackson Lake Lodge, 1995.
- [8] S. Rübél and H. Werle, Preliminary Tests Concerning Tritium Retention in Irradiated Beryllium (Irradiation Mol F-BSBE1), Karlsruhe, August 1996, (to be published).

Staff:

E. Damm
M. Dalle Donne
D. Knebel
F. Scaffidi-Argentina
H. Werle
H. Ziegler

2. Evaluation of the EXOTIC-7 Experiment in HFR/Petten

Pore Formation in Be-Pebbles at High Li-Burnup

In the frame of the Irradiation Experiment EXOTIC 7 also mixed beds of Li_4SiO_4 Pebbles ($d = 0.1 - 0.2$ mm) and Beryllium pebbles ($d = 0.1 - 0.2$ und 2.0 mm) were irradiated. With a high Li^6 -enrichment of 50% the effect of a long term irradiation on the behaviour of the material with Li-burnups of $> 16\%$ should be simulated. The irradiation was conducted over 10 HFR-cycles (cycle 94.02 - 94.11) over a total of 235.61 full power days. (Tab. 1)[1].

The T-release was measured in - pile at HFR/Petten and out of pile in the hot cells at FZK. The results of these measurements are presented below.

An important question for the assessment of the, HCPB blanket was and is the behaviour of both mentioned materials in form of pebbles during irradiation. Results of examination of irradiated Li_4SiO_4 cannot yet be given in conclusion as important examinations with the microprobe and x-rax diffractometry are to be done finally. The influence of Li-burnup on fracture strength of Li_4SiO_4 [2] was already reported. In the Li_4SiO_4 /beryllium mixed bed (capsule 28.2) a bracing due to Be-swelling by He-formation was found. By this difficulties during take out of the mixed bed originated at Petten Hot Cells [4].

The expected formation of pores in the Be matrix due to He-deposition cannot be proved by metallography without a suitable treatment of the irradiated pebbles.

For this reason the big beryllium pebbles from capsule 28.2 were sorted out and annealed at 850°C to provoke a coagulation of the He which is dissolved in the lattice. After the heat treatment some pebbles were cooled in liquid N_2 and broken in a special device. After this treatment pores could be found by investigation with the scanning electron microprobe (SEM).

The pebbles were examined under 3 different conditions: a) not annealed + broken, b) annealed + broken, c) broken + subsequently annealed.

Figs. 1 and 2 show the relevant SEM images. Only pebbles which were prepared by treatment b) show He bubbles. These pores can be found both inter- and intragranular.

Table 1: Irradiation history - capsule 28.2; T - production and Li - burnup [2]

cycle	T prod. at cycle Start		T prod. at cycle end		burn-up %		power (n, a) [W/g]		total T produced	
	atoms/s	mCi/min	atoms/s	mCi/min	⁶ Li	total Li	cycle start	cycle end	atoms	Bq
capsule:	28.2		weight of		Li ₄ SiO ₄ 1.843 [g]		vol. of		Li ₄ SiO ₄ 0.796 [cm ³]	
matenal:	Li ₄ SiO ₄ pebbles		sample volume		8.119 [cm ³]		density of		Li ₄ SiO ₄ 0.227 [g cm ³]	
supplier:	Be pebb. 0.1		vol. % of		Li ₄ SiO ₄ 9.81%		(sample vol)			
	Be pebb. 2									
cycle 94.02	3.50E+14	1.022	3.40E+14	0.993	2.85	1.42	145.39	141.47	5.36E+20	9.650E+11
cycle 94.03	3.57E+14	1.043	3.42E+14	0.999	6.81	3.40	148.31	142.27	1.28E+21	2.300E+12
cycle 94.04	3.47E+14	1.013	3.33E+14	0.973	10.65	5.33	144.36	138.49	2.00E+21	3.597E+12
cycle 94.05	3.26E+14	0.952	3.13E+14	0.914	14.35	7.18	135.64	130.23	2.69E+21	4.841E+12
cycle 94.06	3.09E+14	0.902	2.97E+14	0.867	17.84	8.92	128.29	123.27	3.34E+21	6.015E+12
cycle 94.07	3.08E+14	0.900	2.97E+14	0.867	20.95	10.48	128.05	123.25	3.92E+21	7.060E+12
cycle 94.08	3.08E+14	0.900	2.94E+14	0.859	24.37	12.19	127.84	122.38	4.54E+21	8.178E+12
cycle 94.09	2.95E+14	0.862	2.63E+14	0.827	27.46	13.73	122.52	117.66	5.12E+21	9.223E+12
cycle 94.10	2.71E+14	0.791	2.54E+14	0.771	30.15	15.08	112.29	108.30	5.63E+21	1.013E+13
cycle 94.11	2.58E+14	0.754	2.48E+14	0.724	33.10	16.55	107.37	103.01	6.18E+21	1.113E+13

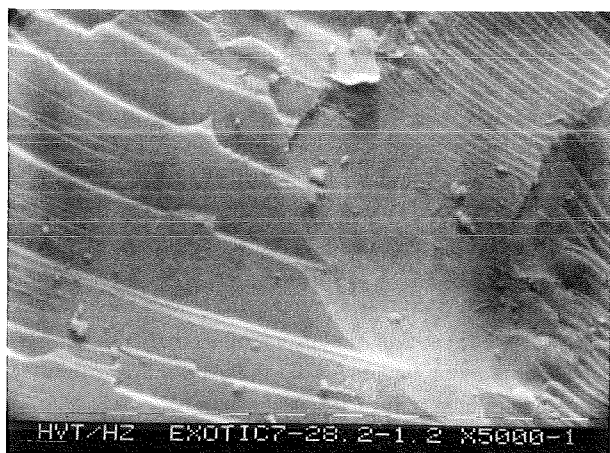


Fig. 1: Be pebble: not annealed + broken

Besides this Be pebbles which were irradiated in the mixed bed show a strong pore formation on their surface due to T-deposition by recoil from the Li - orthosilicate (Fig. 2a) and 2b)).

Literature:

[1] R. Conrad, R. May: Technical Memorandum HFR / 95 /4195 (1995)

[2] P. Weimar, H. Werle: Irradiation Behaviour of Lithium Orthosilicate and Beryllium Pebbles. 4.th Int. Workshop on Ceramic Breeder Blanket Interactions. Kyoto, Japan, Oct. 9 -11 1995

[3] J. G. van der Laan et al.: Irradiation Behaviour of Ceramic Breeder Materials at High Li - Burnup.4.th Int. Workshop on Ceramic Breeder Blanket Interactions. Kyoto, Japan, Oct. 9 -11 1995

Staff:

- H. Häfner
- E. Kaiser
- D. Knebel
- B. Neufang
- R. Pejsa
- O. Romer
- H. Steiner
- A. Wacker
- P. Weimar
- G. Weih
- F. Weiser
- H. Ziegler

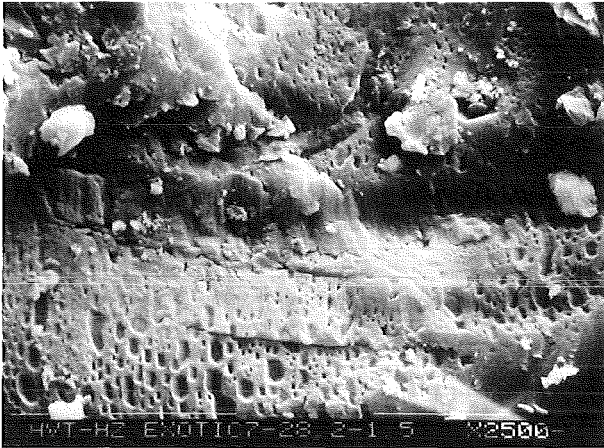


Fig. 2: Be pebble: annealed + broken
a) surface of Be pebble: pores by T-recoil

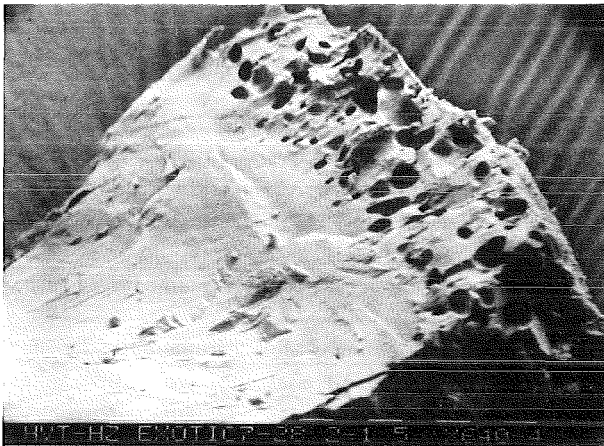


Fig. 2: Be pebble: annealed + broken
b) surface of Be pebble: pores by T-recoil



Fig. 2: Be pebble: annealed + broken
c) pores in the Be matrix

Tritium Release from Be-Pebbles

Tritium release from beryllium pebbles irradiated in the HFR Petten reactor during the EXOTIC-7 experiment [1] has been investigated by means of out-of-pile annealing tests. Tritium release and total released tritium were studied by purging with He + 0.1% H₂ and heating with 5°C/min up to 850 °C and heaping this temperature for several hours.

Release of all investigated Be samples (Be 2mm, Be 2mm broken, Be 0.1-0.2 mm) from the mixed beds of capsules 28.2 and 26.2-1 is very similar (Figs. 1 and 2): in agreement with

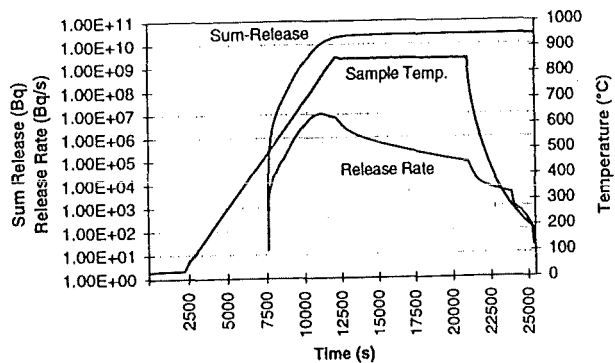
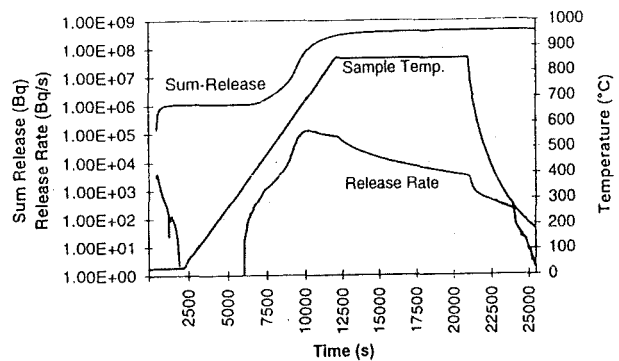
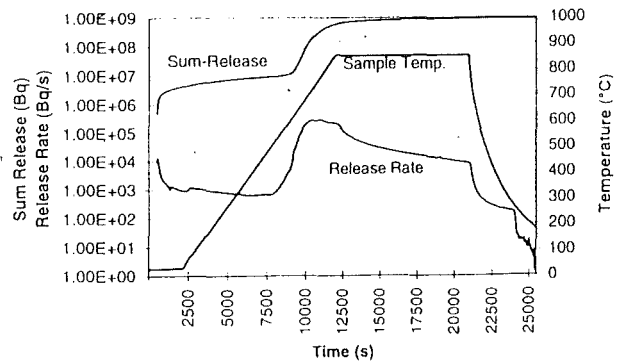


Fig. 1: Tritium release from beryllium of capsule 28.2 (mixed bed).

previous studies [2] the release starts at about 500 °C and achieves a maximum at about 700 °C. The total release of the

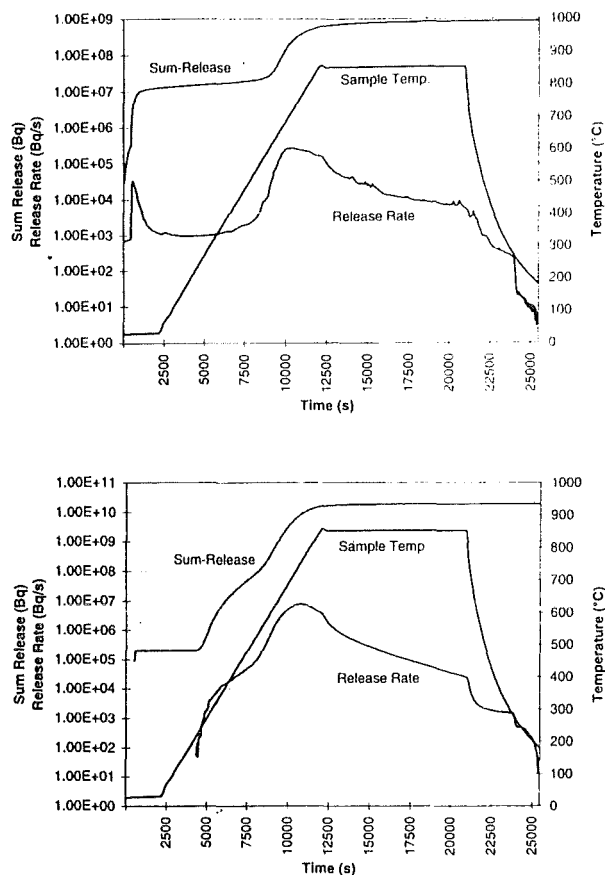


Fig. 2: Tritium release from beryllium of capsule 26.2-1 (mixed bed)

large Be pebbles (Be 2mm) is slightly larger ($\approx 6 \cdot 10^{10}$ Bq/g) than that from Li_4SiO_4 from the same capsules, while that of the small Be pebbles (Be 0.1-0.2mm) is about a factor 30 larger ($\approx 1 \cdot 10^{12}$ Bq/g). Once tritium is produced/implanted in Be it diffuses at a significant rate to sites of lower free energy (i.e. He bubbles) and/or it chemically reacts with impurities for which it has a particular affinity (i.e. BeO) [3]. Release kinetics is, therefore expected to be dependent on the particular trapping mechanisms and, in particular, to be hindered both by structural sinks (physical trapping) and by beryllium oxide impurities (chemical trapping). The observed release at about 500 °C is probably due to tritium escaping from chemical traps, while the maximum release at about 700 °C is due to tritium escaping from physical traps. The latter release should be accompanied by a contemporaneous release of He.

According to previous studies [2] it is expected that, if Be is in direct contact with ceramics during irradiations, a fraction of the 2.74 MeV tritons produced in the Li_4SiO_4 is implanted in a surface layer of beryllium (depth $\approx 40\mu\text{m}$). This leads to an additional inventory which is usually several times larger than the neutron-produced one.

Tritium generation data in Be for both capsules 26.2-1 and 28.2 are not yet available. However, with reference to calculations for the D282.01 experiment [4] one can estimate a ratio He-production/T-production of a about 45. Being the

He-production rate in Be for the HFR reactor about 3440 appm per 10^{22} n/cm² ($E_n \geq 1$ MeV) [5], the total He produced at the end of the EXOTIC-7 experiment (in both capsules 26.2-1 and 28.2) should be 450 appm. This leads to a specific tritium production in Be of $1.3 \cdot 10^9$ Bq/g in reasonable agreement with a value of $2.0 \cdot 10^9$ Bq/g based on tritium production vs. fast fluence graph [6]. In any case, the neutron-generated tritium in Be is about a factor 50 lower than the released tritium from the larger Be pebbles and a about a factor 700 lower than that from the smaller Be pebbles, assuming no release during the irradiation. This high tritium inventory in both the large and small Be pebbles from capsules 26.2-1 and 28.2 can be only due to implantation from ceramics. Furthermore, the total release from the small Be pebbles is about a factor 15 larger than that from the bigger ones. This is probably due to the fact that in the small Be pebbles the implantation depth of tritium coming from ceramics ($\approx 40\mu\text{m}$) is of the same order of magnitude of the pebbles radius ($\approx 50-100 \mu\text{m}$), which results in a higher implantation efficiency than in the case of larger Be pebbles.

Literature:

- [1] R. Conrad, R. May, "EXOTIC-7, Irradiation Progress Report No. 11", Technical Memorandum HFR/95/4196, JRC Petten, April 1995.
- [2] F. Scaffidi-Argentina, H. Werle, "Tritium Release from Neutron Irradiated Beryllium: Kinetics, Long-Time Annealing and Effect of Crack Formation", Proceeding of the 2nd IEA International Workshop on Beryllium for Fusion, Jackson Lake Lodge, September 6-8, 1995.
- [3] F. Scaffidi-Argentina, "Modellierung des Schwellens und der Tritium-Freisetzung von bestrahltem Beryllium", FZKA Report 5632, Forschungszentrum Karlsruhe, October 1995.
- [4] R. Conrad, R. May, "Irradiation of Beryllium and Ortho-Silicate Spheres for the FZK Concept of the Helium-Cooled BOT Ceramic Breeder Blanket for DEMO in the HFR Petten", Technical Memorandum HFR/95/4262, JRC Petten, Mai 1996.
- [5] M. Küchle, "Material Data Base for the NET Test Blanket Design Studies", KfK Internal Report, Kernforschungszentrum Karlsruhe, February 1990.
- [6] H. Werle, "Release of Neutron-Generated Tritium from Beryllium", KfK Internal Report INR-1906, Kernforschungszentrum Karlsruhe, October 1994.

Staff:

- | | |
|----------------|-----------------------|
| E. Damm | S. Rübel |
| M. Dalle Donne | F. Scaffidi-Argentina |
| R. Huber | <u>H. Werle</u> |
| D. Knebel | H. Ziegler |

WP B 5 Tritium Control including Permeation Barriers

B 5.1.1 Calculation of Tritium Permeation Losses from Purge Gas System and First Wall

In the Helium Cooled Pebble Bed blanket for a DEMO reactor [1], the breeder and the neutron multiplier consist of separate beds of Li_4SiO_4 and beryllium pebbles respectively. These beds are contained between steel plates cooled by high pressure helium. The tritium produced in both beds is carried away by helium at atmospheric pressure. The First Wall and the other parts of the blanket, made of martensitic steel MANET, are cooled by high pressure helium.

The heat produced in the blanket is transmitted to the steam turbines by means of large heat exchangers.

The main path by which tritium may get to the ambient is given by:

- injection of tritium from the plasma into the First Wall and then through permeation to the helium main coolant system;
- permeation of tritium from the tritium purging system through the pebble bed containing walls to the helium main coolant system;
- tritium permeation from the helium main coolant system through the Incoloy 800 walls of the steam generators to the steam turbine cycle.

Permeation through the First Wall

The permeation is given by the tritium and deuterium ions impinging on the First Wall. A part of these ions recombines at the FW surface and returns to the plasma (recombination process), the other is implanted into the First Wall and diffuses to the surface of the FW helium coolant channels. Here it can recombine to form molecules, which end up in the main helium coolant system. The molecules can also dissociate at the surface to generate atoms again (dissociation process).

A description of these chemical phenomena and a theoretical formulation of the surface recombination rate is given by Baskes ([2], Eq.24). The recombination rate constant includes factors depending on the material's physical properties and a nondimensional parameter, the *sticking factor*, whose value is dependent on the state of oxidation of the surface. The more oxidized is the surface, the lower is the sticking factor's value, from 1 for a clean surface to 10^{-4} + 10^{-5} for an oxidized one. The relation between the recombination coefficient and the dissociation one, which has a lesser impact on the permeation, is given by the formula $K_d = K_r * K_s^2$ where K_s is the of the material's solubility ([3], Eq.2). The diffusion of the atoms through the material is also influenced by the Soret effect, that is the tendency of gas atoms to move under a gradient in temperature [4]. The properties relative to the

retention of the diffusing atoms are also important in the tritium control issue.

MANET First Wall (DEMO)

At the time of the DEMO Reactor construction the experience acquired by ITER operation should allow a sufficient knowledge of the plasma behaviour to avoid the presence of oxygen at the wall surface, which is the factor affecting the sticking factor, thus making possible to use a bare MANET First Wall. The experiments with deuterium ions performed at INEL [5] have shown that the impinging ions eject away the atoms of oxygen from the specimen surface, thus increasing the sticking factor. The experimental value for the recombination coefficient reported in [5] for HT-9, a ferritic steel very similar to MANET, has been assumed in the present calculations. The correction for the different temperatures in the present design was made by means of the Baskes equation and data about tritium solubility and diffusivity in MANET, measured by Forcey et al. [6]. The calculations were performed by means of the one-dimensional TMAP4 code [7]. The effects of the presence of the FW cooling channels have been assessed by the analogy of the tritium diffusion and the thermal diffusion by the use of the ABAQUS code [8].

Tab. 1 shows the results concerning the tritium permeation in the case of two states of oxidation of the FW cooling channel surface. One can see how the two-dimensional geometry does not reduce the permeation noticeably (less than 6%).

Table 1: Tritium permeation from the DEMO FW and inventory. Incident flux: 1.5×10^{20} (const.)
FW permeating surface: 730 m²

	Two-dim. calculation		One-dim. calculation	
Sticking factor	10^{-4}	10^{-5}	10^{-4}	10^{-5}
Permeation rate (g/d)	11.9	8.47	12.5	8.87
Trapped inventory (g)	1.79	2.21	1.69	2.10
Mobule inventory (g)	0.68	0.78	0.65	0.75
Total inventory (g)	2.47	2.99	2.34	2.85

Beryllium-MANET First Wall

An alternative is represented by a 5mm protective layer of beryllium. This is particular important for the assessment of the tritium permeation in the test module to be irradiated in ITER (pulsed operation incident flux = 1×10^{20} ions/m²·s with 1000 pulses and 1200 s plasma dwell time).

Surface modification of the beryllium by the plasma could strongly influence both the tritium permeation and the retention. Particularly important is the tendency of the surface to become pitted during ion implantation. To model the effects of surface pitting on the reemission and permeation characteristics of implanted hydrogen isotopes a new application of the TMAP4 code has been developed. This modelling technique involves the creation of a fictitious volume between the disturbed surface layer where the pitting occurs and the relatively undisturbed beryllium matrix [9]. A pitting surface area of 10% of the total was assumed for the beryllium layer. Compared with the case of no pitting, the pits result in a reduction of permeation by more than a factor of three, and an increase in the time delay to breakthrough by a similar amount.

Fig.1 shows the permeation rate as a function of time: there is appreciable permeation only after about 80 days and the 95% of the asymptotic value (i.e. 8.9×10^{-3} g/d for 1.2 m^2) is reached after about 130 days.

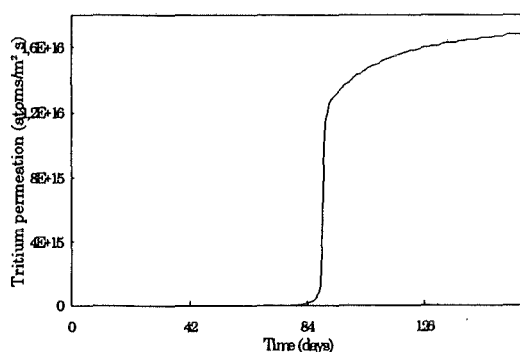


Fig. 1: Be (with pits)-MANET First Wall (ITER test module)

The tritium inventory in the First Wall (1.85 grams for 1.2 m^2) is almost completely retained in the beryllium. Other phenomena such as beryllium erosion and/or the possible formation of a beryllium oxide on the plasma side require further work.

Tungsten-MANET First Wall

An alternative solution to the beryllium as coating material for the First Wall may be given by the tungsten. An estimate of the tritium permeation in the case of a 3 mm thick tungsten layer has been therefore performed with the TMAP4 code. The change in time of the permeation rate is substantially similar to that seen for the beryllium (Fig. 1) except for the fact that the time before noticeable permeation occurs is shorter (17 days) as well as that to reach the asymptote (115 days). The resulting permeation is very low ($7. \times 10^{-5}$ g/d for 1.2 m^2) and this is probably due to the relatively high recombination rate constant suggested by Anderl et al. [10] for the tungsten.

Permeation from the Purge Flow System

Another source of contamination of the helium main circuit is given by the permeation through the walls separating the ceramic breeder and the beryllium from the helium coolant.

The performed calculations are based on the experimental data of Forcey et al. for hydrogen permeation through MANET [6] and the pessimistic assumption that all the tritium in the purge flow is 100% in the form HT ($p_{HT} = 100 \text{ Pa}$ in the helium purge flow). The Li_4SiO_4 bed has been subdivided in eight radial sectors (11, Fig. 2.5.1). For each sector the local partial pressure p_{HT} has been determined as well as the corresponding local dilution, i.e. the ratio p_{H_2}/p_{HT} . The obtained results are reported in Tab. 2.

Table 2: Permeation from the purge flow system (Li_4SiO_4 pebble beds)

	Inboard	Outboard	Total
Perm. surface (m^2)	2665	6455	9120
p_{HT} at the pebble bed outlet (Pa)	0.58	1.20	---
p_{H_2}/p_{HT} ratio at the pebble bed outlet	196	94	---
T-permeation (g/d)	0.13	0.65	0.78
H-permeation (g/d)	41.8	101.7	143.5

Permeation through the Steam Generators

The DEMO main helium coolant system characteristic values are the pressure (8 Mpa), the temperature (inlet=250 °C, outlet=450 °C) and the coolant mass flow (1751 Kg/s outboard, 653 Kg/s inboard), [1].

Because of the presence of tritium and other impurities in the helium circuit, a helium purification system is unavoidable. The main adopted assumptions are hereafter briefly reviewed.

1. The steam generators (helium/water) have been divided in 40 sections, each with the relevant local temperatures and surface dimensions; therefore 40 different contributions to the final permeation have been calculated.
2. In the evaluation of the partial pressures of the hydrogen isotopes in the main coolant system due account has been taken by the fact that these isotopes are continuously extracted by means of the helium purification system (0.1% of the of total helium mass flow) with an efficiency of 95%.

3. The swamping effect on the tritium permeation caused by the other two hydrogen isotopes has been accounted for by using the equation suggested by Bell and Redman for tritium permeation through Incoloy 800 ([11], eq.2).
4. The isotopic effect on the permeability has been also accounted for ([11], eq.8-9).
5. A total water leakage of 4 Kg/d through the heat exchangers into the main helium system has been assumed.

Tab.3 shows the final results. They have been obtained by using the Bell and Redman equation valid for Incoloy 800 without any superficial oxide layer ([11], p.1580). According to Bell, with the temperatures proposed in the DEMO reference design (helium = 250-450 °C, tube wall= 160-360 °C, H₂O=120-320 °C) there will be on the water side a permeation reduction factor (PRF) of at least 10 as well as on the helium side, if the oxygen potential in helium, provided for instance by a certain H₂/H₂O ratio, is capable of oxidizing chromium. This range is quite wide and the oxygen potential in the coolant helium can be easily produced with the help of the helium purification system. The oxide layer with PRF=10 will be very thin and thus very stable against thermal transients. The combined PRF will be then 10+10=20 and will suffice to reduce the tritium permeation through the heat exchangers below 20 Ci/d in both cases considered in Tab.3.

Conclusions

The present calculations show that with the HCPB blanket it is possible to reduce the tritium permeation through the steam generators below an acceptable level (20 Ci/d) without need of special coatings. This requires a sufficiently high oxygen potential in the main helium coolant system, which can be easily produced with the help of the helium purification system, to provide a thin and stable oxide layer on the helium side surface of the steam generators. Of course, these calculations must be validated with experiments which are

presently foreseen by the European DEMO blanket programme.

Furthermore it has been shown that the tritium permeation to the FW cooling channels of the HCPB blanket test module in ITER will be reached after a relative long time (80 days) with a beryllium coating or it is very small in case of a tungsten coating.

Literature:

- [1] M.D alle Donne et al.,KfK 5429,Nov. 1994.
- [2] M.I. Baskes,J.Nucl.Mat. 92 (1980) 318-324.
- [3] D.F. Holland and G.R. Longhurst, Fus. Tech. 8 (1985) 2067-2073.
- [4] G.R. Longhurst et al., J.Nuc.Mat., 131 (1985) 61-69.
- [5] R.A. Anderl et al., INEL, IEEE (1986), 644-649.
- [6] K.S. Forcey et al., J.Nuc.Mat. 160 (1988) 117-124.
- [7] G.R. Longhurst et al., TMAP4 User's Manual, INEL, EGG-FSP-10315 (1992).
- [8] ABAQUS Code, version 5.3, User's Manual, Copyright 1988, Hibbit, Karlsson & Sorensen Inc.
- [9] G.R. Longhurst et al., Fus.Tech. 28 (1995) 1217-1222.
- [10] R.A. Anderl et al., Fus. Tech. 21 (1992) 745-752.
- [11] J.Bell and J.D.Redman, 14th Intersoc. Energy Conservation Engineering Conf., Boston, Mass., August 1979.

Staff:

L. Berardinucci
M. Dalle Donne

Table 3: Permeation through the steam generators (without PRF-20)

	FW permeation = 11.9 g/d			FW permeation = 8.5 g/d		
	Inboard	Outboard	Total	Inboard	Outboard	Total
Permeating surface area (m ²)	11088	28970	40058	11088	28970	40058
p _{H2} partial pressure (Pa)	3000	3000	---	1500	1500	---
p _{HT} partial pressure (Pa)	0.58	0.51	---	0.40	0.36	---
P _{H2O} partial pressure (Pa)	34.9	34.0	---	34.9	34.0	---
Tritium permeation (Ci/d)	121	282	403	119	282	401

B 5.2.1 Permeation Tests in Martensitic Structural Material and INCOLOY 800

Tritium permeation from the helium coolant through the steam generator must be restricted to very small values. An important measure to achieve this is the addition of H₂ and H₂O to the coolant which reduces permeation by

- the build-up of permeation impeding oxide layers on the structural materials (blanket: MANET, heat exchanger: INCOLOY 800) or at least contributes to the healing of defects in these layers occurring during operation. (In the latter case, these layers have to be produced before reactor operation).
- the hydrogen swamping effect
- the conversion of gaseous tritium into nonpermeable HTO.

Experiments will be jointly performed with JRC-Ispra to investigate these separate effects. The experiments will be carried out at JRC-Ispra. An existing permeation test facility will be modified for the measurement of the different hydrogen species upstream and downstream of the test specimen.

For 1996 permeation experiments using deuterium with circular MANET and INCOLOY probes are planned in order to investigate the pressure dependence of the permeation flux.

Up to now results for MANET probes were obtained [1] using both bare probes having a natural oxide layer of about 5 nm and preoxidized probes with layer thicknesses of about 25 to 30 nm. For the bare probes a diffusion limited permeation process was observed down to the lowest investigated deuterium pressures on the upstream side ($p_{\min} \approx 3$ Pa). For the oxidized probes the permeation process was surface-limited (linear pressure dependency); the permeation rates were reduced by about 3 orders of magnitude compared to bare probes.

Literature:

- [1] E. Serra, A. Perujo, "Influence of the Surface Conditions in the Deuterium-MANET System", submitted to J. Nucl. Mat.

Staff:

A. Perujo (JRC Ispra)
J. Reimann
E. Serra (JRC Ispra)

WP B 6 Tritium Extraction

B 6.1.1 Design of Helium Purification and Tritium Purge Flow Systems including Tritium Extraction

1. Tasks of the Purification System

The purification system is provided as a sub-system for the main coolant system of an ITER solid breeder blanket test module. The interrelation between coolant system and purification system is shown in Figure 1.

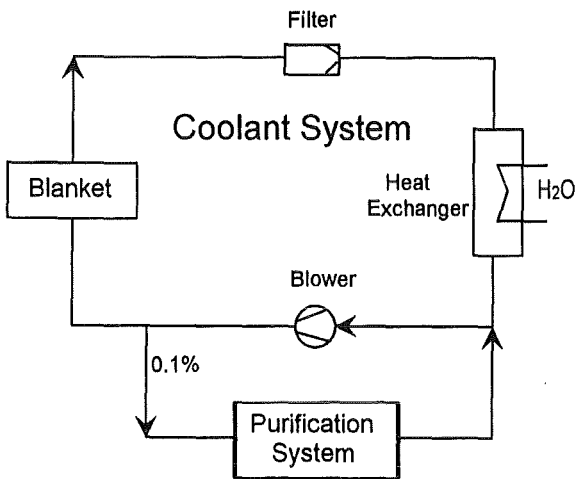


Fig. 1: Interrelation between coolant system and coolant purification system

As indicated in the figure, 0.1% of the coolant gas stream is continuously sent through the purification system. Its main task is the extraction of tritium permeating into the coolant from the first wall and from the breeder zone; this is necessary to avoid a steady increase of the tritium concentration in the coolant and to reduce the tritium permeation through the heat exchanger into the secondary coolant. Additional tasks are:

- to remove water that may be present as a consequence of leakages or failures in the heat exchanger,
- to extract other solid, liquid, or gaseous impurities,
- to provide sufficient intermediate storage capacity to allow an operation time of 6 days (one ITER reactor campaign) without the need to unload or regenerate single components.

Two independent coolant systems are provided for the ITER blanket test module. Each of these systems is equipped with a purification system whose main design data are given in Table 1.

Table 1: Main design data of the purification system

Mass Flow Rate (kg He /s)	1.85*10 ⁻³
Pressure (MPa)	8
Amount of He Coolant (kg)	23
Partial Pressures (Pa)	
p (H ₂)	62
p (HT)	0.24
p (H ₂ O+HTO)	35
p (N ₂)	8
Extraction Rates (mole/day)	
H ₂ O + HTO ^{a)}	0.47
N ₂	0.04
Extraction Efficiency	≥ 95 %
Temperature of the Coolant at the Inlet / Outlet of the Purification System (°C)	250 / 50

^{a)} due to catalytic oxidation, Q₂ is extracted as Q₂O (Q = H, D, T)

2. System Description (Figure 2)

The gas stream entering the coolant purification system downstream of the coolant loop circulation pump is first sent through a water separator to remove condensed water that may be present as a consequence of larger leakages than anticipated in Table 1. The gas is then warmed up to 450 °C by an electrical heater and transferred to an oxidizer unit containing a precious metal catalyst (Pd or Pt on alumina). An over-stoichiometric amount of oxygen is added to obtain a quantitative conversion of Q₂ to Q₂O (Q = H, D, T). The high temperature of the gas is favorable for the kinetics of the oxidation process.

Now the gas temperature is reduced to room temperature by a water cooler. The remaining humidity is frozen out in a cold trap operated at -100°C. The amount of water extracted under the conditions described in Table 1 is 8.5 g/day.

Finally, the gas is passed through a recuperator and then to a 5A molecular sieve bed cooled with liquid nitrogen (LN₂) to adsorb gaseous impurities like N₂; any hydrogen isotopes that have not been oxidized are also adsorbed. The inlet and the outlet side of the bed are equipped with mechanical filters to prevent a carry-over of particulate material during normal operation (downward flow) and regeneration (upward flow).

The second bed provides additional adsorption capacity; it may be used when the first bed has not been unloaded or regenerated.

The pure helium is carried back through the recuperator, further warmed up by an electrical heater, and then returned into the main coolant loop upstream of the circulation pump. Thus, it should be possible to operate the purification system without an additional compressor or circulation pump. Nevertheless, a corresponding pump (No.5) will be available on demand. The total inventory in the main coolant remains below 0.1 mol Q₂ and 0.05 mol Q₂O under the conditions described in Table 1. It will be sufficient, therefore, to continue the operation of the purification system for about 12 hours after reactor shutdown to arrive at a reasonably low concentration of hydrogen isotopes in the coolant.

Regeneration

Some components must be regenerated before their retention capacity has been reached. The particulate filters will be transferred to the waste disposal system after exchange.

The cold trap loaded with ice is depressurized (via relief valve 10) and warmed up to room temperature to liquefy the water which is then drained into a water container and sent to the Water Detritiation System.

The adsorber beds are first depressurized like the cold trap (via relief valve 11). During a normal unloading operation they are warmed up to room temperature, and the desorbing impurities are sent to the Waste Gas System. A complete regeneration is achieved by heating to 300 °C and purging with clean helium.

3. Analytical Tools

The tritium extraction is controlled by continuous measurement of the tritium concentration at several points of the loop. Four ionization chambers are used for this reason:

No.1: At loop inlet upstream of the electrical heater (information about tritium concentration in the coolant),

No.2: Downstream of the cold trap (information about satisfactory functioning of oxidizer and cold trap)

No.3: At the loop outlet (under proper conditions, the reading should be the same as of No. 2),

No.4: Downstream of valve 11 (to monitor the effluent gases).

In addition, the composition of the coolant gas is analyzed with the help of a gas chromatograph by taking gas samples at the loop inlet and outlet.

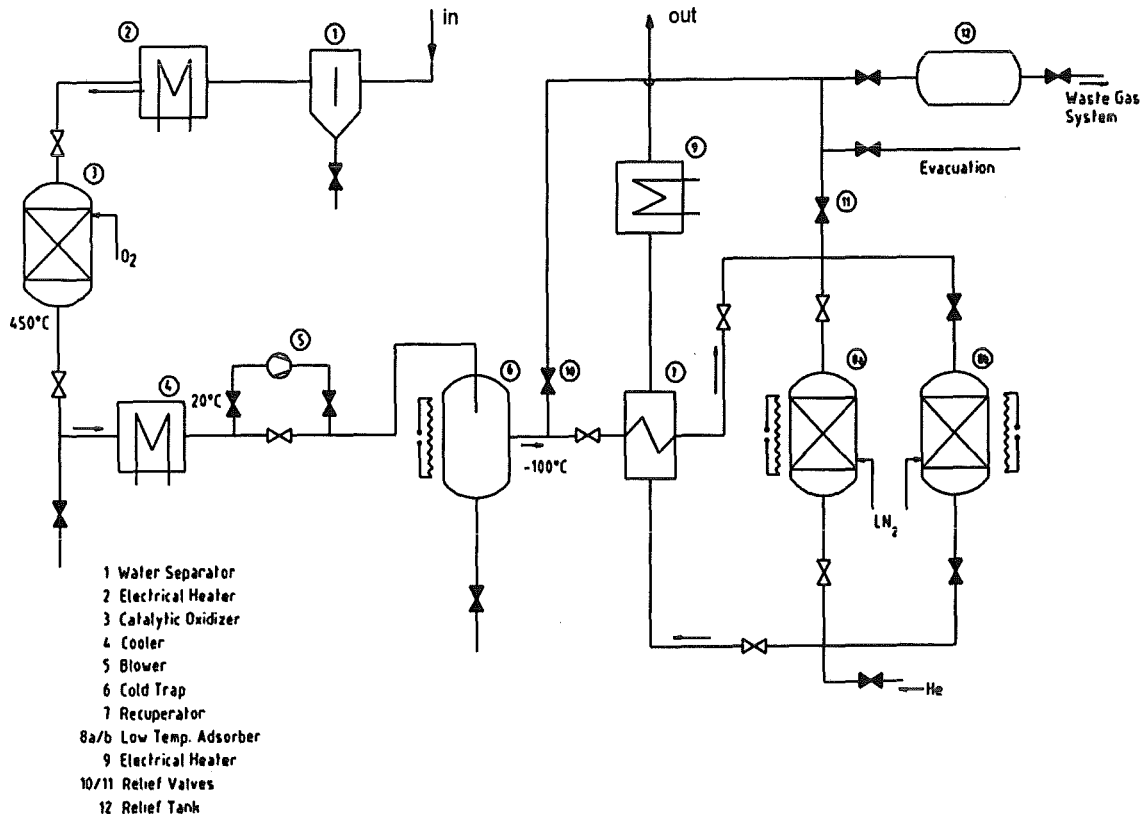


Fig. 2: Principle of the coolant purification system

Literature:

- [1] H. Albrecht and E. Hutter, Tritium Recovery from a Solid Breeder DEMO Blanket, Proc. of the 18th Symposium on Fusion Technology, Aug. 22 - 26, 1994, Karlsruhe, Germany

Staff:

H. Albrecht

E. Hutter

WP B 7 Safety related Activities for DEMO and ITER Test Module

B 7.1.1 Safety Studies for DEMO and ITER Test Module

The safety studies focused on the analysis of the blanket and cooling systems transient behaviour during accidents for the HCPB DEMO blanket system and on the assessment of design basis accident scenarios relevant to the HCPB blanket test module (BTM) in the ITER environment. Documentation was prepared for the previous general safety assessments of DEMO blankets [1, 2, 3, 4].

DEMO Blanket Systems Analysis

To analyse the thermal-hydraulic behaviour of the HCPB blanket and cooling circuits during steady state and accidental conditions, a part of the outboard (OB) cooling system was modelled with the system analysis code RELAP5/MOD3.1. The model represents one cooling system of one OB blanket segment including blanket flow channels and structures, circulator, steam generator, pressure control system, primary side pipework, and part of secondary side. The RELAP5 nodalization scheme is shown in Fig. 1.

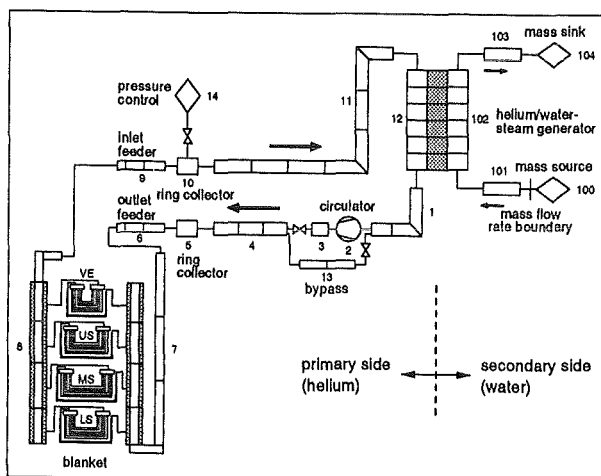


Fig. 1: RELAP5 nodalization of part of OB cooling system.

To obtain information from different areas of the blanket, the OB blanket segment was divided into four poloidal sections, namely, upper vertical extension (VE), upper section (US), middle section (MS), and lower section (LS), see Fig. 1. Section VE comprises the blanket section opposite to the inboard upper divertor, the latter three sections form the curved part of the OB blanket segment. The solid structures of first wall (FW) and breeding zone were modelled by rectangular RELAP5 heat structures. The chosen modelling approach allows determination of steady state conditions and simulation of accidents concerning both cooling circuits of an OB blanket segment.

An important result of the calculated steady state conditions is the necessity for orificing the mass flow rate in different

blanket areas to fulfil the tentative target function of identical helium temperatures at the breeding zone outlets across the whole segment height. Strong orificing was especially necessary at the upper vertical extension, where the heat generation is very small. This gives rise to considering a different design for this blanket section, as compared with the other sections.

Starting from steady state conditions, first transient calculations simulating a loss of flow accident (LOFA) in both cooling systems induced by a circulator trip with and without subsequent plasma shutdown were conducted. Without plasma shutdown the FW temperature in the middle section reaches 700 °C about 40 s after initiation of the LOFA. Failure of the FW in this temperature range is likely to occur. Assuming an intact FW beyond this level, FW MANET/breeder/multiplier would reach their melting points approx. 120 s/125 s/190 s after start of the transient. For a LOFA with plasma shutdown and subsequent decay heat removal via natural circulation a redistribution of the flow inside the blanket was observed. For instance, the poloidal flow distribution 1 h after start of the LOFA shows a strong gradient of the mass flow rate from the lower section with the highest flow rate to the upper vertical extension with the lowest flow rate. Consequently, the poloidal temperature distribution for FW MANET shows a maximum in the upper section and a minimum in the lower section, the differential temperature being ~300 °C. The described flow pattern was observed for a level difference of 5 m between blanket and steam generator. Further calculations with varying parameters are planned.

ITER Test Module Safety Assessment

The accidental safety assessment has been addressed giving first an overview on the material mass inventories and on tritium inventories in the different subsystems, and on the energy sources which are the driving elements in any accident sequence. Enveloping events were identified to serve as design basis for the blanket test module (BTM). These design basis events were, to some extent, analysed with view to their short and long term thermal-hydraulic evolution. Finally, the events were evaluated against a given set of safety requirements to demonstrate that the HCPB-BTM design complies with ITER safety criteria. The results are summarised in this section.

Concerning the materials and toxic inventories the safety relevant quantities are as follows: The test module includes 2700 kg of structural material, 450 kg of beryllium pebbles, 10 kg of beryllium in a 5 mm thick first wall protection layer, and 120 kg of breeder pebbles. The two cooling loops contain a steel mass of 15000 kg, constituting a relatively large heat capacity. The helium enclosed in the main loops amounts to 43 kg. The tritium content in the BTM is in the 20 mg range in the structural and breeder material each, and about 4 g in the beryllium multiplier at the end of the extended performance phase. The primary coolant contains up to 1 mg of tritium.

Typical energy sources in the HCPB-BTM system are displayed in Table 1. It shows that the chemical energy potential of the beryllium multiplier is large compared to the other energies, although the probability for gross Be/water or Be/air reaction is low, especially for the beryllium pebbles.

Table 1: Energy sources in the HCPB test module

Energy Source	Energy (MJ)
Plasma disruption	0.35
Linear plasma shutdown with 1 s delay	
within 100 s (normal)	97
within 20 s (accelerated)	21
within 20 s for surface heat flux and 0 s for internal heat (fast)	4.8
Decay heat integrated over:	
1 minute	1.5
1 hour	69
1 day	445
1 month	4510
Work potential of helium coolant (both loops)	63
Chemical energy	
beryllium/water reaction	18000
beryllium/air reaction	30000

Postulated enveloping events were identified, representing the most demanding design requirements to the BTM, and a preliminary category with respect to the annual expected frequency of occurrence has been assigned to each event. The total of 12 events considered pertain to three families: (a) loss of coolant accidents with leaks in one or both loops at different locations, (b) loss of flow accidents with loss of forced convection flow in one or both loops, and (c) loss of heat sink events assuming complete failure of the secondary heat removal system for one or both primary loops. Two types of transient thermodynamic calculations have been carried out to determine (i) the 3D temperature distribution in a representative section of the BTM in the course of the events with the finite element code FIDAP, and (ii) the thermal-hydraulic and heat transport mechanisms in the whole cooling system with the system code RELAP5.

As example, Fig. 2 shows the temperature evolution at selected spots of the BTM in case of a loss of flow in both cooling loops due to loss of pump power for a normal plasma shutdown (1 s delay with subsequent ramp-down within 100 s). The temperature in the hottest node of the first wall structure (curve MANET/Be) and in beryllium protection layer (curve Be-layer) reach peak values of 625 and 635 °C, respectively, that is about 100 °C above the steady state level which is tolerable. No temperature overshoot is observed in the pebble beds. The mass flow rate decreases with a half-life time of 3 s, reaching natural circulation driven equilibrium at 5.3 % of nominal flow 60 s after start of ramp-down.

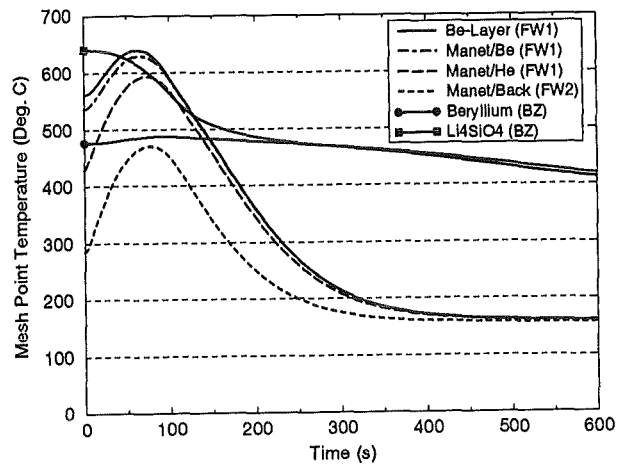


Fig. 2: Typical temperature transients at hot spots of the BTM following loss of flow in both cooling loops

The events have been assessed, to the extent analysed so far, against a set of 15 safety requirements established in the ITER design description document. The pertaining checking matrix indicates that to date, 9 out of 15 safety requirements are fulfilled by the proposed HCPB-BTM design. Several postulated events need to be further investigated with respect to the remaining requirements. Pending these results, no fundamental safety concerns are expected that could violate the ITER safety criteria.

Literature:

- [1] K. Kleefeldt, F. Dammel, K. Gabel: Safety and environmental impact of the BOT helium-cooled solid breeder blanket for DEMO, FZKA 5754.
- [2] K. Kleefeldt et al.: Safety and environmental impact of the dual coolant blanket concept, FZKA 5764.
- [3] K. Kleefeldt, G. Marbach, T. Porfiri: EU DEMO blanket concept safety assessment, FZKA 5781.
- [4] K. Kleefeldt, K. Gabel: Safety assessment of two DEMO blanket concepts: Helium-cooled pebble bed vs. dual coolant, 19th Symposium on Fusion Technology, September 16-20, 1996, Lisbon, Portugal.

Staff:

- K. Gabel
- K. Kleefeldt
- I. Schmuck
- K. Schleisiek

WP B 8 ITER Test Module System and Testing

B 8.1.1 Tests in HEBLO and Preparation of a Submodule for HEFUS-3

In 1995 the second HEBLO [1] experiment was carried out by temperature transient tests on a mixed beryllium/ceramic pebble bed under additional mechanical loading. The configuration of the test bed was based on the blanket concept with cooling coils in a mixed pebble bed.

After a total number of 1915 temperature cycles under different mechanical loadings [1] the experiment was terminated. After removal from the test loop the test section was cut apart at an industrial firm. Because of difficulties in the disassembly of the pressure piston individual samples of pebbles could not be collected. The whole pebble bed was therefore fixed by casting resin. Metallurgic photographs were taken at a cut plane about 20 mm below the pressure piston (Fig. 1). No damage, fracture or deformation of the beryllium and Li_4SiO_4 pebbles were observed.

A third HEBLO test section is presently in the design phase which, according to the HCPB concept for DEMO with cooling plates, contains separate beryllium and ceramic pebble beds. Figure 2 shows a small part of an outboard blanket segment chosen for the third HEBLO experiment. The whole test section is illustrated in Figure 3; it contains the small HCPB test object made from MANET and is installed in a safety tank. The goal of the third HEBLO experiment is to examine the thermal behaviour of the pebble beds and welding joints of the structure under transient loadings. To adapt it to the new thermohydraulics test conditions, the HEBLO loop facility has been modified and extended [2], especially in the temperature transient test loop. Besides modification of the pipe diameters in order to increase the helium flow, the gas

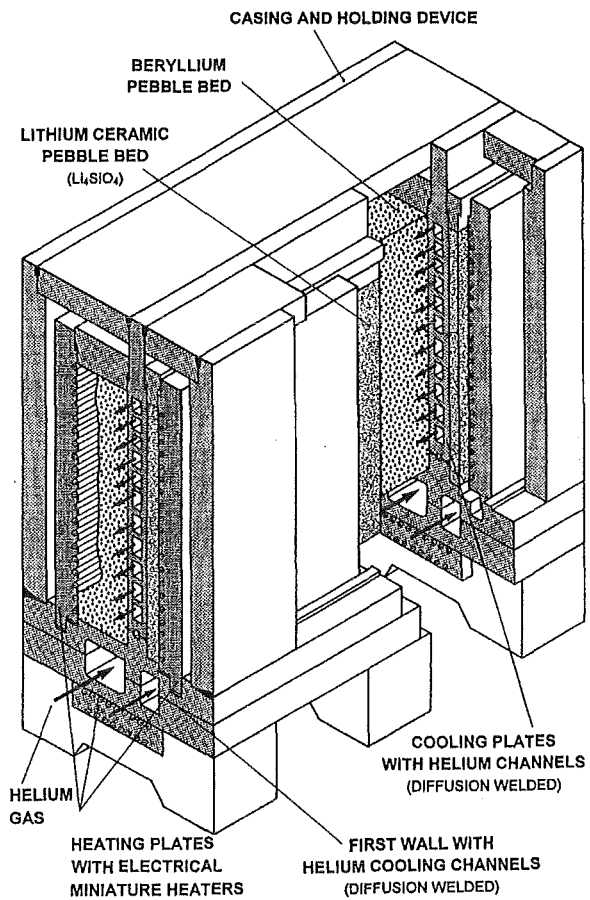


Fig. 2: Small part of HCPB chosen for the third HEBLO experiment

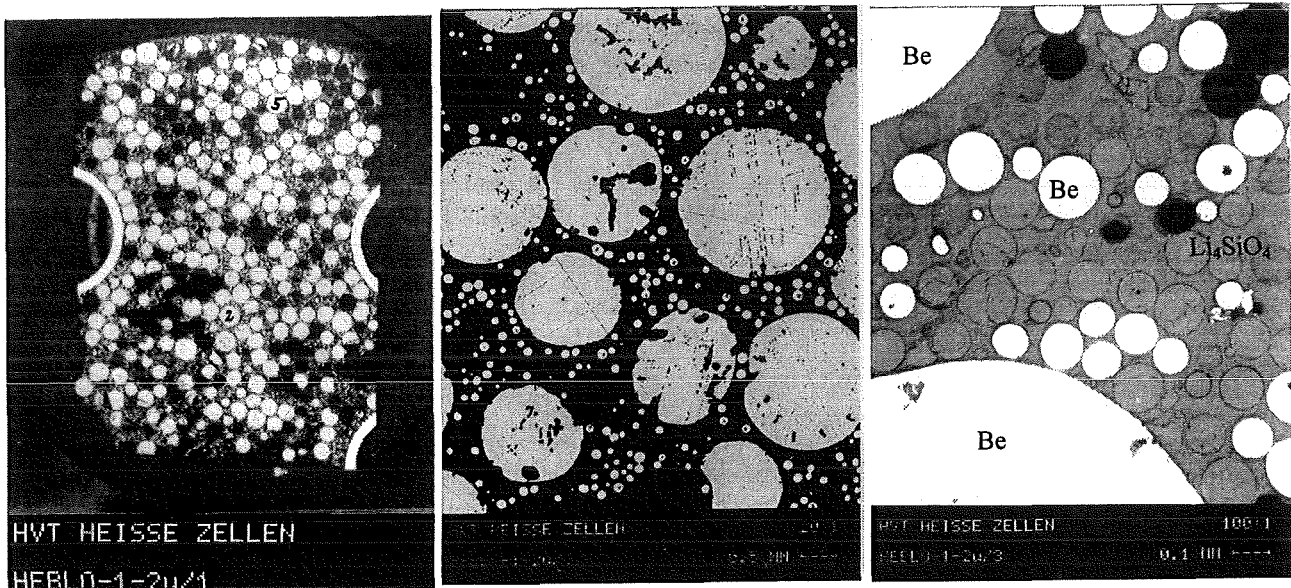


Fig. 1: Metallurgic photographs of the mixed Be/Li ceramic pebble bed of the second HEBLO experiment taken at a cross section below the pressure piston (2.7x, 20x, and 100 x, respectively)

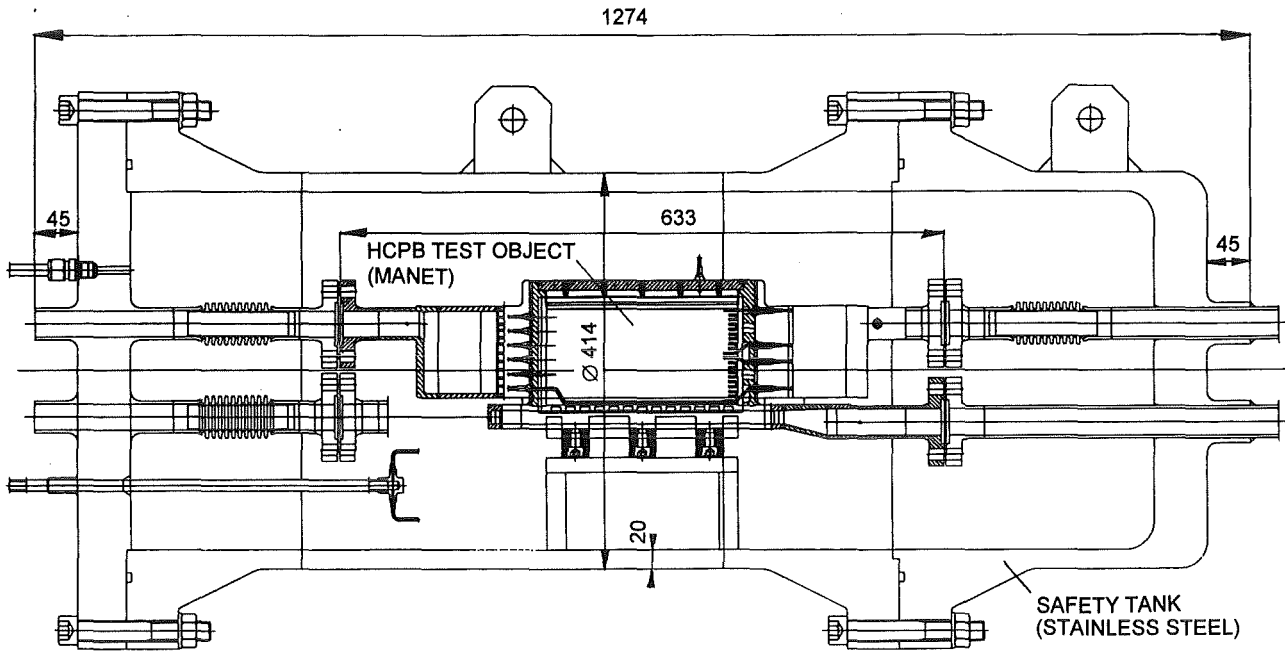


Fig. 3: Third HEBLO test section for HCPB

flow has to be split up further. This requires additional heating sections, control circuits and measuring points.

First thermohydraulics design work has been completed. The first layout and test of heating plates for simulation of the high inner heat sources showed weak points at the cold junctions of the heating wires. The redesigned specimens of the heating plates are now being tested and, if necessary, they will be modified and optimized to fit the real test conditions.

To connect the test object (MANET) to the HEBLO facility (stainless steel) flange tests were carried out successfully with a MANET/stainless steel material pair under temperature cycles of 270/430 °C and at 80 bar helium pressure. After modification and extension, the HEBLO facility will again be put into service in order to test to the new equipment such as loop heaters, measurement systems, and control and safety circuits.

Upon completion of the new test section and integration in HEBLO, it will probably start operation in 1997.

Literature:

- [1] P. Norajitra, D. Piel, G. Reimann, R. Ruprecht, HEBLO, a Helium Blanket Test Loop for Small Test Sections of Helium Cooled Solid Breeder Blankets, Proceedings of the 19th SOFT, Lisbon, 16-20 September, 1996.
- [2] P. Norajitra, Internal Note, July 1995

Staff:

- M. Dalle Donne
- H. Lehning
- P. Norajitra
- D. Piel
- G. Reimann
- R. Ruprecht

Long Term Materials Programme

The Structural Materials Programme is devoted to the development of low activation ferritic/martensitic steels for DEMO and the provision of design-relevant present-day materials data for blanket modules to be tested in ITER.

FZK carries a major part of these activities. The agreed programme has been structured in Work Packages (WP) with a subdivision in tasks and subtasks. Within WP 1 the characterization of MANET with respect to its long-term behaviour (creep-rupture) metallurgical and mechanical properties of Japanese and European reduced activation steels are being determined, and the irradiation behaviour is being measured both by post-irradiation examination and in-beam fatigue testing. A smaller part of activities is devoted within WP4 to fracture-mechanics studies and weldability tests.

Creep rupture tests with MANET-II, which can be treated as a reference material for further improvements to be attained with the reduced-activation alloys, showed that the strong deterioration of creep resistance that occurred with MANET-I after 10 000 h at 550°C, does no longer appear. For the Japanese steel F82H mod. a basic quality assurance and homogeneity test program has been carried through in the different participating European Laboratories with very good and congruent results. The discrepancy in the results on the Nb-content, a very critical element for long-term activation, has been resolved, and the very low values as specified by the supplier have been verified.

The characterization of different OPTIFER heats has also advanced, and the critical role of Ta as an alloying element has been identified.

As for the fatigue properties of the reduced activation alloys, F82H mod. has so far been investigated both in LCF and in thermal fatigue tests, and it has been found that this material shows a cyclically weaker behaviour than MANET-II.

The reactor irradiation and post-irradiation testing program (MANITU) devoted to the critical issue of radiation effects on fracture toughness, has yielded significant improvements for essentially all the new alloys with respect to shifts in USE and DBTT as compared to the MANET steels. The trend in neutron dose dependency as derived from previous measurements on MANET-I could be fully verified.

Investigations with the Dual Beam Facility were concentrated on a fundamental comparison of displacement damage as simulated by light ions, with fusion neutrons. Whereas the elastic component is well characterized by Rutherford scattering, the non-elastic component has, for the first time, been quantitatively described. It could be shown that within a wide range of recoil energies there is good matching between proton- and neutron-induced interactions, except for low energies where some overrating of the Frenkel pair production occurs. Thus, even if α -particles would be much more efficient for displacement production, high energy

proton irradiation gives a better simulation for First Wall fusion neutron induced damage effects.

α -irradiation was used for experimental studies of the impact of He on the tensile properties of F82H mod. Hardening was found below 400°C which increased, the lower the temperature was; but the effect was not as pronounced as for MANET-I. Within WP4 FZK made two contributions, the first of which was related to a common understanding of cleavage or ductile fracture of ferritic steel depending on the temperature, and the deduction of data to be incorporated in design codes. In the experimental part of the work a tension testing device has been adapted for a special type of specimens that is required for the numeral analysis. In the theoretical part a modified Weibull stress analysis to quantitatively describe brittle fracture is being implemented.

The second contribution to WP4 is devoted to the quantification of diffusion welding for the joining of ferritic steel plates in the ITER test blanket design. Tensile, bending and impact tests have been used for a basic evaluation of weldments and it has been found that a certain roughness is essential to ensure acceptable properties of the weldment.

H.D. Röhrig

WP 1 Martensitic Steels

1.1 Metallurgical and Mechanical Characterization MANET

MANET II was the first big heat of the martensitic 10% Cr-steels investigated and characterized by a number of European laboratories. The collected microstructural and mechanical data are the reference properties for further developments in martensitic steels, particularly with regard to the development program of the low activation alloys. This work on characterizing MANET II was completed by evaluation of the creep rupture tests and documented in a final report. Four heats and seven semifinished material dimensions were extensively examined in the temperature range from 450 - 700 °C for up to 20000 hours. Thus, experimental characteristic values on the creep resistance and creep behaviour of this martensitic 10.5%Cr steel are available to the designers. A very important result is that by

strict observance of a positive N/AI-ratio in MANET II, the strong deterioration of creep resistance observed as „S-slope“ in the 1% creep-strength ($t_{1\%}$) and time to rupture (t_r) curves in MANET I is prevented; Fig. 1 [1].

Literature:

- [1] M. Schirra, S. Heger, A. Falkenstein: Das Zeitstandfestigkeits- und Kriechverhalten des martensitischen Stahles MANET-II, FZKA 5722, Oktober 1996

Staff:

- A. Falkenstein
- S. Heger
- E. Materna-Morris
- M. Schirra

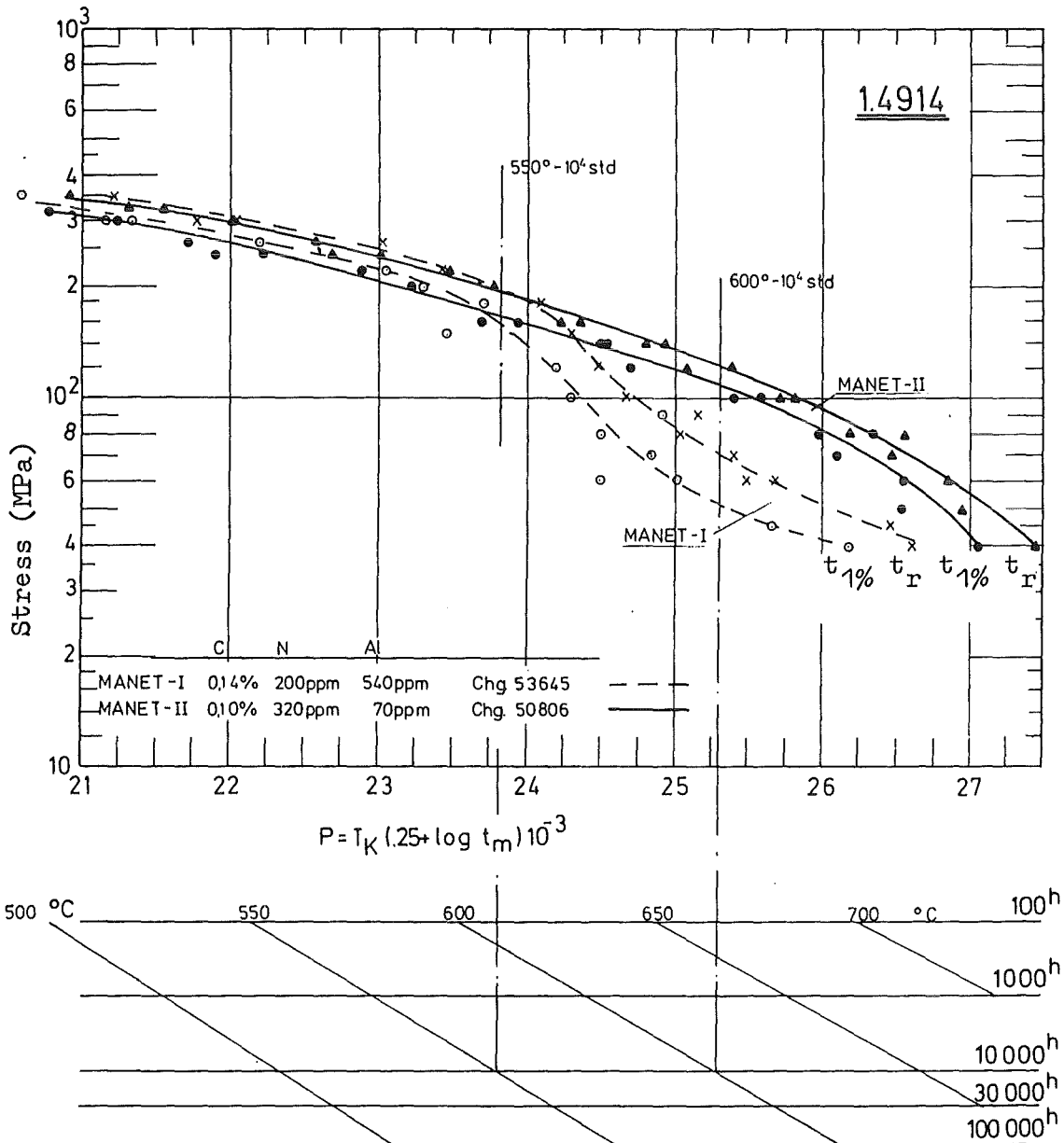


Fig.1: Master curve for 1% creep-strain and rupture (Larson-Miller-Parameter)

1.2.1 Metallurgical and Mechanical Characterization F82H mod.

The basic investigations of the steel F82H mod. (Heat 8741), a 5 ton high-purity melt manufactured by NKK-Japan have been brought to an end. The associated European Laboratories performed a quality assurance and homogeneity test program on all distributed plates. The program included the evaluation of microstructural data and chemical analysis. Additional tensile tests were also performed, the whole test results are reported in [1]. Measurements of Vickers Hardness HV 30, grain size, contents of precipitates and inclusions reveal a homogeneous structure more or less independent of either plate dimension or rolling direction. These findings are confirmed by the test results of comparative tensile tests. Fig. 1 gives the Ultimate Tensile Strength of F82H mod. in

comparable to MANET II, deviations between the different laboratories are due to the different specimen geometry.

The heat treatment has been optimised in order to improve the creep, impact and tensile properties and special attention was given to the transformation behaviour [2,3,4]. First results obtained on tensile strength properties and notch impact toughness behaviour were described in the previous Annual Report 94/95.

One aim of the homogeneity tests was also to determine the uniformity of the chemical composition. Whereas the comparison of the content of the main alloying elements (Cr, W, Mn, V and C) shows good agreement, the determination of the very low contents of impurity elements such as Nb and Mo, which are important for the longterm activation, made some trouble and some deviations occurred due to the determination limits and uncertainties of the applied analytical methods, XRF (X-Ray Fluorescence Analysis) and OES (Optical Emission Spectroscopy). Latest measurements at the Dual-Beam-Facility of FZK using nuclear activation analysis revealed that the contents of Nb and Mo are in the range of 2.5 ± 1 and 46 ± 17 wt-ppm. These results confirm the manufacturer's analysis of 1 and 30 ppm resp. is correct [1,5,6].

Further work on the stability during tempering was investigated in aging tests carried out in the temperature range from 450 to 800 °C for up to 2 000 hours duration. The resulting tempering master plot corresponds to the OPTIFER Ge variant.

The creep rupture tests performed in the range of temperatures from 450 to 700 °C for 10000 hours yield a creep rupture master plot which is well validated and represented in Fig. 3. First tests made on a second plate exhibit a slight tendency towards lower values for the times to rupture and creep strain limits.

The martensitic structure of F82H mod. was investigated intensively with regard to thermal stability. As found in former investigations, the martensitic structure can change partly into the ferritic structure after higher temperatures exposure in the α - γ -transformation range at about 875 °C. This phenomenon was found after the as-received condition of 1040 °C 38 min + 750 °C or after a second austenitization of 1040 °C and higher annealing temperatures. In order to investigate this problem heat treatments were performed in 20°-steps between 800 and 920 °C. The material was studied in etched metallographic cuts by light microscopical and scanning electron microscopical methods.

The temperatures of the analysed samples are marked in the phase diagram of 0.1%C steels (Fig. 4). The full circles indicate the relative content of the ferrite. Ferrite was found between the temperatures of A_{C1b} and A_{C1f} (Fig.4b). The maximum ferrite contents of 17% was found after 880 °C. As can be seen, the α - γ -region was found at a higher temperature range than shown in the Fe-Cr phase diagram of Pickering.

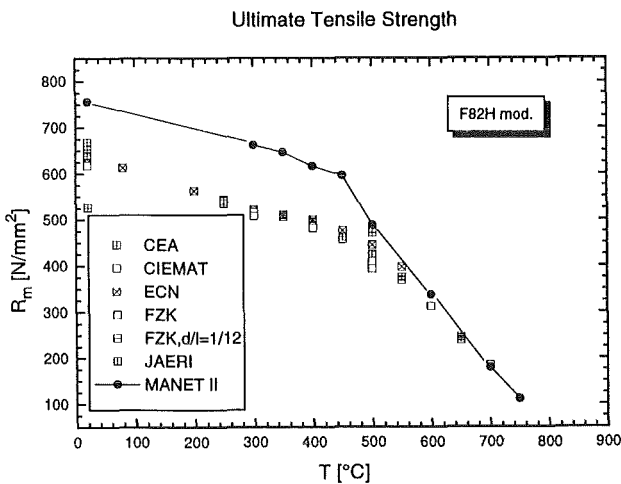


Fig. 1: Ultimate Tensile Strength of F82H mod. vs. temperature

comparison to MANET II, showing lower strength below, and equal strength above 500 °C. The ductility given in Fig. 2 is

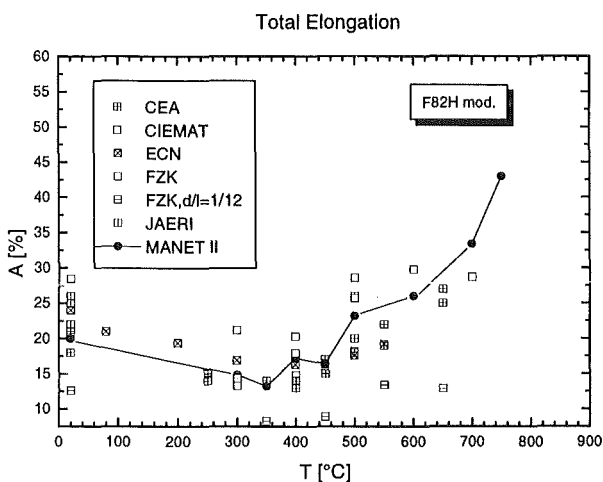


Fig. 2: Total Elongation of F82H mod. vs. temperature

But, this divergence can be explained by the addition of further alloying elements.

The Vickers hardness was measured in the F82H mod., too. The ferrite was very soft with 200 HV_{0.1}. The martensite was relatively hard and the hardness of 450 HV_{0.1} is the value of quenched martensite. The EDX (energy dispersive x-ray analysis) analysis of the Cr contents showed a small increase of about 0.5 - 1.0 wt.% in the martensite. In transmission electron microscopy the structure-less ferrite and the quenched martensite with the additional M₂X phase could be discriminated (Fig. 5).

The experimental results can be explained in the following way: During the heating of the steel F82H mod. up to the α-γ-transformation, some grains changed to the austenitic phase and can dissolve a high concentration of carbon. Most carbides, like M₂₃C₆-type precipitates, are dissolved and the concentration of free carbon is increased. By a diffusion process the retained grains lose carbon, they are nearly carbon-free and form ferrite. During a fast cooling, the transformation is frozen and the ferrite is retained at RT. Partly, the material has the appearance of bainitic structure, too, but this phase could not be proved by dilatometric measurements.

In F82H mod. a part of the carbon is not bound by the strong carbide forming elements such as Ta or Ti, because very often large inclusions could be found in the composition of Al-Ta-

Ti-V-O. Probably, the elements were added too early to the melt and oxidised.

A good mechanical behaviour of the irradiated material is finally important. Probably, the soft ferrite phase can influence positively the mechanical properties during or after irradiation. This will be further investigated.

Literature:

1. R. Lindau (Ed.): Homogeneity Tests of European Laboratories on Alloy F82H-mod.FZK-Report 5814, November 1996
2. M. Schirra et. al.: Ergebnisse von Arbeiten zur Grundcharakterisierung des Stahles F82H mod. Charge 9741. Internal report
3. M. Schirra, H. Finkler: Das Umwandlungsverhalten der hochwärmfesten martensitischen Stähle mit 8-14% Cr. FZKA 5607, Sept. 1995.
4. L. Schäfer, M. Schirra, R. Lindau: Mechanical Properties of the Martensitic Steel F82H Mod., Heat 9741, Proceedings of SOFT 19, Sept. 16 - 20, 1996, Lisbon - Portugal, in press

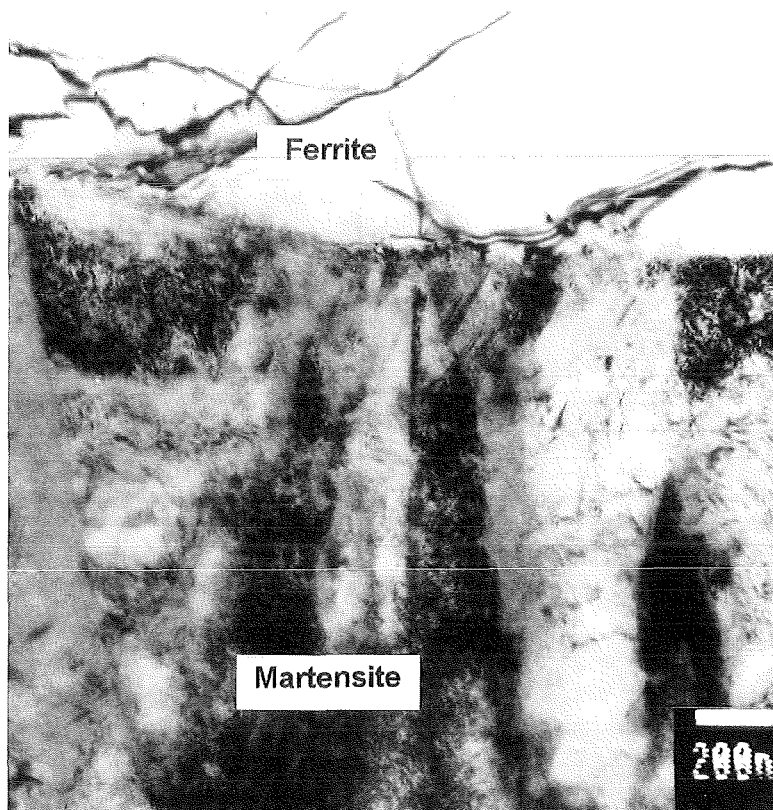


Fig. 5: TEM-micrograph of F82H mod.

5. E. Daum, K. Ehrlich, M. Schirra (Eds.): Milestone 2 - Meeting on F/M - Steels in the European Programme, FZK-Report 5848, November 1996
6. E. Daum : Bestimmung der Nb- und Mo-Verunreinigungskonzentration des Stahls F82H-Mmod (Chg. 9741) mittels Aktivierungsanalyse, Internal Report

Staff:

E. Daum
A. Falkenstein
P. Graf
S. Heger
R. Lindau
E. Materna-Morris
L. Schäfer
M. Schirra
H. Zimmermann

1.2.2 Fatigue and Creep Properties of Base Material on LA Martensitic Steels F82H Mod

1. Introduction

Structural components of a DEMO-blanket are subjected during service to alternating thermal and mechanical stresses as a consequence of the pulsed reactor operation. Of particular concern is the fatigue endurance of martensite steels like MANET II and F82H mod under cyclic strains and stresses induced by these temperature changes. In order to design such structures, operating under combined mechanical and thermal cycling, fatigue life has to be examined in isothermal fatigue tests for materials data generation and in thermal fatigue for verification of design codes.

This report compares recently measured isothermal mechanical and thermal low-cycle fatigue data of the martensite low activation steel F82H mod with those of MANET II martensite steel.

2. Experiments

The F82H mod samples are tested in the tempered as received condition (Normalizing: 1040°C and tempering: 750°C), and the ferrite-martensite MANET II samples after the three-step reference annealing [1].

Cylindrical samples of MANET II and F82H mod, respectively - solid in case of isothermal mechanical fatigue and hollow in case of thermal fatigue - have been used for the experiments. Both materials have been tested in air under isothermal, total strain control low cycle fatigue (LCF) and under thermal fatigue control (TCF), respectively.

The LCF tests have been performed with computer-controlled MTS servohydraulic testing machines operating in strain controlled push-pull mode. Triangle wave forms are applied with constant strain rates of 3×10^{-3} 1/s in case of LCF tests. More detailed informations about the test procedure are received from an actual report [2].

For the LCF experiments, solid specimens of 77 mm length and of 8.8 mm diameter in the cylindrical gauge length of the specimen have been used. The axial extensometer is fixed by knives on both sides of the 21 mm gauge length to allow stable attachment.

The TCF test rig consists of a stiff load frame for mechanical clamping of the sample, which is directly heated by the digitally controlled ohmic heating device. Cylindrical specimens are used with the same outer dimensions as the above mentioned solid specimens, but with a wall thickness of 0.4 mm. Variable strain rates are applied at TCF test mode, due to the constant heating rate of 5.8 K/s and variable temperature changes.

With respect to extensometry a TCF test includes complications of strain measurement not normally

encountered with isothermal LCF tests. Since both temperature and mechanical strain cycling are taking place, mechanical strain is available only after subtraction of the thermal strain from the measured total strain.

3. Results

A comparison of isothermal fatigue behavior between F82H mod and MANET II (plotted in Fig. 1) shows at temperatures of 450°C and 550°C with a total strain range of 1 % only a small reduction in number of cycles to failure, but with decreasing total strain range (0.6 %) the reduction in number of cycles to failure amounts to about 40 to 50 percent of those of MANET II.

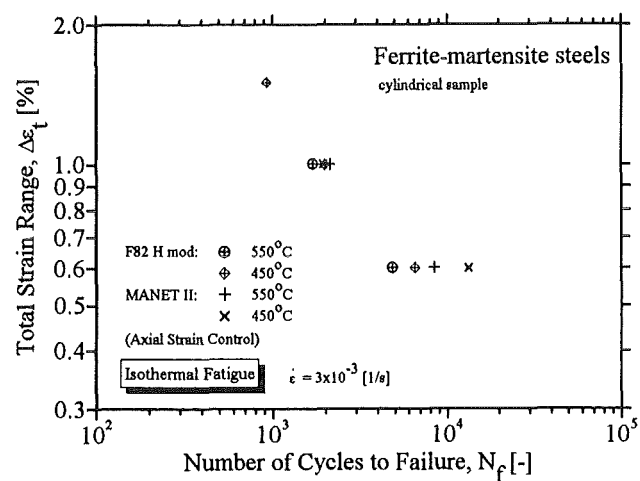


Fig. 1: Comparison of isothermal fatigue behavior between F82H mod and MANET II

The comparison of thermal fatigue behavior between F82H mod and MANET II with respect to total strain range vs. number of cycles to failure (Fig. 2) shows at temperature

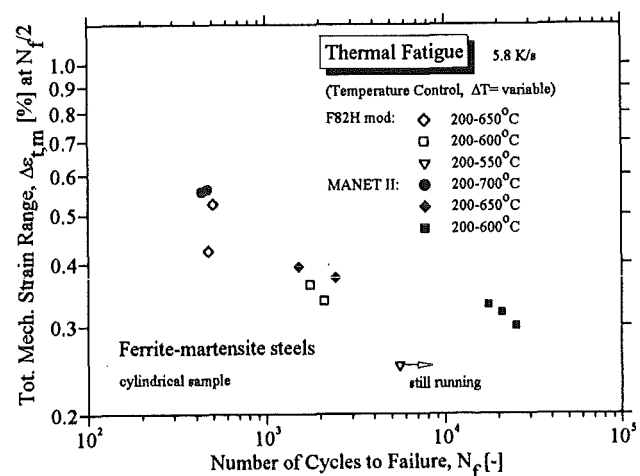


Fig. 2: Comparison of total mechanical strain range of thermal fatigue behavior between F82H mod and MANET II

changes of 200 - 600°C with increasing total mechanical strain ranges a drastic reduction in number of cycles to failure (about one order of magnitude).

The comparison of thermally fatigued samples of both materials with respect to plastic mechanical strain range results for F82H mod samples in much higher values than for MANET II. This is shown in Fig. 3.

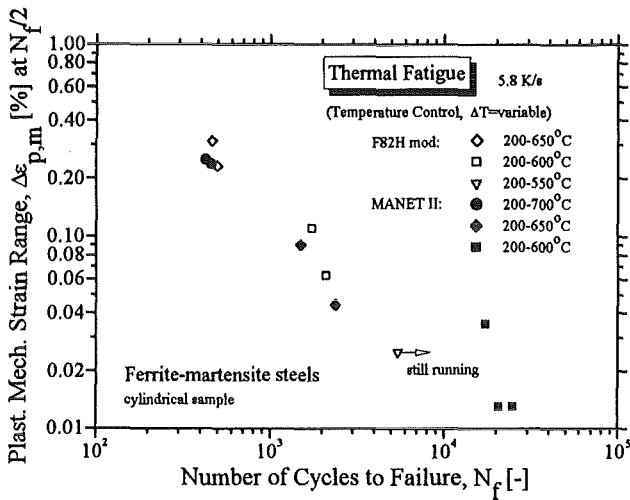


Fig. 3: Comparison of plastic mechanical strain range of thermal fatigue behavior between F82H mod and MANET II

The third comparison of thermally fatigued samples of both materials is made with respect to total stress range and results for F82H mod samples in much lower values than for MANET II. This is shown in Fig. 4.

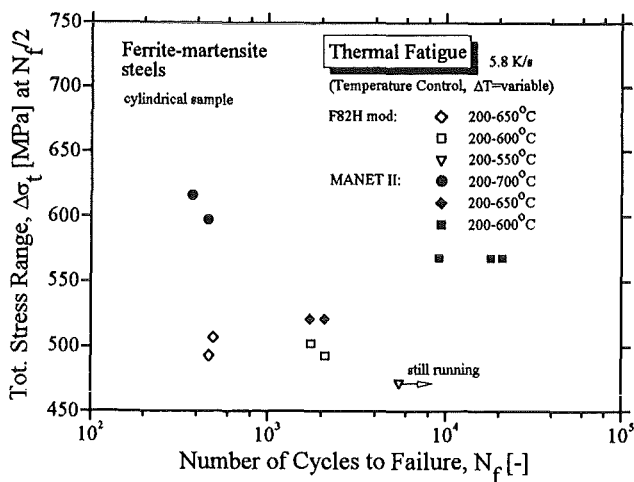


Fig. 4: Comparison of total stress range of thermal fatigue behavior between F82H mod and MANET II

From these first results one can tentatively conclude that F82H mod shows a cyclically weaker behavior than MANET II,

which however can still be described by a Manson-Coffin relationship.

4. Thermal Fatigue Round Robin (TFRR)

The thermal fatigue round robin has been organized among four European laboratories: ENEA, EPFL, JRC and FZK. Chaired by FZK, the following parameter field had been defined:

- Thermal fatigue and thermomechanical fatigue tests will be performed in air atmosphere.
- Heating and cooling rate is 5 K/s.
- Temperature range is defined to 200°C - 600°C, to reach total mechanical strains of about 0.4 % in case of thermal fatigue and convenient testing times.
- Mechanical clamping of the sample in case of thermal fatigue should be performed at the low temperature (200°C) of the cycle.
- Total mechanical strain value in out of phase thermomechanical fatigue experiments should also be chosen to 0.4%.

Sample manufacturing from F82H mod (28 mm plate), perpendicular to the rolling direction, will be finished for the four participants of TFRR - each with their specific sample shape - in Dec. 1996.

Literature:

- [1] C. Petersen, I. Alvarez-Armas and A. F. Armas, Plasma Devices and Operation, 3 (1994) 317
- [2] M. Pfeifenroth and R. Schmitt, FZK-Report: FZKA 5659 (1996).

Staff:

- J. Aktaa
- M. Klotz
- C. Petersen
- M. Pfeifenroth
- D. Rodrian
- R. Schmitt

1.4.1 Metallurgical and Mechanical Characterization of OPTIFER Alloys

Determinations of the physical and mechanical properties of the first OPTIFER alloys have been largely completed and some of them have been documented [1-5]. The current investigations are focused on the long-term tests.

In order to be able to study the stability of tempering in the reference state specimens were aged for 20 to 2 000 hours in the temperature range of 500 to 750 °C and the hardnesses were measured (Fig. 1). The hardness of the respective reference state (205-250 HV₃₀) is largely maintained up to P = 18.5 (550 °C; 20 000 hours) and gradually decreases beyond that value. Only the 1.6% Ta heat 666 features a substantial decrease in hardness from P = 19 on. The cause is secondary recrystallization accompanied by coarse grain formation.

The status of creep rupture tests allows a comparative evaluation to be made of the various OPTIFER heats with reference to the creep rupture master plot (Fig.2). Also this representation makes evident that the 1.6% Ta heat displays a marked decrease in strength from P=24 on, as a result of recrystallization, and that the 1% W heat is more stable in its strength behaviour.

OPTIFER Heats			
1st series		2nd series	
W-Ta-Ce	664	Ge-Ce	734
Ta-Ce	666	W-Ta-Ce	735
W-Ta-Y	667	W-8.5 Cr	736
Ge-Ce	668		

The investigations of the second OPTIFER series have started. It appears from the results of the hardness tests performed in the temperature range 850 - 1100 °C that the hardness behaviour corresponds to that of the heats of the first series (Fig.3a). The determination of grain sizes made evident that a Ta content of 0.06 - 0.1% is necessary to obtain a fine grain. The example of the Ge heat 668 shows that a Ta content of 0.018 causes coarse grain formation at an early stage (Fig.3b).

These alloys are investigated in order to determine their transformation behaviour during AC1b and AC1f, too, as described with steel F82H mod.. In the region of transformation the highest ferrite concentration was found:

Alloy	Ferrite %	Temp. °C
736	12	880
735	5	860
734	3	840

Literature:

- [1] M. Schirra, K. Ehrlich, et.al.: OPTIFER, ein weiterer Schritt zur Entwicklung niedrigaktivierender martensitischer Stähle. FZKA 5624, Nov. 1995.
- [2] M. Hernandez, J. Lapena, M. Fernandez, M. Schirra: OPTIFER: Aceros de baja activacion candidatos como primera pared en los reactores de fusion nuclear par confinamiento magnetico. Proc. XXI Reunion Annual de la SNE 1995.

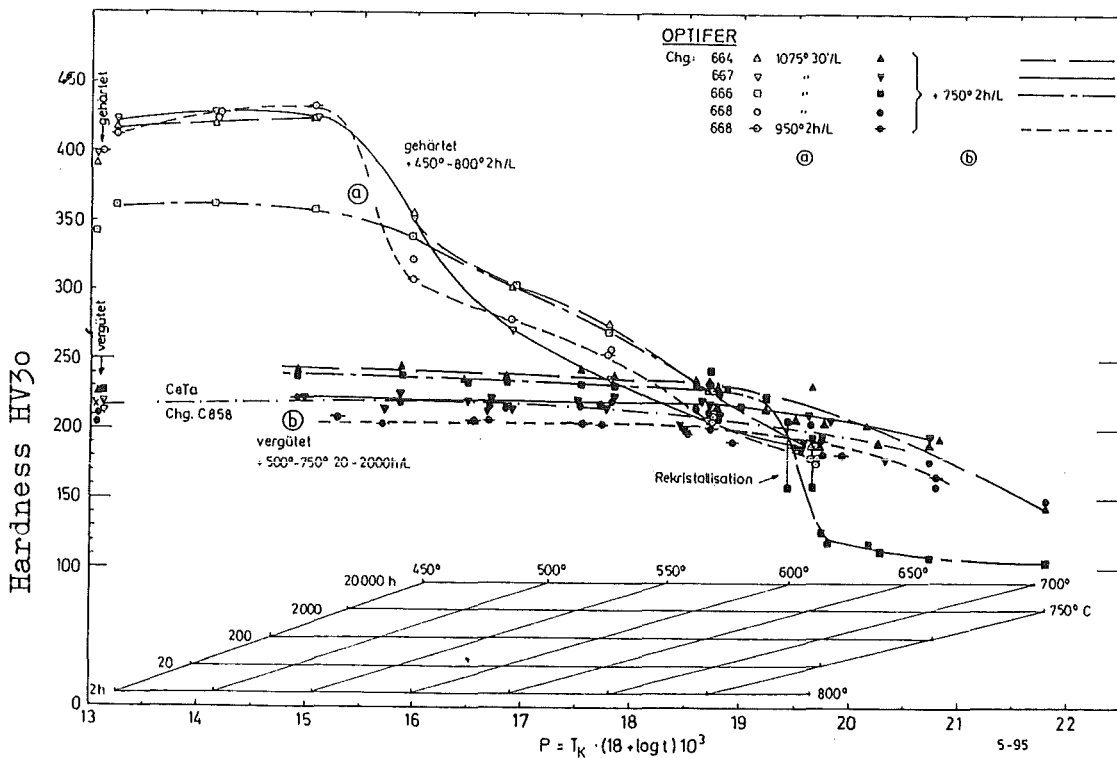


Fig.1: Master curve for aging (Hollomon-Jaffe-Parameter)

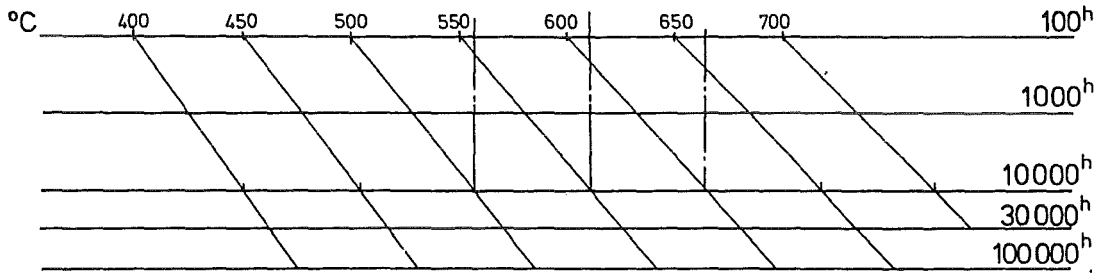
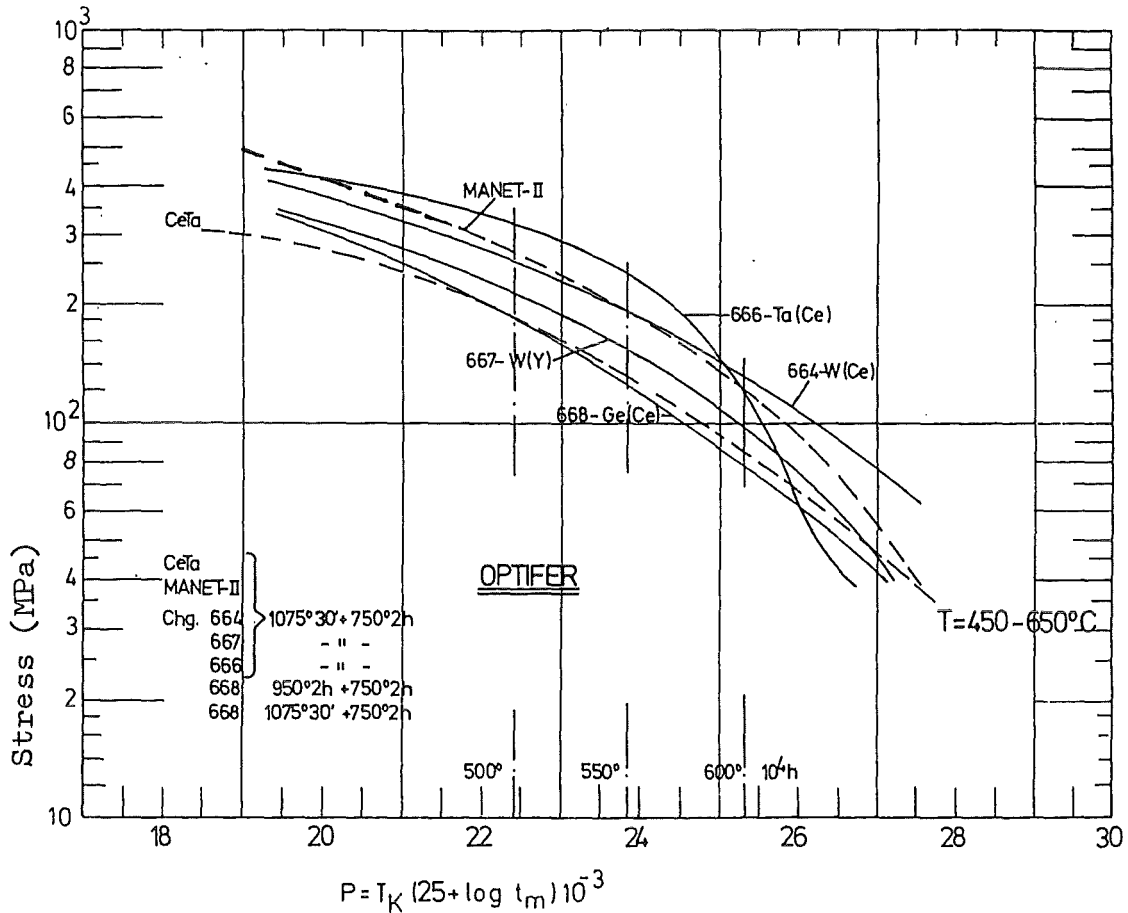


Fig.2: Master curve for rupture time (Larson-Miller-Parameter)

[3] M. Fernandez, J. Lapena, M. Hernandez, M. Schirra: OPTIFER, un paso hacia el desarrollo de un acero martenítico de baja activación. Inf. Técnico CIEMAT 790, Febr. 1996.

[4] M. Schirra, K. Ehrlich: Physikalische und mechanische Untersuchungen an niedrigaktivierenden martensitischen Stählen vom Typ OPTIFER. Proc. KTG Mannheim, 1.5. 1996, Beitrag 812.

[5] K. Ehrlich, S. Kelzenberg, M. Schirra, A. Möslang: Die Entwicklungen von metallischen Strukturmaterialien mit niedriger Aktivierbarkeit für nukleare

Anwendungen. Beitrag: Werkstoffwoche, Stuttgart, Symposium 3, Mai 1996.

Staff:

A. Falkenstein
P. Graf
S. Heger
E. Materna-Morris
D. Preininger
M. Schirra
L. Schäfer
H. Zimmermann

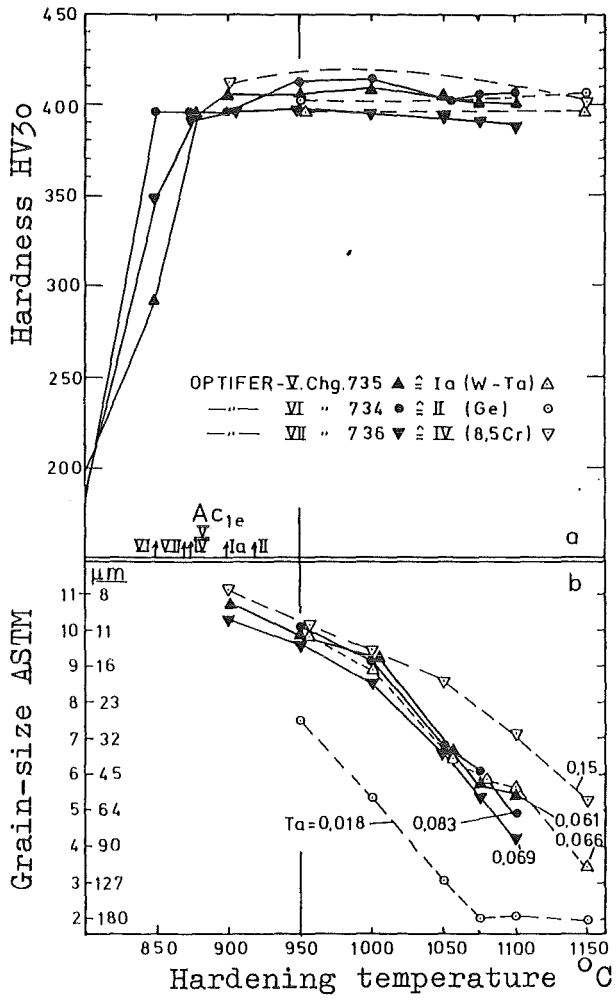


Fig.3: Hardening diagram

1.4.2 Fatigue and Creep Properties of Base Material on LA Martensitic Steels OPTIFER

1. Experimental

Since 23 mm thick and wide bars of OPTIFER IV are available now, preparation of cylindrical samples has been initiated, to run low cycle fatigue scoping tests under isothermal, total strain control and under thermal control, respectively.

Staff:

J. Aktaa

M. Klotz

C. Petersen

M. Pfeifenroth

D. Rodrian

R. Schmitt

1.5.0 / 1.5.1 MANITU Irradiation Program

1. Introduction

The problem of radiation-induced deterioration of fracture toughness remains to be a key issue for the application of ferritic/martensitic steels as structural materials for fusion reactors. In the previous investigation (SIENA program) it has been demonstrated that, after irradiation in a materials testing reactor to a dose of 10 dpa or even less, at temperatures around 300 °C, the shift in Charpy impact properties of 10-12 % Cr steels, as characterized by an increase of the ductile-to-brittle transition temperature (DBTT) and a decrease of the upper shelf energy (USE), can be unacceptably high. In the context of these results there was, at that time, a vital interest to learn more about the evolution of this degradation with fluence and about the possibility of even more damage (or lack of annealing effects) at lower irradiation temperatures.

With these objectives the MANITU irradiation project was started with staged doses of 0.2, 0.8, and 2.4 dpa and temperatures between 250 and 450 °C as target values. During the planning of the experiment several new aspects came at right time, which enabled us to fill the available space in the rigs in addition to the MANET steels with specimens of different promising low-activation alloys and thus redirect the goals of the experimental program.

Up to now all of the results from the 300 °C irradiation are available and allow us to draw interesting conclusions with respect to the dose effect on impact properties and the improvement attained by the introduction of new alloys with reduced long-term activation.

2. Experiments

The heat treatments of the alloys have not in all cases been optimized to the utmost and may thus leave some room for further improvement. Table 1 gives the chemical composition of the steels with a ranking order of the alloying elements that facilitates the distinction of characteristic deviations and allows for numerous speculations about the influence of composition on the different impact properties before and after irradiation.

Charpy specimens have been produced from the available materials according to the European standard for subsized specimens. All tests have been carried out with the same, instrumented facility which is installed in the Hot Cells.

The irradiations of the MANITU programme are all carried out in the HFR, Petten. The target values of the neutron doses was reached within about -2 % and +15 % depending on the core position of the specimens. The irradiation temperature of 300 °C was maintained within about ±5 % by a proper balance between n,g-heating and compartment cooling with different He-Ne mixtures. A total number of 180 specimens for each dose level (or at least 5 for each material and temperature) ensured a sufficient number of measurement

Table 1: Chemical composition of the different alloys in wt. %

	10-11 % Cr-NiMoVNb steels		low activation alloys			
	MANET I	MANET II	OPTIFER Ia	OPTIFER II	F82H std.	ORNL
Cr	10.8	9.94	9.3	9.43	7.73	8.9
W			0.965	0.005	2.06	2.01
Ge				1.1		
N	0.02	0.023	0.015	0.016	0.0027	0.0215
C	0.14	0.1	0.1	0.125	0.092	0.11
Mn	0.76	0.79	0.5	0.5	0.083	0.44
Ta			0.066	ca. 0.02	0.018	0.06
P	0.005	<0.006	0.0047	0.004	0.003	0.015
S	0.004	<0.007	0.005	0.002	0.003	0.008
V	0.2	0.22	0.26	0.28	0.189	0.23
B	0.0085	0.007	0.006	0.006	0.003	<0.001
Si	0.37	0.14	0.06	0.036	0.09	0.21
Ni	0.92	0.66	0.005	0.005	0.032	<0.01
Mo	0.77	0.59	0.005	0.005	0.0053	0.01
Al	0.054	<0.02	0.008	0.008	0.01	0.017
Co	0.01	<0.02			0.0024	0.012
Cu	0.015	<0.01	0.035	0.007	0.0059	0.03
Nb	0.16	0.14	0.009	0.009	0.0057	
Zr	0.059	0.034				<0.001
Ce			<0.001	<0.001		
Ti			0.007	0.007	0.0104	<0.01
Fe	balance	balance	balance	balance	balance	balance

points in order to connect and group them to curves with the irradiation temperature as abscissa and the materials as parameter.

3. Results

Fig. 1 shows the USE as a function of irradiation dose. The number of curves can be divided into two groups where the low activation alloys (LAA) generally maintain a high impact energy in the whole dose range, whereas the MANET steels behave much poorer.

If we now look at the DBTT curves (Fig. 2) we find again that the MANET steels behave quite bad, whereas the LAA are significantly better. At an irradiation dose of 2.4 dpa the difference in DBTT between MANET-I and the ORNL steel is 220 °C and it seems, if we extrapolate the DBTT curves to higher dose levels, that the further embrittlement of the LAA is much smaller compared to the MANET steels.

The dynamic yield stress measured at 100 °C is shown in Fig. 3. Up to the dose level of 0.8 dpa all LAA are suffering less of irradiation hardening compared to the MANET-II steel. But above 0.8 dpa the ORNL and OPTIFER-II steels show a bigger increase in dynamic yield strength compared to the other alloys. At 2.4 dpa the dynamic yield strength of the ORNL steel is even comparable to the MANET-II steel.

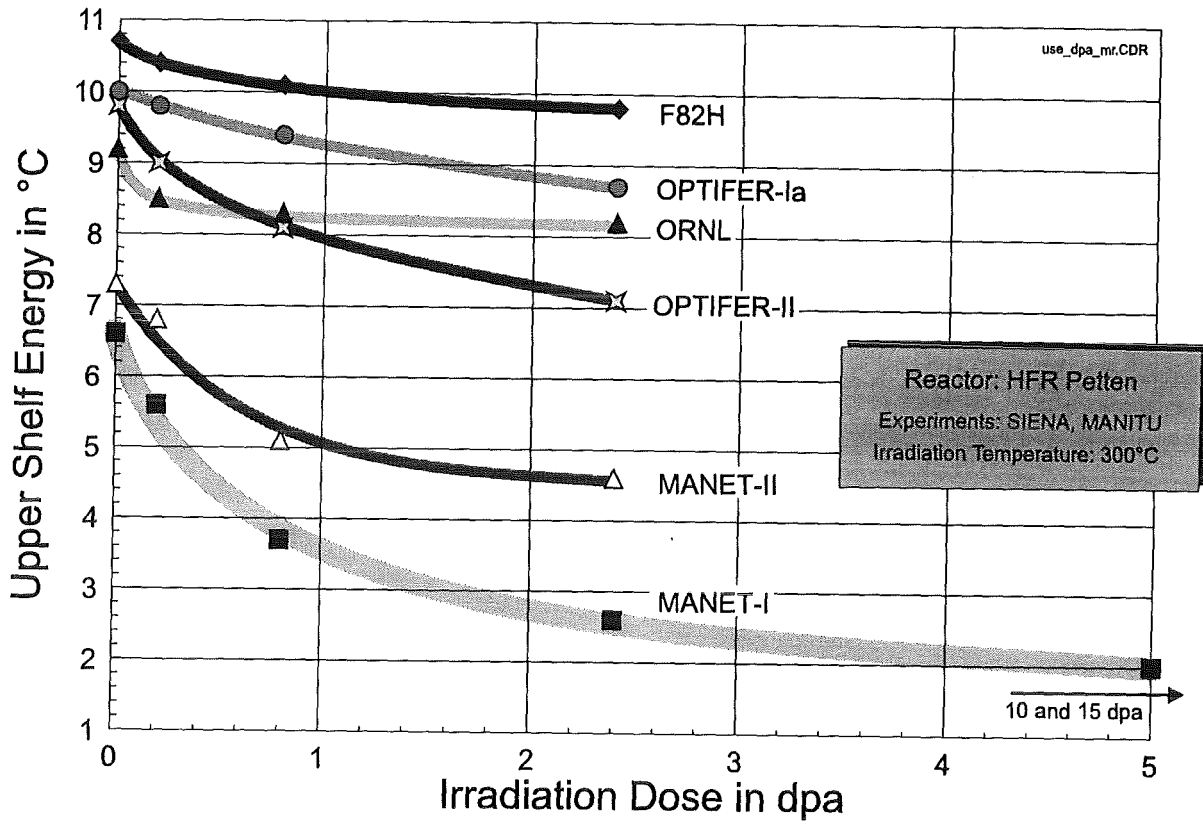


Fig. 1

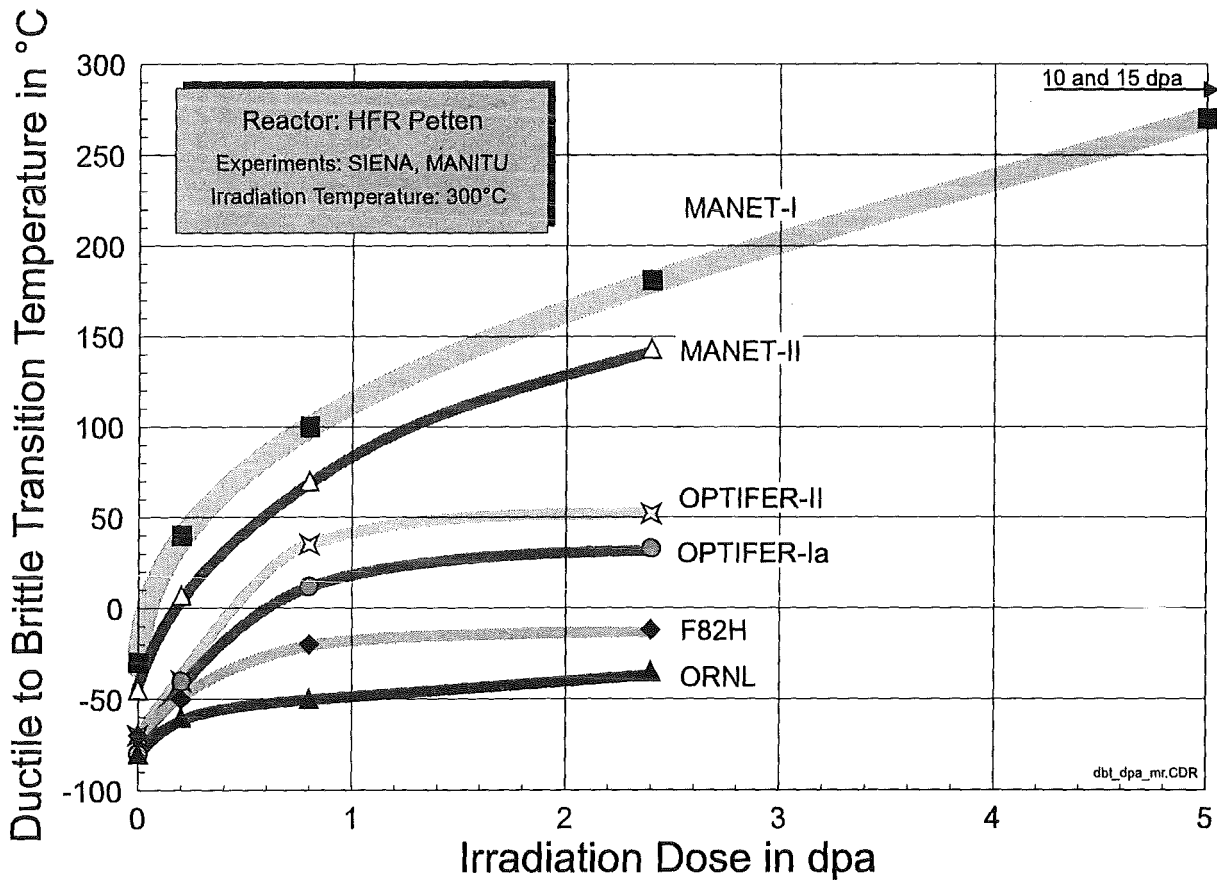


Fig. 2

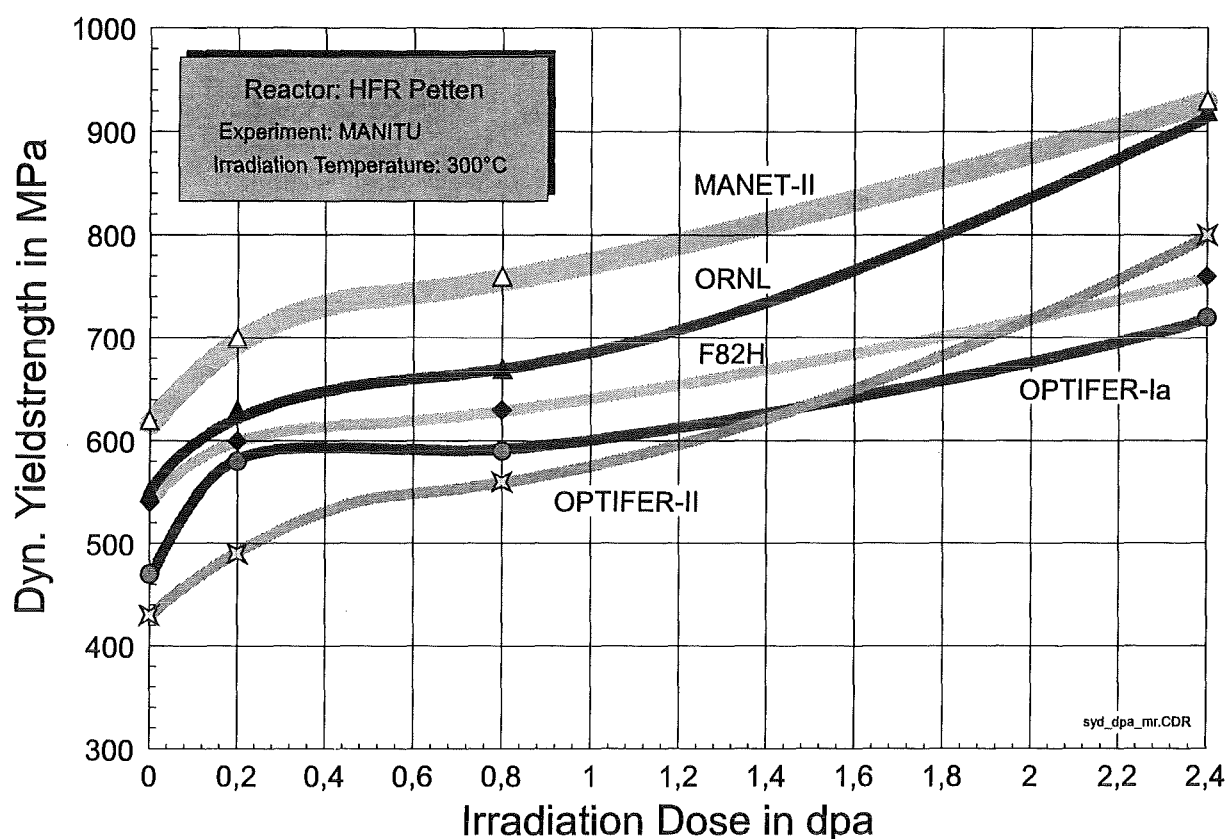


Fig. 3

4. Conclusions

- All LAA show a better embrittlement behaviour after neutron irradiation compared to the MANET steels. Especially in the higher dose range (>0.8 dpa) the difference becomes more and more significant.
- Among all examined materials the ORNL steel shows the very best embrittlement behaviour. Prior investigations have shown, that below irradiation temperatures of 400 °C the already minor deterioration in DBTT remains practically constant.
- All materials show irradiation hardening which increases with higher neutron doses. The ORNL and OPTIFER-II steels show the biggest increase in dynamic yield stress compared to the other alloys.
- Though the low neutron fluence of this irradiation experiment does not yet allow to draw general conclusions, it can be stated that all examined low activation materials provide clearly better impact properties than the corresponding MANET alloys.
- Further irradiation experiments have to verify these encouraging results with the low activation alloys at higher and especially more fusion relevant dose levels.

Literature:

- [1] M. Rieth, B. Dafferner, H.D. Röhrig, C. Wassilew, Fusion Engineering and Design 29 (1995) 365-370.
- [2] M. Rieth, B. Dafferner, H.D. Röhrig, Charpy Impact Properties of Low Activation Alloys for Fusion Applications after Neutron Irradiation, Seventh International Conference on Fusion Reactor Materials, Obninsk, Russia, 25-29 September, 1995.

Staff:

B. Dafferner
W. Kunisch
H. Ries
M. Rieth
O. Romer

1.6.1 / 1.6.2 Effects of Radiation Hardening and He in LAM / In-Beam Fatigue

Task 1.6: Mechanistic Investigations

The Dual Beam Facility of FZK, where α -particles (≤ 104 MeV) and protons (≤ 40 MeV) are focussed onto a target, was developed as a research tool for materials within the European Fusion Technology Program. This high energy dual beam technique allows the simulation of fusion neutrons by systematic variation of hydrogen, helium, and damage production in thick metal and ceramic specimens as well as the simulation of Tokamak relevant thermal and mechanical loads in proposed plasma-facing materials. In the present program the mechanistic investigations include

- a fundamental analysis of the displacement damage under light ion irradiation including a comparison with fusion neutrons,
- investigations of the impact of helium on tensile, charpy and microstructural properties, and
- investigations of the push-pull fatigue and fracture behaviour of postirradiated and in-situ irradiated specimens.

In the reporting period activities to the first two items are summarized.

1. Comparison of Displacement Damage of Light Ions with Fusion Neutrons

1.1 Introduction

In this work the applicability of light ion simulation irradiations with respect to the displacement damage under fusion neutron irradiation is investigated by theoretical and experimental activities. The production of primary knock-on atoms (PKA) and the displacement of lattice atoms (DPA) under proton and α -particle irradiation is considered in pure iron. The main focus is put on the effect of the non-elastic processes which are characterized by nuclear reactions and taken into account quantitatively for the first time.

1.2 Elastic displacement damage

In the energy range covered by the Dual-Beam facility the light projectiles lead by high probability through Rutherford scattering to elastic displacements. This displacement process is well known. For incident particles with energies from up to 100 MeV on pure iron the elastically PKA-spectra shows, that the lower the projectile energy the higher is the probability of recoil production but the lower the maximum transferable energy.

1.3 Non-elastic displacement damage

Under irradiation with high-energetic light ions nuclear reactions take place. These reactions lead to energetic residue nuclides called non-elastic PKA. The profiles of the non-elastic PKA-spectra can be characterized by the excitation functions of the corresponding nuclear reactions and by the mean recoil ranges of the residual nuclides. Based on theoretical calculations with nuclear and range models and on experimental measurements, non-elastic PKA spectra are obtained for all open reaction channels. This effort lead for the first time to a quantitative description of the light ion induced non-elastic displacement damage. For α -particle irradiations with energies $E_\alpha = 10$ MeV and $E_\alpha = 100$ MeV the non-elastic PKA-data are plotted in Fig. 1. In the case of

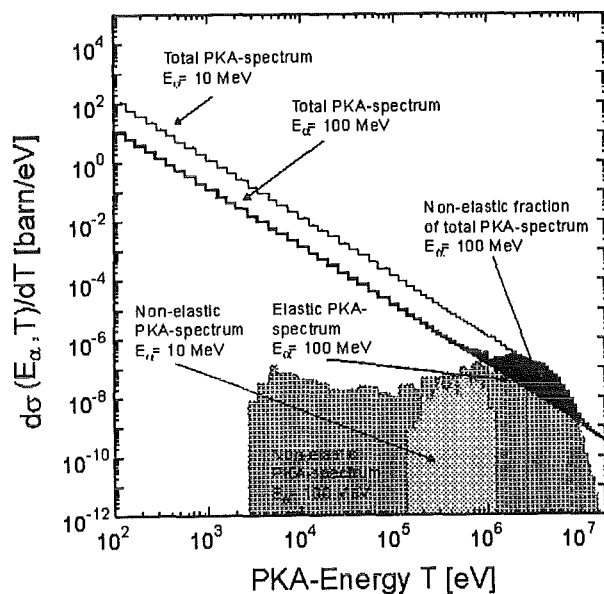


Fig. 1: Comparison of elastic and non-elastic PKA-spectra at α -particle energies of $E_\alpha = 10$ and 100 MeV

$E_\alpha = 10$ MeV the elastically produced PKA are more than two orders of magnitude higher than the non-elastic PKA. With increasing projectile energy the non-elastic fraction becomes more pronounced. At $E_\alpha = 100$ MeV the non-elastic fraction has increased while the elastic fraction has decreased. This means, that for PKA-energies higher than $T = 1$ MeV the non-elastic fraction is predominant and gives a well pronounced contribution to the total PKA-spectrum.

1.4 Comparison of light ions and fusion neutrons

The comparison of elastic and non-elastic damage can be done on the basis of the PKA- and the DPA-level. However, the PKA-level gives the more detailed insight in what kind of materials damage is produced.

1.4.1 PKA-spectra

In Fig. 2 a comparison of proton- and α -induced total PKA-spectra with a fusion neutron induced PKA-spectrum is shown. In general, comparing the top and bottom figure it is

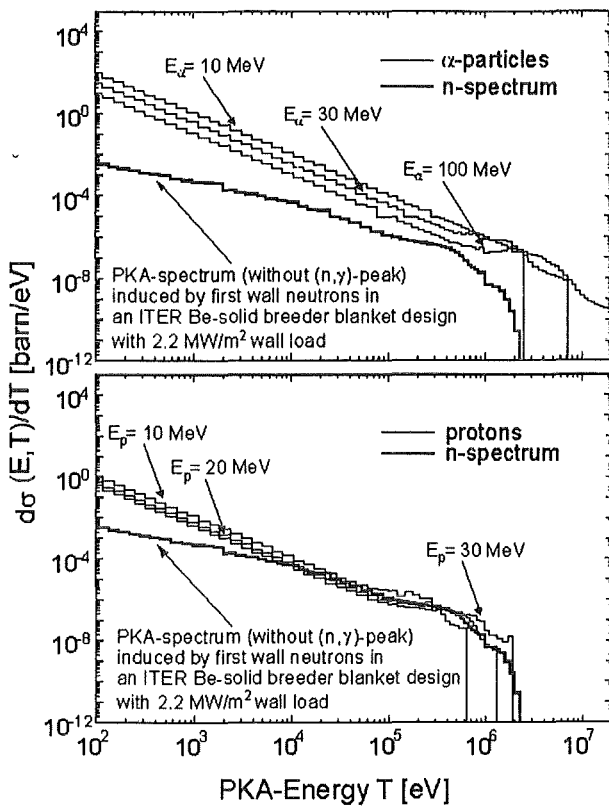


Fig. 2: Comparison of α -particle induced (top) and proton induced (bottom) PKA-spectra with a fusion neutron induced PKA-spectrum

obvious, that the probability of recoil atom production with α -particles is at comparable projectile energies one to two orders of magnitude higher than with protons. It is also obvious, that only for higher projectile energies the high energy recoil tail becomes more pronounced. The comparison between charged particle induced and neutron induced PKA-spectra shows that within a wide range of recoil energies the proton- and neutron-induced PKA-spectra matches very well, while the α -particles are characterized by a higher production probability and a larger recoil energy tail. However, at low energies the proton-induced recoil production probability is still significantly above the first wall fusion neutrons. It is important to mention that only the shape and not the magnitude of the PKA-spectrum is important in comparing charged particle and neutron induced PKA-spectra.

1.4.2 DPA-profiles

For DPA calculations the NRT-model was used. The elastically and non-elastically DPA-values were calculated separately. In Fig. 3 a comparison of the DPA-rates vs. penetration depth for protons, α -particles and fusion neutrons is plotted. It is distinguished between the elastic and non-elastic fraction of the DPA-rates. The top figure is calculated for incident 104 MeV α -particles on iron. The maximum energy refers to 0 μm . With increasing depth the particle energy is degraded. The elastic DPA-rate shows, that with increasing depth the displacement efficiency increases, because of the lowered α -energy. At the mean penetration depth the maximum

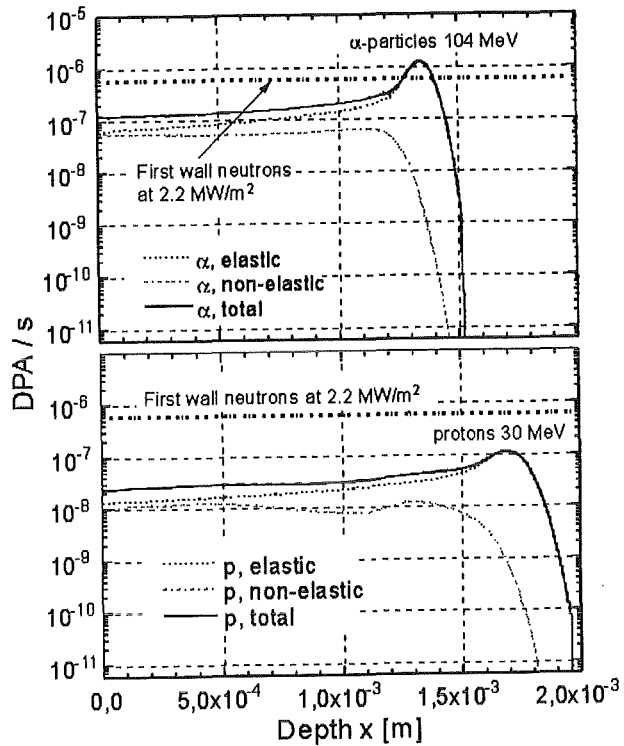


Fig.3: Comparison of the DPA-distribution in function of the penetration-depth in iron for protons (bottom), α -particles (top) and fusion neutrons. The charged particle DPA-rates are normalized to $1\mu\text{A}/\text{cm}^2$ particle flux density while the neutrons are normalized to $2.2\text{ MW}/\text{m}^2$ wall load

elastically produced damage occurs. On the other hand the non-elastic DPA-rate shows an almost constant level until the particle energy becomes close to the nuclear reaction thresholds, where the non-elastic DPA-rate decreases very rapidly. At the highest examined α -energy the non-elastic/total DPA-ratio turns out to be 0.47. This leads to an increase of the total DPA-rate of almost a factor of 2 at the high energy region.

Due to the large scattering length of fusion neutrons in iron the neutron induced DPA-production rate (bold dashed line in Fig. 3) can be treated as constant over the range of 2000 μm . The comparison of the neutrons and the α -particles shows that in the depth around the stopping range of the α -particles the DPA-rate exceeds the neutron-DPA-rate by almost a factor of 2 and in the range from 0 - 750 μm it is in average lower by a factor of five.

The bottom figure is calculated for incident 30 MeV protons on iron. The general behaviour is the same as the α -particles for elastic and non-elastic DPA. At the highest examined proton energy the non-elastic/total DPA-ratio turns out to be 0.43. This leads to a increase of the total DPA-rate of almost a factor of 2 at the high energy region. The comparison shows, that in general the proton-induced DPA-rates are significantly lower than the neutron induced ones. At the depth region of 0 - 750 μm it is lower by a factor of 25 while at the peak position it is lower by a factor of 6. The comparison between

proton- and α -induced DPA shows that the α -particles are much more efficient in producing displaced atoms than the protons.

1.5 Conclusion

The presented results show, that the investigation of non-elastic displacement damage under charged particle irradiation is indispensable for a valuable characterization of light ion induced damage parameters. Therefore, the main conclusion is that fusion neutron induced displacement damage can be simulated much better by charged particles than thought in the past. The softness of the PKA-spectra at high PKA-energies will no longer be a main point of criticism.

2. Tensile Properties of Helium Implanted F82H Mod

In plasmanear structural materials hydrogen isotopes and helium will be generated by inelastically scattered fusion neutrons. For the next generation of fusion reactors helium production rates of about 100 appm/y and hydrogen production rates of about 500 appm/y are expected in typical structural alloys. As ongoing controversial discussions in the present international literature indicate, is the behavior of helium in some reduced activation materials a serious matter of concern. HFIR

irradiations on f/m steels often show a significant ductility reduction and a pronounced DBTT increase if the steels are doped with B or Ni additions to increase the helium content by non-elastically produced transmutations. However, due to the nature of these experiments it is hardly possible to distinguish between B/Ni segregation induced and helium bubble generated embrittlement.

Helium implantations at the FZK Dual Beam Facility are a suitable tool to get a very homogeneous helium distribution in sufficiently thick specimens without the need to change the materials composition. This work describes changes in the tensile properties of F82H mod specimens implanted between 50 and 420 °C with 500 appm helium at the high energy Dual beam facility of FZK. Although a fusion similar ratio of He/dpa was not used, these experiments provide suitable information of the impact of helium on strength and ductility parameters within a wide temperature range. Sheet tensile specimens with a reduced gauge volume of 7.0x2.0x0.20 mm³ were produced by spark erosion from foils following the reference heat treatment. The irradiation conditions are listed in Table 1. Special emphasize was put on fairly low helium and damage production rates.

In Figs 4-6 the tensile properties of α -particle irradiated tensile specimens are shown together with unirradiated control specimens. The irradiation induced yield strength change (80 MPa at 250 °C decreases moderately with increasing temperature up to 350 °C and diminishes rapidly above about 400 °C.

Irradiation induced hardening predominant at temperatures below 400 °C and small softening prevailing above about 450

Table 1: Irradiation parameters at the Dual Beam Facility

Temperature range	50 - 420 °C
Helium production rate	(2.5-3)x10 ⁻³ appm/s (1.4-1.8)x10 ⁻⁶ dpa/s
Displacement damage rate	~ 50 h
Irradiation time	500 appm He
Implanted concentration	0.3 dpa
Displacement damage dose	purified He-gas
Specimen environment	

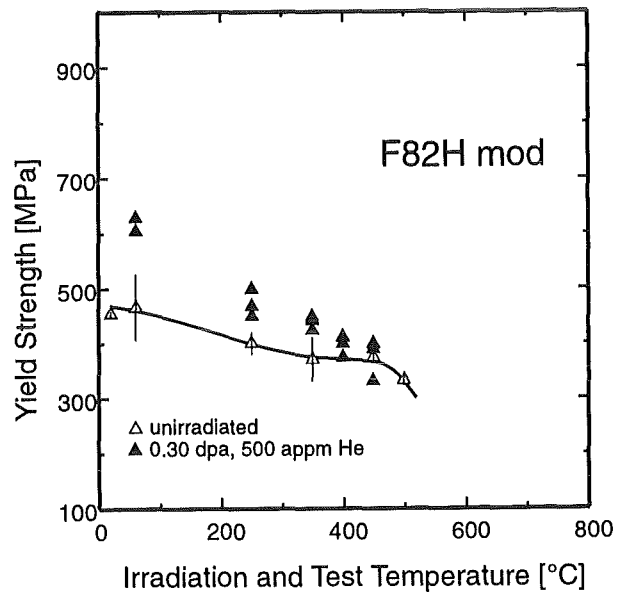


Fig. 4: Yield strength of F82H-mod specimens after He-implantation

°C is a common feature of martensitic/ferritic Cr-steels. By analyzing various strengthening contributions the authors have shown in the past that the dominant hardening contribution can be explained by dislocation loop formation or irradiation enhanced precipitation. Helium only tends to stabilize these effects. However, if Figs. 4 and 5 are compared with earlier α -particle irradiations on MANET tensile specimens under the same conditions, it turns out that the irradiation induced hardening is much smaller in the F82H mod specimens. For helium implanted specimens the hardening ratio between F82H and MANET 1 is about 0.55±0.09 within a wide temperature region. Microstructural examinations of the defect and helium bubble morphology are planned to investigate the different hardening efficiencies of both steels.

While a significant ductility reduction has been observed at the lowest irradiation temperature (Fig. 6) in F82H mod specimens, the uniform and total elongation are nearly unaffected by the helium implantations at 250°C and above.

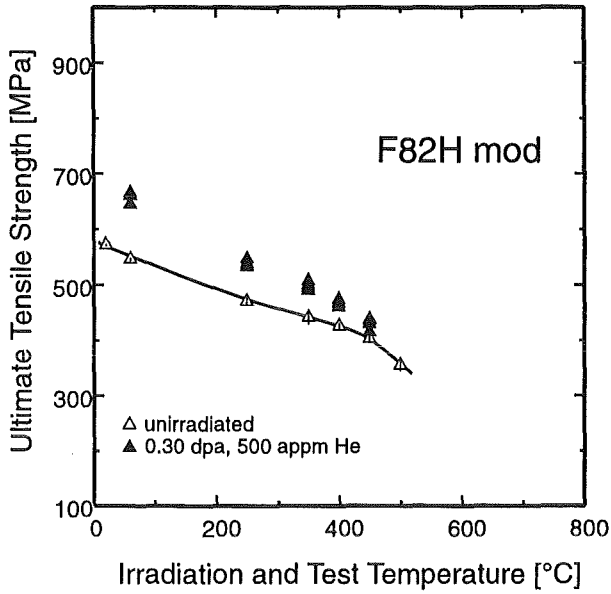


Fig. 5: Ultimate tensile strength of F82H-mod specimens after He-implantation

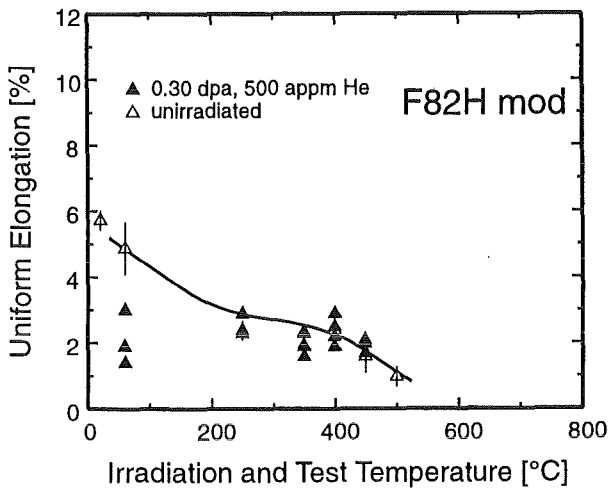


Fig. 6: Uniform elongation of F82H-mod specimens after He-implantation

It is important to note that in contrast to MANET 1 specimens that showed a pronounced, dynamic strain aging related ductility drop from 3 to 0.3% after helium implantation between 280 and 350 °C, no DSA was observed in unirradiated and helium implanted F82H mod specimens. At all temperatures investigated, the rupture mode always remains ductile and transcrystalline for the implanted specimens and unirradiated controls.

Literature:

[1] K. Ehrlich, S. Cierjacks, S. Kelzenberg and A. Möslang, "The development of structural materials for reduced long-term activation", in Effects of Radiation on Materials; Editors: D.S. Gelles, R.K. Nanstad, A.S. Kumar and E.A. Little; ASTM STP 1270, p. 1109 (1996).

[2] E. Daum et al, Comparison of elastic and non-elastic displacement damage under light ion simulation irradiation", ICFRM-7, Obninsk, Russia, Oct. 1995, Proceedings in JNM, in press.

[3] E. Daum, FZKA 5833, September 1996

[4] J. Bertsch, R. Lindau and A. Möslang, "In-situ and postirradiation fatigue properties of the ferritic-martensitic steel MANET at 250 °C", ICFRM-7, Obninsk, Russia, Oct. 1995, Proceedings in JNM, in press.

[5] D. Preininger, "Ductility and workhardening behaviour of 8-12% Cr and austenitic Cr/Ni steels"; Proceedings of the Intern. Congress on Stainless steels '96, 3-5 June (1996).

[6] D. Preininger, FZKA 5701, 1996

[7] D. Preininger, "Härtungsbedingte Duktilitätsverminderung und Sprödbbruchverschiebung martensitischer 7-12% Cr-Stähle", Werkstoffkunde '96, 28/31.5.96.

Staff:

- S. Baumgärtner
- G. Bürkle
- E. Daum
- G. Hecker
- R. Lindau
- A. Möslang
- D. Preininger

WP 4 Materials Application and Technology

4.1.2 Fracture Mechanics Studies

1. Introduction

Fracture appearance of ferritic steels in a wide temperature range is characterized by a ductile-to-brittle transition if the testing temperature decreases or strain rate increases. For neutron irradiated materials, this transition is shifted towards higher temperatures. The transition behaviour is usually characterized by impact testing of Charpy-type specimens, a fast and long established experimental procedure. On the other hand, results of impact testing are hardly to use for design calculations and difficult to transfer on other specimen geometries. During the last 10-20 years, big progress was made in understanding of mechanisms which trigger cleavage fracture in the low-temperature regime or ductile fracture in the high-temperature regime. Progress in computational power and numerical modelling enabled a new kind of approach on fracture which is based on the local mechanisms of material failure. This "Local Approach" is based on the physical description of fracture initiation sites in an elasto-plastic stress field and, therefore, includes already the basic framework which is necessary to obtain transferability of fracture mechanics parameters between different geometries. Standardisation of the basic methodology is currently in progress and it is the aim of this task to apply the Local Approach methodology for a consistent framework of fracture mechanics material characterization which also meets requirements of design calculations.

2. Methodology

The Local Approach requires a numerical analysis of carefully designed experiments. Notched round bars are used to determine the so-called Weibull stress for brittle fracture. The Weibull stress at fracture is a stochastic variable and has to be determined by statistical evaluation of the numerical elasto-plastic analysis of experiments. Essentially, a numerical integration of the stress field of the specimen has to be performed. Hence, accurate stress-strain data of the material is required for the numerical analysis.

For ductile fracture, which is triggered by void formation and growth, material damage has to be considered in the numerical analysis. Parameters of ductile fracture are determined from metallographic data and from elasto-plastic analysis of experiments using constitutive modelling of void growth.

In the transition regime, competition of these two mechanisms takes place. Modelling of the transition behaviour is still incomplete, however, there are basic ideas of how to do this.

3. Progress of Work

Work on this task started end of 1995. It consists essentially of two parts: experimental work and numerical analysis. The first step in the experimental part, which was reached during the last year was the modification of a tension test device which was equipped with a temperature control device allowing tests at different temperature levels between -150°C and 100°C. Round unnotched bars are tested for the stress-strain data at -150°C, -120°C, -100°C and RT. For the numerical part, these data are required to select suitable notch geometries for the notched tensile tests which are used for the determination of the Weibull stress for brittle (cleavage) fracture. At the moment, a modified Weibull stress analysis is under implementation which allows constraint correction and unified description of cleavage data from different tests. This is an important tool for the prediction of geometry effects and hence transferability of data.

Staff:

J. Aktaa
E. Diegele
M. Klotz
C. Petersen
H. Riesch-Oppermann
G. Rizzi

4.3.1 Weldability Tests (Diffusion Welding)

Literature:

It had been tested in a series of experiments [1] which diffusion welding conditions (temperature, pressure, time, deformation of welding layer) are necessary to obtain good weldments. We have taken from the welded plates some specimens for tensile, bending and impact bending tests, in order to evaluate the strength, ductility and toughness of the weldments. According to Figure 1 the mechanical properties

[1] G. Haufler: Diffusionsschweißen von Probenplatten aus MANET 2 für gekühlte Blanketstrukturen (Abschlußbericht), KE Stuttgart, 1-TB-241/94 (1994).

Staff:

L. Schäfer

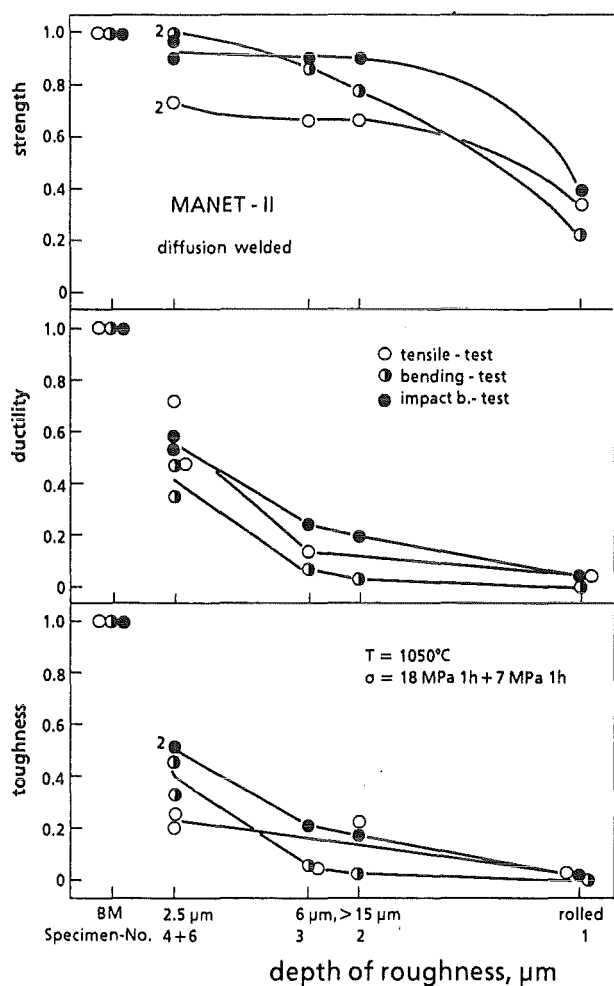


Fig. 1: Strength, ductility and toughness of diffusion welded MANET-II steel in dependence of the depth of roughness of the joined surfaces.

tested here are strongly dependent on the former depth of roughness of the joined surfaces. The weldments of not machined as received (rolled) plates reveal, dependent on the test method, a strength of 20 to 40 % of the base material. The ductility and the toughness of these weldments amounts to only 0.5 % of the value of the base material, it means that only elastic deformation is possible. The machined surfaces with a depth of roughness of $\geq 15 \mu\text{m}$ show a strength of about 80 % of the base material, and ductility and toughness increases remarkably, too. But only a toughness of 2.5 μm yields a ductility of about 50 % and a toughness of about 30 % related to the base material. Maybe only these results and this roughness are acceptable.

Neutron Source

ERB 5000 CT 950013 NET (NET/94-366) Conceptual Design of the International Fusion Materials Irradiation Facility IFMIF (Phase 2)

After a Conceptual Design Activity (CDA) study on an International Fusion Materials Irradiation Facility has been launched under the auspices of the IEA, specialists from Europe, Japan and the United States came together during two workshops held in Karlsruhe [1,2] to define the concepts for the three major technical systems

- Accelerator System
- Lithium Target System
- Test Cell System

During summer 1995 another subgroup, the Design Integration Group, has been established. The mission of IFMIF is to provide an accelerator based, Deuterium-Lithium (D-Li) source to produce neutrons with a suitable energy spectrum at sufficient intensity and irradiation volume to test samples of candidate materials to full lifetime of anticipated use in fusion energy reactors. IFMIF would also provide calibration and validation of data from fission reactor and other accelerator-based irradiation testing.

The IFMIF concept is derived from requirements from the materials community for test volumes and neutron fluences needed to obtain useful irradiation data in a reasonably short operating time [3]. Studies indicate that a volume of about 0.5 L is required in a region producing a flux equivalent to 2 MW/m² (0.9 x 10¹⁸ n/m²-s, uncollided flux) or greater. A fraction of this volume, about 0.1L would be available at a flux equivalent to 5 MW/m² for accelerated testing. The design concept consists of a deuteron accelerator producing particle energies in the range of 30 to 40 MeV. The deuterons interact with a flowing liquid lithium target (D-Li) producing high energy neutrons with a peaked flux around 14 MeV. The resulting high energy neutrons will interact with a set of test assemblies located immediately behind the Li-Target.

For the Test Cell system 11 tasks were identified which can be grouped into the three major fields neutronics, test matrix/users and test cell engineering. While the users requirements could be mainly defined already during the first half of the CDA phase, the second half of the CDA can be characterized by a significant progress both in the neutronics and in the design of the Test Facilities. Within the present two years CDA phase the international coordination for the „User's requirements" and the „Test Facilities Systems" is organized by two FZK members. The final IFMIF CDA report will be published in December 1995.

1. Neutronics

Detailed neutron transport calculations are needed for designing the IFMIF material test cell with its loadings. This

requires the development of an appropriate code and nuclear data file system that is underway at FZK The

main computational tool for the neutron transport calculations is the continuous-energy Monte-Carlo code MCNP that allows a very flexible description of the IFMIF target and cell system. The neutron cross-section evaluation and processing effort as well as the development of the neutron source model and supplementary codes is directed to the goal to allow reliable MCNP transport calculations for IFMIF.

1.1 High Energy Neutron Cross-Section Evaluation

A comprehensive nuclear data evaluation programme has been launched in a co-operation between Forschungszentrum Karlsruhe (FZK) and the Obninsk Institute of Nuclear Power Engineering (INPE) to provide high energy neutron cross-section data needed for neutronic design analyses of IFMIF. Data evaluation is being performed for the neutron energy range above 20 MeV making use of modern reaction theory [1]. Below that energy, neutron cross-section data are being adopted from well established data files like ENDF/B-VI and JENDL-3.

Evaluated data files have been prepared for the nuclides ⁵⁶Fe, ²³Na, ³⁹K, ⁵²Cr, ⁵¹V, ¹²C and ²⁸Si following the ENDF-6 format rules. As an example, Fig. 1 shows the evaluated neutron

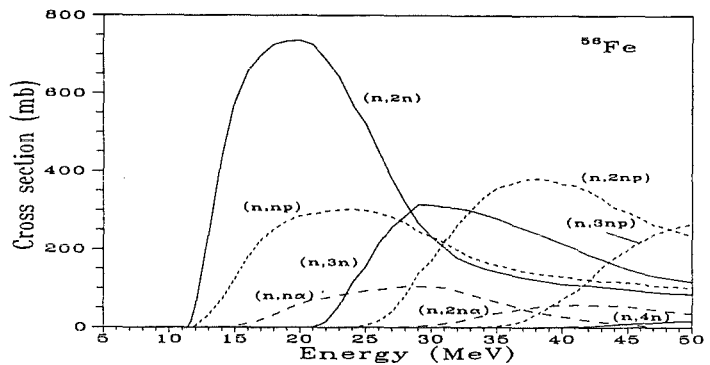


Fig. 1: Evaluated ⁵⁶Fe neutron emission cross-sections

emission cross-sections for ⁵⁶Fe. The data evaluation for ⁵⁶Fe includes gamma-production data and recoil spectra needed for the calculation of the nuclear heating and the neutron induced radiation damage in the test specimens. Work is underway to complete the data files for the other nuclide evaluations in this respect.

1.2 Cross-Section Processing for MCNP-Calculations

The evaluated high energy cross-section data have been prepared in the ENDF-6 format to allow the processing with the NJOY-code. The ENDF-6 reaction type MT=5 (neutron in, anything out) has been used to represent the multiple particle emission reaction cross-sections with their energy-angle distributions and energy-dependent particle yields on ENDF-6 file MF=6. This data representation is appropriate for

subsequent use with the MCNP Monte Carlo transport code requiring energy dependent particle yields. Using the ACER module of the NJOY processing code, an MCNP library has been prepared for the nuclides ^{56}Fe , ^{23}Na , ^{39}K , ^{52}Cr , ^{51}V , ^{12}C and ^{28}Si with neutron cross-section data up to 50 MeV. For ^{56}Fe , the MCNP data file already includes gamma-production data and recoil spectra in a preliminary version. Sub-sections for p, α , γ and recoil nuclei have been integrated to MT=5, MF=6 for that purpose.

1.3 Monte Carlo Neutron Source Modeling

For use with the MCNP transport code, a Li(d,n) reaction model has been developed that allows for sampling the angle- and energy-dependent emission of neutrons following compound nucleus and stripping reactions of the deuterons with the lithium target nuclei [2]. The model assumes a linear combination of the two neutron production mechanisms. Thick target yield data measured by Sugimoto et al. for 32 MeV deuterons incident on a lithium target were used to adjust the share of the two components to the total yield.

The sampling of the neutron source distribution is being performed in a source routine linked to the MCNP-code. The following beam and target characteristics can be specified and passed to the source routine via the standard MCNP input file: number of beams and targets, beam current, deuteron energy, beam direction and orientation, beam spot centre location, target surface normal and target density. In addition, the beam profile can be modified to allow a non-uniform distribution in the transversal directions. For that, use is made of a linear combination of three functions in each direction based on Gaussian distributions (Fig. 2)

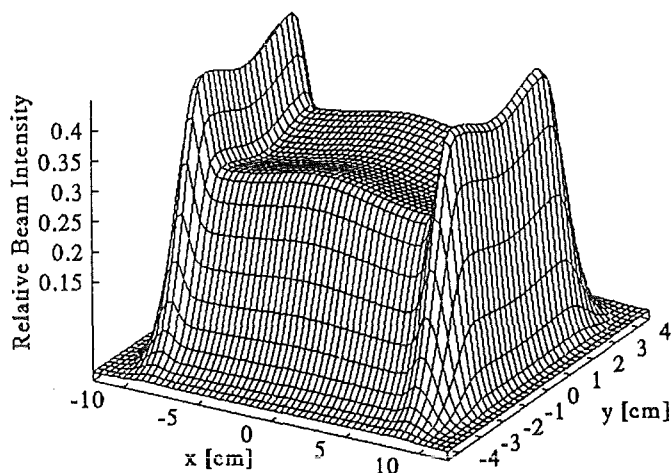


Fig. 2: Non-uniform beam profile for the MCNP neutron source routine

1.4 MCNP-calculations for He- and NaK-cooled Test Cell Assemblies

MCNP test calculations have been performed for the helium and the NaK-cooled high flux material test cell assemblies using the ^{56}Fe -, ^{23}Na -, and ^{39}K data. Fig. 3 shows the MCNP

model of the NaK-cooled test cell. The main objective of these calculations was to test the evaluated high-energy cross-section data along with the neutron source model for MCNP transport calculations of IFMIF. Fig. 4 shows a typical neutron spectrum in a lateral cell of the NaK-cooled test assembly as compared to the uncollided neutron spectrum in the same cell (voided case).

Literature:

- [1] Yu. A. Korovin et al.: Evaluation and Test of High Energy Neutron Cross-Section Data for the IFMIF Intense Neutron Source, 19th Symposium on Fusion Technology, Lisbon, Portugal, September 16-20, 1996.
- [2] P. H. Wilson, U. Fischer: Analysis and Implementation of a Monte Carlo High Energy Neutron Source for IFMIF, 19th Symposium on Fusion Technology, Lisbon, Portugal, September 16-20, 1996.

Staff:

U. Fischer
M. Sokcic-Kostic
U. v. Möllendorff
P. P. H. Wilson
D. Woll

2. Test Facilities Engineering

Significant progress could be achieved during the 2nd half of the CDA phase based on an integrated concept for the test module irradiation in the Test Cell, the various related remote handling tools, and the post-irradiation examination in dedicated hot cells. Advanced design concepts are available.

As shown in the FZK design (Fig. 5), the IFMIF Test Cell contains (i) two vertically oriented test assemblies, referred to as Vertical Test Assemblies (VTAs) 1 and 2, which support the test modules used for long-term irradiation of specimens in the high and medium flux regions, (ii) an array of tubes, referred to as Vertical Irradiation Tubes (VITs), used for inserting test capsules in the low and very low flux regions, (iii) a vacuum liner that encloses the test modules and also accommodates the lithium target, (iv) a helium gas cooled heat shield surrounding the liner to protect the concrete neutron shielding from overheating, (v) the Test Cell Removable Cover, which can be lifted with an overhead crane to gain access to the entire Test Cell, and (vi) a seal plate for providing a vacuum seal between the removable vertical test assemblies and the Removable Cover.

The three Vertical Test Assemblies considered in the present design are sufficient for the four flux regimes. That is, test beds for instrumented and/or in situ experiments in metals and nonmetals can be provided meanwhile for any loading

regime from >20 dpa/y to 0.01 dpa/y. In the present reference design the high flux region consists of either NaK cooled test modules for low and medium irradiation temperatures or helium gas cooled test modules for high temperature applications with the strong option to replace the NaK cooled version after the feasibility of the helium concept has been shown experimentally mainly by thermal hydraulics tests. Major advantages of helium gas instead of NaK are flexibility with respect to irradiation temperatures as well as safety and maintenance considerations (NaK has more than 10 times higher decay heat than Fe during the first day after irradiation).

Either simultaneous in-situ push-pull creep fatigue tests on three individual specimens or in-situ tritium release tests on breeder materials are foreseen in the medium flux region. Fig. 6 shows a birds view of the test module for in situ creep fatigue experiments. The approximate size of the in-situ test equipment is 100 mm high, 80 mm thick, and 400 mm wide. Three creep fatigue specimens may be tested independently at one time in this equipment. A total of 4 coolant pipes, three for the specimens and one for the hollow frame, as well as 15 electrical wires for thermocouples and the load-displacement signals are required. Three actuators for loading the specimen and the piping for the actuators are also installed in the VTA module.

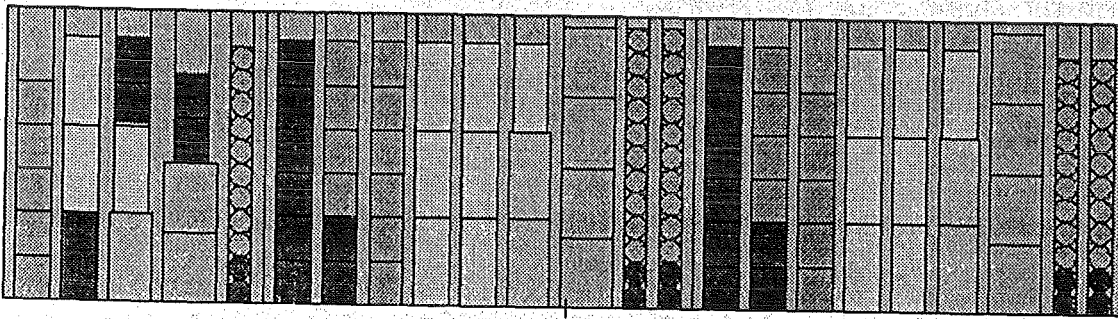


Fig. 3: MCNP-model of NaK cooled high flux material test cell

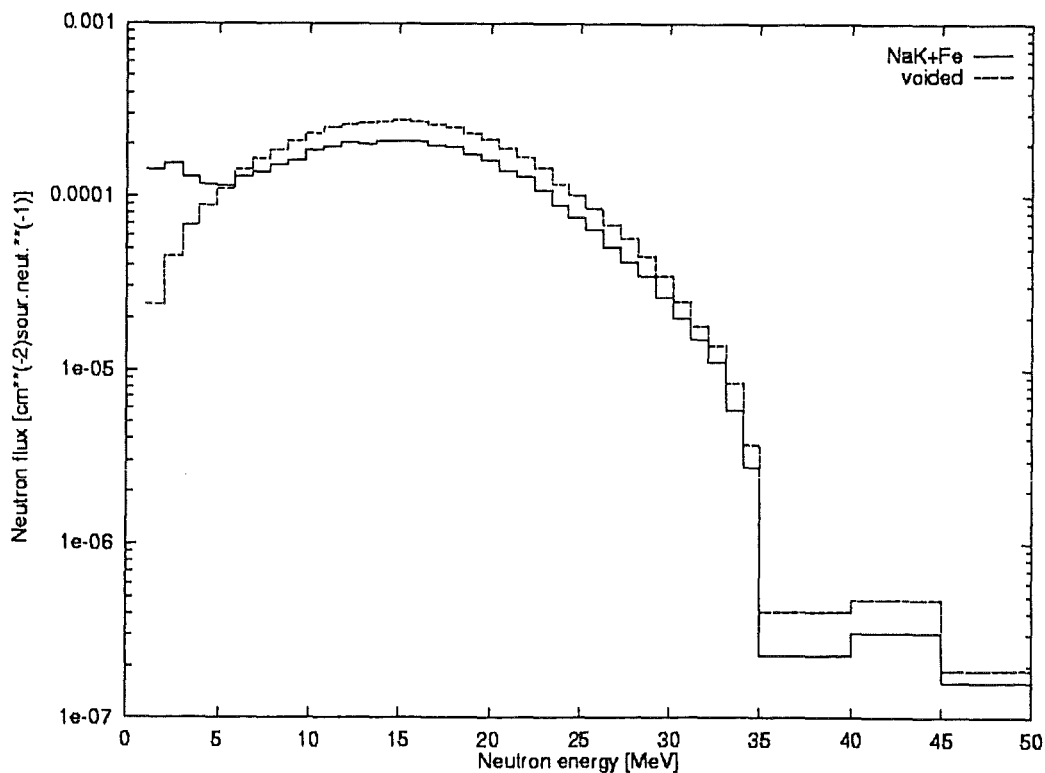


Fig. 4: Neutron spectra in lateral cell of NaK cooled high flux material test cell

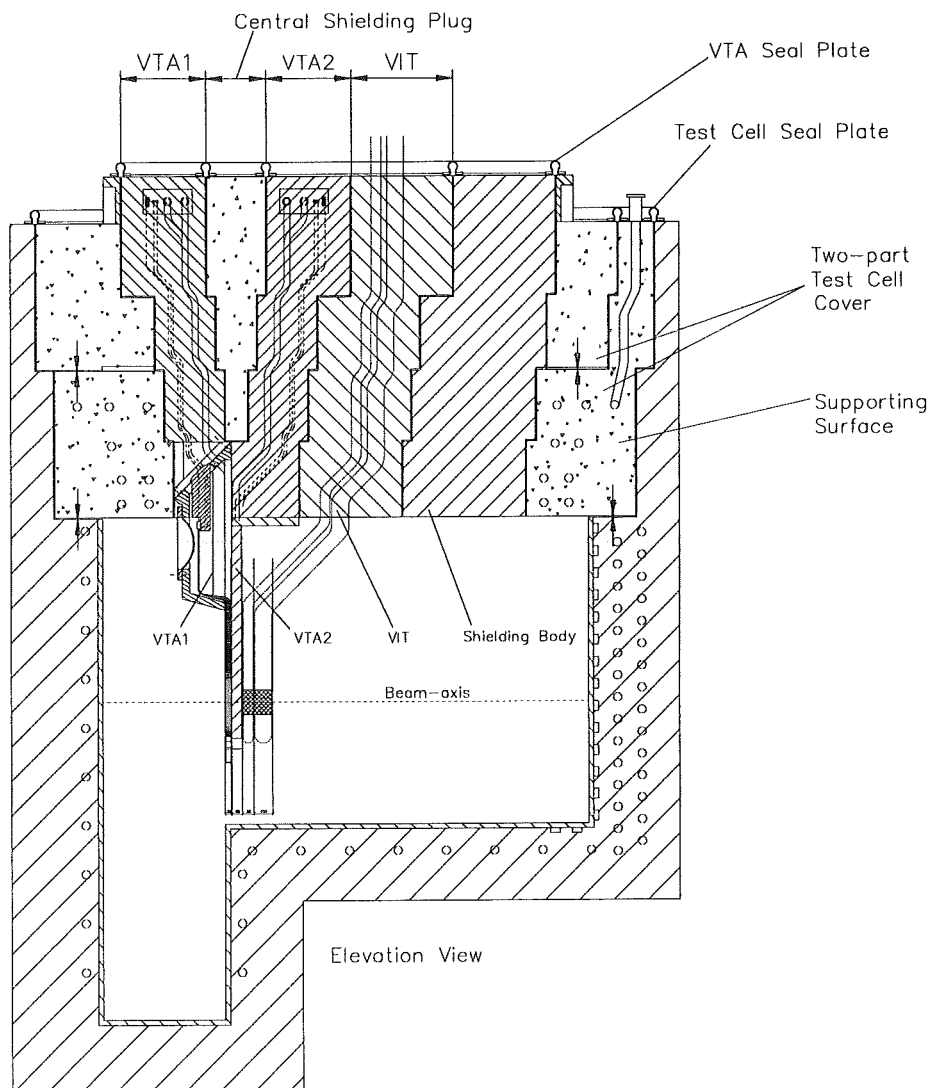


Fig. 5: FZK design of the IFMIF Test Cell

During the reporting period, FZD has developed a variety of detailed designs for the high and medium flux VTAs, the related test modules and the specimen instrumentation [6,7]. Major engineering efforts have been also undertaken to completely remote control any maintenance and assembling/disassembling activities in the Test Cell, the Access Cell and the Service Cell during normal and off-normal operation scenarios. Once the specimens are retrieved from the capsules in the Test Module Handling Cell, they will be mechanically tested in the PIE Hot cells followed by microstructural investigations like SEM or TEM in the Glove Box Laboratory.

Literature:

[3] K. Ehrlich and R.Lindau, Proceedings of the IEA Technical Workshop for the Intern. Fusion materials Irradiation facility, KfK, 26-29 Sept. 1994, FZKA report 5553 (1995).

[4] A. Möslang and R. Lindau, Proceedings of the IEA-Technical Workshop on the Test cell system for an

Intern. Fusion Materials Irradiation Facility; FZK, 3-6 July 1995, FZKA report 5633 (1995).

[5] T. Kondo, T. Shannon and K. Ehrlich; 8th Intern. Conf. on Fusion Reactor Materials (ICFRM-8), Obninsk, Russia, Sept. 25-29 1995, to be published in Journ. Nucl. Matter.

[6] A. Möslang, E. Daum, J.R. Haines, D.M. Williams, S. Jitsukawa, K. Noda and R. Viola, Overview of the IFMIF Test Cell Design, 12th Topical Meeting of the American Nucl. Society, Reno, NV, June 16-20, 1996.

[7] T.E. Shannon, M. Rennich, T. Kondo, H. Hatsuta, H. Maekawa, R.A. Jameson, M. Martone and A. Möslang, Conceptual Design of IFMIF, 16th IAEA Internat. Conf. on Plasma Physics and Controlled Nuclear Fusion Research, Montreal, Oct. 7-11, 1996.

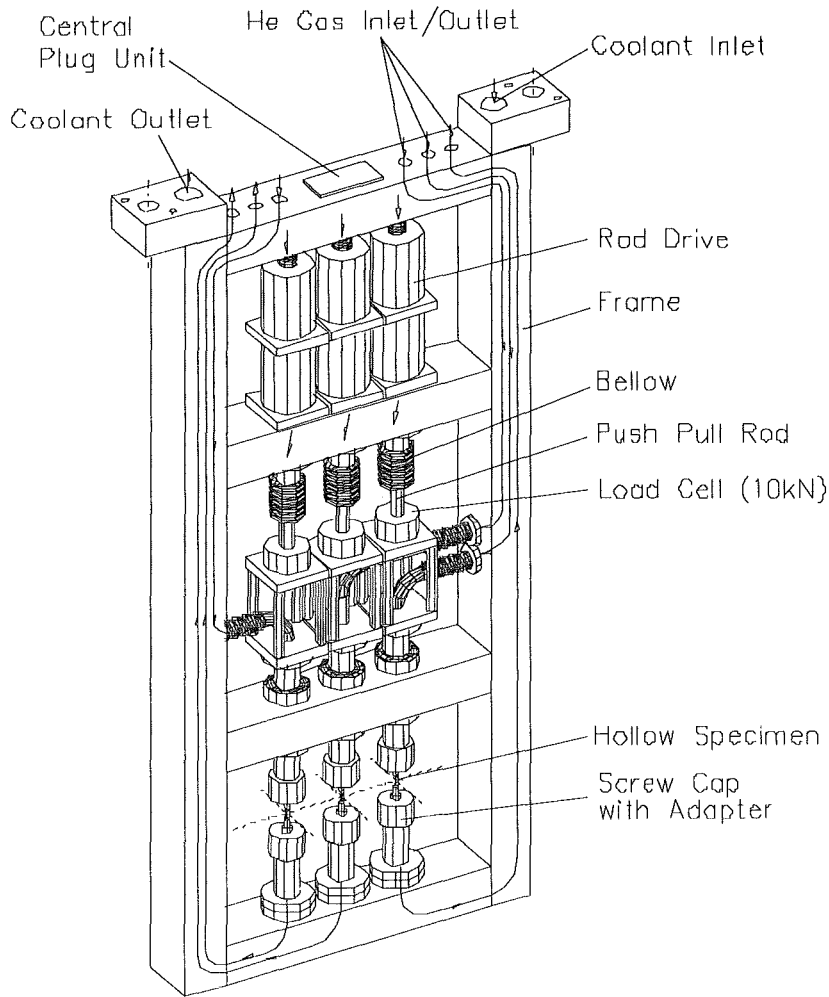


Fig. 6: Test module for in situ creep-fatigue experiments on three independent specimens

Staff:

E. Daum
K. Ehrlich
A. Möslang

- hence it derives the significance of an accurate velocity profile at the nozzle exit
- while the laminar model gives acceptable solution for the core flow, only a turbulence approach can satisfactorily describe the global velocity and temperature field distributions, especially in the boundary regions.

3. Target System

The Conceptual Design Activity for the IFMIF Target System has been started in FZK in 1995 by establishing an working environment for the evaluation of the thermal hydraulic response of the lithium target with incident deuteron beam. As computational tool the finite element fluid flow analysis code FIDAP has been selected.

Preliminary calculations [8] have revealed that:

- as the flow is convection dominated it is particularly important to provide an accurate simulation of the velocity distribution

Therefore we extended our studies to incorporate both the hydraulic analysis of the flow in the nozzle and the thermal hydraulic simulation of the lithium jet with free surface.

The basic configuration studied is represented in Fig. 7.

As target nozzle we assumed a 2-D symmetric Shima type reducer which has the advantage of an analytical shape description. The target itself is of a curved backwall type, as recommend in [9] The heat deposition is modeled through the stopping of a deuteron beam with the characteristics listed in Fig. 7.

Thermal Hydraulic Response of Li Target with Incident Deuteron Beam

Simulation:

- Finite element code FIDAP
- Turbulence model: k-ε
- Heat transfer model: turbulent Prandtl number

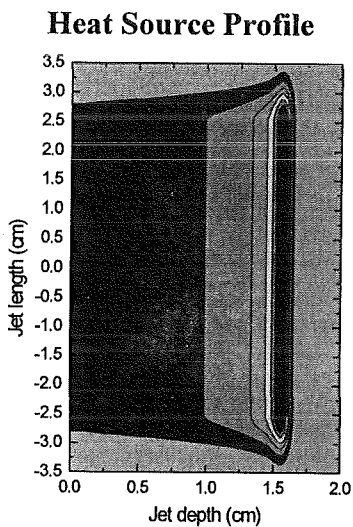
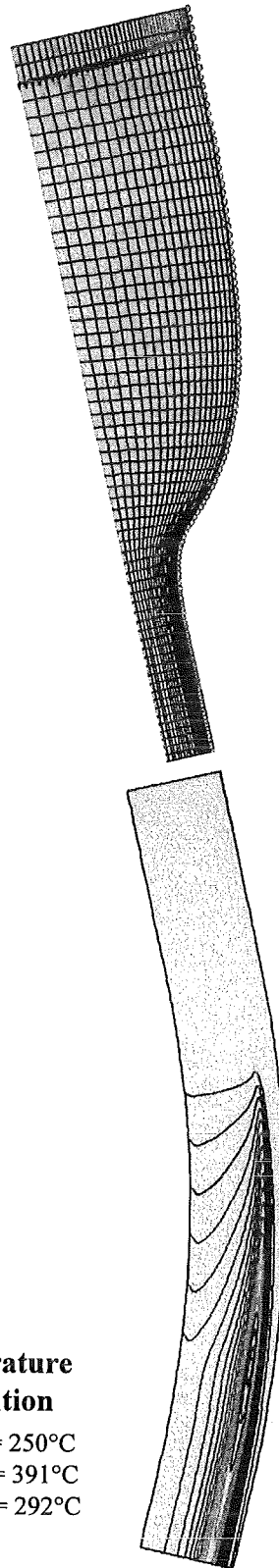
Configuration:

- 2-D Shima reducer model
- Curved backwall target design

Heat Source Calculation:

Based on the heat deposition distribution of the following beam spatial profile

- Vertical direction: flat top of 5 cm; Gaussian edges of 1 cm
- Horizontal direction: flat with sharp edges
- current density on flat top = 2.08 mA/cm²
- average power deposition = 76 kW/cm²



(max. power density ≈ 150 kW/cm³)

Temperature distribution

- $T_{inlet} = 250^{\circ}C$
- $T_{max}(jet) = 391^{\circ}C$
- $T_{max}(FS) = 292^{\circ}C$

Fig. 1: Set-up for the calculation of the thermal hydraulic response of lithium target with incident deuteron beam

Typical results for different initial flow conditions are given in Table 1. The reference calculation results correspond to the case B ($U = 17.4$ m/s @ $Pt = 1.6$).

As expected, the laminar model predicts higher temperatures both in the jet and at the free surface (FS) and, consequently a narrower boiling margin at the free surface. The heat transfer

in the turbulent flow was described within the turbulent Prandtl number model. A value of $Pt = 1.6$ has been chosen in agreement with the global Reynolds number of the flow. The evaporation rate was calculated in the molecular beam approach. The use of Monte Carlo Direct Simulation method

Table 1: Laminar and standard $k-\epsilon$ turbulence model calculations for different flow initial conditions

		CAS A	CAS B	CAS C	
max. velocity at nozzle inlet (m/s)		4.2	5	6	
max. jet velocity (inlet) (m/s)		15	17.9	21.5	
average jet velocity (inlet) (m/s)		14.6	17.4	20.9	
inlet temperature (°C)		250	250	250	
jet max. temp. (°C)	laminar	504.7	467	433	
	$P_t = 1.6$	420.8	391.1	367.7	
F.S. max. temp. (°C)	laminar	309.4	300	291.7	
	$P_t = 1.6$	301.3	292.8	285.6	
max. press. diff. across jet (Pa)	laminar	9238	13147	18986	
	$P_t = 1.6$	9110	12967	18733	
F.S. boiling margin (°C)	laminar	33.6	43	51.3	
	$T_b = 343^\circ\text{C}$ at $P = 10^{-3}$ Pa	$P_t = 1.6$	41.7	50.2	57.4
	$T_b = 300^\circ\text{C}$ at $P = 10^{-4}$ Pa				
evaporation rate $\times 10^{10}$ (Kg/s)	laminar	6.89	4.38	2.96	
	$P_t = 1.6$	4.58	3.04	2.15	

vaporization in general seems to be small for beam and jet parameters studied. However, for relatively low pressures in the vacuum chamber one can note that the boiling margin at the free surface is the limiting issue of the lithium target design.

The impact of the amount of vaporized lithium, its deposition and its interaction with incident deuteron beam need further analysis. The hydraulic analysis and optimization of target nozzle of different configurations is in progress.

Literature:

- [8] W. Cherdron, W. Schütz and I. Tiseanu, Thermal hydraulic analysis of IFMIF target with incident deuteron beam, Proc. of Jahrestagung Kerntechnik '96, Mannheim 21-23 Mai 1996, pp.609
- [9] IFMIF-CDA, Interim Report ORNL/M-4908, compiled by M.J. Rennich, Oak Ridge, USA, December 1995

Staff:

W.Cherdron
 W.Schütz
 I.Tiseanu

for the mass and energy transfer in the reaction chamber is also considered.

Boiling margins in the jet and at the FS have been calculated using the local pressure distribution (Fig. 8).

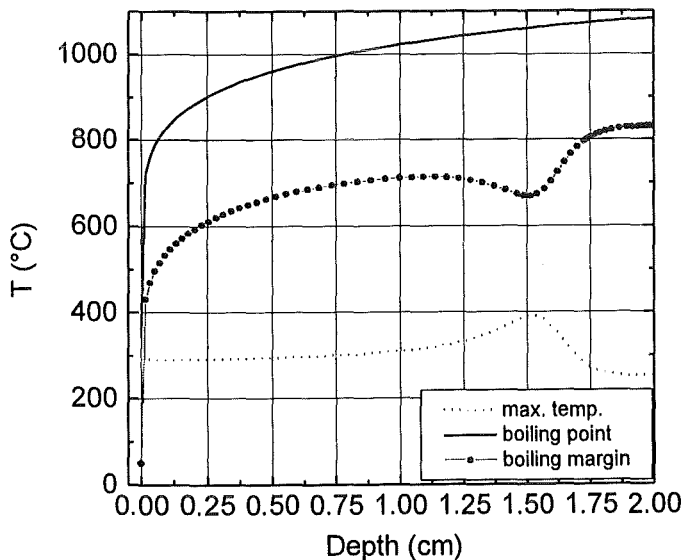


Fig. 8: Distribution of the boiling point and boiling margin

Due to centrifugal force inside the jet the pressure increases quasi-linearly until $p \approx 1.3 \cdot 10^4$ Pa. Two cases for the pressure in the vacuum chamber were considered:

$p = 10^{-3}$ Pa which correspond to a lithium boiling point $T_b = 343^\circ\text{C}$ and $p = 10^{-4}$ Pa with $T_b = 300^\circ\text{C}$. Surface

Nuclear Data Base

Since 1959 the development of a nuclear data base is an integral part of the European Long-Term Programme.

In the framework of this programme, FZK contributes to the development and qualification of the European Fusion File (EFF), the European Activation File (EAF) and the International Fusion Evaluated Nuclear Data Library (FENDL).

Validation of the FENDL-1 nuclear data library and development of an improved file version FENDL-2

An international benchmark validation task, co-ordinated by FZK, has been conducted to validate the Fusion Evaluated Nuclear Data Library FENDL-1 through data tests against integral 14-MeV neutron experiments [1,2]. The main objective of this task was to qualify the FENDL-1 working libraries for fusion applications and to elaborate recommendations for further data improvements. With regard to data quality, it was summarised that fusion nuclear data have reached a high confidence level with the available FENDL-1 data library. With few exceptions this is true for the materials of highest importance for fusion reactor applications. As a result of the performed benchmark analyses, existing deficiencies and discrepancies have been identified that were recommended to be removed in the forthcoming FENDL-2 data file.

In an IAEA Advisory Group Meeting on the start of FENDL-2, a priority list was adopted of candidate evaluations considered for replacing current FENDL-1 evaluations [3]. The materials included are Be, V, Fe, W (first priority), C, O, Al, Si, Zr (second priority) and D, N, Nb, Mo, Sn (third priority). As part of the selection procedure, the candidate evaluations from the data files JENDL-FF (Japan), ENDF/B-VI (USA), BROND (RF) and EFF-2, -3 were benchmarked against available integral experiments and FENDL-1 test calculations. Based on the data testing results and a careful review of the submitted cross-section evaluations, the selection shown in Table 1 was adopted in an IAEA Consultants' Meeting on the FENDL-2 selection [4].

Benchmark analyses for EFF-2.4 and EFF-3 data evaluations

In the framework of the EFF project, benchmark analyses are being performed as part of the quality assurance procedure for EFF-2 and -3 evaluations.

In 1996, the major effort was devoted to the benchmarking of the EFF-2 and -3 candidate evaluations for the FENDL-2 data library: ^9Be , ^{27}Al , ^{28}Si , ^{51}V , ^{56}Fe and the Mo-isotopes. A series of one- and three-dimensional benchmark calculations was performed for 14 MeV neutron transmission experiments on beryllium, iron, aluminium, silicon and molybdenum assemblies in spherical shell and slab geometry. Three-dimensional calculations were performed with the MCNP-code using EFF-1 -2, JENDL-FF and FENDL-1 data. One-dimensional calculations were performed with the ONEDANT transport code and multi-group data from the EFF-1, -2 and

the FENDL-1 data files. Table 2 shows an overview of the performed benchmark analyses. A comprehensive documentation of the benchmark results is under preparation.

Preparatory calculations for a breeder blanket mock-up experiment.

A nuclear breeder blanket mock-up experiment is planned to be performed at the Frascati Neutron Generator (FNG) [5]. The objective of this experiment will be to validate the nuclear performance of the ITER breeding blanket with regard to its breeding and shielding performance and the nuclear heating. The ITER shielding blanket mock-up, being currently investigated at FNG, will have to be replaced by a suitable mock-up of the ITER breeding blanket. Three-dimensional MCNP-calculations were performed to define a suitable material configuration for the breeder blanket mock-up that is backed by a vacuum vessel and a toroidal field coil mock-up in the FNG experiment. In the calculations for the breeder blanket mock-up, the ITER inboard breeder blanket has been modelled with regard to its radial build (two 1 cm thick breeder layers embedded between large beryllium blocks with a total blanket thickness of 25 cm). The lateral dimensions were varied from 100 cm x 100 cm to 40 cm x 40 cm and the impact of different reflector materials on the nuclear responses in the central mock-up channel was analysed. The results indicate that the lateral dimensions of the breeder blanket mock-up can be reduced to 40 cm x 40 cm when it is surrounded by a suitable reflector like steel or aluminium (Fig. 1).

Literature:

- [1] U. Fischer et al., Benchmark Validation of the FENDL-1 Nuclear Data Library - A Co-ordinated International Effort, 12th Topical Meeting on the Technology of Fusion Energy, Reno, NV, June 16-20, 1996.
- [2] U. Fischer (Ed.), Integral Data Tests of the FENDL-1 Nuclear Data Library for Fusion Applications, Summary Report of the International Working Group on 'Experimental and Computational Benchmarks on Fusion Neutronics for FENDL Validation', FZKA-5785, INDC(GER)-41, August 1996.
- [3] A. B. Pashchenko, Summary Report of the IAEA Advisory Group Meeting on Completion of FENDL-1 and Start of FENDL-2, Del Mar, CA, December 5-9, 1995, INDC(NDS)-352, March 1996.
- [4] A. B. Pashchenko, Summary Report of the IAEA Consultants' Meeting on Selection of Basic Evaluations for the FENDL-2 Library, Karlsruhe, June 24-28, 1996, INDC(NDS)-356, September 1996.

Table 1: Nuclear data evaluations selected for the FENDL-2 library

Material	Priority	FENDL-1 Evaluation	FENDL-2 Selection
⁹ Be	1	ENDF/B-VI	JENDL-FF
⁵¹ V	1	ENDF/B-VI	JENDL-FF
⁵⁶ Fe	1	ENDF/B-VI	EFF-3
^{nat} W	1	ENDF/B-VI (W isotopes)	JENDL-FF
¹² C	2	ENDF/B-VI	JENDL-FF
¹⁶ O	2	ENDF/B-VI	JENDL-FF
²⁷ Al	2	JENDL-3	EFF-3
^{28, 29, 30} Si	2	BROND-2 (^{nat} Si)	ENDF/B-VI
^{nat} Zr	2	BROND-2 (Zr isotopes)	JENDL-FF
² H	3	BROND-2/ENDF/B-VI	BROND-2
¹⁴ N	3	BROND-2/ENDF/B-VI	JENDL-FF
Ga	3	-	JENDL-FF
⁹³ Nb	3	BROND-2	JENDL-FF
^{nat} Mo	3	JENDL-3 (Mo isotopes)	JENDL-FF
^{nat} Sn	3	BROND-2	BROND-2

[5] U. Fischer, Nuclear Mock-up Experiment for ITER Breeding Blanket, EFF-Doc-488, Fusion Data & Neutronics Monitoring Meeting (EFF/EAF-Projects), NEA Data Bank, Paris, July 2-4, 1996.

Staff:

U. Fischer
E. Wiegner
Y. Wu

Activation Library

Low activation materials are one of the critical issues in the design of reactor blanket and first wall. The activation performance of a material is predicted with codes and data libraries such as the European Activation System (EAS, [6]). The objectives of the subtask are the experimental validation of these tools and integral activation measurements with potential structural materials.

The programme started in 1995 with investigations on the low activation steel MANET from FZ Karlsruhe and the ITER structural material SS316. Complementary to irradiations at FZ Karlsruhe with a cyclotron-based fast neutron source, the

contribution of TU Dresden consists in activation experiments with 14 MeV neutrons.

The irradiations were carried out at the facility SNEG-13 which is the most powerful existing 14 MeV neutron generator, in Sergiev Posad in collaboration with the Russian Research Centre "Kurchatov Institute" Moscow and the Coordination Centre "Atomsafety".

14 MeV neutron fluences of $1.36 \times 10^{14} \text{ cm}^{-2}$ and of $2.16 \times 10^{14} \text{ cm}^{-2}$ were simultaneously applied at two sample positions of 4 deg and of 73 deg, respectively, with respect to the generator axis. The slightly different spectral distributions of the source neutrons at these positions were selected, because many of the fast neutron activation reactions have thresholds just around 14 MeV. The neutron fluences were monitored by the Nb(n,2n)-reaction.

The activities induced were measured with Ge-detectors at several cooling times. The count rates are sufficient to take gamma-spectra up to three years after the irradiation. Calculations of the sample activities were carried out with the code FISPACT [6] and data from the European Activation File (EAF-4.1 [7] and EAF-DEC-41).

An example of the calculations is given in Fig. 1. It shows the different dominating activities appearing with increasing cooling time. With the activities determined at two or three

Table 2: Benchmark analyses performed for EFF-2 and -3 evaluations

Material	Experiment	Measured Quantity	Computational Analyses
Beryllium	KANT spherical shell transmission experiment	Neutron leakage spectra	MCNP & EFF-2, JENDL-FF, FENDL-1 ONEDANT & EFF-1, -2, FENDL-1
	FNS slab experiment	TOF angular neutron spectra	MCNP & EFF-2, JENDL-FF, FENDL-1
	OKTAVIAN spherical shell experiment	Neutron leakage spectra	MCNP & EFF-2, JENDL-FF, FENDL-1 ONEDANT & EFF-1, -2, FENDL-1
	IPPE spherical shell experiment	Neutron leakage spectra	MCNP & EFF-2, JENDL-FF, FENDL-1 ONEDANT & EFF-1, -2, FENDL-1
Iron	TUD slab transmission experiment	Neutron & gamma leakage spectra	MCNP & EFF-2, JENDL-FF, FENDL-1
	FNS slab transmission experiment	TOF angular neutron spectra	MCNP & EFF-2, JENDL-FF, FENDL-1
	FNS slab experiment	„In-system“ neutron spectra	MCNP & EFF-2, JENDL-FF, FENDL-1
	IPPE spherical shell experiments	Neutron leakage spectra	MCNP & EFF-2, JENDL-FF, FENDL-1
Aluminium, silicon, molybdenum	OKTAVIAN spherical shell transmission experiments	Neutron leakage spectra	MCNP & EFF-2, JENDL-FF, FENDL-1

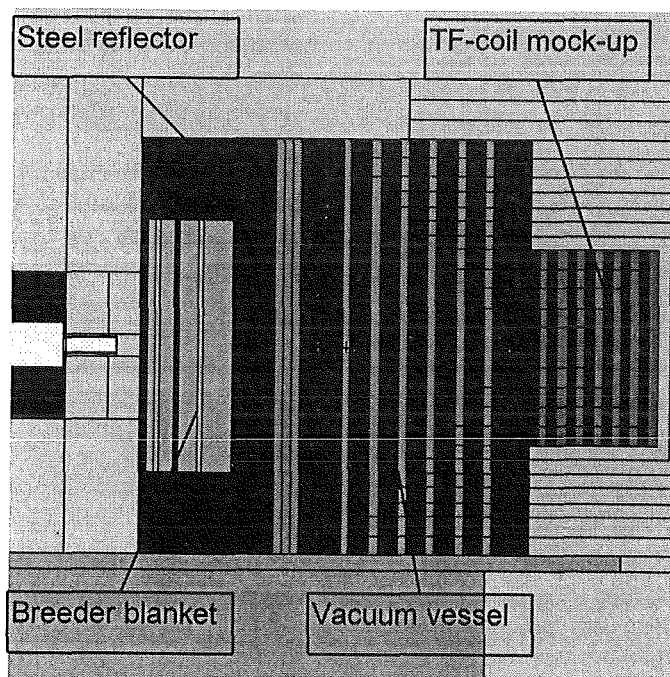


Fig. 1: MCNP model of the breeder blanket mock-up assembly

SS316(TUD)+14MeV NEUTRONS(4DEG)

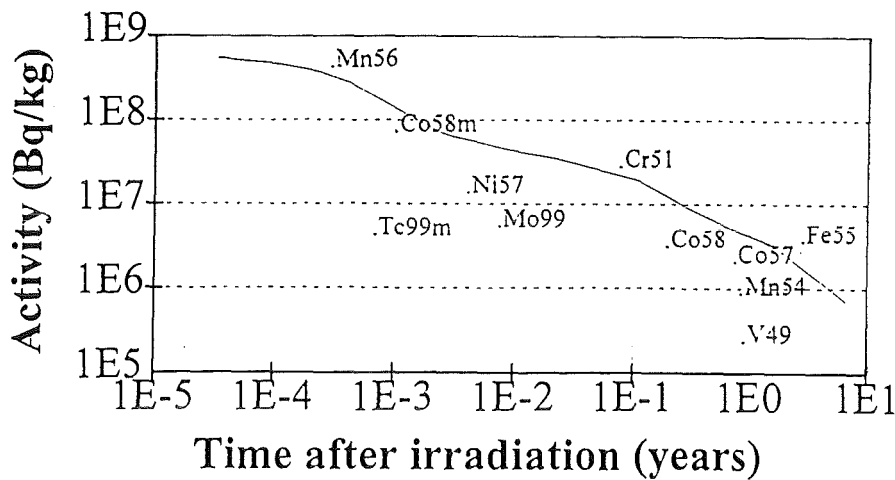


Fig. 2: Calculated total activity of a SS316 sample vs cooling time and indication of the dominating partial activities

years after irradiating the sample performance can be extrapolated to several ten years.

A comparison of experimental with calculated results is presented in Table 3. The ratios of calculated-to-experimental values (C/E) are good at this short cooling time. They are different for the source neutron spectra at 4 deg and at 73 deg, respectively, although this was taken into account in the calculations.

A detailed discussion of all activities measured over a period of about nine months is in progress. It includes comparisons with the results obtained at the Karlsruhe cyclotron-based neutron source.

Literature:

- [6] R. A. Forrest and J.-Ch. Sublet, Report UKAEA-FUS 287, Culham, 1995
- [7] J. Kopecky and D. Nierop, Report ECN-95-072, Petten, 1995

Staff:

H. Freiesleben
D. Richte
K. Seidel
S. Unholzer

In the framework of the European Activation File (EAF) task of the European Fusion Technology programme, the EAF data relevant to the steel types MANET-2 and F82H-mod have been tested ('benchmarked') experimentally. Samples were activated in a 'white' neutron field of about 1.4×10^{11} /cm²/s produced on a thick beryllium target by a 19-MeV deuteron

beam of the Karlsruhe Isochron-Zyklotron. This flux density is higher than what is available at any d+T neutron source existing in the European Union. The γ activity of the samples was measured repeatedly after different cooling times using a 150 cm³ high-purity germanium detector with a personal-computer based multichannel analyzer. The number of channels was 4096, covering an energy range of either 0 to 2 or 0 to 4 MeV.

The data are compared with 175-group calculations using the FISPACT-4.1/00 code and the EAF-4.1(0) library. The d+Be neutron spectrum for use in the calculations was derived from an existing semiempirical spectrum valid for 54-MeV deuterons, which is the superposition of a measured spectrum for neutron energies above 12 MeV and a calculated evaporation neutron spectrum down to 1 MeV. This spectrum was scaled to the deuteron energy of 19 MeV using some simple physical assumptions. The resulting spectrum at the irradiation sample is shown in Fig. 3. It has a broad maximum at about 9 MeV, where a typical fusion reactor spectrum (as also shown in Fig. 3) has a minimum. Below this energy, the d+Be source spectrum decreases steeply and is practically zero at thermal energy. It is, therefore, very different from a d+T fusion spectrum (see below). This is considered an advantage because, together with similar experiments using d+T neutron sources, it should result in a broader data base for validating the evaluated activation cross sections.

The chemical composition of MANET-2 was taken from the manufacturer's certificate for the production batch. In case of F82H-mod, chemical analyses performed at Karlsruhe were used.

The absolute d+Be neutron source strength at a given deuteron beam current is difficult to estimate. Therefore, the C/E results shown in Table 4 have been arbitrarily normalized to the value for Mn-54. A measurement of the source spectrum by activating selected pure foils has been

Table 3: Comparison of measured and calculated activities (A) and C/E values for a SS316 sample irradiated at the 73 deg position, after a cooling time of 9h:57min (as well as C/E for the 4 deg position)

Nuclide	E_{γ}/keV	I_{γ} per decay	$A_{\text{exp}}/\text{s}^{-1}$	$A_{\text{calc}}/\text{s}^{-1}$	C/E	C/E (4 deg)
Cr 51	320.1	0.0983	3.51E+4	3.48E+4	0.99	1.22
Ni 57	1377.6	0.7790	1.13E+4	1.31E+4	1.16	1.43
Mo 99	181.1	0.1219	6.22E+3	7.56E+3	1.22	1.45
Co 58	811.8	0.9945	5.59E+3	5.95E+3	1.06	1.02
Co 57	122.1	0.8552	2.99E+3	2.85E+3	0.99	1.01
Mn 54	834.8	0.9998	1.12E+3	1.38E+3	1.23	1.43
Nb 96	460.0	0.2765	3.17E+2	2.83E+2	0.83	0.53
Nb 92m	934.4	0.9900	1.89E+2	1.58E+2	0.84	1.35
Zr 89	909.2	0.9987	1.51E+2	1.55E+2	1.03	1.53
Sum			6.28E+4	6.62E+4	1.05	1.25

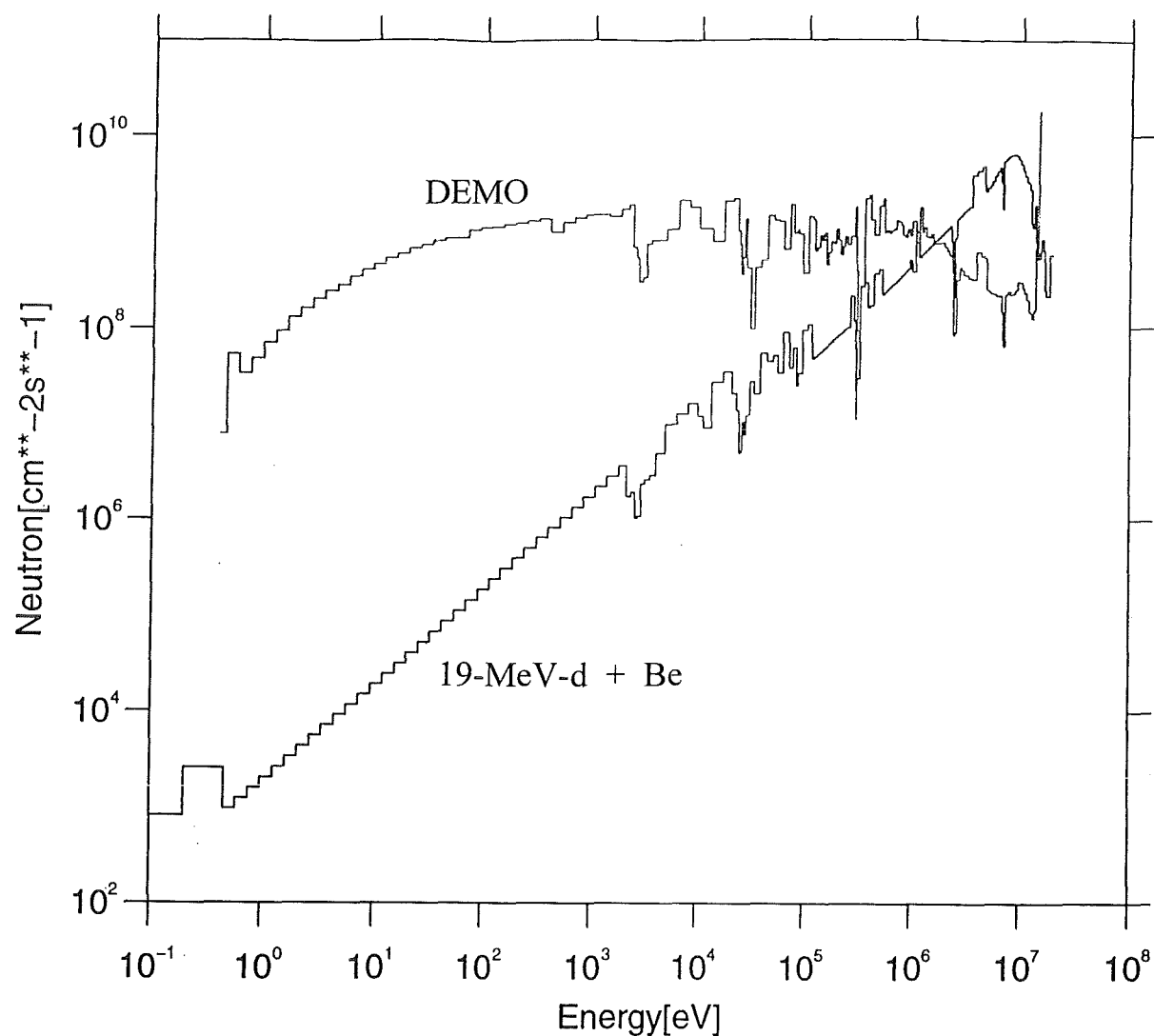


Fig. 3

performed in collaboration with JAERI (Japan). Its evaluation is in progress. The resulting absolute spectral source strength will lead to a more reliable and absolute determination of the C/E values.

Table 1: Calculation/experiment ratios C/E, normalized to Mn-54

Nuclide	$T_{1/2}$	f_a %	$(C/E)_{norm}$
MANET-2, $T_c = 181$ h			
Mn-54	312 d	24.7	1.00
Cr-51	28 d	39.3	0.76
Mo-99m	66 h	5.7	0.76
Nb-92m	10 h	3.2	0.86
F82H-mod, $T_c = 87$ h			
Mn-54	312 d	33.9	1.00
Cr-51	28 d	41.7	0.45
Fe-59	45 d	0.04	0.60
Co-57	272 d	0.01	0.36
Co-58	71 d	0.4	0.96
Co-60	5.3 a	<0.008	0.93
Nb-92m	10 d	0.01	1.92

$T_{1/2}$: Halflife
 T_c : Cooling time
 f_a : Fraction of sample activity at T_c

The conclusion from the present, preliminary results is that FISPECT/EAF reproduces the major medium-half-life radionuclides in the two steels reasonably, but that improvements to some minor activation cross sections may be required. The C/E are reasonable even in case of radionuclides resulting from sample constituents of very low concentration, such as Mo-99m and Nb-92m in MANET, which originate from the 0.6% Mo content, or Nb-92m in F82H-mod, originating from an 800-ppm Nb content. This indicates that the experimental method is quite reliable independently of the relative intensity of the γ ray lines. The rather low Co-57 activity, due to the $^{58}\text{Ni}(n,d)$ reaction, is an exception and will be verified further.

Staff:

U. von Möllendorff

H. Giese

H. Tsige-Tamirat

Safety and Environmental Assessment - Long Term Programme

SEAL is a follow-up to the SEAFP-Study, "Safety and Environmental Assessment of Fusion Power", which was completed in December 1994.

SEAFP is a comprehensive European study on the subject matter and incorporates all relevant aspects of fusion power safety environmental impact for which data were available. However, some of the input data used in the study had to be extrapolations or guesswork, or simply could not be precise enough, so that conclusions in the study were drawn with some reservations and need to be hardened. Therefore, some of the aspects of the study have to be elaborated in more detail.

In addition, it seemed to be desirable to apply to the blankets and materials which are the subject matter of the European Long-Term Technology Programme, a "SEAFP-Type" analysis in order to see how they would perform, from the safety point of view, in a power reactor.

Therefore, a long-term safety and environmental assessment programme (SEAL) was generated by the Commission. This programme is composed of 10 Tasks and encompasses amongst others

- the assessment of tritium retention by, and chemical reactions of, irradiated Beryllium;
- the analysis of multiple failure sequences;
- the missing safety analysis of blankets and materials.

FZK contributes to the Tasks:

- SEAL 1 Investigation of irradiated Beryllium,
- SEAL 2 Activation of Source Terms, and
- SEAL 6 Blanket Safety Analysis.

SEAL 1.3 Modelling of Beryllium Behaviour Under Irradiation

Solid breeder blankets of fusion reactors require beryllium as neutron multiplier to achieve adequate tritium breeding. In the fast neutron field of the blanket, helium and tritium are produced in beryllium. Therefore, besides compatibility with other blanket materials, helium-induced swelling and tritium retention are of concern.

To describe the irradiation behaviour of beryllium the computer code ANFIBE has been developed at the Forschungszentrum Karlsruhe[1]. In order to better understand the physical mechanisms governing tritium release behaviour in beryllium, as well as to generate

confidence in the results provided by the code ANFIBE and to assess its prediction capabilities, it was necessary to compare the calculated results with a large number of reliable experimental data as described in [1].

In the frame of the SEAL Programme, release kinetics of neutron-generated tritium of beryllium samples provided by SCK/CEN Mol [2,3] irradiated up to very high fast neutron fluences of $3.9 \cdot 10^{22} \text{ cm}^{-2}$ in the BR2 reactor and successively out-of-pile annealed at high temperature at the Forschungszentrum Karlsruhe [4] was investigated.

In the first case the behaviour of the sample 110A-9c.3 (fast fluence $0.8 \cdot 10^{22} \text{ cm}^{-2}$) was investigated. The in-pile irradiation was followed by a temperature ramp with a slope of about $5 \text{ }^\circ\text{C}/\text{min}$ from room temperature up to $850 \text{ }^\circ\text{C}$. As shown in Fig. 1, the tritium release rate has a rapid increase during the temperature ramp and then it tends to slowly decrease as the annealing temperature remains constant. The comparison between calculated and experimental data shows in this case a good agreement. On the contrary, for the sample 110A-9a.3, which was irradiated with a fast neutron fluence of $2.8 \cdot 10^{22} \text{ cm}^{-2}$ and successively out-of-pile annealed up to $850 \text{ }^\circ\text{C}$ in the same way as the previous one, a sharp peak is observed in the experimental tritium release rate curve during the temperature ramp probably because of microcracks formation. Due to the higher neutron fluence, in fact, the beryllium specimens has become more brittle than in the previous case and consequently it easily cracked under thermal stresses. Since ANFIBE doesn't account yet for the effect of the microcracks, the code prediction cannot be, in this case, in good agreement with the experimental data as for sample 110A-9c.3.

Pre and post calculations of other SCK/CEN irradiation experiments performed under the subtask 1.1 as well as of the JRC experiments performed under the subtask 1.4 will be further performed depending on the availability of the experimental results. However, although at this stage not all the mechanisms governing the release of tritium in irradiated beryllium have been fully understood, comparison of the code predictions with experiments [1] indicate that, for the cases considered so far, the most important phenomena were accounted for by ANFIBE.

Literature:

- [1] F. Scaffidi-Argentina, "Modellierung des Schwellens und der Tritium-Freisetzung von bestrahltem Beryllium", FZKA Report 5632, Karlsruhe, Oktober 1995.
- [2] L. Sannen, "Characterization of Irradiated Beryllium", CEN Mol Report FT/Mol/92-01, July 1992.
- [3] L. Sannen, Ch. de Raedt, "The Effects of Neutron Irradiation on Beryllium", Proceedings of the SOFT-17 Conference, Rome, 1992.

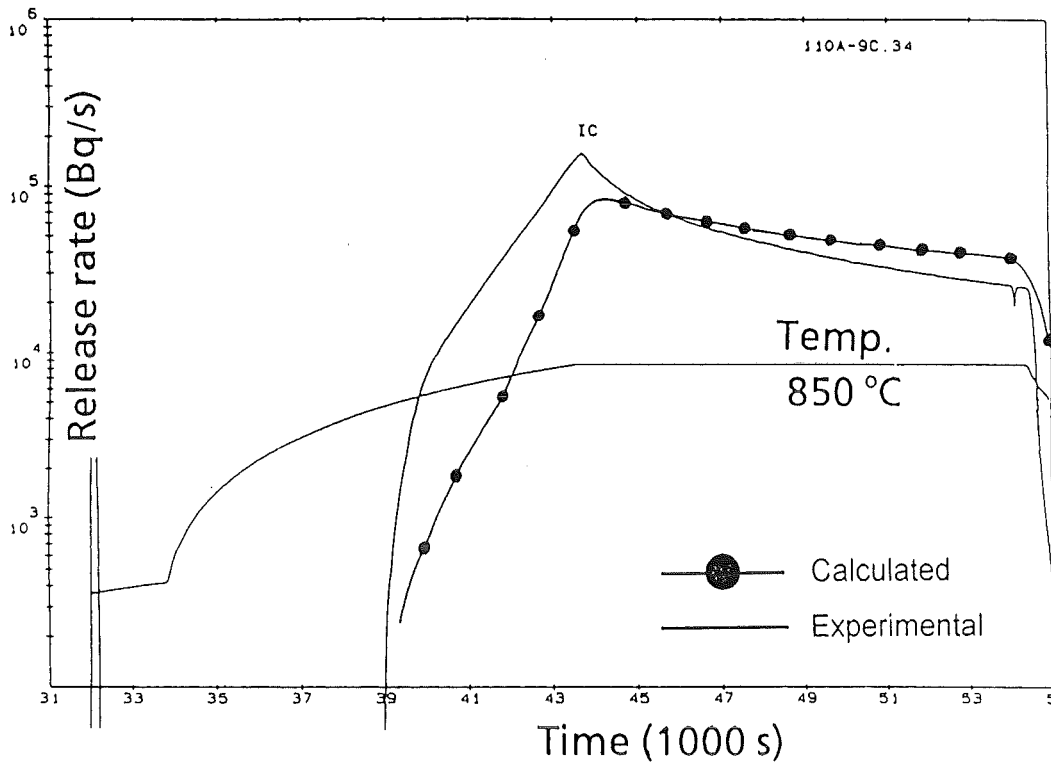


Fig. 1: Comparison of calculated and measured tritium release rate as a function of time for moderately irradiated beryllium (fast fluence $0.8 \cdot 10^{22} \text{ cm}^{-2}$, MOL sample 110A-9c.3)

[4] F. Scaffidi-Argentina, H. Werle, "Tritium Release from Neutron Irradiated Beryllium: Kinetics, Long-Time Annealing and Effect of Crack Formation", Proceedings of the 2nd IEA International Workshop on Beryllium For Fusion, Jackson Lake Lodge, September 6-8, 1995, CONF-9509218.

Staff:

M. Dalle Donne
 F. Scaffidi-Argentina

SEAL 2.2 Activation and Source Terms

Safety and environmental assessments of fusion power plants need a sound and reliable data base of the activation product inventory accumulated in the reactor components during power operation. To this end, three-dimensional activation and afterheat calculations have been performed in the framework of sub-task 2 for the SEAFP reference blanket model [1], a helium-cooled ceramic B.O.T. blanket with Li_2O pebbles, 30 at% ^6Li -enrichment, beryllium multiplier and V-5Ti alloy structure.

Coupled activation and neutron transport calculations were performed with the FISPACT-code linked through an interface to the Monte Carlo transport code MCNP. A torus sector model of the SEAFP baseline reactor concept [2], developed previously by ENEA Frascati, formed the basis of the three-dimensional calculations (Fig. 1). Activation cross-

section data were taken from the European Activation File EAF-4. Activation characteristics have been determined for the poloidally arranged blanket segments, the manifolds and the divertor.

Comprehensive numerical results of the activation calculations are given in the documentation report on SEAL sub-task 2 [3].

Literature:

- [1] W.Dänner, G. Simbolotti: Final Report on Task M6, Blanket Design, SEAFP/R-M6 (95), March 1995.
- [2] J. Raeder, H. W. Bartels: Reference Blanket Model and Alternative Plant Model, SEAFP/R-2(94), August 1994.
- [3] U. Fischer, L. Petrizzi, H. Tsige-Tamirat: Three-dimensional Activation Calculations for the SEAFP Reference Blanket Model, Forschungszentrum Karlsruhe, Draft Report, May 1996

Staff:

U.Fischer
 H.Tsige-Tamirat

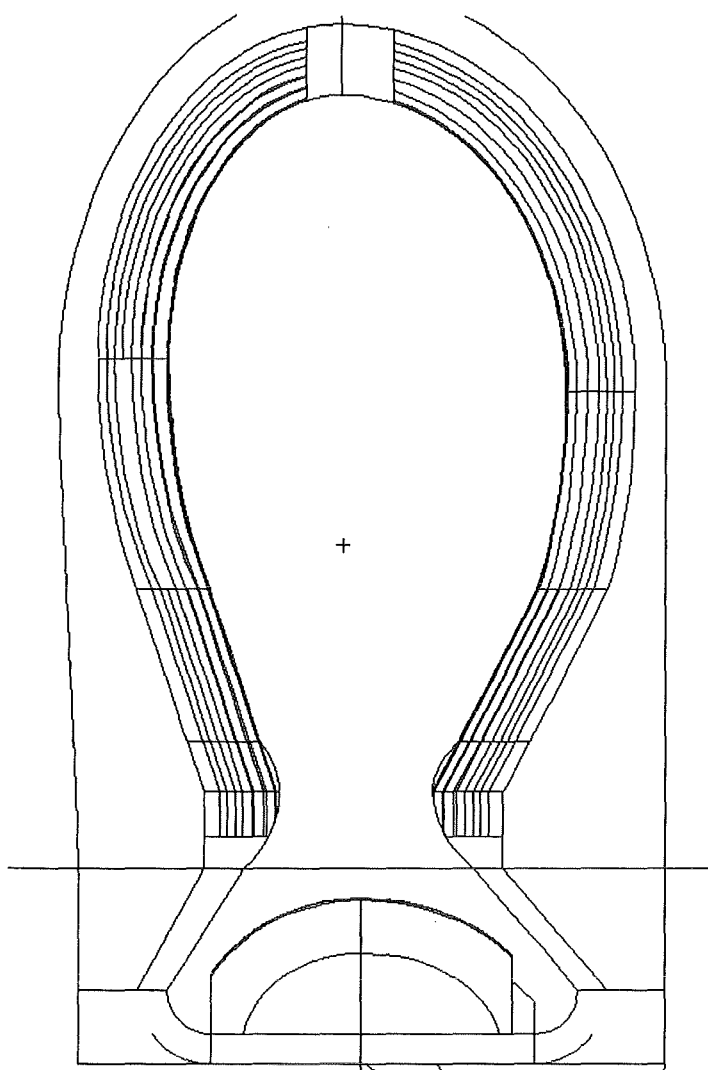


Fig. 1: Vertical cross-section of the SEAFP reactor model as used in the three-dimensional activation calculations

SEAL 6.2 Blanket Safety Analysis - Input of the Dual-Coolant Blanket and the Ceramic Breeder Blanket

The task as a whole comprises studies, performed mainly by UKAEA, of the safety and environmental impact of the four DEMO blankets developed until 1995 within the European fusion programme. Under this subtask the necessary input for the two blanket designs developed at Karlsruhe, the dual coolant concept and the helium-cooled pebble bed concept, was provided by means of documentation (References [1] and [2] from section B 7.1.1) and recurring discussions of the results.

Staff:

K. Kleefeldt

Appendix I: Allocation of Tasks

Task No.		Title	FZK Departments
----------	--	-------	-----------------

Plasma Facing Components and Plasma Engineering

G 17 TT 25	(T 227)	Tritium Permeation and Inventory	INR
CTA-EU-T 9		Fabrication and Test of Water-Cooled, Small Size FW Mockups	IMF II, IATF
G 17 TT 25	(T 226 b)	Plasma Disruption Simulation	INR
G 55 TT 01	(T 26/T 246)	Ceramics for Heating and Current Drive and Diagnostic Systems	IMF I

Superconducting Magnets

MCOI		ITER TF-Model Coil Development	ITP
N 11 TT 19 94-02-15 FE 0	(MTOS 1)	Preparation of ITER TF-Model Coil Test Facility	ITP, HPE, HVT
MBAC		High Field Operation of NbTi at 1.8 K	ITP, HPE
M 27		Critical Current vs. Strain Tests on EU Strands and Subsize CICC's with Stainless Steel and Incoloy Jackets	ITP
M 31		Development of 60 kA Current Leads Using High Temperature Superconductors	ITP
N 11 TD 58	(SEA 3)	Reference Accident Sequences - Magnet Systems	IRS
CTA-EU-D 36	(SEP 2)	Environment Impact	INR

Vacuum and Fuel Cycle

G 18 TT 22	(T 228)	Cryopump Development	HIT
T 234 A		Oil-Free Mechanical Pump Development	HIT
N 32 TT 06	(T 299/T 332 b)	Plasma Exhaust Processing Technology	HVT/TLK
TEP 3		Tritium Storage	HVT/TLK

Vessel in-Vessel

G 16 TT 82	(T 218)	Shielding Neutronics Experiments	TU Dresden, INR
G 16 TD 21	(D 203)	ITER Breeding Blanket Development and Design	IRS, IMF III

Gyrotron and Window Development

Gyrotron Development (includes ITER Tasks T 24 and T 245/6)			ITP
High Power ECW Windows (includes ITER Tasks T 25, T 245/6 and D 321)			IMF I, IMF III, ITP

Blanket Development Programme

WP A 1 Design and Analysis			
	A 1.1.1	Design and Fabrication Alternatives for the Blanket Box	IRS
	A 1.4.1	Availability Analysis and Data Base	IRS

WP A 3 Pb-17Li Physico-Chemistry Experiments

A 3.1.1	Radiological Important Impurities and Nuclides	HIT
A 3.1.2	Behavior and Removal of Corrosion Products	HIT
A 3.3.1	Li Behavior and Adjustment	HIT

WP A 4 MHD

A 4.1.1 / 4.2.1	Theoretical and Experimental Investigations on Natural Convection in WCLL under MHD Conditions	IATF
-----------------	--	------

WP A 5 Tritium Control including Permeation Barriers

A 5.1.1	Coating and Tritium Barrier Development	IRS
A 5.3.2	Influence of the Magnetic Field on the Self-healing of Tritium Permeation Barriers in Flowing Pb-17Li	IATF

WP A 7 Safety related Activities for DEMO and ITER Test Module

A 7.1.1	Safety Studies for DEMO Blanket and ITER Test Module	IRS
---------	--	-----

WP B 1 Design and Analysis

B 1.1.1	Design Optimization/Adaptation to Updated DEMO Conditions	IMF III, INR, IRS
B 1.2.1	Design, Layout and Integration of ITER Test Module and Internal Circuits	IMF III, INR, IRS
B 1.3.1	Electromagnetic Effects with a Ferromagnetic Structural Material	INR, IRS
B 1.3.2	Calculation of the Combined Stresses in the Blanket and Test Module	INR
B 1.4.1	Reliability Assessment including Ancillary Systems	IRS

WP B 2 Fabrication, Assembly and Development Studies of Blanket Segments

B 2.1.1	Fabrication, Assembly and Development Studies of Segment Box and Cooling Plates	IMF II, IMF III, IRS
---------	---	----------------------

WP B 3 Ceramic Breeder Pebbles

B 3.1.1	Li ₄ SiO ₄ Pebbles Characterization and Optimization of Large Scale Production	INR
B 3.2.1	Irradiation of Li ₄ SiO ₄ + TeO ₂ pebbles	INR, HVT/HZ

WP B 4 Beryllium Pebble Development

B 4.1.1	Characterization and Optimization of 2 mm and 0.1-0.2 mm Beryllium Pebbles	IMF I, IMF III, INR, HVT/HZ
B 4.2.1	Evaluation of Beryllium Irradiation Experiments and Improvements of ANFIBE	IMF III, INR, IVT/HZ

WP B 5 Tritium Control including Permeation Barriers

B 5.1.1	Calculation of Tritium Permeation Losses from Purge Gas System and First Wall	INR
B 5.2.1	Permeation Tests in Martensitic Structural Material and INCOLOY 800	IATF

WP B 6 Tritium Extraction

B 6.1.1	Design of Helium Purification and Tritium Purge Flow Systems including Tritium Extraction	HIT, HVT/TLK
---------	---	--------------

WP B 7 Safety related Activities for DEMO and ITER Test Module

B 7.1.1	Safety Studies for DEMO and ITER Test Module	IRS
---------	--	-----

WP B 8 ITER Test Module System and Testing

B 8.1.1 Tests in HEBLO and Preparation of a Submodule for HEFUS-3 IMF III, INR

Long Term Materials Programme

WP 1 Martensitic Steels

1.1 Metallurgical and Mechanical Characterization MANET IMF I
1.2.1 Metallurgical and Mechanical Characterization F82H mod. IMF I
1.2.2 Fatigue and Creep Properties of Base Material on LA Martensitic Steels F82H Mod IMF II
1.4.1 Metallurgical and Mechanical Characterization of OPTIFER Alloys IMF I
1.4.2 Fatigue and Creep Properties of Base Material on LA Martensitic Steels OPTIFER IMF II
1.5.0 / 1.5.1 MANITU Irradiation Program IMF II, HVT/HZ
1.6.1 / 1.6.2 Effects of Radiation Hardening and He in LAM / In-Beam Fatigue IMF I

WP 4 Materials Application and Technology

4.1.2 Fracture Mechanics Studies IMF II
4.3.1 Weldability Tests (Diffusion Welding) IMF II

Neutron Source

ERB 5000 CT 950013 NET (NET/94-366)
Conceptual Design of the International Fusion Materials Irradiation Facility IFMIF (Phase 2) IMF I, INR, IRS

Nuclear Data Base

TU Dresden, INR

Safety and Environmental Assessment - Long Term Programme

INR, IRS

Appendix II: Table of ITER / NET Contracts

Theme	Contract No.	
ITER Magnets and TFMC Stress Analysis	ERB 5000 CT 95 0064 NET	(NET/95-384)
Transient Voltage Behaviour for the ITER TF Coil	ERB 5004 CT 960050 NET	(NET/96-405)
Characterization of Jacket Material	ERB 5004 CT 960053 NET	(NET/96-408)
Conceptual Design of the International Fusion Materials Irradiation Facility IFMIF (Phase 2)	ERB 5000 CT 950013 NET	(NET/94-366)

Appendix III: FZK Departments Contributing to the Fusion Project

FZK Department	FZK Institut/Abteilung	Director	Ext.
Institute for Materials Research	Institut für Material- und Festkörperforschung (IMF)	I. Prof. Dr.K.-H. Zum Gahr	3897
		II. Prof. Dr. D. Munz	4815
		III. Prof. Dr. J. Haußelt	2518
Institute for Neutron Physics and Reactor Engineering	Institut für Neutronenphysik und Reaktortechnik (INR)	Prof. Dr. G. Keßler	2440
Institute for Applied Thermo- and Fluiddynamic	Institut für Angewandte Thermo- und Fluiddynamik (IATF)	Prof. Dr. U. Müller	3450
Institute for Reactor Safety	Institut für Reaktor-sicherheit (IRS)	Prof. Dr. D. Cacuci	2550
Central Engineering Department	Hauptabteilung Ingenieur-technik (HIT)	Dr. H. Rininsland	3000
Institute for Technical Physics	Institut für Technische Physik (ITP)	Prof. Dr. P. Komarek	3500
Central Experimental Engineering Department - Hot Cells - Tritium Laboratory Karlsruhe	Hauptabteilung Versuchstechnik (HVT) - Heiße Zellen (HVT-HZ) - Tritiumlabor Karlsruhe (TLK)	Dr. K. Schubert	3114
		Dr. W. Nägele	3650
		Dr. R.D. Penzhorn	3239
Central Department for Real-time Data Processing and Electronics	Hauptabteilung Prozeßdatenverarbeitung und Elektronik	Prof. Dr. H. Gemmeke	5635
<u>Contributing:</u>			
Institute for Nuclear and Particle Physics, Technical University Dresden	Institut für Kern- und Teilchenphysik der Technischen Universität Dresden	Prof. Dr. H. Freiesleben	0351/463.5461

Appendix IV: Fusion Project Management Staff

Head of the Research Unit	Dr. J. E. Vetter	ext. 5460
Secretariate:	Fr. I. Sickinger	ext. 5461
	Fr. I. Pleli	ext. 5466
	Fr. V. Lallemand	ext. 5466
Project Budgets, Administration, Documentation	BW G. Kast	ext. 5462
Studies, ITER / NET Contacts	Dr. J.E. Vetter	ext. 5460
Superconducting Magnets, Gyrotron Development		
Tritium Technology Structural Materials	Dr. H.D. Röhrig	ext. 5463
Blanket Technology	DI A. Fiege	ext. 5465

Address: Forschungszentrum Karlsruhe GmbH
 Nuclear Fusion Project Management

 Post Office Box 3640, D-76021 Karlsruhe / Germany

Telephone No: 07247-82- Extensions

Telefax No: 07247 - 82 - 5467

Telex No: 17 724 716

e-mail: de:d400:fzk:kfk:pro:pkf-leitung: or
 pkf-projektleitung@pro.kfk.fzk.d400.de

world wide web: <http://www.fzk.de.8080/PKF>